

UNIVERSIDADE DE LISBOA
INSTITUTO SUPERIOR TÉCNICO

Composite sandwich panel floors for building rehabilitation

Mário Alexandre de Jesus Garrido

Supervisor: Doctor João Pedro Ramôa Ribeiro Correia
Co-Supervisors: Doctor Fernando António Baptista Branco
Doctor Thomas Keller

Thesis approved in public session to obtain the PhD Degree in
Civil Engineering

Jury final classification: Pass With Distinction and Honour

Jury

Chairperson: Chairman of the IST Scientific Board

Members of the Committee:

Doctor Thomas Keller, Full Professor, École Polytechnique Fédérale de Lausanne, Switzerland
Doctor Rui Jorge Sousa Costa de Miranda Guedes, Associate Professor (with habilitation), Faculdade de Engenharia, Universidade do Porto
Doctor João Paulo Janeiro Gomes Ferreira, Associate Professor (with habilitation), Instituto Superior Técnico, Universidade de Lisboa
Doctor Nuno Miguel Rosa Pereira Silvestre, Associate Professor (with habilitation), Instituto Superior Técnico, Universidade de Lisboa
Doctor João Pedro Ramôa Ribeiro Correia, Associate Professor (with habilitation), Instituto Superior Técnico, Universidade de Lisboa
Doctor José Manuel da Sena-Cruz, Associate Professor, Escola de Engenharia, Universidade do Minho

Funding Institutions

Fundação para a Ciência e Tecnologia

2016

Abstract

Buildings with load-bearing masonry walls and timber floors often present serious rehabilitation needs. Structural strengthening or replacement of structural elements is a recurring necessity, and timber floors are among the structural elements that frequently need to be replaced. In fact, they often suffer from excessive deformations and are not able to comply with the current structural performance requirements. Traditional rehabilitation solutions, involving the construction of new timber floors or the adoption of different floor systems made of either reinforced concrete (RC), steel or composite (steel-concrete or timber-concrete) elements present numerous limitations.

In this thesis, an innovative building floor system is proposed for the replacement of degraded timber floors, making use of lightweight composite sandwich panels especially developed for application in building rehabilitation. The sandwich panels comprise glass-fibre reinforced polymer (GFRP) faces and ribs, and three different types of low density core materials: (i) polyurethane (PUR) foam, (ii) polyethylene terephthalate (PET) foam, and (iii) balsa wood. The proposed sandwich floor panels constitute a pre-fabricated solution that may be quickly assembled on site, with high strength- and stiffness-to-weight ratios, and not requiring additional maintenance during their service lives.

This thesis addresses three main aspects of the sandwich panel development: (i) the assessment of the most suitable materials and panel architectures for application in building floors, (ii) the development of the necessary connection technology, and (iii) the characterisation of the creep behaviour of the sandwich panels.

Regarding the assessment of materials and panel architectures, the solutions with the highest potential were selected based on a careful review of the technical literature combined with a technical and market study. Material characterisation tests were carried out for the different materials, in some cases taking into account the effects of temperature on their behaviour, as well as full-scale flexural characterisation tests to determine the static and dynamic mechanical response of the various sandwich panel typologies.

Connection systems were developed for the joints between adjacent sandwich panels (panel-to-panel) and for the connections between the floors and the building walls (panel-to-wall). The proposed panel-to-panel connections make use of Z-shaped adhesively bonded joints, whereas the developed panel-to-wall connections comprise steel angles anchored to the walls, and connected to the panels by either bolting, adhesive bonding, or a combination thereof. An experimental programme was carried out to assess the mechanical response of each type of connection. This was complemented with an extensive finite element modelling of the connections to assess local stress distributions and perform further numerical analyses.

The creep behaviour of the panels, which can be a limiting factor for their serviceability design due to the viscoelasticity of the polymers used in the panels, was studied both at the material (small-scale) and at the panel (full-scale) levels. The effects of service temperatures on the creep response of the PUR foam and the GFRP laminates was experimentally assessed and analytically modelled. The creep response of the remaining core materials was also evaluated, as well as that of full-scale panels of different typologies under uniformly distributed loads. A composed creep model (CCM) is proposed to predict the creep response of such panels, by taking into account the individual and independently determined viscoelastic responses of their constituent materials. Such a model has the advantage of allowing the substitution of onerous and cumbersome full-scale creep tests by small-scale material characterization tests, whose results can be readily used in the design of sandwich panels.

Keywords: composite sandwich panels, building floors, building rehabilitation, glass-fibre reinforced polymers (GFRP), polyurethane (PUR) foam, polyethylene terephthalate (PET) foam, balsa wood, adhesive connections, bolted connections, creep behaviour.

Sumário

Os edifícios antigos com paredes resistentes em alvenaria e pisos em madeira apresentam frequentemente necessidades de reabilitação prementes. O seu reforço estrutural ou a substituição de certos elementos estruturais representam algumas das intervenções mais recorrentes neste tipo de edificado, sendo que pisos de madeira são dos elementos estruturais que mais frequentemente carecem de substituição. De facto, muitas vezes, os pisos deste tipo apresentam deformações excessivas, não sendo capazes de cumprir as actuais exigências normativas relativas ao comportamento estrutural de edifícios. Soluções de reabilitação tradicionais, tais como a substituição por novos pisos de madeira, ou a instalação de novos pisos de betão armado, em aço ou mistos (aço-betão ou madeira-betão), apresentam diversas limitações quanto à sua aplicabilidade neste contexto.

Na presente tese, é proposto um sistema de piso inovador para a substituição de pisos de madeira degradados, fazendo uso de painéis sanduíche compósitos especialmente desenvolvidos para a reabilitação de edifícios. Os painéis sanduíche são constituídos por faces e nervuras em polímero reforçado com fibra de vidro (PRFV), utilizando três tipos diferentes de material de núcleo: (i) espuma de poliuretano (PUR), (ii) espuma de politereftalato de etileno (PET) e (iii) madeira de balsa. Os painéis propostos constituem um sistema pré-fabricado que pode ser rapidamente aplicado em obra, com elevados rácios resistência-peso e rigidez-peso, não requerendo manutenção adicional durante a sua vida útil.

Esta tese aborda três aspectos principais relativos ao desenvolvimento dos painéis: (i) a avaliação dos materiais e das arquitecturas de painel mais adequados para aplicação em pisos de edifícios, (ii) o desenvolvimento da tecnologia de ligações, e (iii) a caracterização do comportamento em fluência dos painéis sanduíche.

Relativamente à avaliação dos materiais e arquitecturas de painel, as soluções com mais potencial foram seleccionadas com base na revisão da literatura em conjunto com um estudo técnico-económico. Foram realizados ensaios de caracterização material, em alguns casos tendo em consideração os efeitos da temperatura nas propriedades mecânicas dos diferentes

materiais, assim como ensaios de flexão à escala real em painéis com diversas tipologias de forma a determinar a sua resposta estática e dinâmica.

Foram desenvolvidos sistemas para as ligações entre painéis adjacentes (painel-painel) e para as ligações entre os pisos e as paredes do edifício (painel-parede). As ligações painel-painel consistem em juntas adesivas com geometria em “Z”, enquanto as ligações painel-parede foram executadas utilizando cantoneiras metálicas chumbadas às paredes de alvenaria, e ligadas aos painéis por (i) colagem, (ii) aparafusamento, ou (iii) a combinação das duas técnicas anteriores. Foi desenvolvido um programa experimental para avaliar a resposta mecânica de cada tipo de ligação. Os diferentes tipos de ensaio foram simulados com modelos de elementos finitos, que permitiram obter uma melhor compreensão sobre as distribuições locais de tensões nas zonas de ligação e o desenvolvimento de análises numéricas adicionais.

A fluência dos painéis sanduíche, frequentemente condicionante para o seu dimensionamento em serviço dada a viscoelasticidade dos materiais poliméricos envolvidos, foi estudada à escala dos materiais e dos painéis. Os efeitos da temperatura de serviço na viscoelasticidade da espuma de PUR e dos laminados de PRFV foram determinados experimentalmente e modelados analiticamente. A fluência dos restantes materiais de núcleo foi também determinada, assim como a fluência dos painéis sanduíche de várias tipologias sob a acção de cargas uniformemente distribuídas. Foi proposto um modelo de fluência composto (MFC) para a previsão das deformações de fluência dos painéis, no qual são utilizadas as propriedades viscoelásticas dos seus diferentes materiais constituintes determinadas de forma individual e independente. Este modelo apresenta a vantagem de permitir a substituição de ensaios à escala real, onerosos e difíceis de realizar, por ensaios em pequena escala aos diferentes materiais, podendo ser facilmente utilizado na análise e dimensionamento de painéis sanduíche.

Palavras chave: painéis sanduíche compósitos, pisos de edifícios, reabilitação de edifícios, polímero reforçado com fibras de vidro (PRFV), espuma de poliuretano (PUR), espuma de politereftalato de etileno (PET), madeira de balsa, ligações adesivas, ligações aparafusadas, fluência.

Acknowledgements

More than an individual work, this thesis is the result of the combined efforts, the support and the good will of the many people with whom I have had the honour and the pleasure of working, discussing, collaborating, or simply living alongside with. Here, I would like to show my and appreciation for all of those who have helped me, in one way or another, throughout this journey.

I would like to thank my thesis supervisor, Prof. João Ramôa Correia, and my co-supervisors, Prof. Thomas Keller and Prof. Fernando Branco. The ever valuable advice, the wisdom beyond his years, and the constant comforting optimism of Prof. João Ramôa Correia were fundamental in the development of this thesis, and continue to help shape my attitude as a researcher and a professional. I owe much to his support, and I am especially grateful for his friendship. The impressive experience of Prof. Thomas Keller, combining civil engineering practicality with architectural awareness in both their academic and industrial dimensions, as well as his pragmatism and keen eye to quickly find the most important aspects within complex problems, were essential in defining the course of my research, and will remain with me as an inspiration for years to come. The continuous support of Prof. Fernando Branco, sharing his experience and providing guidance, while always bearing in mind the “big picture”, are particularly appreciated. But I would especially like to wholeheartedly thank him for his trust in me and in my work, which I have been graced with for many years, since I was still a student doing my degree at IST, and giving my first steps in research.

The support of *Fundação para a Ciência e a Tecnologia* (FCT), through the individual doctoral scholarship SFRH/BD/78584/2011, which allowed me to carry out my work with the comfort of financial stability (a chance not shared by all PhD students), is greatly appreciated.

I would especially like to thank Luís Oliveira and the *Pólo de Inovação em Engenharia de Polímeros* (PIEP), who played a crucial part in the development of this work by producing the sandwich panel prototypes studied in this thesis. Their support was fundamental, and even more appreciated in light of all the difficulties found throughout the execution of the *RehabGFRP* project.

The support of Dr. Susana Cabral-Fonseca and Prof. António Correia Diogo in the execution of the DMA tests carried out for this thesis are also greatly appreciated. Furthermore,

Dr. Susana Cabral-Fonseca's interest in the creep experiments that were carried out, and her availability to provide the means to conduct them under controlled environmental conditions is especially appreciated.

The valued help of Diogo Ferreira, Elisa Videira, and Pedro Barbosa, who worked with me in the context of their respective MSc dissertations, is greatly appreciated. It was a pleasure and a valuable learning experience to guide them in their work, and count on each one of them to share in the everyday successes and frustrations of laboratory work.

I would also like to thank the help, the support and the friendship of my colleagues at IST, namely, João Firmo, José Gonilha, Mário Sá, João Sousa, Francisco Nunes, Luís Valarinho, Tiago Morgado, Mário Arruda, David Martins, André Castelo, Cristina López, and André Sampaio. All those times that you helped me load and unload the panels for the creep tests are much appreciated!

The support and friendship of all my colleagues at CCLab, namely, Michael Osei-Antwi, Roohollah Sarfaraz, Moslem Shahverdi, Wei Sun, Carlos Pascual, Sonia Yanes Armas, Myrsini Angelidi, Maria Savvilotidou, Haifeng Fan, Vahid Movahedirad, Aida Cameselle Molares, Kyriaki Goulouti, Alireza Moshtaghin, Anastasios Vasilopoulos, and Julia de Castro San Roman, is also dearly appreciated. I hope that we can meet again many times in the future (starting as soon as possible)!

In my thesis, I developed a substantial amount of lab work, which would not have been possible without the help, guidance and companionship of the technicians that were there to support me, namely Mr. Fernando Alves, Mr. Fernando Costa, Mr. Leonel Silva, Mr. João Lopes, Mr. Sylvain Demierre, and Mr. Gilles Guignet.

I also want to express my genuine appreciation for the help of Mrs. Maria Helena Salvado in dealing with the administrative aspects of this work, but especially for her constant care and dedication shown for all of us working for our PhD degrees in Prof. João Correia's research team.

My deepest gratitude goes to my family, especially my mother, father, and brother, who have always been supportive of my work, my goals, my ambitions, and who have always done everything in their power to provide me with all I need in order to achieve them. Their unconditional love gives me strength and helps me overcome all obstacles, and for this I will be eternally grateful.

Finally, and most importantly, I want to thank Andreia Gonçalves, who is my soulmate and the person with whom I can, and want, to share everything in life. Her support, friendship and love throughout all these years have been priceless, and her simple presence at my side is enough to give me strength and keep me balanced. I dedicate this work to you, Andreia, so that together we may build the life we want.

“There is no subject so old that something new cannot be said about it.”

– Fyodor Dostoyevsky, in *Diary of a Writer*

Table of Contents

Abstract	i
Sumário	iii
Acknowledgements	v
Table of Contents	ix
List of figures	xv
List of tables	xxv

PART I Introduction

Chapter 1 Introduction	3
1.1. Context and motivation	3
1.2. Objectives and methodology	5
1.3. Main scientific contributions and publications.....	8
1.4. Document outline	11
1.5. References	14
Chapter 2 Sandwich panels in civil engineering	15
2.1. Introduction	15
2.2. Industrial applications	16
2.2.1. Non-structural or lightly structural sandwich panels.....	16
2.2.2. Structural sandwich panels	17
2.3. Research developments	20
2.3.1. Building floors	20
2.3.3. Building façades	21
2.3.4. Reinforcement and optimisation techniques	22
2.3.5. Multifunctional integration.....	25
2.4. Concluding remarks.....	26

2.5. References	27
Chapter 3 Design, materials and panel architectures	31
3.1. Introduction	31
3.2. Design of sandwich panels	32
3.3. Materials	35
3.3.1. GFRP laminates	35
3.3.2. Core materials	36
3.4. Panel architectures	37
3.4.1. Simple sandwich panels	37
3.4.2. Panels with longitudinal ribs	38
3.4.3. Truss-foam core panels	39
3.4.4. Variable density core panels	39
3.4.5. Connection panels	40
3.5. Production costs	41
3.6. Concluding remarks	42
3.7. References	42

PART II Characterisation of materials

Chapter 4 Characterisation of constituent materials	47
4.1. Introduction	47
4.2. Glass-fibre reinforced polymer (GFRP)	48
4.2.1. Experimental procedures	48
4.2.2. Results	51
4.3. Core materials	55
4.3.1. Diagonal tension shear	55
4.3.2. Effects of temperature on the shear response of polymer foams	61
4.4. Sandwich panel assemblies	69
4.4.1. Experimental procedures	69
4.4.2. Results	71

4.5. Concluding remarks.....	74
4.6. References	75
Chapter 5 Flexural behaviour of full-scale panels	77
5.1. Introduction	77
5.2. Effective flexural properties tests	78
5.2.1. Experimental programme	78
5.2.2. Results and discussion	79
5.3. Dynamic tests	83
5.3.1. Experimental programme	83
5.3.2. Results and discussion	84
5.4. Failure tests.....	87
5.4.1. Experimental programme	87
5.4.2. Results and discussion	88
5.5. Concluding remarks.....	104
5.6. References	105
PART III Connection systems	
Chapter 6 Connections between sandwich panels.....	109
6.1. Introduction	109
6.2. Current practice	109
6.3. Investigated connection system.....	111
6.4. Experimental investigation	112
6.4.1. Programme overview and materials	112
6.4.2. Transverse direction results	117
6.4.3. Longitudinal direction results	119
6.5. Numerical simulation	123
6.5.1. Objectives	123
6.5.2. Simulation of transverse direction behaviour	123
6.5.3. Simulation of longitudinal direction behaviour.....	128

6.6. Concluding remarks	134
6.7. References	135
Chapter 7 Connections to building walls	139
7.1. Introduction	139
7.2. Experimental investigation.....	140
7.2.1 Test setup and materials	140
7.2.2 Results and discussion.....	143
7.3. Numerical simulation	148
7.3.1 Objectives.....	148
7.3.2 Modelling approach.....	148
7.3.3 Results	150
7.4. Moment-rotation relationships	153
7.4.1 Basis of calculation	153
7.4.2 Cantilever models.....	154
7.4.3 Characteristic curves	155
7.5. Connection contribution for SLS verifications	157
7.6. Concluding remarks	161
7.7. References	162

PART IV Creep behaviour

Chapter 8 Effect of service temperature on the creep of PUR foam	167
8.1. Introduction	167
8.2. Literature review	168
8.3. Theoretical formulation.....	169
8.3.1. Findley's power law	169
8.3.2. Temperature dependence.....	170
8.3.3. Time and temperature dependent properties	171
8.4. Experimental programme.....	173
8.4.1. Materials and test setup	173

8.4.2. Experimental results and simple power law fitting	175
8.5. Modelling and predictions	178
8.5.1 General power law	178
8.5.2 Temperature dependence	178
8.5.3 Time and temperature dependent properties	181
8.6. Comparison with TTSSP	183
8.7. Concluding remarks.....	186
8.8. References	188
Chapter 9 Effect of service temperature on the creep of GFRP laminates ..	191
9.1. Introduction	191
9.2. Literature review.....	192
9.3. Theoretical formulation	194
9.3.1. Findley’s power law	194
9.3.2. Temperature dependence	195
9.3.3. Time and temperature dependent properties	196
9.4. Experimental programme	197
9.4.1. Material properties.....	197
9.4.2. Static failure tests	197
9.4.3. Creep tests	199
9.5. Modelling and predictions	203
9.5.1. General power law parameters	203
9.5.2. Temperature dependence	203
9.5.3. Time and temperature dependent properties	206
9.6. Comparison with TTSSP	208
9.7. Concluding remarks.....	211
9.8. References	212
Chapter 10 Creep of full-scale sandwich panels	215
10.1. Introduction	215
10.2. Literature review.....	216

10.3. Experimental programme	218
10.3.1. Materials and panel architectures	218
10.3.2. Experiments and test setups	219
10.4. Creep of PET foam and balsa wood	222
10.5. Creep of GFRP ribs	223
10.6. Creep of full-scale panels	224
10.7. Composed creep modelling	227
10.7.1. Modelling assumptions	227
10.7.2. Model predictions.....	229
10.8. Concluding remarks	233
10.9. References	234

PART V Conclusions and future developments

Chapter 11 Conclusions and future developments	239
11.1. Conclusions	239
11.1.1. General conclusions	239
11.1.2. Production methods.....	240
11.1.3. Sandwich panel architectures	241
11.1.4. Connection systems.....	242
11.1.5. Creep behaviour	244
11.2. Future developments	246
11.2.1. Connection systems.....	246
11.2.2. Creep behaviour	247
11.2.3. Further research topics	249
11.3. References	252

List of figures

Figure 2.1. Examples of sandwich panels in building façades and roofs: (a) commercial building in Kuopio, Finland, and (b) industrial pavilion in Tabriz, Iran.	16
Figure 2.2. Heavy duty sandwich panels with steel facings and solid elastomer cores: (a) in-fill floor at the Carnegie Hall (Manhattan, New York, USA), and (b) Grand Pier in Weston-super-Mare (UK).	17
Figure 2.3. <i>Novartis Campus Entrance Building</i> (Basel, Switzerland): (a) installation of the prefabricated panels, and (b) finished building.	18
Figure 2.4. Private <i>Villa</i> roof installation (near Basel, Switzerland): (a) air-lifting of the roof, and (b) reception of the roof at the construction site.	19
Figure 2.5. Avançon River bridge deck near Bex, Switzerland: (a) assembly of the deck components on the river bank, and (b) placement of the deck.	19
Figure 2.6. Roofs of the Haramain High Speed Railway (HHR) station: (a) mock-up installation, and (b) construction phase.	20
Figure 2.7. Sandwich floor panels: (a) deck panels, and (b) slab panels.	21
Figure 2.8. Large scale sandwich cladding panels: (a) schematic of the pressure test setup, and (b) execution of the experiments.	22
Figure 2.9. Reinforcement ribs/webs: (a) along the panel edges, and (b) within the core. .	23
Figure 2.10. Reinforcement stitches (with core removed): (a) columns, and (b) truss.	23
Figure 2.12. Structurally graded cores: (a) “horizontal” grading, (b) “vertical” grading, and (c) arch-like grading.	24
Figure 2.13. Multifunctional integration: (a) translucency for daylighting use, and (b) solar cell encapsulation.	26

Figure 3.1. Composite sandwich panels production: (a) fibre mat layup, (b) detail of vacuum infusion feeder lines, (c) general view of the vacuum infusion process, and (d) finished sandwich panel prototype..... 32

Figure 3.2. Core materials: (a) PUR foam, (b) PET foam and (c) balsa wood. 37

Figure 3.3. Cross-section of the simple sandwich panels. 38

Figure 3.4. Cross-section of the RIB panels..... 38

Figure 3.5. Longitudinal section of the TFC panels..... 39

Figure 3.6. Longitudinal section of the VDC panels..... 40

Figure 3.7. Cross-section of the sandwich panels with panel-to-panel connection system. 40

Figure 4.1. Experimental setups for the: (a) tensile tests, and (b) compression tests. 49

Figure 4.2. Strain gauge installation configurations: (a) single axial strain gauge, (b) axial and transverse strain gauges, and (c) strain gauge rosette..... 50

Figure 4.3. Representative curves from the tensile experiments on the GFRP laminates: (a) load vs. displacement, (b) axial stress vs. strain, and (c) shear stress vs. distortion. 52

Figure 4.4. Failure modes of the GFRP laminates in tension for face sheet specimens along the: (a) 0°, (b) 90°, and (c) 10° directions, and (d) rib laminates in the 10° direction. 53

Figure 4.5. Representative curves from the compression experiments on the GFRP laminates..... 54

Figure 4.6. Failure modes of the GFRP laminates in compression for specimens along the: (a) 0°, and (b) 90° directions. 54

Figure 4.7. DTS test specimen geometry and dimensions. 55

Figure 4.8. Schematic representation of the DTS test fixture and its components. 56

Figure 4.9. Calculation assumptions for the DTS test method: (a) force distribution, and (b) imposed deformations..... 57

Figure 4.10. Diagonal tension shear test setup..... 58

Figure 4.11. Representative shear stress *vs.* distortion curves from the DTS tests of the core materials. 59

Figure 4.12. Failure modes of the core materials in the DTS tests: (a) PUR foams, (b) PET foam, and (c) balsa wood..... 60

Figure 4.13. Comparison between results obtained for the different core materials: (a) shear strength, and (b) shear modulus..... 61

Figure 4.14. DMA results for the: (a) PUR foam, and (b) PET foam. 63

Figure 4.15. DSC/TGA results for the PUR and PET foams. 64

Figure 4.16. Iosipescu test setup: (a) fixtures, (b) thermal chamber and video extensometer, and (c) test execution..... 65

Figure 4.17. Iosipescu shear specimens: (a) dimensions and target dot locations, and (b) displacements of target dots due to shear deformation..... 66

Figure 4.18. Representative shear stress *vs.* distortion curves from the Iosipescu tests: (a) PUR foam, and (b) PET foam. 67

Figure 4.19. Residual shear moduli for the PUR and PET foams. 68

Figure 4.20. Setups for sandwich panel assemblies' tests: (a) flatwise tension, and (b) flatwise compression..... 70

Figure 4.21. Axial stress *vs.* displacement curves obtained in the: (a) flatwise tension, and (b) flatwise compression tests. 71

Figure 4.22. Failure modes of the sandwich panel assemblies in flatwise tension: (a) PUR, (b) PET, and (c) balsa wood; and in flatwise compression: (d) PUR, (e) PET, and (f) balsa wood. 72

Figure 4.23. Comparison between different sandwich panel assemblies: (a) failure stresses in flatwise tension, (b) stiffness in flatwise tension, (c) failure stresses in flatwise compression, and (d) stiffness in flatwise compression. 73

Figure 5.1. Span lengths for the effective flexural properties tests: (a) $L1 = 0.85$ m, (b) $L2 = 1.50$ m, (c) $L3 = 2.10$ m, (d) $L4 = 2.70$ m and (e) $L5 = 3.30$ m. 79

Figure 5.2. Plot of results (L^2 vs. $1/KL$) obtained from the effective flexural properties tests.
 80

Figure 5.3. Experimental setup used for the dynamic tests..... 83

Figure 5.4. Typical acceleration response (data from RIB panels)..... 84

Figure 5.5. Power spectral density curves obtained with the FFT algorithm: (a) flexural curve for the VDC panels, and (b) flexural and torsional curves for the RIB panels. 85

Figure 5.6. Comparison between estimated damping ratios for the different panel typologies.
 86

Figure 5.7. Failure test setups: (a) four-point bending configuration, and (b) six-point bending configuration. 87

Figure 5.8. Results obtained in the failure tests of the PUR panels: (a) load vs. displacement curves, and (b) load vs. strain curves. 89

Figure 5.9. Failure of the PUR panels: (a) general view of PUR-1, and (b) shear fracture in PUR-2..... 90

Figure 5.10. Results obtained in the failure tests of the PET panels: (a) load vs. displacement curves, and (b) load vs. strain curves. 91

Figure 5.11. Failure of the PET panels: (a) general view of PET-1, and (b) shear fracture in PET-1..... 92

Figure 5.12. Results obtained in the failure tests of the BAL panels: (a) load vs. displacement curves, and (b) load vs. strain curves. 93

Figure 5.13. Failure of the BAL panels: (a) general view of BAL-1, and (b) shear fracture in BAL-1..... 94

Figure 5.14. Results obtained in the failure tests of the TFC panels: (a) load vs. displacement curves, and (b) load vs. strain curves. 95

Figure 5.15. Failure of the TFC panels: (a) TFC-4, and (b) TFC-3. 95

Figure 5.16. Results obtained in the failure tests of the VDC panels: (a) load vs. displacement curves, and (b) load vs. strain curves. 97

Figure 5.17. Failure of the VDC panels: (a) shear failure of the core in VDC-1, and (b) buckling failure of compressed face in VDC-2. 97

Figure 5.18. Results obtained in the failure tests of the RIB panels: (a) load vs. displacement curves, (b) load vs. strain curves, and (c) load vs. distortion curves. 99

Figure 5.19. Failure of the RIB panels: (a) general view of RIB-1, (b) detail of RIB-1, (c) geometric imperfection, and (d) failure at the imperfection of RIB-2..... 100

Figure 5.20. Comparison between stiffness values obtained in the failure tests: (a) stiffness, (b) stiffness per width, and (c) stiffness per width per mass per area ($\times 10^{-3}$). 101

Figure 5.21. Comparison between failure load values obtained in the failure tests: (a) failure load, (b) failure load per width, and (c) failure load per mass per area..... 103

Figure 6.1. Connections in pultruded bridge decks: (a) DuraSpan, (b) ASSET, and (c) interlocking connection for ASSET system..... 110

Figure 6.2. Proposed panel-to-panel connection system: (a) joint components, (b) interior panel cross-section, (c) end panel cross-section, and (d) cross-sectional dimensions. 111

Figure 6.3. Transverse direction test setups: (a) four-point bending, and (b) cantilever... 113

Figure 6.4. Support anchoring system for the cantilever tests. 114

Figure 6.5. Instrumentation and load application areas for alternate loading of jointed panel. 115

Figure 6.6. Alternate loading cases: (a) L1, and (b) L1+L2+L3+L4. 116

Figure 6.7. Test setup and instrumentation for the flexural failure test of the jointed panel. 116

Figure 6.8. Experimental load vs. displacement curves for the transverse direction: (a) four-point bending, and (b) cantilever..... 117

Figure 6.9. Failure modes in the transverse direction: specimens (a) B-BAL-1, (b) B-PUR-1, (c) C-BAL-1, and (d) C-PUR-1..... 118

Figure 6.10. Strain profiles at the mid-span section for the various alternate load cases of the jointed panel. 119

Figure 6.11. Graphical determination of effective flexural properties of jointed and ribbed panels..... 120

Figure 6.12. Experimental results of four-point bending failure tests: (a) load vs. mid-span displacement curves for jointed and ribbed panels, and (b) axial strains at mid-span (strain gauges *cf.* Figure 6.7) in the jointed panel. 121

Figure 6.13. Failure of the jointed panel in four-point bending: (a) damage initiation at imperfection (load of 75 kN), and (b) final failure. 122

Figure 6.14. Failure of the ribbed panels in four-point bending: (a) failure at geometrical imperfection, (b) general view of failure at the loading points, and (c) detail of top face sheet and rib after failure at loading point..... 122

Figure 6.15. Deformed shapes for the FE models of the transverse direction behaviour: (a) four-point bending, and (b) cantilever. 124

Figure 6.16. Comparison between experimental and numerical load vs. displacement curves for the transverse direction: (a) four-point bending, and (b) cantilever. 125

Figure 6.17. Tsai-Hill criterion (at experimental failure load) for the laminates in the balsa wood cored specimens (transverse direction): (a) four-point bending, and (b) cantilever.126

Figure 6.18. Adhesive stresses (midline) at failure for the four-point bending configuration (transverse direction): (a) σ_{11} , (b) σ_{22} , and (c) τ_{12} 127

Figure 6.19. Adhesive stresses (midline) at failure for the cantilever configuration (transverse direction): (a) σ_{11} , (b) σ_{22} , and (c) τ_{12} 127

Figure 6.20. Deformed shape for the model with eccentric loading corresponding to the L1+L3 configuration used in the alternate loading tests. 129

Figure 6.21. Comparison between experimental results and numerical predictions for the axial strains in the face sheets of the jointed panel at the mid-span section (alternate loading). 130

Figure 6.22. Stress profile predictions along the adhesive length (midline) at the mid-span section for the L1+L3 load configuration. 130

Figure 6.23. Load vs. mid-span displacement curves from FEM and comparison with experimental results (four-point bending). 131

Figure 6.24. Shear stresses (in MPa) in the PUR foam core in (a) a transverse section view, (b) a longitudinal section view, and (c) the inner and outer ribs (four-point bending). 132

Figure 6.25. Shear stresses (in MPa) in the balsa wood core in (a) a transverse section view, (b) a longitudinal section view, and (c) the inner and outer ribs (four-point bending). 133

Figure 7.1. Connection between a timber floor and timber-framed masonry walls using steel angles. 139

Figure 7.2. Proposed connection systems (A – adhesive, B – bolted, 1 – single bottom steel angle, 2 – top and bottom steel angles): (a) A1, (b) A2, (c) B1, (d) B2, (e) AB2. 140

Figure 7.3. Experimental setup and instrumentation: (a) schematic, and (b) general view. 141

Figure 7.4. Load vs. displacement at D1 for all tested connection systems: (a) specimens with PUR foam core, and (b) specimens with balsa wood core. 143

Figure 7.5. Failure modes of the A1 and A2 connection systems: (a) A1 specimen with PUR foam core, (b) A1 specimen with balsa wood core, and (c) A2 specimen with balsa wood core. 144

Figure 7.6. Failure modes for the B1 and B2 connection systems: (a) B1 specimen with balsa wood core, (b) B1 specimen with PUR foam core, (c) damage in GFRP for a B2 connection, (d) damage in the bolts for a B2 connection, and (e) B2 specimen with balsa wood core. 146

Figure 7.7. Failure in the AB2 connection system: (a) crack opening in the top adhesive layer, and (b) shear failure of the PUR foam. 147

Figure 7.8. Load vs. displacement (D1) curves obtained from FEM: (a) specimens with PUR foam core and single (bottom) steel angle, (b) balsa wood core and single steel angle, (c) PUR foam core and two (top and bottom) steel angles, and (d) balsa wood core and two steel angles. 150

Figure 7.9. Through-thickness stresses in the epoxy adhesive: (a) A1 connections, and (b) top layer in the A2 connections. 152

Figure 7.10. Plastic strains in the bolts: (a) B1-PUR, and (b) B2-PUR. 153

Figure 7.11. Deflections for (a) cantilever beam, and (b) elastically restrained beam (with connection system). 153

Figure 7.12. Comparison between deformed shapes for the B2-PUR model (top) and the corresponding PUR-Clamp cantilever model (bottom). 155

Figure 7.13. Comparison between $P-\delta$ curves of the B2-BAL and BAL-Clamp models. 155

Figure 7.14. $M-\theta$ curves for connection systems (per unit width) with: (a) single steel angle (bottom only), and (b) two steel angles (top and bottom). 156

Figure 7.15. Deformed shape for the 4 m span sandwich panel, either supported using the B2 connection (top) or simply supported (bottom). 158

Figure 7.16. Deflection reductions for different spans using the proposed connection systems for panels with: (a) PUR foam core, and (b) balsa wood core. 159

Figure 7.17. Shear contribution to total mid-span deflection (δ) for different spans using the proposed connection systems for panels with: (a) PUR foam core, and (b) balsa wood core. 160

Figure 7.18. Deflections for different spans using the proposed connection systems for panels with: (a) PUR foam core, and (b) balsa wood core. 160

Figure 8.1. Representative stress vs. strain curve from shear failure testing of the PUR foam (horizontal lines represent stress levels used in the creep experiments). 173

Figure 8.2. Experimental setup for the shear creep tests: (a) overall view, (b) frontal view of the assembly, (c) lateral view of the assembly, and (d) schematic view. 175

Figure 8.3. Evolution of experimental shear strains with time for the different load levels and temperatures [including power laws fittings, cf. Equation (8.1a)]: (a) linear plot of total strain, and (b) \log_{10} plot of creep strain. 176

Figure 8.4. Creep amplitude (m) and time exponent (n) values per temperature and stress level. 177

Figure 8.5. Fitting of Arrhenius equations to the reference creep amplitude (m') and average time exponent (n). 179

Figure 8.6. Comparison between experimental creep curves and model [Equation (8.10)] estimates of shear strain over time as a function of stress and temperature. 180

Figure 8.7. (a) Time-temperature dependent shear modulus of the PUR foam, and (b) creep coefficient and shear modulus reduction factor curves. 182

Figure 8.8. Time-temperature-stress superposition of experimental creep curves for reference conditions of 20°C and 11% shear stress and comparison with model predictions. 185

Figure 8.9. Time-stress superposition of experimental creep curves at different temperatures for the reference shear stress of 11% and comparison with model predictions. 186

Figure 9.1. Flexural stress vs. strain curves obtained in the failure tests..... 198

Figure 9.2. Typical flexural failure of the GFRP laminates. 199

Figure 9.3. Flexural creep tests: (a) general view, (b) detail of specimen, and (c) dial gauge indicators. 199

Figure 9.4. Experimental creep strains and fittings from Equation (9.1a): (a) linear plot, and (b) \log_{10} plot. 202

Figure 9.5. Creep amplitude (m) and time exponent (n) values per temperature and stress level. 202

Figure 9.6. Fitting of Arrhenius equation to the reference creep amplitude (m') and average time exponent (n). 205

Figure 9.7. Comparison between experimental creep curves and the model [Equation (9.12)] estimates of strain over time as a function of stress and temperature. 206

Figure 9.8. Long-term flexural modulus predictions: (a) effect of stress level, and (b) effect of temperature. 207

Figure 9.9. Creep coefficient and reduction factor curves: (a) effect of stress level, and (b) effect of temperature..... 208

Figure 9.10. Time-temperature-stress superposition of experimental creep curves for reference conditions of 20°C and 15% stress and comparison with model predictions. .. 210

Figure 9.11. Time-stress superposition of experimental creep curves at different temperatures for the reference stress of 15% and comparison with model predictions.... 211

Figure 10.1. Cross-sectional dimensions of the sandwich panels: (a) PUR, PET, and BAL, and (b) RIB..... 219

Figure 10.2. Full-scale creep tests setups for: (a) PUR, PET and BAL panels, and (b) RIB panels..... 220

Figure 10.3. Experimental shear creep curves: (a) linear plot of total strains, and (b) bi-logarithmic plot of creep strains..... 222

Figure 10.4. Experimental creep curves and individual power law fittings for the: (a) PUR, (b) PET, (c) BAL, and (d) RIB panel series..... 226

Figure 10.5. Moduli reduction factors for the shear modulus of the PUR foam, PET foam and GFRP ribs, and the Young’s modulus of the GFRP faces. 230

Figure 10.6. Comparison between CCM predictions and experimental creep curves for the: (a) PUR, (b) PET, and (c) RIB panel series. 232

Figure 10.7. Time-dependent relative contributions of the ribs (α_r) and foam core (α_c) to the panel’s shear stiffness, $GAVh$ 233

List of tables

Table 3.1. Production cost estimates (materials only) for the different sandwich panels. ..	41
Table 4.1. Summary of GFRP mechanical properties.	51
Table 4.2. Summary of mechanical properties for the core materials.	59
Table 4.3. Glass transition temperatures (in °C) of the PET and PUR foams tested at 1 °C/min (average ± standard deviation, from 3 specimens).	64
Table 4.4. Shear modulus (G) of PET and PUR foams for each temperature (average ± standard deviation or maximum difference to average) and corresponding relative percentage reduction compared to ambient temperature (Δ_{G20}).	69
Table 4.5. Summary of results obtained in flatwise tension and compression tests.....	74
Table 5.1. Summary of results obtained from the effective flexural properties tests.....	81
Table 5.2. Natural flexural (and torsional) vibration frequencies [Hz].	85
Table 5.3. Damping ratios (ζ) obtained in the dynamic tests (in percentage).....	86
Table 5.4. Summary of results obtained in the flexural failure tests of the PUR panels.....	90
Table 5.5. Summary of results obtained in the flexural failure tests of the PET panels.	92
Table 5.6. Summary of results obtained in the flexural failure tests of the BAL panels. ...	94
Table 5.7. Summary of results obtained in the flexural failure tests of the VDC panels. ...	96
Table 5.8. Summary of results obtained in the flexural failure tests of the VDC panels. ...	98
Table 5.9. Summary of results obtained in the flexural failure tests of the RIB panels.....	99
Table 5.10. Summary of flexural stiffness values and stiffness related performance indicators.	102
Table 5.11. Summary of failure load values and failure load related performance indicators.	103

Table 6.1. Alternate loading test programme (<i>cf.</i> Figure 6.5).....	114
Table 6.2. Contribution of the different panel components to shear force resistance (300 mm from support edge, experimental failure load applied).	133
Table 7.1. Specimen distribution per connection system and core material.	142
Table 7.2. Summary of experimental results (average \pm standard deviation).....	143
Table 7.3. Orthotropic material properties of GFRP and balsa wood used for FEM.....	149
Table 7.4. Comparison between FEM and experimental stiffness values at D1 and I1.....	151
Table 7.5. Rotational stiffness values of the proposed connection systems.	156
Table 7.6. Short-term deflections from analytical and FEM models for the 4 m span sandwich panel.	158
Table 8.1. Summary of experimental results.....	177
Table 8.2. General power law parameters per temperature.....	178
Table 8.3. Horizontal shift factors (<i>ah</i>) used for TTSSP and TSSP.....	185
Table 9.1. Summary of experimental results.....	201
Table 9.2. General power law parameters per temperature.....	203
Table 9.3. Horizontal shift factors (<i>ah</i>) used for TTSSP and TSSP.....	209
Table 10.1. Summary of results from the shear creep tests of PET foam and balsa wood.....	223
Table 10.2. Summary of flexural creep experimental results.	225

Part I

Introduction

Preamble

In the rehabilitation of traditional old buildings with stone rubble masonry or timber-framed masonry resisting walls, the existing timber floors are often replaced with heavier reinforced concrete or hybrid steel-concrete solutions. Such interventions substantially increase the floor mass, prompting the need for significant additional structural strengthening of the existing building structure. In this context, lightweight high-performance sandwich panel floors may be an interesting alternative solution. Presenting comparable mass to timber floors, sandwich panels potentially allow for fast construction times and good durability.

Part I of this thesis introduces the concept of sandwich construction and how it can be applied in the rehabilitation of building floors. The potential advantages of this system are discussed, and a state-of-the-art review is presented regarding the use of sandwich construction in civil engineering. Finally, the different sandwich panel architectures investigated in this study are presented and detailed, laying out the basis for the analyses carried out in the following parts of the thesis.

Chapter 1

Introduction

1.1. Context and motivation

In 2011, close to 500 000 residential buildings with masonry walls and timber floors existed in Portugal, corresponding to 13.6% of the total number of residential dwellings [1]. These buildings, mostly erected before 1945, often present pressing rehabilitation needs. Strengthening or replacement of structural elements is a recurring necessity, and timber floors are among the members that more frequently need to be replaced. In fact, they often suffer from excessive deformations and are not able to comply with current structural performance requirements [2].

Traditional rehabilitation solutions generally involve the construction of new timber floors or the adoption of different floor systems made of either reinforced concrete (RC), steel or composite (steel-concrete or timber-concrete) elements. However, timber floors have limited durability, whereas RC, steel, and composite solutions substantially increase the structural mass, generally making it necessary to significantly strengthen the building walls and to erect additional vertical structural elements, especially in seismic regions [3].

In this thesis, an innovative building floor system is proposed for the replacement of degraded timber floors. This system makes use of lightweight composite sandwich panels especially developed for application in building rehabilitation. The use of lightweight floors is particularly advantageous in this context, as the additional dead loads transferred to the existing structure are limited. This is quite relevant for building floors, since they typically represent a very significant portion of the total structural mass in buildings [3,4].

Sandwich construction, characterised by two relatively thin and stiff faces separated by a relatively thick and lightweight core, presents high potential as a lightweight structural system. For this reason, it has been profusely used in “weight-sensitive” industries for the past decades, such as in the aerospace, naval, automotive, and rail industries. In the

construction industry, recent examples of their successful use as primary structural elements¹ highlight the potential of sandwich construction for load-bearing applications. The sandwich panels proposed in this thesis comprise glass-fibre reinforced polymer (GFRP) faces, a material with relatively high strength- and stiffness-to-weight ratios, and whose mechanical properties can be extensively customised by tailoring their fibre architecture. Regarding core materials, three different types of low-density materials were considered: (i) polyurethane (PUR) foam, (ii) polyethylene terephthalate (PET) foam, and (iii) balsa wood.

The proposed sandwich floor panels constitute a pre-fabricated solution that may be quickly assembled on site. Lightweight pre-fabricated panels may be easily installed by a relatively limited number of workers, requiring only light lifting equipment. In fact, their final placement and installation may be carried out manually. This presents the advantage of allowing for time-savings during the construction process, which in turn is associated with a reduction of various construction costs (labour, heavy equipment, occupancy of public spaces, etc.). Furthermore, the lightness of such sandwich panel floors allows for potential additional savings related to the lower strengthening needs of the existing structure.

Glass-fibre reinforced polymer laminates have been shown to be very durable even in harsh environments [5,6]. This characteristic suggests that composite sandwich panel floors may provide long service lives with little or no maintenance. Thus, exploration costs associated with this solution are expected to be quite limited during that period. Furthermore, the low-density materials used in the cores of sandwich panels have low thermal conductivity values. This confers very interesting characteristics to the sandwich panel floors from the building physics and energy efficiency standpoints. By intrinsically providing thermal insulation, the floors may contribute to a reduction of energy consumption related to climatisation needs².

These different potential economies and efficiency gains mean that sandwich panel floors may have an interesting economic performance throughout their life cycle. In fact, the typically higher production costs associated with composite materials, by comparison with traditional construction materials, might be offset by the accumulated potential gains obtained with this solution.

¹ As will be discussed further in Chapter 2.

² Namely in roofs and floors contacting with the exterior environment.

1.2. Objectives and methodology

The development of a novel structural system necessarily comprises the assessment of multiple aspects related to the design methodologies and the construction technology related to that new system. The definition of structural design and calculation methodologies, the selection of the most suitable materials and the assessment of their best arrangement, as well as the identification of specific areas of development that must be addressed are among the aspects to be considered in that process.

This thesis addresses such issues, focusing on the following three main objectives: (i) the assessment of the most suitable materials and sandwich panel architectures for application in building floors, (ii) the development of the necessary connection technology, and (iii) the characterisation of the creep behaviour of the sandwich panels.

Regarding the first objective, the assessment of the materials and panel architectures for application in building floors, it was addressed through the following three tasks:

- initial selection of materials and panel typologies, based on current practice for structural sandwich panels and on the exploration of novel panel architectures;
- mechanical (and in certain cases physical) characterisation of the different materials;
- mechanical characterisation of the different architectures of full-scale panels, produced by vacuum infusion.

The first task was carried out based on a literature review combined with a technical and market study, to determine an array of different materials and panel typologies that could provide sandwich panels with the different characteristics required for the envisaged application. This was carried out in parallel with the structural design of the panels³, according to applicable requirements for building floors. Besides the traditional sandwich panel architecture, the considered solutions comprised panels with cores of variable density along their span length, and panels with hybrid cores made of a low-density polymeric foam reinforced with GFRP laminates, either in the form of a truss or of longitudinal ribs.

³ As detailed in Chapter 3.

For the second task, an experimental campaign was carried out for the characterisation of the different materials, including tests on the GFRP laminates (tension, compression, and shear), test on the different core materials (in shear, using a novel test method developed for this study), and tests on sandwich panel specimens (flatwise tension and compression). For the two polymer foams, PUR and PET, additional experiments were conducted to assess the effects of temperature on their mechanical response. These included shear tests for temperatures between $-20\text{ }^{\circ}\text{C}$ and $120\text{ }^{\circ}\text{C}$, as well as physical characterisation tests to assess their glass-transition and decomposition processes.

The third task motivated an experimental campaign aiming at the characterisation of the flexural behaviour of the different sandwich panel typologies. The sandwich panels used for this task (and for the remainder of this thesis) were produced by vacuum infusion at the *Pólo de Inovação em Engenharia de Polímeros* (PIEP) research institute. Full-scale static tests were carried out to determine their effective bending and shear stiffness values under serviceability conditions, dynamic tests to determine their natural frequencies and damping ratios, and failure tests to assess their flexural behaviour up to failure.

Regarding the second objective, the development of connection technology, it pertains to two different types of connections, for which the two following tasks were carried out:

- development of connections between adjacent panels (panel-to-panel);
- development of connections between the floors and the building walls (panel-to-wall).

For both of these tasks, the available literature was reviewed in order to define the connection systems with the highest potential to be used in the floor panels. Subsequently, experimental campaigns were carried out on full-sized (but shortened length) specimens to test the different connection configurations. The tests were made using sandwich panels with PUR foam and balsa wood cores, the former being the softest and weakest core among those that were tested, the latter being the stiffest and strongest. For the panel-to-panel connections, a full-length prototype was also prepared by connecting two full-sized sandwich panels. This jointed panel was subjected to flexural characterisation tests, in order to determine the joint's behaviour along the main floor span. For all the tested configurations of the panel-to-panel and panel-to-wall connections, and for the two different core materials, finite element models (FEM) were developed. These were aimed at simulating the experimentally observed

responses, and gathering further knowledge about the stress distributions within the various panel and connection components.

The third objective, concerning the characterisation of the creep behaviour of the sandwich panels, was fulfilled by carrying out the following five tasks:

- a preliminary creep study to assess the importance of the creep phenomenon in composite sandwich panels and to design a set of experiments to be performed in the subsequent tasks;
- characterisation of the creep behaviour of the core materials in shear;
- characterisation of the creep behaviour of the GFRP laminates in bending;
- characterisation of the creep behaviour of the full-scale panels under uniformly distributed loading;
- modelling of the creep response of full-scale panels by considering the individual creep response of each constituent material.

The first task was developed in a preliminary stage of this thesis, and served to define the methodology that was used in the rest of the creep behaviour study. Because part of the results obtained from this task are more limited than those obtained from the subsequent tasks (and are partially redundant), they are not presented in this document. Nonetheless, as mentioned in section 1.3, the results obtained from this preliminary task are reported in an international journal paper [7].

The second to fourth tasks involved experimental creep tests on the different materials and panels, under controlled temperature conditions. A baseline temperature of 20 °C was adopted in these experiments. For the PUR foam and the GFRP laminates, additional creep tests were carried out at 24 °C and 28 °C to assess the influence of temperature on the viscoelasticity of those materials. The experimental results were analysed using Findley's power law methodology, which was modified with Arrhenius equation to consider the effects of temperature.

The fifth task concerned the development of an analytical approach to model the creep behaviour of full-scale sandwich panels. This model is based on Timoshenko's beam theory and on Findley's power law formulation, and uses the viscoelastic properties of the sandwich panels' constituent materials – faces, core, and ribs (if applicable) – to predict the creep

response of the panels. The model was validated through the comparison of the analytical predictions with the experimental creep curves obtained from the full-scale panel tests.

It is worth mentioning that the topics of acoustic behaviour and fire resistance, while being of great importance for applications in building floors, fall outside the scope of this thesis. Notwithstanding, the acoustic behaviour of the sandwich panels proposed herein was experimentally and numerically assessed under the scope of the *RehabGFRP* research project [8], and considerations about possible measures to address these two aspects of the floors' behaviour are given and proposed as topics for future research.

1.3. Main scientific contributions and publications

The research presented in this thesis provided scientific contributions regarding (i) the mechanical behaviour of sandwich panels with different materials and architectures, presenting novel experimental results obtained at a (large) scale that is uncommon in the existing literature, (ii) provided new insights regarding sandwich panel design methodologies, (iii) systematically approached the effects of temperature in different core materials, namely regarding their elastic and viscoelastic properties (iv) proposed new panel-to-panel and panel-to-wall connection systems, (v) provided a wealth of new experimental data about the creep response of full-scale sandwich panels and their constituent materials, and (vi) proposed an analytical model to predict the creep of those panels. These contributions, which are further detailed in the following paragraphs, are considered to have promoted the use of sandwich panels in civil engineering.

Regarding the experimental characterisation of the effects of temperature on the shear modulus of PUR and PET foams, this work provided relevant data for the design of temperature-sensitive structures incorporating such foams (*e.g.*, outdoor constructions or roofs). This type of data was scarce in the existing literature. Additionally, the foams' thermophysical properties were characterised, namely in terms of the glass-transition and the decomposition processes. This particular work resulted in the following publication:

1. Garrido, M., Correia, J.R., Keller, T. (2015). "Effects of elevated temperature on the shear response of PET and PUR foams used in composite sandwich panels". *Construction and Building Materials*, Vol. 76, pp. 150-157.

In this thesis, novel experimental results concerning the flexural behaviour of large-scale sandwich panels are provided, which were scarce in the technical literature. In fact, most studies concerning sandwich panels considered smaller scale specimens, outside of the scope of structural applications in civil engineering. Furthermore, the experimental results presented in this thesis for sandwich panels with variable density core materials and hybrid truss-foam cores are also novel, and provide an interesting contribution regarding the optimisation and reinforcement techniques for sandwich panels.

It was shown that in sandwich panels with longitudinal reinforcement ribs or with the proposed panel-to-panel joints, the core materials can have a significant contribution to the shear stiffness of the floors. Previously, this contribution was often considered as being negligible [9]. This scientific contribution was partly developed during the work carried out concerning the panel-to-panel joints, which resulted in the following publication:

2. Garrido, M., Correia, J.R., Keller, T., Branco, F.A. (2015). “Adhesively bonded connections between composite sandwich floor panels for building rehabilitation”. *Composite Structures*, Vol. 134, pp. 255-268.

The panel-to-wall connections were shown to provide a significant restriction to the rotation of the sandwich panel floors, limiting their out-of-plane deformability. This effect may be taken into account during the design of the sandwich panels, allowing for significantly more economical and material efficient designs, since the maximum allowable deformability is typically the limiting design criterion. The work concerning the panel-to-wall connections resulted in the following publication:

3. Garrido, M., Correia, J.R., Keller, T., Branco, F.A. (2016). “Connection systems between composite sandwich floor panels and load-bearing walls for building rehabilitation”. *Engineering Structures*, Vol. 106, pp. 209-221.

The viscoelastic response of the different materials used in this thesis was experimentally characterised. Depending on the material, such data was scarce or inexistent in the literature. For the GFRP laminates and the PUR foam, the effect of service temperature on their viscoelasticity was characterised and modelled using Findley’s power law modified with the Arrhenius equation, providing a novel way to incorporate the effects of temperature on the creep response of such materials. Furthermore, design tools were obtained in the form of time-dependent creep coefficients and moduli reduction factors. These may be used to expeditiously estimate the creep deformations in those materials. The work carried out

concerning the effects of temperature on the creep behaviour of the panels' constituent materials resulted in the following publications:

4. Garrido, M., Correia, J.R., Keller, T. (n.d.). "Effect of service temperature on the shear creep response of rigid polyurethane foam used in composite sandwich floor panels". *Construction and Building Materials*, submitted to publication.
5. Garrido, M., Correia, J.R., Keller, T. (2016). "Effect of service temperature on the flexural creep of vacuum infused GFRP laminates used in sandwich floor panels". *Composites Part B: Engineering*, Vol. 90, pp. 160-171.

The viscoelasticity of large-scale sandwich panels under uniformly distributed flexural loads was also characterised. Such data was particularly scarce in the existing literature, and the current thesis provides a fairly large set of novel experimental data. These include results for different: (i) sandwich panel architectures, (ii) core materials, and (iii) load levels. Finally, a composed creep model capable of predicting the viscoelastic deflections of a full-scale sandwich panel by considering only the individual creep behaviour of each of its constituent materials was developed. This model allows the replacement of cumbersome large-scale creep tests on full-scale sandwich panels with small-scale creep experiments on their constituent materials, which are much easier to conduct. This constitutes a significant advantage in terms of laboratorial characterisation of creep. Similarly, regarding the consideration of creep in the design of sandwich panels, this methodology has the potential to uncouple the viscoelastic properties of the materials from their geometric characteristics. In other words, the viscoelastic properties of the panel's constituent materials may potentially be used independently of their cross-sectional dimensions in the full-scale sandwich panels. The work carried out concerning the creep behaviour of full-scale sandwich panels resulted in the following publications⁴:

6. Garrido, M., Correia, J.R., Branco, F.A., Keller, T. (2013). "Creep behaviour of sandwich panels with rigid polyurethane foam core and glass-fibre reinforced polymer faces: Experimental tests and analytical modelling". *Journal of Composite Materials*, Vol. 48, pp. 2237-2249.

⁴ The first of these publications (no. 6) concerns the preliminary work carried out to assess the importance of the creep phenomenon in composite sandwich panels, and to define the experimental design of the subsequent investigations.

7. Garrido, M., Correia, J.R., Keller, T., Cabral-Fonseca, S. (n.d.). “Creep of sandwich panels with longitudinal reinforcement ribs for civil engineering applications: experiments and composed creep modelling”. *Journal of Composites for Construction*, submitted to publication.

In addition to the above-mentioned publications in ISI journal papers, the research developed in this thesis was published in the proceedings of three international conferences and one national (Portuguese) conference:

8. Garrido, M., Correia, J.R., Branco, F.A., Sá, M. (2012). “Creep behaviour of GFRP sandwich panels with PU foam cores for civil engineering structural applications”. *Proceedings of the 6th International Conference on FRP Composites in Civil Engineering (CICE 2012)*, June 13-15, Rome, Italy.
9. Garrido, M., Correia, J.R., Branco, F.A. (2012). “Creep behavior of GFRP sandwich panels for civil engineering structural applications: experimental assessment of PU core shear creep and panel flexural creep”. *Proceedings of the 10th International Conference on Sandwich Structures (ICSS10)*, August 27-29, Nantes, France.
10. Garrido, M., Correia, J.R., Branco, F.A. (2013). “Composite sandwich panels made of GFRP faces and PU foam cores for rehabilitation of building floors – Study about the creep behaviour”. *Proceedings of the XII Congreso Latinoamericano de Patología de la Construcción & XIV Congreso de Control de la Calidad en la Construcción (CONPAT 2013)*, 30 September to 04 October, Cartagena, Colombia.
11. Garrido, M., Correia, J.R., Barbosa, P., Cabral-Fonseca, S., Branco, F.A. (2014). “Fluência em corte de núcleos em espuma de poliuretano utilizados em painéis sanduíche compósitos: Efeito da temperatura”. *Proceedings of the 3^o Congresso Português de Engenharia de Materiais e Estruturas Compósitas (ENMEC 2014)*, October 24-25, Lisbon, Portugal.

1.4. Document outline

This thesis is organised in eleven chapters, which were grouped into the following five parts:

- Part I – Introduction (chapters 1, 2, and 3);
- Part II – Characterisation of materials (chapters 4 and 5);

- Part III – Connection systems (chapters 6 and 7);
- Part IV – Creep behaviour (chapters 8, 9, and 10);
- Part V – Conclusions (chapter 11).

The first and present chapter introduces the thesis subject. The context and the motivation framing this research are laid out, as well as the methodology adopted and the main scientific contributions.

Chapter 2 of this thesis presents a state-of-the-art review of the use of sandwich panels in civil engineering. The principles guiding sandwich construction are briefly introduced, and its main industrial applications and research developments discussed.

Chapter 3 presents a summary of the panel design and production processes, and of the materials and panel architectures that were adopted in this thesis. The design options that were made are explained, as well as the reasons justifying the selection of materials. Similarly, each panel typology is explained in terms of how it was expected to perform, and detailed regarding the relevant dimensions and the layout of materials.

Chapter 4 presents the small-scale material characterisation experimental programme. Relevant material properties are provided for the GFRP laminates and the different core materials used. The experiments carried out are presented and the test procedures adopted are detailed. For the core material shear characterisation, a novel test method was developed under the scope of this thesis. The principles, calculation procedures, and test fixtures that were especially produced for those experiments are also described.

Chapter 5 of this thesis presents the experimental programme carried out for the full-scale flexural characterisation of the sandwich panels. The performance of each panel typology under vertical loads is assessed, regarding both their serviceability and failure behaviour. The performance of the different types of panels is compared, allowing to draw conclusions regarding their relative advantages and disadvantages.

Chapter 6 of this thesis presents the study about the connections between adjacent sandwich panels. A literature review regarding this particular topic is provided, and the proposed connection system is introduced. This system was subjected to an experimental characterisation programme, considering the behaviour of the connections along the transverse and longitudinal directions of the panels. Additionally, finite element (FE) models

are developed to simulate the joints and provide a better understanding of their local behaviour and of their effects on the behaviour of full-scale panel assemblies.

Chapter 7 presents the study concerning the connections between the floors and the building walls. Similarly to the previous chapter, a state-of-the-art review regarding this particular topic is first presented, leading to the proposed connection configurations. In this case, multiple variations of the connection system are explored, and an experimental programme for their characterisation is presented. The experimental results are used to validate FE models of the connections, which in turn allow assessing the effects of the connections on the global behaviour of the floors.

Chapter 8 of this thesis presents a study on the creep behaviour of the PUR foam under shear stresses. The effects of service temperature are considered in the presented experimental programme. The viscoelastic response of the foam is analytically modelled using Findley's power law, modified with the Arrhenius equation, allowing for the characterisation of the foam's time- and temperature-dependent behaviour in shear.

Chapter 9 presents a study on the flexural creep behaviour of the GFRP laminates used in the face sheets of the sandwich panels. A methodology similar to that used in the previous chapter is followed, allowing the time-, stress-, and temperature-dependent creep response of the laminates to be characterised.

Chapter 10 presents the creep response of the full-scale sandwich panels under uniformly distributed loads. These were subjected to an experimental programme in order to characterise their creep response. Additionally, shear creep tests of the PET foam and the balsa wood are also presented, completing the viscoelastic characterisation of the panels' constituent materials. Using the viscoelastic properties of those materials (independently determined), a composed creep model is developed to predict the creep behaviour of the full-scale panels. The model's predictions are compared with the experimentally obtained creep curves.

Chapter 11 presents the main conclusions that can be drawn from the work carried out in the thesis, and presents suggestions for future developments and research needs based on the experience gathered throughout this research.

1.5. References

- [1] Instituto Nacional de Estatística (Statistics Portugal, INE) (2013). *O parque habitacional e a sua reabilitação – análise e evolução 2001-2011* (in Portuguese). Instituto Nacional de Estatística (INE), Laboratório Nacional de Engenharia Civil (LNEC), Lisbon.
- [2] Costa, A., Guedes, J.M., Varum, H. (eds.) (2013). *Structural Rehabilitation of Old Buildings*, Springer Berlin Heidelberg.
- [3] Branco, M., Guerreiro, L.M. (2001). “Seismic rehabilitation of historical masonry buildings”, *Engineering Structures*, Vol. 33(5), pp. 1626-1634.
- [4] Correia, J.R., Branco, F.A., Ferreira, J. (2009). “GFRP–concrete hybrid cross-sections for floors of buildings”, *Engineering Structures*, Vol. 31(6), pp. 1331-1343.
- [5] Sousa, J.M, Correia, J.R., Cabral-Fonseca, S. (2013). “Durability of glass fibre reinforced polymer pultruded profiles: Comparison between QUV accelerated exposure and natural weathering in a Mediterranean climate”, *Experimental Techniques*, DOI: 10.1111/ext.12055.
- [6] Sousa, J.M., Correia, J.R., Cabral-Fonseca, S., Diogo, A.C. (2014). “Effects of thermal cycles on the mechanical response of pultruded GFRP profiles used in civil engineering applications”, *Composite Structures*, 116, 720-731.
- [7] Garrido, M., Correia, J.R., Branco, F.A., Keller, T. (2013). “Creep behaviour of sandwich panels with rigid polyurethane foam core and glass-fibre reinforced polymer faces: Experimental tests and analytical modelling”. *Journal of Composite Materials*, Vol. 48, pp. 2237-2249.
- [8] Neves e Sousa, A. (2014). *Experimental and numerical analysis of the acoustic behaviour of GFRP and GFRP-ECC hybrid sandwich panels*. Report IST 8, FCT project PTDC/ECM/113041/2009 “Rehabilitation of Building Floors with Lightweight High Performance GFRP Sandwich Panels”, Task 8, ICIST Report DTC 42/2014, 24 p.
- [9] Correia, J.R., Garrido, M., Gonilha, J.A., Branco, F.A., Reis, L.G. (2012). “GFRP sandwich panels with PU foam and PP honeycomb cores for civil engineering structural applications: Effects of introducing strengthening ribs”. *International Journal of Structural Integrity*, Vol. 3, pp. 127-147.

Chapter 2

Sandwich panels in civil engineering

2.1. Introduction

Sandwich construction is widely used in several industries where weight restrictions are a governing factor. This is mainly due to the relatively high strength- and stiffness-to-weight ratios achievable using sandwich panels, making them quite efficient from a material utilisation standpoint. Furthermore, sandwich construction is very versatile in terms of the different types of materials and geometries that it can incorporate, allowing for various ranges of mechanical properties, for the integration of non-structural functions (*e.g.*, thermal insulation, day-lighting, energy production), and for the integration of diverse finishing/aesthetic options.

In the construction industry, sandwich panels are also widely used for the same reasons. Their main applications are found in building façades and industrial roofing, where their lightweight, low thermal conductivity, and versatile aesthetics are particularly useful. However, in such applications, their structural functions are fairly limited, as the panels frequently have relatively short span lengths, and are required to resist only to their self-weight and live actions such as wind pressure or snow loads. Nonetheless, during recent years, sandwich structures have been increasingly considered (and used) for structural civil engineering applications. Some of the successful examples include bridge decks and relatively long span architectural roof structures, among others.

In this chapter, the main applications of sandwich panels in the construction industry are discussed, providing some examples of non-structural or lightly structural panels, but focusing especially on case studies where they have been applied with important structural functions. Finally, some of the most recent research efforts regarding the development of sandwich construction for civil engineering applications are presented, illustrating the

growing interest in this type of structural solution and providing a forecast of their potential future applications.

2.2. Industrial applications

2.2.1. Non-structural or lightly structural sandwich panels

In general, the use of sandwich panels in industrial, commercial and office buildings is currently quite frequent. Most of these applications involve non-structural or lightly structural building components, such as façade cladding or roofing (Figure 2.1). Typically, in such applications panels are supported by other structural members and are mostly required to provide thermal and acoustic insulation and water-tightness, being often comprised of aluminium faces (flat or profiled) and lightweight polymeric foam or mineral wool cores.

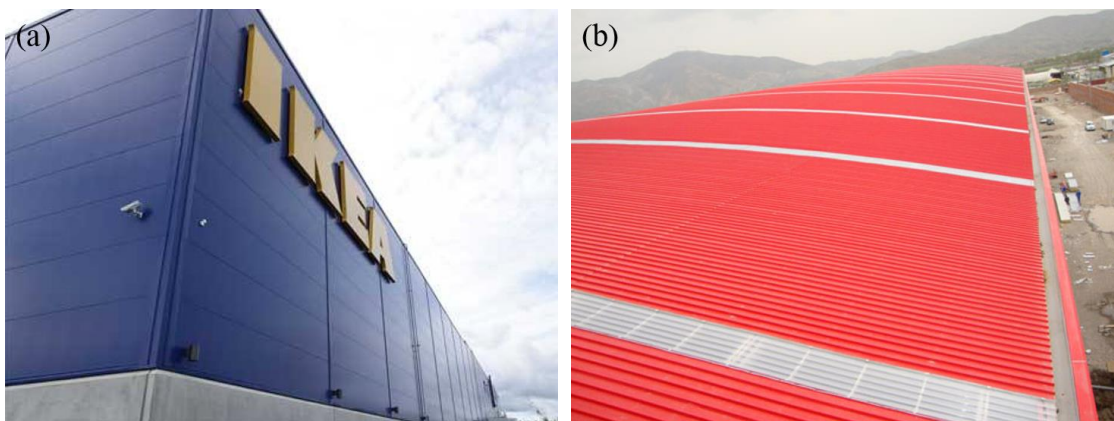


Figure 2.1. Examples of sandwich panels in building façades and roofs: (a) commercial building in Kuopio, Finland [1], and (b) industrial pavilion in Tabriz, Iran [2].

The industry that supplies this type of sandwich panels is already quite mature, with several companies producing and commercialising such products for the construction industry. These panel systems are technologically well developed, with various panel typologies existing for different applications and requirements, each having their own proprietary connection systems and installation techniques. The high modularity and repeatability of the sandwich panels in this type of application helps justify their successful industrialisation.

2.2.2. Structural sandwich panels

Recent years have seen an increasing use of sandwich panels for important structural functions in civil engineering projects. Depending on the type structure and the respective design loads, different panel typologies are being considered by the industry. In general, these fit into two relatively specific categories: (i) heavy duty sandwich panels comprising steel facings and solid polymeric cores, and (ii) lightweight sandwich panels comprising fibre-reinforced polymer (FRP) facings and low-density cores.

Heavy duty sandwich panels, while being significantly lighter than reinforced concrete or steel structures of equivalent stiffness, still have a relatively high self-weight owing to their steel facings and high density solid elastomeric cores. Nevertheless, they have found numerous applications during the last decade in the construction industry, having been applied in buildings, arenas, piers and bridges (Figure 2.2).



Figure 2.2. Heavy duty sandwich panels with steel facings and solid elastomer cores: (a) in-fill floor at the Carnegie Hall (Manhattan, New York, USA) [3], and (b) Grand Pier in Weston-super-Mare (UK) [4].

The sandwich panels considered in this thesis fall within the second category mentioned above, lightweight FRP panels, and thus these are the main focus of this chapter. FRP sandwich panels provide especially lightweight solutions by using facings that are approximately four times lighter than steel and low-density core materials such as polymer foams or balsa wood. Furthermore, FRP laminates are easily moulded into complex geometries, allowing for unconventional shapes to be achieved, thus adding significant architectural value to this type of solution.

An example that perfectly illustrates how such advantages may be put to use can be found in the *Novartis Campus Entrance* building, in Basel (Switzerland) [5]. This building, erected

in 2006, has a lightweight sandwich panel roof comprised of glass-fibre reinforced polymer (GFRP) faces and polyurethane (PUR) foam core. The building envelope is made of a load-bearing glass structure, made possible by the low self-weight of the roof panels. Furthermore, these panels have a double curvature (mimicking a wing form), which was achievable due the FRP's ability to be formed into different shapes.

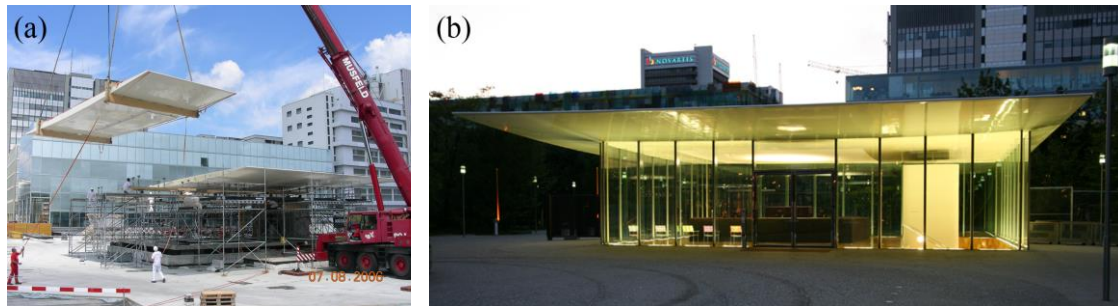


Figure 2.3. *Novartis Campus Entrance Building* (Basel, Switzerland): (a) installation of the prefabricated panels, and (b) finished building.

The sandwich panels used in the *Novartis Campus Entrance* building were prefabricated in a specialised facility, and transported by road to the construction site. However, the low weight of such composite sandwich panels also allows them to be air-lifted to locations where ground accessibility is conditioned. An example may be found in the roof structure of a private *Villa* near Basel, erected in 2011 [6]. This roof was prefabricated in a single piece with dimensions of 21 m by 6 m, using GFRP sandwich panels with polyethylene terephthalate (PET) foam core, incorporating the required thermal insulation and rainwater drainage installations. The prefabricated part was easily air-lifted to the construction site by helicopter for its final installation (Figure 2.4).

FRP sandwich panels have also been used for road bridge decks, such as the one in the bridge over the Avançon River near Bex (Switzerland), erected in 2012 [7]. This bridge, with a span of approximately 11.5 m, originally had a reinforced concrete deck that had to be replaced due to excessive degradation. With this restoration, the traffic capacity of the bridge and the maximum traffic load were increased. Constraints related to the local accessibilities of nearby populations imposed a minimal traffic disruption during the course of the works. Therefore, a lightweight deck solution compensating for the increased traffic loads while enabling the maintenance of the original quarry stone abutments was adopted. This consisted of a composite sandwich deck comprising GFRP faces and balsa wood core, adhesively bonded to two longitudinal steel girders. The prefabricated sandwich panels were

preassembled together with the steel girders on the river bank (Figure 2.5-a), and placed in position onto the stone masonry abutments using a crane (Figure 2.5-b). With this solution, the road was closed for a total period of 10 days, shortening the duration of the works by approximately 40 days by comparison with a conventional cast-in-place concrete bridge solution.

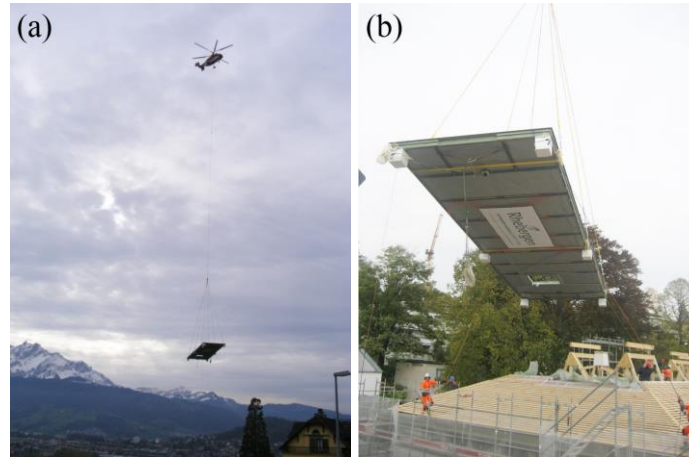


Figure 2.4. Private *Villa* roof installation (near Basel, Switzerland) [6]: (a) air-lifting of the roof, and (b) reception of the roof at the construction site.



Figure 2.5. Avançon River bridge deck near Bex, Switzerland [7]: (a) assembly of the deck components on the river bank, and (b) placement of the deck.

One of the most recent large-scale applications of GFRP sandwich panels is currently under construction, corresponding to the roofs of the stations in the Haramain High Speed Railway project, in Saudi Arabia [8] (Figure 2.6). A modular arrangement is being used for the station roofs, composed of a steel main structure supporting structural GFRP roof panels with a PET foam core. These will have span lengths of up to nine metres, and a total of over 160,000 m² of GFRP sandwich panels will be used across the project's four stations. The modularity of these panels allows for significant reductions in their production costs, while construction

time associated with the roof structures is relatively low, with two panels being manufactured and installed per day.

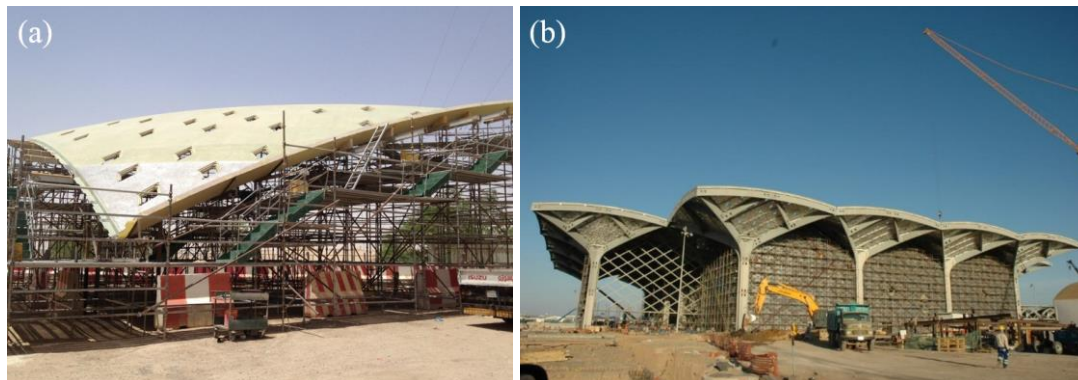


Figure 2.6. Roofs of the Haramain High Speed Railway (HHR) station: (a) mock-up installation [9], and (b) construction phase [8].

The examples shown here illustrate the potential of lightweight sandwich panels for civil engineering structural applications. So far, this potential has been mostly used to create lightweight roof structures and bridge decks. Their application in building floors is still mostly unexplored in the construction industry, with this segment constituting a research and industrialisation opportunity with a high potential for the civil engineering domain.

2.3. Research developments

2.3.1. Building floors

Lightweight FRP sandwich panels are still not commonly used in building floors as load bearing structures, but their possible application to this end has been a research subject during recent years. It is worth highlighting the investigations carried out by Awad *et al.* [10] and Correia *et al.* [13] regarding this subject.

Awad *et al.* [10] investigated sandwich panels for building floors that were designed to function as a deck supported on regularly spaced timber joists. Consequently, such panels were designed for relatively small span lengths (0.6 m), thus having a relatively small thickness of 15 mm. The panels comprised 1.8 mm thick GFRP faces and 11.4 mm thick high density (850 kg/m^3) phenolic cores. The authors focused this study on the panels' response to point loads applied at mid-span (Figure 2.7-a). Further studies were also carried out regarding the free vibration behaviour of the panels and the restraint effects on their

behaviour owing to the connections to the timber joists [11,12]. While this represents a use of sandwich panels in building floors, in this case the panels are not their main structural element.



Figure 2.7. Sandwich floor panels: (a) deck panels [12], and (b) slab panels [13].

On the other hand, Correia *et al.* [13] investigated composite sandwich panels developed to function as a monolithic slab, not requiring additional support joists or beams along the floor span. The authors carried out a comprehensive study regarding the mechanical behaviour of sandwich panels with GFRP faces and ribs, comprising cores of low density PUR foam (68 kg/m^3) and polypropylene (PP) honeycomb (110 kg/m^3). The panels were designed for spans up to 2.3 m, having a total thickness of approximately 105 mm, with 7 mm thick faces and 6 mm thick ribs. Besides characterising the mechanical properties of the materials and panel assemblies through small-scale tests, the authors carried out full-scale static and dynamic flexural experiments to determine the response of the panels for serviceability and ultimate limit states conditions (Figure 2.7-b). Numerical investigations were also carried out using finite element models (FEM) of the panels. This work confirmed the high potential of such composite sandwich panels for building floors and other civil engineering structural applications, showing that adequate stiffness and strength may be obtained using this solution.

2.3.3. Building façades

Sharaf and Fam [14] investigated large-scale building cladding panels. Such panels differ from existing sandwich cladding due to their significantly larger dimensions, having a height of 9.1 m and width of 2.4 m. The panels were fixed at six points, as shown in Figure 2.8, with a maximum distance between fixation points of 4.1 m. The panel thickness was 78 mm, and it comprised GFRP faces and ribs (thickness between 1.6 and 3.2 mm) and PUR foam core with density of 31.6 kg/m^3 . The authors tested the panels under a uniformly distributed

air pressure load, achieved by installing the panel on a self-reacting airtight frame fed by pressure load actuators. Using this configuration, the maximum span of the panels was effectively reduced to 2.4 m, corresponding to the distance between the panel's lateral edges. In addition to the experimental work, numerical investigations were carried out to simulate the behaviour of the cladding panels considering the material nonlinearity of the PUR foam and the GFRP ribs. The authors concluded that the proposed panels were fit for application in building façades, having a safety factor of 2.95 relative to the factored design pressure for the windiest region in Canada (where this study was conducted), and exhibiting deflections lower than $\text{span}/360$ for the maximum design service wind pressure.

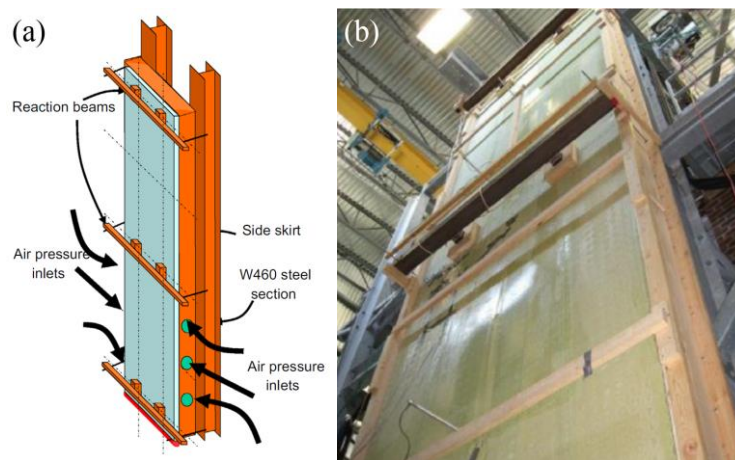


Figure 2.8. Large scale sandwich cladding panels [14]: (a) schematic of the pressure test setup, and (b) execution of the experiments.

2.3.4. Reinforcement and optimisation techniques

Various researchers have investigated multiple ways of reinforcing sandwich panels and optimising their design, regardless of the application. The reinforcement and optimisation techniques typically focused on improving the mechanical properties of the panel cores or face-core interfaces (including stabilisation of compressed faces), which often represent the weakest/critical points in sandwich panel's design. These may be classified into three main categories: (i) laminated ribs or webs, (ii) core stitching, and (iii) functionally graded cores.

2.3.4.1. Ribs/webs

Laminated (FRP) ribs/webs are through-thickness plate elements that connect the top and bottom face sheets and function in parallel with the usual low density core materials. These may be incorporated along the panel edges (Figure 2.9-a) or within the core (Figure 2.9-b). Being typically much stiffer than traditional low-density core materials, these elements are

able to significantly increase the shear stiffness of the sandwich panel, provided that they are incorporated along the span direction. Several authors have carried out studies to assess the performance of sandwich panels with various rib configurations [13-17]. The increase in flexural stiffness and strength obtained in these studies varies significantly, as it depends on multiple factors (materials used, cross-sectional dimensions, number and placement of ribs); however, improvements of 40-100% in those properties per added rib/web are often reported. Such figures make this a very interesting shear reinforcement technique, especially when taking into account that incorporating rib/webs in the production of the sandwich panels is fairly simple.

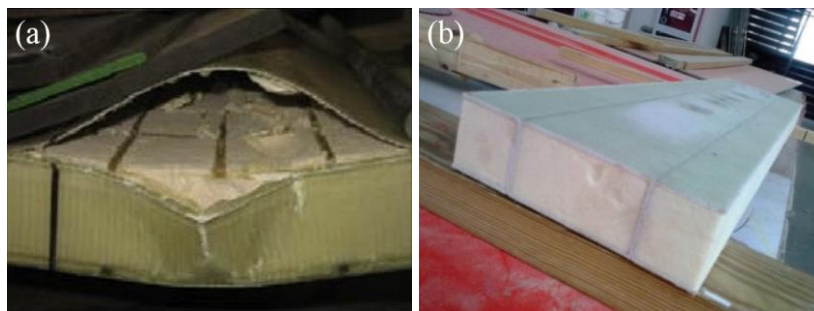


Figure 2.9. Reinforcement ribs/webs: (a) along the panel edges [15], and (b) within the core [16].

2.3.4.2. Core stitching

Core stitching consists of connecting the top and bottom face sheets by relatively thin through-thickness FRP inserts. These are produced by stitching together the dry fibre fabrics of the faces and the core using fibre strands, and subsequently infusing them with the polymer resin. These stitches may be perpendicular (columns, *cf.* Figure 2.10-a) or oriented at a certain angle (trusses, *cf.* Figure 2.10-b) with the face sheets.

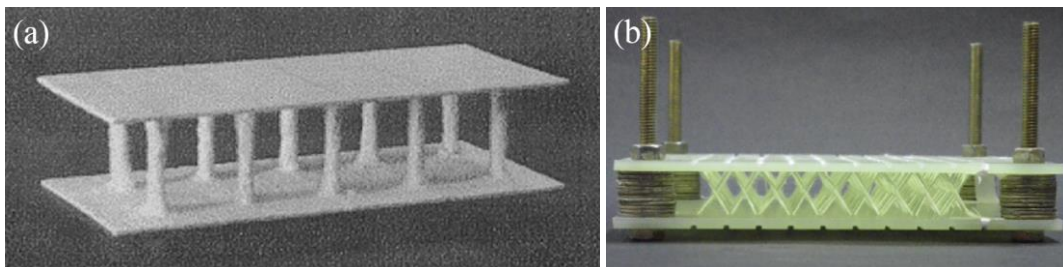


Figure 2.10. Reinforcement stitches (with core removed): (a) columns [18], and (b) truss [23].

Several authors have investigated this type of reinforcement solution, which has the potential to improve the shear properties of the core, and especially to improve the face-core connection [18-23]. However, this technique is relatively challenging to implement, as the

stitching procedures are fairly labour intensive. This may hinder the widespread adoption of this type of reinforcement technique.

2.3.4.3. Functionally graded cores

Functionally graded cores have different properties at different locations in the panel according to particular reinforcement needs or optimisation strategies. These different properties are typically achieved by using different core materials, or different densities of the same type of material. This grading may generally be grouped into two main types: (i) along the panel span (“horizontal” grading), and (ii) along the panel thickness (“vertical” grading).

Having different mechanical properties along the panel span (as illustrated in Figure 2.11-a) may be interesting for panels with loads applied uniformly or at multiple locations along their length. The underlying principle is that the strength and stiffness of the core may be increased when shear forces are higher, and reduced in less stressed zones of the panel. This allows reducing the overall panel weight while maintaining its overall strength. The downside is that for load configurations different from the design load case (*i.e.*, for shear force distributions different from the design distribution) the panel’s performance may be negatively affected. Another issue that arises are the stress concentrations that appear at the joints between core materials. These may, however, be minimised by using scarf joints instead of butt joints [25,26].

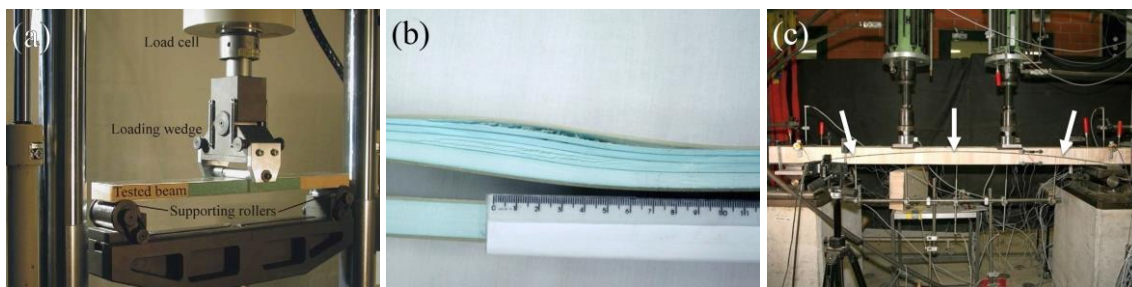


Figure 2.11. Structurally graded cores: (a) “horizontal” grading [25], (b) “vertical” grading [27], and (c) arch-like grading [29].

On the other hand, a layerwise distribution of core materials with different properties along the thickness of the panel (*cf.* Figure 2.11-b) allows improving certain aspects of its behaviour. For example, it is possible to increase the instability/wrinkling stress of the compressed face sheet by having a layer of stiffer and stronger material next to this face, given that such material will constitute a more stable elastic foundation, when compared

with a softer and weaker foam [27,28]. Similarly, having a layer with improved properties close to the face sheets allows improving the panel performance under point loads, as this improved core will withstand higher loads and help distribute the localised stresses over a larger area of the weaker core.

Osei-Antwi *et al.* [29] proposed a sandwich panel architecture that incorporates aspects of both “vertical” and “horizontal” grading of the core (Figure 2.11-c). This panel comprised an arch-like core distribution, where a stiffer core material (250 kg/m^3 balsa wood) is used near the panel edges/supports and for the interface with the top (compressed) face sheet, while a lower density core (95 kg/m^3 balsa wood) is used in the lower central area of the core. Between these two materials, an FRP laminate was incorporated, acting as an arch structure. This panel configuration was compared with simple sandwich panels with homogenous cores of the high-density balsa wood. The authors found that the structurally graded cored panels had higher stiffness and failure loads than those with homogenous high density cores, illustrating how a complex core assembly may be used to improve the performance of sandwich panels, further optimising them in terms of total strength- and stiffness-to-weight ratios.

2.3.5. Multifunctional integration

As previously mentioned, composite sandwich panels allow for the integration of multiple functions into a single construction element. Low-density materials used for sandwich cores typically have very low thermal conductivity, conferring thermal insulation properties to the panels, which may thus offer a solution combining structural and building physics functions.

A different example stems from the possibility of achieving translucency in the sandwich panels (Figure 2.12-a) through a judicious selection of materials, permitting the integration of daylighting functions⁵ with those already mentioned regarding thermal insulation and structural performance [30].

Recently, such translucency has been regarded as an opportunity to integrate solar cells within the sandwich panel faces, as illustrated in Figure 2.12-b. In fact, it has been shown that it is possible to embed opaque thin-film amorphous-silicon (a-Si) solar cells and

⁵ The all-GFRP *Eyecatcher* building, in Basel (Switzerland) is an example of such integration, albeit the panels used therein have secondary load-carrying functions [30].

transparent coloured dye solar cells (DSCs) within translucent structural GFRP laminates, and that efficiencies as high as 90% compared to those obtained with encapsulation in traditional glass materials are achievable with such solutions [31]. This represents a further functional integration, adding solar power generation potential to the architectural, building physics and structural functions already afforded by composite sandwich panels.

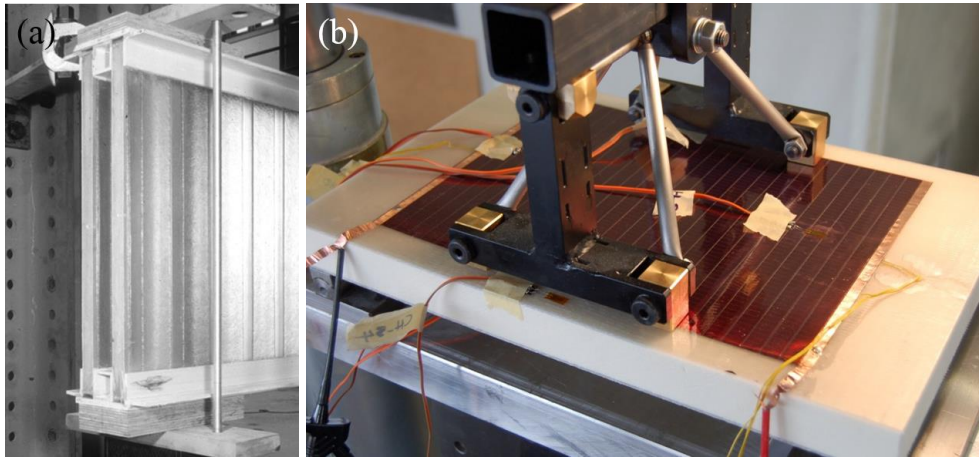


Figure 2.12. Multifunctional integration: (a) translucency for daylighting use [30], and (b) solar cell encapsulation [31].

2.4. Concluding remarks

From the general review of civil engineering applications of sandwich panels presented here, it is clear that this type of structural element has found various applications in the construction industry. These are quite diverse in terms of their functions, panel typologies and materials, and degrees of structural importance. The most industrialised uses of sandwich construction, and consequently those which are most known by practitioners in the field, concern non-structural or lightly structural sandwich panels.

However, in recent years, and especially during the last decade, several examples of structural applications of sandwich panels have been registered. These applications have varied from purely functional structures, such as bridge decks, to elements with high architectural value, such as architectural free-form roofs. The latter help increasing the visibility of sandwich construction as a technically viable solution which the potential to add value to the construction product.

The presented review shows that buildings floors are still not within the common applications of sandwich panels. In fact, it is still necessary to develop technological aspects related to this particular application. The best panel architectures and materials, the adequate connection technology, and the behaviour of the sandwich floors under long-term sustained loads are among the aspects that must be studied. The following chapters of this thesis address these three issues. The most promising reinforcement and optimisation techniques reviewed here are considered, such as the incorporation of ribs/webs and the structurally graded core arrangements. For the chapters concerning particular scientific aspects, such as those related to connection technology or the viscoelastic behaviour of the sandwich panels and their materials, the literature review presented here is complemented with specific state-of-the-art assessments within the respective chapters.

2.5. References

- [1] Rautaruukki Corporation (n.d.). *Ikea Kuopio – Save energy and stand the test of time*. Available online at: <http://www.ruukki.com/References/Commercial-buildings/Ikea-Kuopio---Save-energy-and-stand-the-test-of-time> (latest access in 09-11-2015).
- [2] Detart Roof and Wall Systems Inc. (n.d.). *Tebriz Printing Facilities*. Available online at: http://www.detart.com.tr/en/gallery/projects/tebriz_baski.html (latest access in 09-11-2015).
- [3] Intelligent Engineering Ltd. (n.d.). *In-fill floor – Carnegie Hall South & North Tower*. Available online at: <http://www.ie-sps.com/downloads/741.pdf> (latest access in 09-11-2015).
- [4] Intelligent Engineering Ltd. (n.d.). *Structural Floor – The Grand Pier*. Available online at: <http://www.ie-sps.com/downloads/741.pdf> (latest access in 09-11-2015).
- [5] Keller, T., Haas, C., and Vallée, T. (2008). “Structural concept, design, and experimental verification of a glass fiber-reinforced polymer sandwich roof structure”. *Journal of Composites for Construction*, Vol. 12(4), pp. 454–468.
- [6] Gurit Holding AG (n.d.). *Villa Roof, Switzerland*. Available online at: <http://www.gurit.com/villa-roof-switzerland-2011.aspx> (latest access in 09-11-2015).

- [7] Keller, T., Rothe, J., de Castro, J., and Osei-Antwi, M. (2014). "GFRP-balsa sandwich bridge deck: concept, design, and experimental validation". *Journal of Composites for Construction*, Vol. 18(2), 04013043.
- [8] Saudi Railways Organization (n.d.). Haramain *High Speed Rail Project*. Available online at: http://www.saudirailways.org/portal/page/portal/PRTS/root/Home/04_Expansion_Specification/03Introduction/03Phase-%20I%20Package-2 (latest access in 09-11-2015).
- [9] Durand, S., Lubineau, G., Chapelle, H. (2012). "Design analysis of GRP panels for the roof of the Haramain High Speed Railway Jeddah Station". *Proceedings of the 10th International Conference on Sandwich Structures (ICSS-10)*, Nantes, France, August 27-29.
- [10] Awad, Z.K., Aravinthan, T., Zhuge, Y. (2012). "Experimental and numerical analysis of an innovative GFRP sandwich floor panel under point load", *Engineering Structures*, Vol. 41, pp. 126-135.
- [11] Awad, Z.K., Aravinthan, T., Zhuge, Y. (2012). "Investigation of the free vibration behaviour of an innovative GFRP sandwich floor panel", *Construction and Building Materials*, Vol. 37, pp. 209-219.
- [12] Awad, Z.K., Aravinthan, T., Zhuge, Y., Manalo, A. (2013). "Geometry and restraint effects on the bending behaviour of the glass fibre reinforced polymer sandwich slabs under point load", *Materials and Design*, Vol. 45, pp. 125-134.
- [13] Correia, J.R., Garrido, M., Gonilha, J.A., Branco, F.A., Reis, L.G. (2012). "GFRP sandwich panels with PU foam and PP honeycomb cores for civil engineering structural applications: Effects of introducing strengthening ribs". *International Journal of Structural Integrity*, Vol. 3(2), pp. 127-147.
- [14] Sharaf, T., Fam, A. (2013). "Analysis of large scale cladding sandwich panels composed of GFRP skins and ribs and polyurethane foam core". *Thin-Walled Structures*, Vol. 71, pp. 91-101.
- [15] Fam, A., Sharaf, T. (2010). "Flexural performance of sandwich panels comprising polyurethane core and GFRP skins and ribs of various configurations". *Composite Structures*, Vol. 92, pp. 2927-2935.

- [16] Wang, L., Liu, W., Fang, H., Wan, L. (2015). "Behavior of sandwich wall panels with GFRP face sheets and a foam-GFRP web core loaded under four-point bending". *Journal of Composite Materials*, Vol. 49(22), pp. 2765–2778.
- [17] Tuwair, H., Hopkins, M., Volz, J., ElGawady, M.A., Mohamed, M., Chandrashekhara, K., Birman, V. (2015). "Evaluation of sandwich panels with various polyurethane foam-cores and ribs". *Composites Part B: Engineering*, Vol. 79, pp. 262-276.
- [18] Kim, J.H., Lee, Y.S., Park, B.J., Kim, D.H. (1999). "Evaluation of durability and strength of stitched foam-cored sandwich structures". *Composite Structures*, Vol. 47, pp. 543-550.
- [19] Wang, B., Wu, L., Jin, X., Du, S., Sun, Y., Ma, L. (2010). "Experimental investigation of 3D sandwich structure with core reinforced by composite columns". *Materials and Design*, Vol. 31, pp. 158-165.
- [20] Dawood, M., Taylor, E., Rizkalla, S. (2010). "Two-way bending behavior of 3-D GFRP sandwich panels with through-thickness fiber insertions". *Composite Structures*, Vol. 92, pp. 950-963.
- [21] Wu, Z., Zeng, J., Xiao, J., Liu, J. (2014). "Flexural performance of integrated 3D composite sandwich structures". *Journal of Reinforced Plastics and Composites*, Vol. 33(16), pp. 1496–1507.
- [22] Wang, B., Zhang, G., He, Q., Ma, L., Wu, L., Feng, J. (2014). "Mechanical behavior of carbon fiber reinforced polymer composite sandwich panels with 2-D lattice truss cores". *Materials and Design*, Vol. 55, pp. 591-596.
- [23] Kim, H., Cho, B.H., Hur, H.-K., Kang, K.-J. (2015). "A composite sandwich panel integrally woven with truss core". *Materials and Design*, Vol. 65, pp. 231-242.
- [24] Mostafa, A., Shankar, K., Morozov, E.V. (2014). "In-plane shear behaviour of composite sandwich panel incorporated with shear keys methodology at different orientations: finite element study". Vol. 48(24), pp. 2945–2959.
- [25] Bozhevolnaya, E., Thomsen, O.T. (2005). "Structurally graded core junctions in sandwich beams: quasi static loading conditions". *Composite Structures*, Vol. 70, pp. 1-11.

- [26] Osei-Antwi, M., de Castro, J., Vassilopoulos, A.P., Keller, T. (2014). “Analytical modeling of local stresses at Balsa/timber core joints of FRP sandwich structures”. *Composite Structures*, Vol. 116, pp. 501-508.
- [27] Ávila, A.F. (2007). “Failure mode investigation of sandwich beams with functionally graded core”. *Composite Structures*, Vol. 81, pp. 323-330.
- [28] Osei-Antwi, M., de Castro, J., Vassilopoulos, A.P., Keller, T. (2014). “Modeling of axial and shear stresses in multilayer sandwich beams with stiff core layers”. *Composite Structures*, Vol. 116, pp. 453-460.
- [29] Osei-Antwi, M., de Castro, J., Vassilopoulos, A.P., Keller, T. (2013). “FRP-balsa composite sandwich bridge deck with complex core assembly”. *Journal of Composites for Construction*, Vol. 17(6), 04013011.
- [30] Keller, T., de Castro, J., Schollmayer, M. (2004). “Adhesively bonded and translucent glass fiber reinforced polymer sandwich girders”. *Journal of Composites for Construction*, Vol. 8(5), pp. 461–470.
- [31] Pascual, C. (2014). *Translucent load-bearing GFRP envelopes for daylighting and solar cell integration in building construction*. PhD thesis, École Polytechnique Fédérale de Lausanne (EPFL), Switzerland.

Chapter 3

Design, materials and panel architectures

3.1. Introduction

The sandwich panels studied in this thesis were designed considering the structural and building physics⁶ requirements applicable to building floors. Multiple panel architectures were considered, comprising different materials and reinforcing solutions, to assess panel optimisation strategies for the envisaged application. In this context, core materials with different mechanical properties were incorporated into the sandwich panels. Other panels were produced with cores of variable density along the span, providing additional strength and stiffness where necessary and reducing the panel mass where possible. Glass-fibre reinforced polymer (GFRP) elements were also judiciously introduced in the cores of the sandwich panels, whether in truss or rib configurations, complementing the traditional core materials to produce hybrid-cored panels with increased shear stiffness.

The sandwich panels were manufactured by vacuum infusion, a commonly used process for the production of fibre-reinforced polymer (FRP) parts, at the *Pólo de Inovação em Engenharia de Polímeros* (PIEP) research institute. In this process, the dry materials that comprise the panel (*i.e.*, all materials with the exception of the polymer resin) are laid up in the appropriate order (Figure 3.1-a) and encased in a thin plastic vacuum bag sealed around its perimeter. Using a vacuum pump, the air is extracted from inside the bag, while the atmospheric pressure consolidates the dry materials.

Using the pressure differential between the interior of the vacuum bag and the exterior environment, resin is introduced into the part through resin feeder lines installed within the

⁶ This design and development effort was carried out in the scope of the *RehabGFRP* research project in collaboration with building physics researchers, who investigated the acoustic and thermal performance of the sandwich panels [1,2]. However, the scope of this thesis pertains only to the structural behaviour of the floors, and consequently the building physics aspects are not directly addressed.

sealed bag (Figure 3.1-b). The resin injection process is carried out until the complete infusion of the parts is reached (Figure 3.1-c), at which point the resin intake is interrupted. The vacuum is maintained during the first hours of the resin's curing process, in order to ensure the consolidation and homogeneity of the part. After the part is cured to a sufficient degree, the vacuum bag may be removed and the part may be trimmed and/or subjected to additional surface treatments, if necessary (painting, varnishing, etc.). A finished sandwich panel prototype is shown Figure 3.1-d. A detailed description of the manufacturing process of the panels can be found in [3].

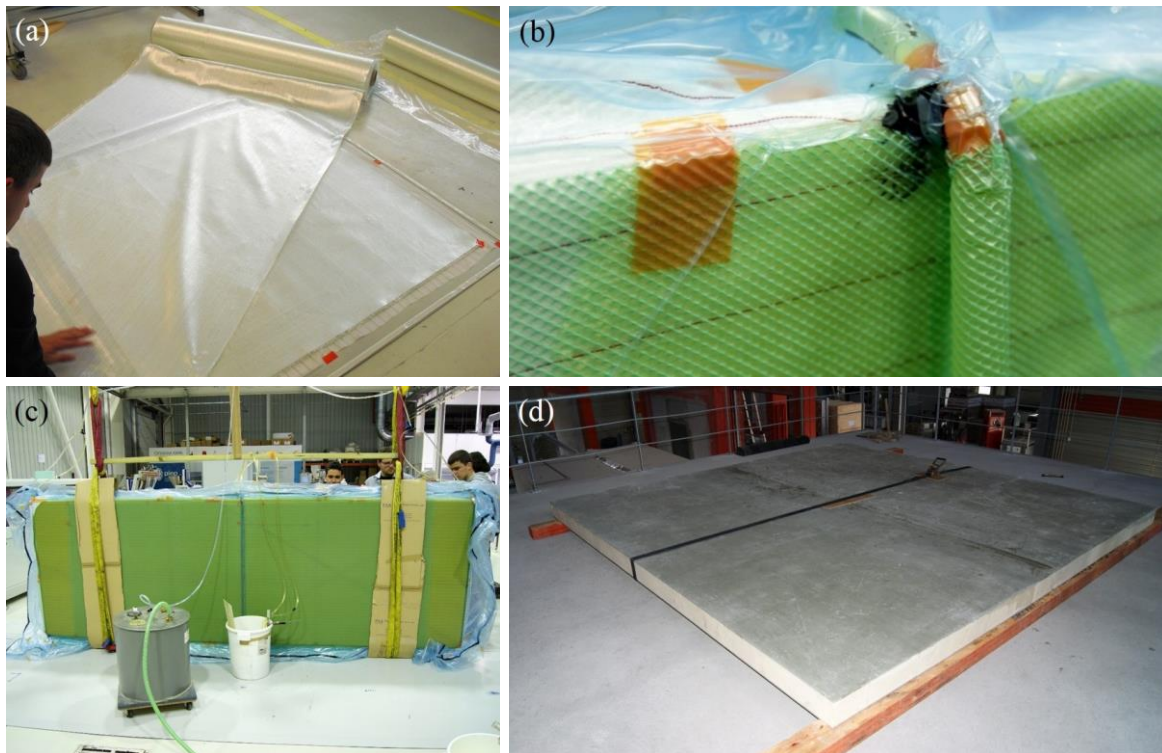


Figure 3.1. Composite sandwich panels production: (a) fibre mat layup, (b) detail of vacuum infusion feeder lines, (c) general view of the vacuum infusion process, and (d) finished sandwich panel prototype.

3.2. Design of sandwich panels

The structural design of the sandwich panels was carried out according to the requirements of the Eurocode standards, namely Eurocode 0 (EN 1990, [4]) and Eurocode 1 (EN 1991, [5]). The design calculations are described in detail in [6], where the various safety verifications that were carried out are explained, and the design equations that were used are given. The current section

aims to provide a global overview of the design process, complementing the information given in those references.

The sandwich panels were designed for spans of 3.3 m⁷. They were conservatively considered as simply supported unidirectional slabs subjected to uniformly distributed loads. In reality, depending on the connections between the floors and their vertical support elements (in principle, the building's load-bearing walls), a significant degree of rotational restriction can be achieved at the panels' supports⁸. This effect helps reducing the vertical deflections exhibited by the panels (which were found to be the limiting design factor, as discussed further ahead in this section) and the maximum bending moments. However, this aspect was not taken into account in the sandwich panel design, as the degree of rotational restriction conferred to the floors by the supports is highly dependent on the support configuration, thus justifying the conservative design approach.

Prior to the definition of the cross-sectional dimensions, a selection of materials to be incorporated in the sandwich panels was carried out. This comprised the selection of (i) core materials, and (ii) GFRP laminate layups.

A survey of core materials was carried out, and based on the eligible materials found and on their respective mechanical properties, a nominal density of approximately 100 kg/m³ was chosen as being adequate for the intended application. Such density was found to guarantee a good balance between the structural performance of the panels and their overall mass (which should be kept as low as possible). Following this principle, three core materials were selected: (i) polyurethane (PUR) foam, (b) polyethylene terephthalate (PET) foam, and (c) balsa wood. For the panels with variable density core mentioned earlier, three different densities of PUR foam were adopted, chosen to provide sandwich panel designs with similar self-weight as the simple sandwich panels (that comprised uniform and homogeneous cores).

For the GFRP laminates, target mechanical properties were defined, namely concerning minimum values for the longitudinal and transverse Young's moduli and the in-plane shear moduli. Considering the typical mechanical properties of unidirectional E-glass fibres and

⁷ This span length was limited by the dimensions of a prototype floor manufactured for the acoustic experiments (3.56 m by 3.56 m) carried out under the scope of the *RehabGFRP* research project [2]. However, the proposed sandwich floor panels may be easily designed for longer spans within the range typically found in buildings with stone rubble or timber-framed masonry walls.

⁸ As discussed in detail in Chapter 7.

orthophthalic polyester resins, laminate layups fulfilling those requirements were developed. This was achieved by applying the Classical Laminate Theory (CLT) (*e.g.*, [7]), which was implemented in a MATLAB code developed for the purpose of obtaining estimates of the laminates' mechanical properties as a function of their constituent materials, the number of plies and their orientations, the lamina stacking sequence, and the final laminate thickness.

The various panel architectures, comprising different core materials and reinforcement solutions, inherently have different mechanical responses in terms of flexural stiffness and strength. Independently designing each panel type would result in the adoption of different cross-sectional dimensions across the different typologies, as a function of their particular mechanical properties. However, to ensure direct comparability between the different panel architectures, a baseline design with identical cross-sectional dimensions was adopted for all typologies. This design was defined considering the case of simple sandwich panels (without reinforcements) with a PUR foam core⁹. The remaining typologies, incorporating materials with higher mechanical properties, are consequently oversized to a certain degree. As mentioned, this was considered preferable to having individual designs for each typology, since adopting identical cross-sectional dimensions allows for a direct performance comparison between the different panel architectures.

It was found that the sandwich panel design was, as previously mentioned, limited by serviceability criteria pertaining to maximum allowable vertical deflections, which were considered as $\text{span}/500$, or 6.6 mm for a span 3.3 m. Creep deformability was also considered in the design process. However, at the design stage, the data concerning the creep behaviour of the core materials and of GFRP laminates produced by vacuum infusion was found to be scarce or inexistent. This limited the possibility of accurately predicting and quantifying the long-term creep deformations of the sandwich panels. The lack of data regarding the creep of such materials motivated the comprehensive creep testing programme that was carried out for this thesis, and is presented in Part IV of the current document.

It is worth mentioning that, from a building physics standpoint, while sandwich panels are typically able to provide high thermal insulation, their acoustic insulation performance can be weak due to their low mass. To address this issue, additional layers, such as floating floors

⁹ Typology as defined in section 3.4.1.

or drop-down ceilings may be required to comply with legal acoustic requirements [2]. The addition of plenum spaces resulting from the addition of drop-down ceilings presents additional advantages, providing room for any necessary building installations, and allowing the incorporation of fire protection systems (passive and/or active) into the floor system, essential to guarantee the fire resistance of the floors. However, these two aspects (acoustic performance and fire behaviour) are outside the scope of this thesis, and thus will not be discussed in-depth.

3.3. Materials

3.3.1. GFRP laminates

The GFRP laminates were produced using *UNIE 300* (300 g/m²) and *UNIE 400* (400 g/m²) stitched unidirectional E-glass fibre mats (produced by *Selcom SRL.*, [8]), and an orthophthalic polyester resin (*Distitron 3501*, [9]).

Three types of GFRP laminates were used in the production of the sandwich panels, differing in their fibre layup sequence: (i) face sheet laminates, (ii) longitudinal reinforcement rib laminates, and (iii) truss laminates.

The fibre layups used for each type of laminate were as follows:

- (i) *face sheets*: [0/0/30/-30/90/0]_s, thickness of 7 mm;
- (ii) *longitudinal ribs*: [0/30/-30/0]_s, thickness of 5 mm;
- (iii) *truss*: unidirectional 0°, thickness of 4 mm.

The face sheet laminates were developed to have the highest Young's modulus along the longitudinal (0°) direction, which corresponds to the main span direction of the sandwich panels. However, it was also important to guarantee reasonably high values of the Young's modulus in the transverse direction and of the in-plane shear modulus of the laminates, as the floors are expected to be able to present some bi-directional plate behaviour and act as a rigid diaphragm in the event of horizontal loads. For this reason, 90° and ±30° oriented fibres were also considered in the layup.

It was essential to ensure fibre continuity between the face sheet and rib laminates to guarantee the effectiveness of the connection between these two components. Consequently,

the fibre layup of the rib laminates was defined by suppressing two plies from the face sheet layup, at 0° and 90° , with the remaining plies continuously wrapping the sandwich panels.

For the truss laminates, a mainly unidirectional laminate with fibres oriented along the longitudinal (0°) direction was adopted, as the truss elements are expected to be subjected mainly to axial stresses. It was not possible to guarantee a consistent fibre continuity between the face sheets and the truss elements in a cost effective manner using the vacuum infusion production method adopted for the panel production¹⁰.

3.3.2. Core materials

The following different types of core materials, illustrated in Figure 3.2, were considered for the sandwich panels:

- (i) polyurethane (PUR) foams, with nominal densities of 40, 80, 100, and 120 kg/m³;
- (ii) polyethylene terephthalate (PET) foam with nominal density of 105 kg/m³;
- (iii) balsa wood with nominal density of 94 kg/m³.

The 40, 80 and 120 kg/m³ PUR foams were produced by the company *ALTO – Perfis Pultrudidos, Lda.* (technical data sheets were not provided), while the 100 kg/m³ foam was produced by the company *Polirígido* [10]. The PET foam and the balsa wood were produced by the company *3A Composites A.G.*, under the commercial designations *Airex T92* [11] and *Baltek SB50* [12], respectively.

Thermosetting PUR foams are widely used in the construction industry for various ends, including for sandwich construction (typically in lightweight roofing, or in non-structural or lightly structural partition and façade panels). Its widespread application and relatively low cost make it an interesting core material option for the sandwich panels in the current study.

The thermoplastic PET foam is less common in civil engineering applications, but presents significantly higher mechanical properties than typical PUR foams of the same density. Furthermore, this foam presents the advantage of being recyclable. However, its cost is higher than that of the typical PUR foams.

¹⁰ As discussed in Chapter 5 (section 5.4.2.4), such lack of continuity of the fibre reinforcement negatively influenced the flexural performance of the panels, considerably limiting their load capacity.

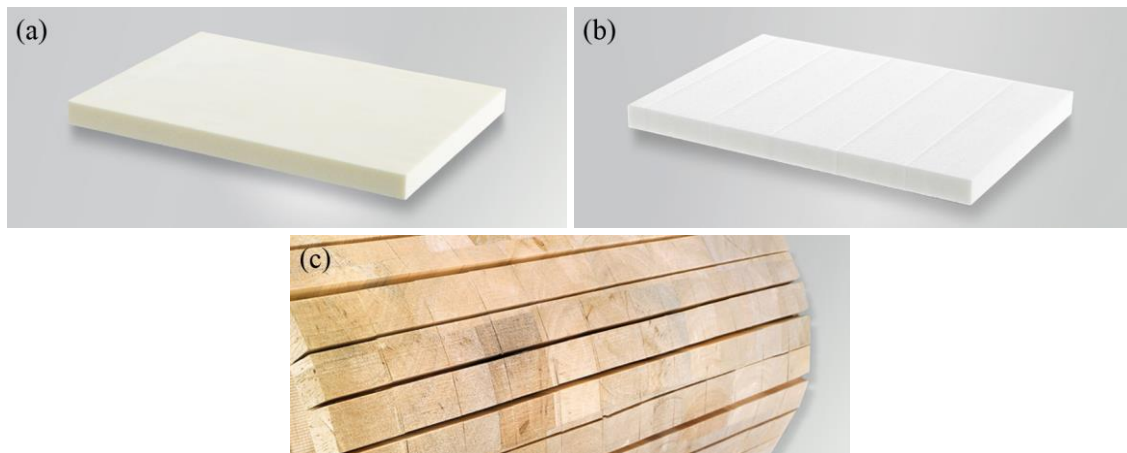


Figure 3.2. Core materials: (a) PUR foam [13], (b) PET foam [11] and (c) balsa wood [12].

Finally, the balsa wood presents the highest mechanical properties among the three types of core materials considered here, with its bulk cost also being significantly higher. However, its better structural performance means that thinner sandwich panels can be designed, possibly compensating for the material's higher cost. Balsa wood is a natural and highly orthotropic material, and thus the material orientation and high scatter of the properties must be taken into account in the design of the sandwich panels.

3.4. Panel architectures

3.4.1. Simple sandwich panels

The simple sandwich panels present a typical sandwich architecture, with two identical and relatively thin face sheets being separated by a relatively thick and homogenous core. Three different types of simple sandwich panels were considered in this study, each comprising a different core material: (i) PUR foam, (ii) PET foam, and (iii) balsa wood. These were labelled according to their core material as the PUR, PET and BAL panel typologies.

The PUR foam with a nominal density of 100 kg/m^3 was used for these panels. The simple sandwich panels were produced in large slabs (one for each type of core material), which were then machined into individual beams with the cross section presented in Figure 3.3.

As previously mentioned, the simple panel architecture with a PUR foam core was used in the baseline structural design of the panels. The cross-sectional dimensions pertaining to

core and face sheet thickness values obtained for this typology (cf. Figure 3.3) were then used in the other panel typologies.

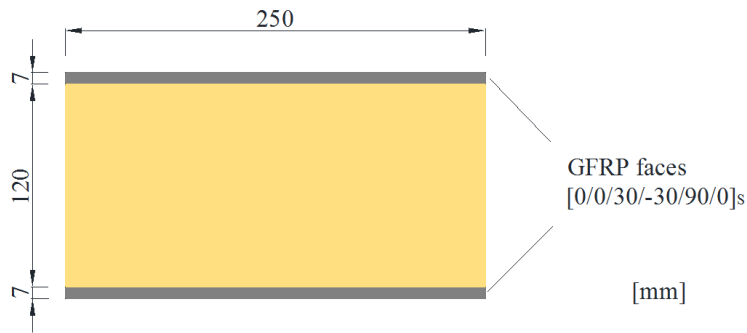


Figure 3.3. Cross-section of the simple sandwich panels.

3.4.2. Panels with longitudinal ribs

The simple sandwich panels typically present significant shear deformability owing to the relatively low shear moduli of the core materials used in sandwich construction. To mitigate this issue, shear reinforcement solutions were implemented in the sandwich panels, aiming at reducing their shear deformability and thus increasing their overall stiffness under vertical loads. One of those reinforcement solutions consisted of introducing longitudinal GFRP ribs (or webs) in the panel core. This hybrid core panel typology was labelled as RIB (Figure 3.4).

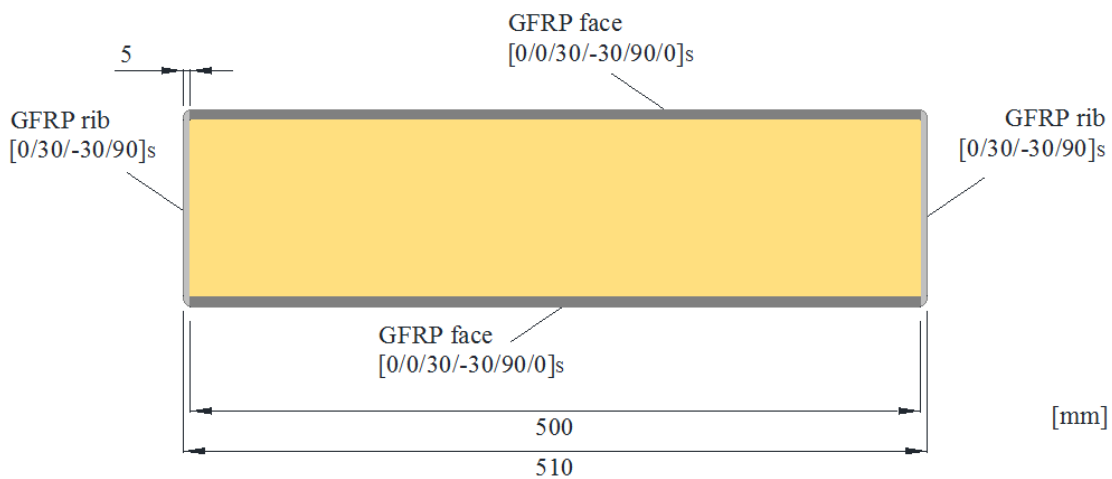


Figure 3.4. Cross-section of the RIB panels.

The RIB panels were produced in a single continuous panel, which was later machined into individual panels. The GFRP ribs were incorporated into the cross-section at its outer edges. The adopted cross-sectional dimensions are shown in Figure 3.4, and the core material used

was the 100 kg/m^3 PUR foam. The different types of laminate used for the faces and ribs are also indicated, having been achieved through the selective suppression of specific plies during the fibre layup procedure, as previously explained (section 3.3.1).

3.4.3. Truss-foam core panels

The truss-foam core panels (labelled TFC) constitute a different solution for the shear reinforcement of the sandwich panel cores. These hybrid-cored panels comprise a GFRP truss, embedded in PUR foam, in which transversely positioned webs angled at 45° transfer the shear loads between the top and bottom sandwich panel faces.

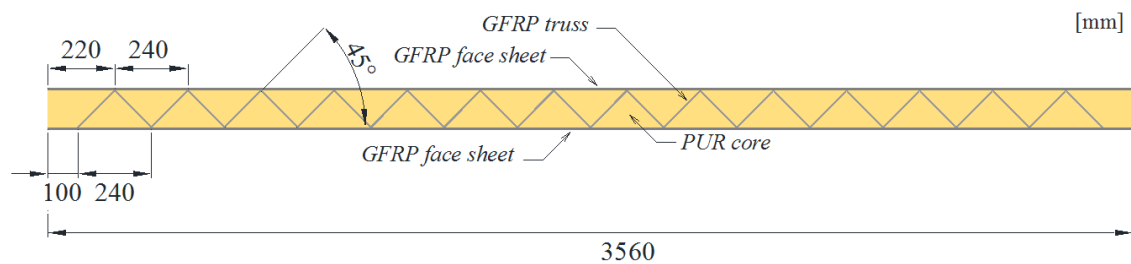


Figure 3.5. Longitudinal section of the TFC panels.

The longitudinal development of these panels was defined as shown in Figure 3.5. These panels were produced in a single large slab, which was then machined into individual beams with the same cross-section as the simple panels (*cf.* Figure 3.3). The PUR foam used in the TFC panels had a nominal density of 100 kg/m^3 .

3.4.4. Variable density core panels

The variable density core panels (labelled VDC) aimed at optimising the core material distribution along the panel span. To this end, the sandwich panel's core was longitudinally divided into multiple segments, each with a different core material density (and thus different shear strength and stiffness values) positioned according to the shear forces acting on the panel.

The adopted core material distribution followed the longitudinal development shown in Figure 3.6, and was optimised for uniformly distributed vertical loads acting on the panel. This optimisation was carried out considering average properties of typical rigid PUR foams of different densities. Foam densities of 40 kg/m^3 , 80 kg/m^3 and 120 kg/m^3 were used. In chapter 5 of this thesis (section 5.4.2.5) this aspect is further explored by analysing the shear stress distributions obtained in full-scale flexural tests of this panel typology, and how these

compare with the shear strength values of the different core material segments, as determined in the material characterisation tests presented in chapter 4 (section 4.3.1.3). The cross-section of these panels was similar to that adopted for the simple sandwich panels, according to the dimensions shown in Figure 3.3.

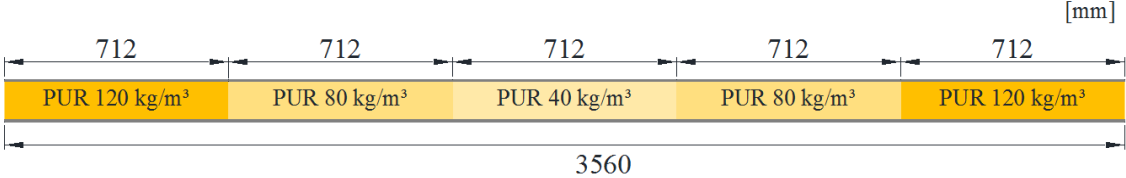


Figure 3.6. Longitudinal section of the VDC panels.

3.4.5. Connection panels

This study also involved the development of connection systems for the connections between adjacent sandwich panels. The research conducted in this regard and the concepts behind the adopted connection are detailed in chapter 6.

The sandwich panels that were produced for the panel-to-panel connections had a PUR foam core, with a density of 100 kg/m³. An additional shorter panel (1.0 m in length) was also produced with a balsa wood core, for use in the experiments reported in section 6.4.2. The connection panels included GFRP face sheets and ribs similar to those of the RIB panels. The connection system was incorporated into the GFRP envelope of the sandwich panels according to the cross-section shown in Figure 3.7. To achieve the protruding connection element (lower right side in Figure 3.7), fibre mats from the adjacent face sheet and rib were folded outward and prolonged to the required length.

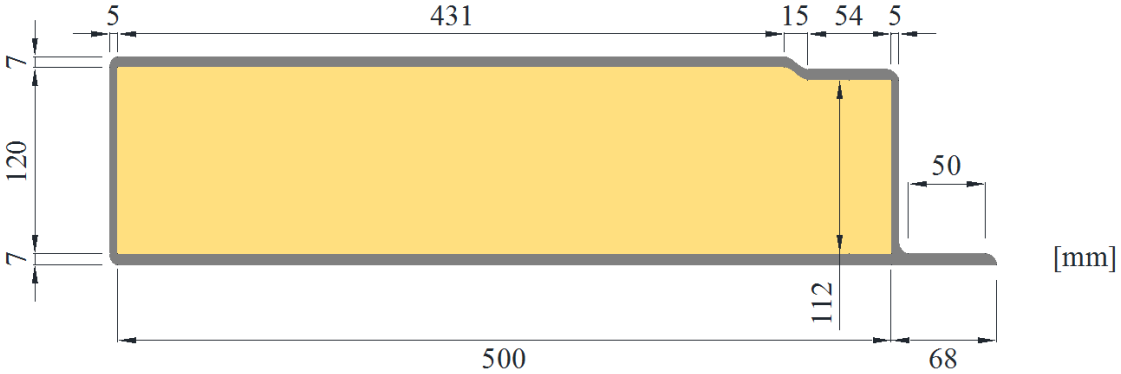


Figure 3.7. Cross-section of the sandwich panels with panel-to-panel connection system.

3.5. Production costs

The production costs associated with each panel typology can vary significantly due to the different materials that are incorporated into each specific panel architecture, but also due to the different labour intensity associated with manufacturing each type of panel. The in-depth economic analysis of the production costs of the sandwich panels, and of their impacts on the building construction costs, is outside the scope of this thesis. However, a simple analysis was carried out based on the costs of the materials acquired for the production of the sandwich panel prototypes manufactured for this thesis.

Table 3.1 presents the cost of materials (per square metre) per panel typology, estimated based on the costs incurred during the development of this investigation. These do not include the cost of labour nor of disposable materials associated with the vacuum infusion process. However, these costs were obtained in the context of prototype development. It is expectable that such costs may be significantly lower in an industrialised production context.

Table 3.1. Production cost estimates (materials only) for the different sandwich panels.

Typology	Cost [€/m ²]
PUR	198.00
PET	222.90
BAL	278.70
RIB	210.96
TFC	226.82
VDC	188.47

The VDC panels were the most economical panel typology, followed by the PUR panels (cost increase of approximately 10 €/m²) and the RIB panels (cost increase of approximately 22 €/m²). The PET and TFC panels presented relatively similar material costs; however, if labour costs were to be considered in the analysis, the significantly higher workmanship and production time necessary for the TFC panels would offset their cost to higher values. Finally, the BAL panels were the most expensive panel typology per floor unit area, owing to the high cost of the balsa wood used in their core.

3.6. Concluding remarks

Several sandwich panel architectures were taken into account, adopting different core materials and reinforcing solutions. Similar cross-sectional dimensions (thickness of faces and core) were adopted across the various panel typologies, guaranteeing that these are directly comparable. In the next part of this thesis, the experimental assessment of the mechanical performance of the different materials and full-scale sandwich panels is presented, allowing for conclusions to be drawn regarding their suitability for use in building floors. Regarding the connection panels, these were studied in detail in the context of the investigations concerning the panel-to-panel connections, which are reported in chapter 6.

3.7. References

- [1] Fernandes, P., Glória Gomes, M., Moret Rodrigues, A. (2014). *Thermal behaviour of GFRP sandwich panels for applications in building floors*. Report IST 7, FCT project PTDC/ECM/113041/2009 “Rehabilitation of Building Floors with Lightweight High Performance GFRP Sandwich Panels”, Task 7, ICIST Report DTC 15/2014, 31 p.
- [2] Neves e Sousa, A. (2014). *Experimental and numerical analysis of the acoustic behaviour of GFRP and GFRP-ECC hybrid sandwich panels*. Report IST 8, FCT project PTDC/ECM/113041/2009 “Rehabilitation of Building Floors with Lightweight High Performance GFRP Sandwich Panels”, Task 8, ICIST Report DTC 42/2014, 24 p.
- [3] Garrido, M., Correia, J.R., Branco, F.A., Barros, J.O.A., Valente, I.B., Mastalli, M. (2014). *Materials development and manufacturing of the sandwich panels*. Report IST/UM 3, FCT project PTDC/ECM/113041/2009 “Rehabilitation of Building Floors with Lightweight High Performance GFRP Sandwich Panels”, Task 3, Report ICIST DTC 40/2014, 31 p.
- [4] European Committee for Standardization (CEN) (2002). *Eurocode – Basis of structural design (EN 1990:2002)*. Technical Committee CEN/TC 250, Brussels.
- [5] European Committee for Standardization (CEN) (2002). *Eurocode 1: Actions on structures – Part 1-1: General actions – Densities, self-weight, imposed loads for buildings (EN 1991-1-1:2002)*. Technical Committee CEN/TC 250, Brussels.

- [6] Garrido, M., Correia, J.R., Branco, F.A. (2014). *Preliminary structural design of GFRP sandwich panels for applications in building floors*. Report IST 2-1, FCT project PTDC/ECM/113041/2009 “Rehabilitation of Building Floors with Lightweight High Performance GFRP Sandwich Panels”, Task 2-1, Report ICIST DTC 17/2011, 20 p.
- [7] Bank, L.C., 2006, *Composites for construction: Structural design with FRP materials*, John Wiley & Sons, New Jersey, 551p.
- [8] Selcom SRL Multiaxial Technology (n.d.). Product listing: <http://www.multiaxialfabricselcom.com/images/stories/selcom-articoli/pdf-eng/unidirectional.pdf> (latest access on 28.09.2015).
- [9] Polynt SPA (2007). *Technical data sheet Distitron 3501*. http://www.polynt.it/user/download_tds.aspx?file=DISTITRON_3501_FR.PDF&tipo=tds&nome=DISTITRON_3501 (latest access on 28.09.2015).
- [10] Polirígido Isolamentos Térmicos e Acústicos, Lda (n.d.). Data sheet available at: <http://www.polirigido.com/content/catalogos/11/CARACTERISTICAS%20TECNICAS%20PLACAS%20E%20PERFIS.pdf> (latest access on 28.09.2015).
- [11] 3A Composites [n.d.]. Airex T92 data sheet available at: <http://www.3accorematerials.com/airex-t92-pet-foam.html> (latest access on 28.09.2015).
- [12] 3A Composites [n.d.]. Baltek SB data sheet available at: <http://www.3accorematerials.com/baltek-sb-balsa.html> (latest access on 28.09.2015).
- [13] 3A Composites [n.d.]. Airex C51: <http://www.3accorematerials.com/airex-c51-foam.html> (latest access on 28.09.2015).

Part II

Characterisation of materials

Preamble

Various materials were used in the development of the sandwich panels considered in this study. Their different properties confer different mechanical responses to the panels. The sandwich panel architecture may thus be tailored and optimised for the envisaged application in building floors rehabilitation, as long as the mechanical properties of the constituent materials are known, and their influence on the sandwich panel behaviour is assessed.

Part II of this thesis presents the results of the experimental programme carried out to assess the mechanical response of the materials considered, as well as the structural behaviour of the sandwich panels.

The work presented in this chapter resulted in the following publication:

Garrido, M., Correia, J.R., Keller, T. (2015). "Effects of elevated temperature on the shear response of PET and PUR foams used in composite sandwich panels". *Construction and Building Materials*, Vol. 76, pp. 150-157.

Chapter 4

Characterisation of constituent materials

4.1. Introduction

The structural response of a sandwich panel depends on the mechanical properties of its constituent materials. For standard sandwich panel typologies, the faces determine the bending response, while the core material determines the shear response. The material properties considered in the design of the sandwich panels produced for this study were first taken from the materials' technical datasheets, when provided by the manufacturers. However, this type of information was not available for the glass-fibre reinforced polymer (GFRP) laminates, which were purposely designed and manufactured for the sandwich panels according to a custom fibre layup. Consequently, it was necessary to estimate their most relevant mechanical properties by using analytical methods, namely the Classical Lamination Theory (CLT) (*e.g.*, [1]).

The above mentioned values of the material properties required experimental confirmation. Furthermore, a complete material characterisation was required, providing details regarding each material's behaviour up to failure (*e.g.*, assessing the existence of nonlinear responses), failure modes, failure loads, and scatter in the properties. In addition, it was important to determine the behaviour of the different sandwich panel assemblies, addressing aspects such as their behaviour under localised compression loads, the effectiveness of the bonds between the GFRP faces and the different core materials, or the in-plane behaviour of the panels.

For the aforementioned reasons, an experimental programme was carried out comprising: (i) tensile and compression tests of the GFRP laminates used in the panel faces, and tensile tests of the GFRP laminates used in the longitudinal reinforcement ribs, (ii) shear tests of the core materials, and (iii) flatwise tension and compression tests of the sandwich panel assemblies. The effect of temperature on the shear response of polyethylene terephthalate (PET) and polyurethane (PUR) foams was also experimentally assessed.

The GFRP laminates were tested in tension and in compression along two different directions: (i) the longitudinal direction, *i.e.*, oriented at 0° relative to the main reinforcement fibres, and (ii) the transverse direction, *i.e.*, oriented at 90° relative to those fibres. In addition, tensile tests were carried out along the 10° off-axis direction to determine the in-plane shear properties of the facing and rib laminates, according to the procedures suggested by Chamis and Sinclair [2].

The core materials (40, 80, 100, and 120 kg/m^3 PUR foams, PET foam and balsa wood) incorporated in the sandwich panels produced for this study were tested in shear using a test method purposely developed for that end, the diagonal tension shear (DTS) test. This method, described in detail in section 3.3.1 of this document, allowed testing the core materials using their actual thickness as incorporated in the sandwich panel cores. In addition, Iosipescu shear tests were carried out for temperatures between -20°C and 120°C using two different polymer foams, a PUR foam with a density of 68 kg/m^3 and a PET foam comparable to the one incorporated in the panels, but produced by a different manufacturer. These tests were complemented by dynamic mechanical analyses (DMA) and differential scanning calorimetry and thermogravimetric analyses (DSC/TGA) in order to assess the glass transition and decomposition processes underwent by the two foams.

Finally, specimens were extracted from the full-scale sandwich panels and were tested in two configurations: (i) flatwise tension, and (ii) flatwise compression. In the flatwise tension experiments, the specimens were tensioned along the direction normal to the panel plane, thus creating a “pull-off” load on the face-core interfaces. In the flatwise compression experiments, the compression loads were applied along that same direction, simulating panel crushing that might occur at supports or under concentrated loading points.

4.2. Glass-fibre reinforced polymer (GFRP)

4.2.1. Experimental procedures

4.2.1.1. Tension

A plate of GFRP was manufactured for the material characterisation tests using the same materials, fibre layup, nominal thickness and vacuum infusion process as the face sheets of the full-scale sandwich panels. The tensile experiments for the face sheet laminates were

carried out on specimens extracted from this plate¹¹, while for the rib laminates the specimens were extracted from the manufactured RIB panels. The experiments were executed according to the recommendations of the ASTM D3039/D3039M [3] and the ISO 527-1,4 standards [4,5].

The face sheet specimens had nominal thickness of 7 mm and were machined using diamond tipped cutting tools to a nominal length of 300 mm and width of 25 mm. For the rib laminates, a nominal thickness of 5 mm, nominal width of 45 mm and nominal length of 300 mm were adopted. These dimensions were defined according to the recommendations for “balanced and symmetric” laminates found in “Table 2” of the ASTM D3039/D3039M standard, and for the “Type 2” specimen in paragraph 6.1 of the ISO 527-4 standard.

The tensile tests were carried out using a universal testing machine with a load capacity of 200 kN and an integrated load cell (Figure 4.1-a). The loading was performed in displacement control at a constant speed of 2 mm/min. The grip length was set as 75 mm, with a distance between grips of 150 mm, of which 50 mm corresponded to twice the width and 100 mm corresponded to the gauge length. The specimens were gripped using a pressure of 40 bar, defined in order to minimise slipping of the specimens at the grips while avoiding the local crushing of the specimens.



Figure 4.1. Experimental setups for the: (a) tensile tests, and (b) compression tests.

¹¹ In addition, tensile experiments were carried out using laminates extracted from the face sheets of a produced sandwich panel. A good agreement was found between the two sets of results, and thus the latter are not presented.

For the face sheet laminates, ten specimens per principal material direction (0° and 90°) were used: (i) three specimens were instrumented with axially installed strain gauges (along the loading direction) to determine the Young's moduli along the two principal material directions (Figure 4.2-a), (ii) three specimens were instrumented with axially and transversely installed strain gauges to additionally determine the major and minor Poisson's ratios of the laminates (Figure 4.2-b), and (iii) four specimens were tested without strain measurement. For the 10° off-axis specimens, seven specimens were tested, of which: (i) three contained strain gauge rosettes to determine the in-plane shear modulus values (Figure 4.2-c), and (ii) four were tested without strain measurement. For the rib laminates, three specimens were tested, all instrumented with strain gauge rosettes.

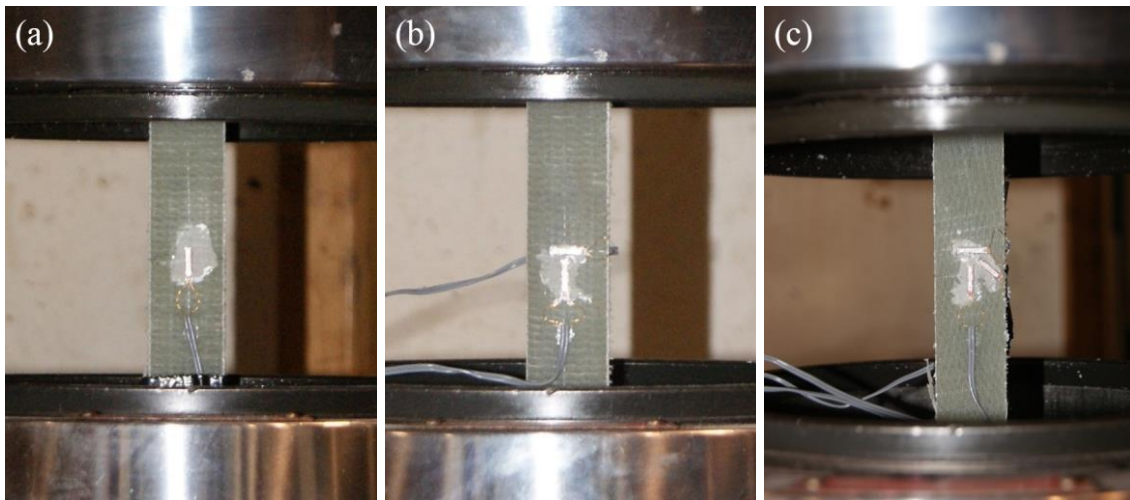


Figure 4.2. Strain gauge installation configurations: (a) single axial strain gauge, (b) axial and transverse strain gauges, and (c) strain gauge rosette.

4.2.1.2. Compression

The compression tests were carried out following the guidelines of the ASTM D695 standard [6]. Eight specimens with length of 25 mm, width of 10 mm and thickness of 7 mm were tested for each of the two principal material directions, longitudinal (0°) and transverse (90°).

The tests were carried out on a testing machine (Figure 4.1-b) with a load capacity of 10 kN, and an integrated load cell with precision of 0.01 kN. The load application rate was controlled manually, and kept at values between 0.10 and 0.15 kN/s, producing failures for test periods of 2 to 3 minutes. The crosshead displacement was measured using a displacement transducer with a stroke of 25 mm and precision of 0.01 mm.

4.2.2. Results

4.2.2.1. Main properties

Table 4.1 presents a summary of the main mechanical properties obtained in the material characterisation tests of the GFRP laminates. A longitudinal Young's modulus (E_L) of 29.4 ± 0.8 GPa, a transverse Young's modulus (E_T) of 15.6 ± 1.0 GPa and an in-plane shear modulus (G_{LT}) of 4.1 ± 0.3 GPa were determined. Using Classical Laminate Theory (CLT), a longitudinal Young's modulus of 27.1 GPa, transverse Young's modulus of 12.8 GPa and in-plane shear modulus of 4.7 GPa had been estimated for this laminate. The experimentally obtained mechanical properties and the respective CLT predictions are in relatively good agreement (particularly regarding the longitudinal Young's modulus), with the experimental properties being higher than the corresponding analytical estimates.

Table 4.1. Summary of GFRP mechanical properties.

Laminate	Direction	Tension			Compression	Shear	
		σ_u [MPa]	E [GPa]	ν [-]	$\sigma_{C,u}$ [MPa]	τ_{max} [MPa]	G_{LT} [GPa]
	Longitudinal	437.3 ± 28.1	29.4 ± 0.8	0.31 ± 0.03 (L,T)	249.8 ± 34.3	-	-
Faces	Transverse	179.6 ± 10.0	15.6 ± 1.0	0.17 ± 0.002 (T,L)	194.2 ± 10.5	-	-
	10° off-axis	-	-	-	-	49.4 ± 1.9	4.1 ± 0.3
Ribs	10° off-axis	-	-	-	-	34.8 ± 1.8	2.3 ± 0.2

The obtained strength values are within the typical range for GFRP laminates [1]. As expected, the strength values in the longitudinal direction were significantly higher than those in the transverse direction, especially in tension, due to the higher fibre reinforcement along this direction. In compression, the difference is less marked, as the compressive behaviour is more influenced by the matrix.

In the following sections, the results obtained in the tension and compression experiments of the GFRP laminates are further detailed.

4.2.2.2. Tension

Representative curves obtained from the tests, which showed relatively limited scatter, are shown in Figure 4.3 regarding the (i) load vs. displacement (Figure 4.3-a), (ii) axial stress vs. strain (Figure 4.3-b), and (iii) shear stress vs. distortion (Figure 4.3-c) responses. The laminates exhibited a certain degree of nonlinearity in the load vs. displacement curves, to

some extent caused by slipping in the grips. This nonlinearity was more significant for the 10° and (especially) the 90° direction specimens.

The GFRP specimens exhibited brittle failure modes, typically occurring in the gauge length, as illustrated in Figure 4.4. In the 0° and 90° specimens, rupture of axial fibres and through thickness delamination were observed. For the 10° off-axis specimens, matrix failure along the main (0°) reinforcement fibres was observed, with subsequent fibre delamination.

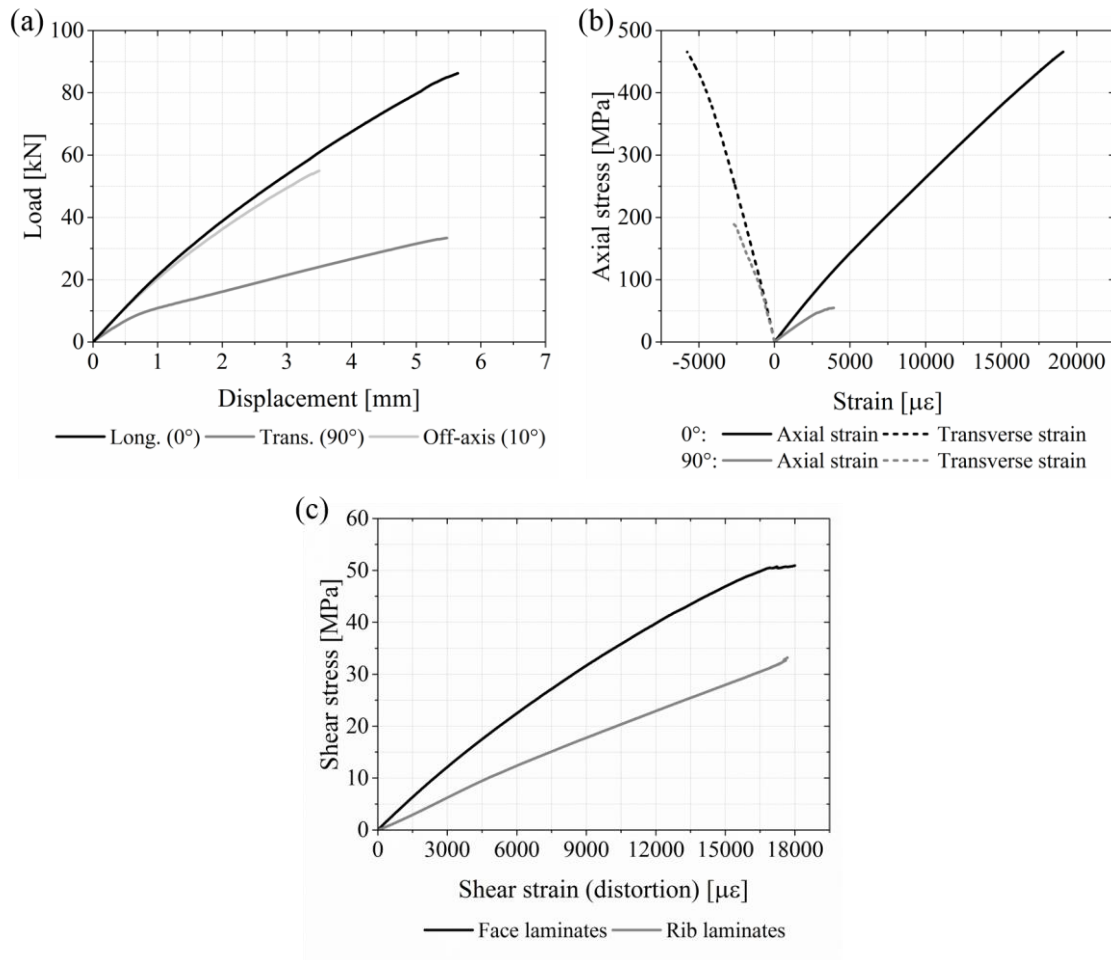


Figure 4.3. Representative curves from the tensile experiments on the GFRP laminates: (a) load vs. displacement, (b) axial stress vs. strain, and (c) shear stress vs. distortion.

For the 0° specimens, the stress vs. strain curves showed a quasi linear-elastic behaviour up to failure, confirming that in that case the above-mentioned nonlinearity in the load vs. displacement curves stemmed mostly from the slight slipping at the grips. However, this slipping did not affect the measured laminate strength values, and furthermore the Young's moduli values were determined from the strain measurements (which are also insensitive to this issue).

The 90° specimens exhibited significant cracking in the polymer matrix for stresses above ~35 MPa (around 20% of the laminate strength in that direction). The cracks were perpendicular to the loading direction and distributed evenly throughout the specimen length. The axially installed strain gauges were consistently damaged due to such cracking, preventing the axial strains to be measured beyond that point. A significant loss of stiffness was observed in the specimens, which was coincident with the crack initiation, this being the main factor contributing to the observed material nonlinearity.

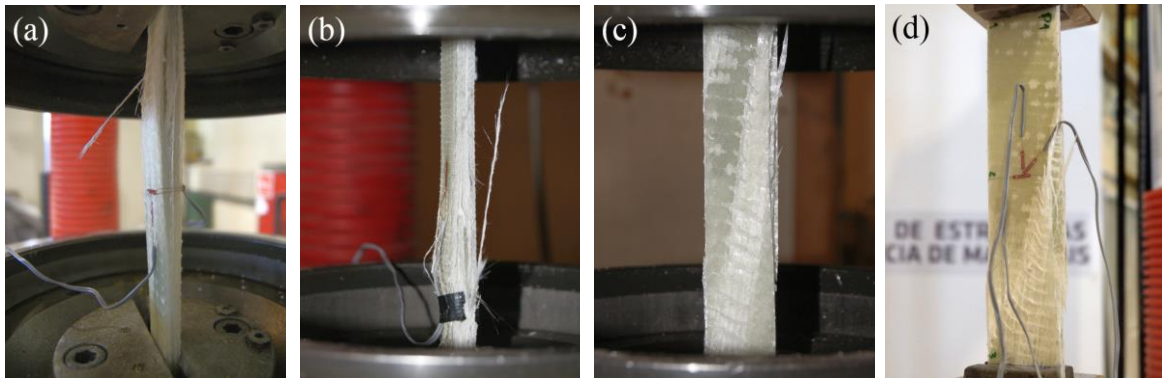


Figure 4.4. Failure modes of the GFRP laminates in tension for face sheet specimens along the: (a) 0°, (b) 90°, and (c) 10° directions, and (d) rib laminates in the 10° direction.

The 10° off-axis specimens (face and rib laminates) presented nonlinear shear stress vs. strain behaviour, characterised by a gradual loss of stiffness with increasing stress. This nonlinearity, which was expectable, stems from the (typically nonlinear) shear response of the laminate's polyester matrix, and from the gradual variations in angle between the reinforcement fibres and the direction of loading due to the increasing shear deformation in the laminate.

4.2.2.3. Compression

Figure 4.5 shows representative curves of the axial compression stress vs. displacement (relative position between the specimens' loaded ends) results obtained for the two types of specimens, *i.e.*, along the longitudinal (0°) and transverse (90°) laminate directions. The failure modes obtained are illustrated in Figure 4.6. Similar initial developments were observed along both main directions, characterised by toe regions stemming from the adjustments between the loading system and the specimens. After this initial segment, the laminates exhibited a linear elastic response, showing higher stiffness in the longitudinal direction than in the transverse direction, owing to the higher quantity of 0° fibre reinforcement.

Chapter 4 Characterisation of constituent materials

The laminates failed in a brittle way for both specimen types. The failure loads were higher along the longitudinal direction, with failures occurring due to through thickness delamination, as illustrated in Figure 4.6-a. In the transverse direction, failure occurred in the polymer matrix by through thickness shear, resulting in the formation of shear wedges in planes parallel to the 0° fibres (as per the arrows in Figure 4.6-b).

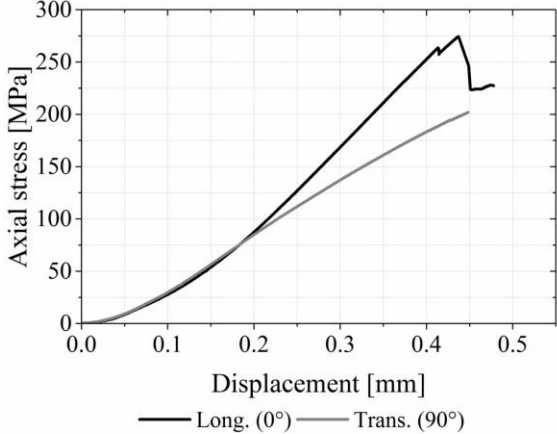


Figure 4.5. Representative curves from the compression experiments on the GFRP laminates.

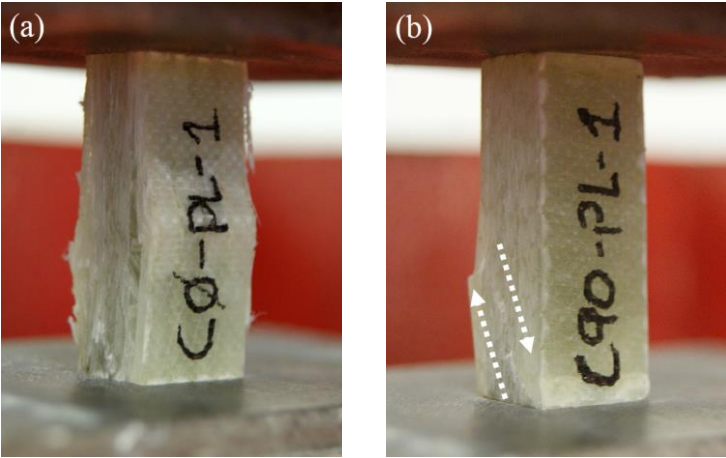


Figure 4.6. Failure modes of the GFRP laminates in compression for specimens along the: (a) 0°, and (b) 90° directions.

4.3. Core materials

4.3.1. Diagonal tension shear

4.3.1.1. Specifications and calculation procedures

The sandwich panels developed in the current study comprise relatively thick cores (120 mm), owing to the structural and building physics requirements imposed by their application in building floors. One of the concerns when designing the shear testing programme was to perform the material characterization on specimens with the same thickness as in the full-sized sandwich panels.

However, the conventional shear test methods (*e.g.*, [7]) are often inadequate for specimen dimensions such as those required in this study. For this reason, the shear testing of the core materials was carried out using a test method developed at IST specifically for that purpose, the diagonal tension shear (DTS) test, which was based on a test setup/principle briefly described in [7].

In the test method proposed herein, a chamfered cubic specimen (Figure 4.7) is adhesively bonded to a set of test fixtures designed to subject the specimen to shear deformation. The fixtures consist of four metallic plates, connected to form a quadrilateral frame encasing the specimen. The connection between plates is made using metallic rods that provide hinging, and allow the angle between plates to change thus causing the quadrilateral frame to distort from a squared shape into a rhombic shape (Figure 4.8).

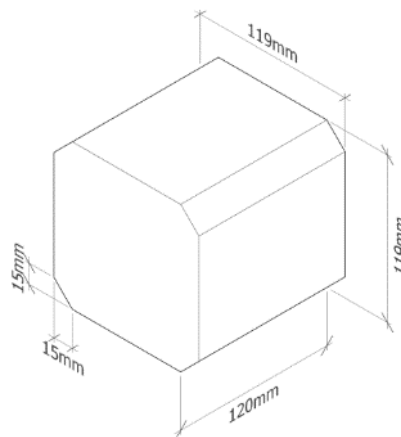


Figure 4.7. DTS test specimen geometry and dimensions.

Tension is applied along one of the frame's diagonals by loading two opposing metallic rods, the loading rods. In order to do so, the loading rods are extended outwards on both sides from the metallic plates and are connected to the loading system. Each end of the loading system is comprised of two connection blocks that link the loading rod to a loading beam, to which a gripping handle is attached. The loading system was designed to be self-aligning, and to be gripped by a universal testing machine and transfer an axial tensile load into the plates encasing the specimen.

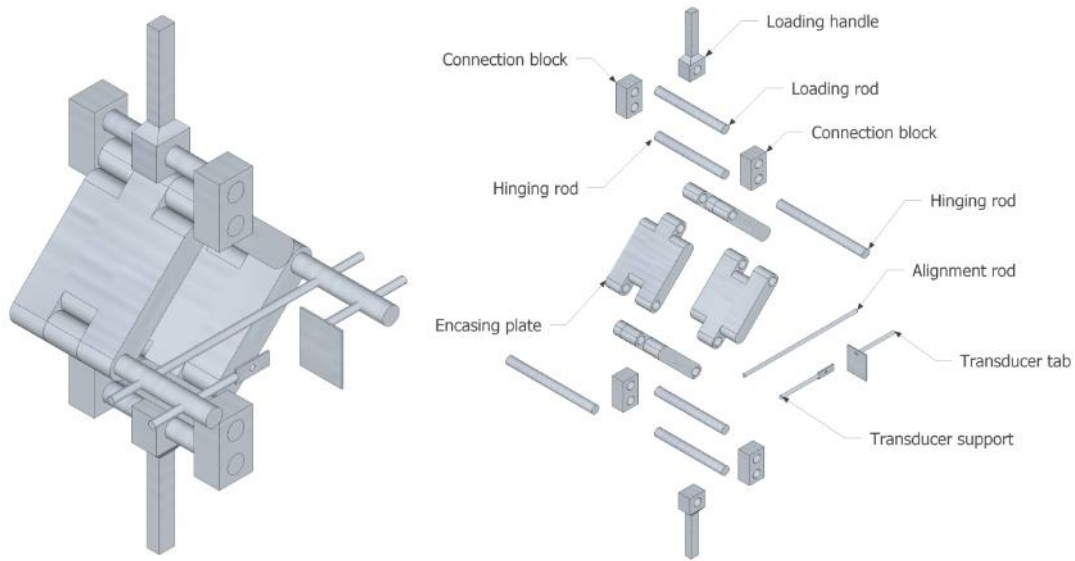


Figure 4.8. Schematic representation of the DTS test fixture and its components.

The force distribution and imposed deformations are shown in Figure 4.9. In homogeneous and isotropic materials, specimen failure is expected to occur along the horizontal direction, which would correspond to a 45° failure in the core of a sandwich panel. The shear stress (τ) acting on the specimen may be computed by considering that $\tau = 0.707P/A$, where P is the applied load, and A is the specimen area. This area may be taken as $A = (W + h) \times t/2$, where W is the specimen width, h is the specimen height, and t is the specimen thickness.

The shear strain (γ) may then be calculated by considering $\gamma = (\Delta V + \Delta H)/g$, where ΔV is the vertical extension, ΔH is the horizontal shortening, and g is the gauge length, *i.e.*, the length of the diagonal in a square with a $(W + h)/2$ side. Finally, the shear modulus (G) may be calculated as $G = (\tau_2 - \tau_1)/(\gamma_2 - \gamma_1)$, where τ_1 and τ_2 are shear stress values at two points in the linear-elastic region of the stress-strain curve, and γ_1 and γ_2 are the respective shear strain values at those points. It should be noted that the DTS test fixture allows installing a displacement transducer to measure the specimen deformation ΔH .

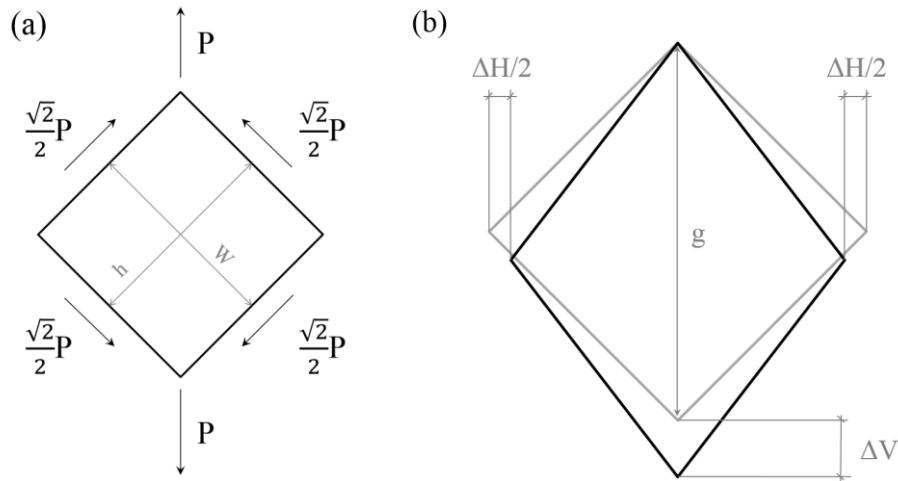


Figure 4.9. Calculation assumptions for the DTS test method: (a) force distribution, and (b) imposed deformations.

4.3.1.2. Experimental procedures

The adhesive bonding between the specimens and the test fixtures was achieved using a polyurethane based adhesive (*Sikaforce 7710 LI00*) for the PUR foams and an epoxy based adhesive (*Sikadur 330*) for the PET foam and balsa wood. A uniform bond thickness of 0.5 mm was guaranteed by using stainless steel spacers. The number of specimens tested per core material were as follows: (i) three for the 40, 80, and 120 kg/m³ PUR foams, (ii) four for the balsa wood, and (iii) five for the 100 kg/m³ PUR foam and for the PET foam.

The diagonal tension experiments were carried out in the same universal testing machine described in section 3.2.1.1 for the tension tests of the GFRP laminates. Loading was applied under displacement control at a constant cross-head speed of 1 mm/min. The vertical displacement (ΔV) was obtained from the crosshead displacement measurements, whereas the horizontal displacement (ΔH) was measured using a displacement transducer with a 25 mm stroke and precision of 0.01 mm, mounted on the transducer support as shown in Figure 4.10.

4.3.1.3. Summary of results

Representative shear stress vs. distortion curves obtained from the DTS tests are shown in Figure 4.11, and a summary of the results is given in Table 4.2. This table also provides the estimated density values of the materials as received, and their comparison with the nominal values provided by the manufacturers. The estimated density values for the PUR foams were consistently lower than the nominal densities, especially for the 100 kg/m³ foam (12.6%

lower). The PET foam and balsa wood both had slightly higher density values compared to the nominal values provided by the manufacturer.

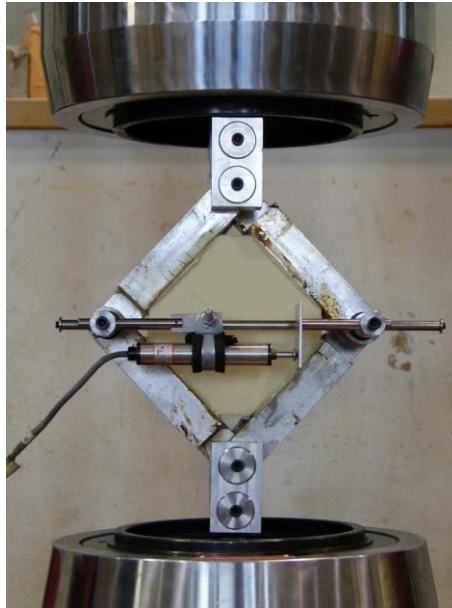


Figure 4.10. Diagonal tension shear test setup.

The 80, 100, and 120 kN/m³ PUR foams presented similar qualitative shear stress *vs.* strain developments, exhibiting initial segments of linear elastic behaviour, followed by slight stiffness reductions preceding the brittle failure. The response of the 40 kg/m³ PUR foam exhibited a slightly higher degree of nonlinearity (stiffness reductions were slightly more marked), and progressive cracking along the horizontal diagonal was observed prior to failure. However, failure for all PUR foams consistently occurred along the horizontal diagonal (as expected), as shown in Figure 4.12-a.

Generally, the PUR foams showed some degree of scatter in their mechanical properties. Taking as an example the shear modulus of the 100 kg/m³ foam, for which an average value of 8.7 MPa was obtained, the lowest and highest values were respectively 7.6 MPa and 10.0 MPa. This represents an amplitude of 28% relative to the average shear modulus, possibly associated either with differences in material orientation in relation to the shear plane or with inherent material variability/heterogeneity. However, it was not possible to further explore this aspect during the development of this thesis.

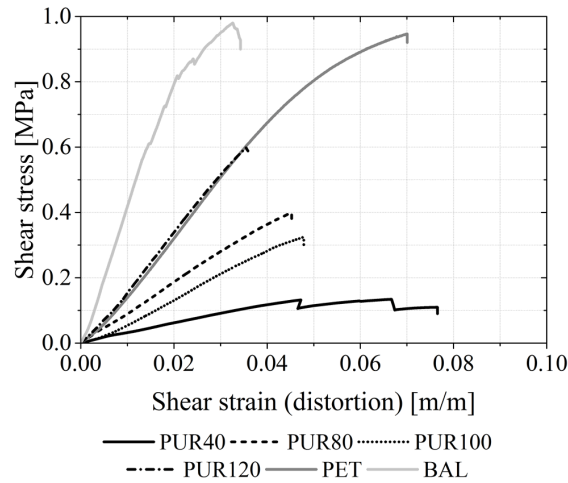


Figure 4.11. Representative shear stress vs. distortion curves from the DTS tests of the core materials.

Table 4.2. Summary of mechanical properties for the core materials.

Core material	Nominal density [kg/m ³]	Estimated density [kg/m ³] (difference to nominal)	Shear strength (τ_u) [MPa]	Shear modulus (G) [MPa]
PUR foam	40	36.4 (-9.0%)	0.13 ± 0.01	2.8 ± 0.4
	80	78.5 (-1.9%)	0.39 ± 0.08	10.8 ± 1.1
	100	87.4 (-12.6%)	0.32 ± 0.06	8.7 ± 1.0
	120	119.0 (-0.8%)	0.59 ± 0.02	17.7 ± 0.9
Balsa wood	94	101.4 (+7.9%)	0.93 ± 0.19	48.8 ± 6.2
PET foam	105	105.4 (+0.4%)	0.94 ± 0.04	19.2 ± 1.1

It is important to note that the 80 kg/m³ PUR foam presented higher failure stress and shear modulus values than the 100 kg/m³ foam. This result is contrary to the typical increase in mechanical properties with the density of PUR foams (as found for the 40, 80, and 120 kg/m³ foams). However, it is worth mentioning that the 100 kg/m³ foam was produced by a different manufacturer (*cf.* chapter 3, section 3.3.2) than the remaining PUR foams. Thus, differences in the chemical composition and production methods of the two foams are to be expected, leading to final products with different mechanical property ranges.

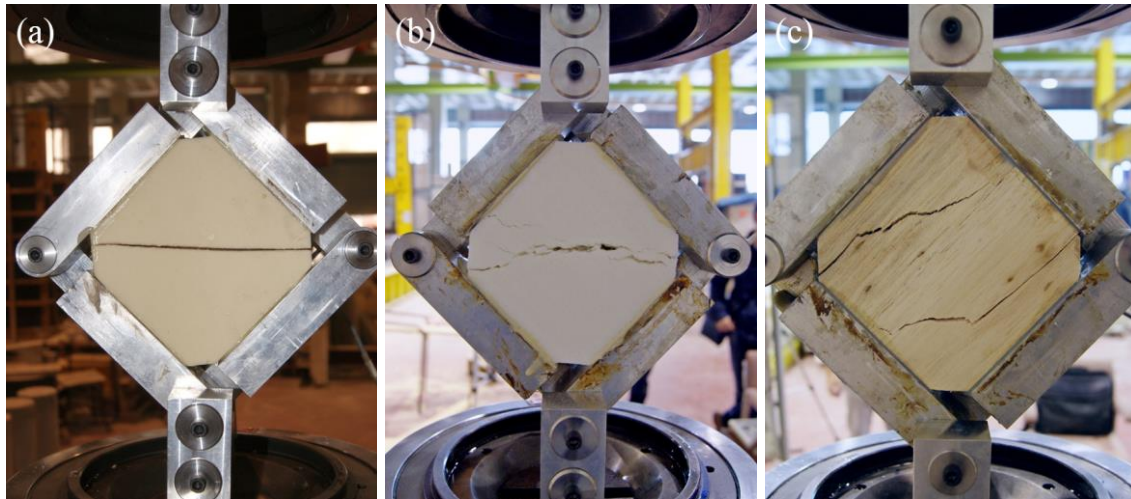


Figure 4.12. Failure modes of the core materials in the DTS tests: (a) PUR foams, (b) PET foam, and (c) balsa wood.

The PET foam presented very consistent results (low property scatter), characterised by an initial segment of linear elastic behaviour followed by a significant gradual loss of stiffness for shear stresses above approximately 0.7 MPa. Failure occurred in a brittle manner by extensive cracking/crumbling of the foam along the specimen horizontal diagonal (Figure 4.12-b).

The balsa wood again presented significant degree of scatter¹² in its shear response. This material exhibited linear elastic response up to shear stresses of approximately 0.6 MPa, above which progressive cracking was observed, associated with sudden stress and stiffness reductions. Failure occurred with the opening of significant cracks, initiating at the edges of the horizontal diagonal and propagating in the direction of the wood's grain (Figure 4.12-c), which represents a material weakness direction.

Figure 4.13 compares the shear strength and moduli obtained for the different core materials. The balsa wood presented the highest average shear modulus among all core materials (48.8 MPa), followed by the PET foam (19.2 MPa). Regarding shear strength, the balsa wood and the PET foam presented comparable average failure stresses (0.93 MPa vs. 0.94 MPa, respectively), although the scatter of results obtained for balsa wood (coefficient of variation, C.V., of 20.4%) was significantly higher than that obtained for the PET foam (C.V. of 4.3%).

¹² Such scatter in balsa wood mechanical properties, stemming from the wood's natural heterogeneity, has also been reported by Osei-Antwi *et al.* [8].

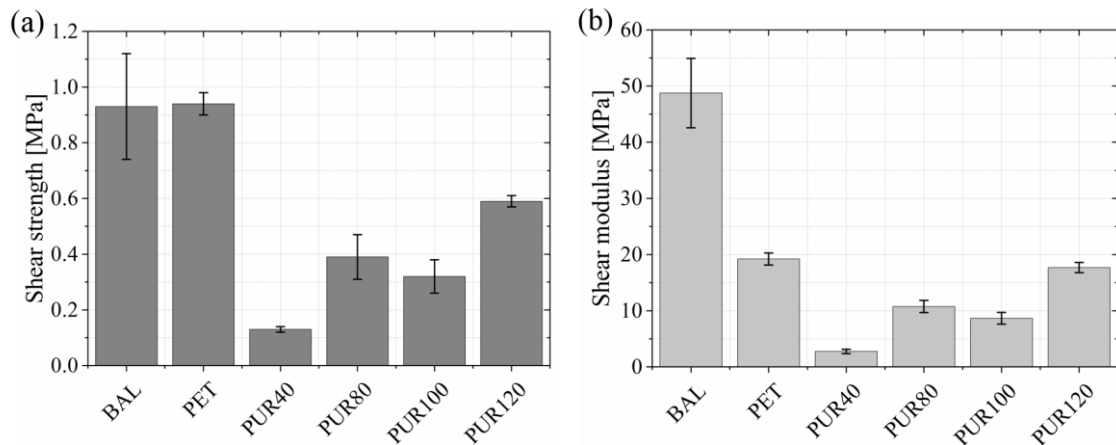


Figure 4.13. Comparison between results obtained for the different core materials: (a) shear strength, and (b) shear modulus.

Considering the PUR foams with nominal densities of 40, 80 and 120 kg/m³, a consistent increase in mechanical properties was found for increasing density values, as expected. The highest density PUR foam exhibited an average shear modulus comparable to that of the PET foam (17.7 MPa vs. 19.2 MPa, respectively), despite having a significantly lower average shear strength (-37%).

4.3.2. Effects of temperature on the shear response of polymer foams¹³

4.3.2.1. Experimental programme

In order to assess the effects of temperature on the shear response of PUR and PET foams, the following two polymeric foams were used in a specific experimental programme: (i) a thermoplastic PET foam with density of 94 kg/m³ (*G-PET 90* produced by *Gurit*), and (ii) a thermosetting PUR foam with density of 68 kg/m³ (produced by *Polirígido*). The foams were characterised physically and mechanically. Physical characterisation was aimed at assessing the glass transition and decomposition processes of the foams. For this purpose, DMA tests as well as DSC/TGA experiments were carried out on both materials. Mechanical characterisation focused on the determination of shear properties over a wide range of temperatures. For this purpose, the Iosipescu (ASTM D 5379/D 5379M) [10] method was

¹³ The experimental work presented in this section was carried out at the *École Polytechnique Fédérale de Lausanne* (EPFL), and is published in a journal article [9] in which an analytical modelling of the temperature effects on the shear response of the foams is also presented.

used in combination with a thermal chamber, allowing to condition the foam specimens at predetermined temperatures (between $-20\text{ }^{\circ}\text{C}$ and $120\text{ }^{\circ}\text{C}$, with steps of $20\text{ }^{\circ}\text{C}$) during the shear tests. The shear strains were measured using a video extensometer with an accuracy of $\pm 0.005\text{ mm}$. The following sections provide additional information regarding each of the experiments that were carried out.

4.3.2.2. DMA

Dynamic mechanical analyses of the PUR and PET foams were performed on a *TA Instruments Q800* dynamical mechanical analyser. Specimens with nominal thickness of 4 mm and nominal width of 12 mm were loaded in a 20 mm length dual cantilever setup. The specimens (3 for each material) were heated at a rate of $1\text{ }^{\circ}\text{C}/\text{min}$, from room temperature up to maximum temperatures of $250\text{ }^{\circ}\text{C}$ and $150\text{ }^{\circ}\text{C}$, respectively for the PUR and PET foams, and dynamically loaded at a frequency of 1 Hz. Two additional specimens of each material were tested from $-50\text{ }^{\circ}\text{C}$ to about $200\text{ }^{\circ}\text{C}$ at heating rates of $1.0\text{ }^{\circ}\text{C}/\text{min}$ and $0.3\text{ }^{\circ}\text{C}/\text{min}$, in order to trace the DMA response from very low temperatures and to assess the influence (if any) of the heating rate in the experiments conducted at $1\text{ }^{\circ}\text{C}/\text{min}$. The glass transition temperatures (T_g) were estimated based on the onset of the storage modulus (E') curves and also on the peaks of the loss modulus (E'') and loss factor (tan-delta) curves.

Figure 4.14 plots the DMA results obtained for the PET and PUR foams in the tests performed at a heating rate of $1.0\text{ }^{\circ}\text{C}/\text{min}$. In both cases, the DMA curves reflect the typical behaviour of polymeric materials and foams at temperatures across glass transition: the storage modulus curves present a sigmoidal decrease (much steeper in the PET foam), whereas the loss modulus and loss factor curves present peaks. It is worth mentioning that the storage modulus decrease is much steeper in the PET foam and the peak of its loss modulus curve is much sharper than that of the PUR foam. In other words, the glass transition of the PET foam occurs in a shorter temperature range.

Table 4.3 presents the estimates of the glass transition temperature (T_g) for both polymeric foams, based on the storage modulus decay (taken as the extrapolated onset of the sigmoidal change in the storage modulus, according to the definition of ASTM E1640 [10]), and the peaks of the loss modulus and tan-delta curves, for a heating rate of $1\text{ }^{\circ}\text{C}/\text{min}$. Similar results were obtained for the lower heating rate of $0.3\text{ }^{\circ}\text{C}/\text{min}$, suggesting that a heating rate of $1\text{ }^{\circ}\text{C}/\text{min}$ is low enough to avoid the effects of thermal lag in the measured material response.

As expected, the lowest and highest estimates were obtained from the storage modulus and tan-delta curves, respectively.

Taking as reference the onset of the storage modulus curves for a frequency of 1 Hz, T_g values of 65 °C and 90 °C are obtained respectively for the PET and PUR foams, the latter being about 40% higher than the former. The *Eurocomp Design Code and Handbook* [11] specifies a maximum “usable temperature” (service temperature) of T_g minus 10 to 20 °C, which corresponds to 45 to 55 °C and 70 to 80 °C for the PET and PUR foams, respectively. While the “usable temperature” range for the PET foam can be easily exceeded in several civil engineering outdoor applications (*e.g.*, bridge decks), the maximum “usable temperature” of the PUR foam should fulfill those requirements.

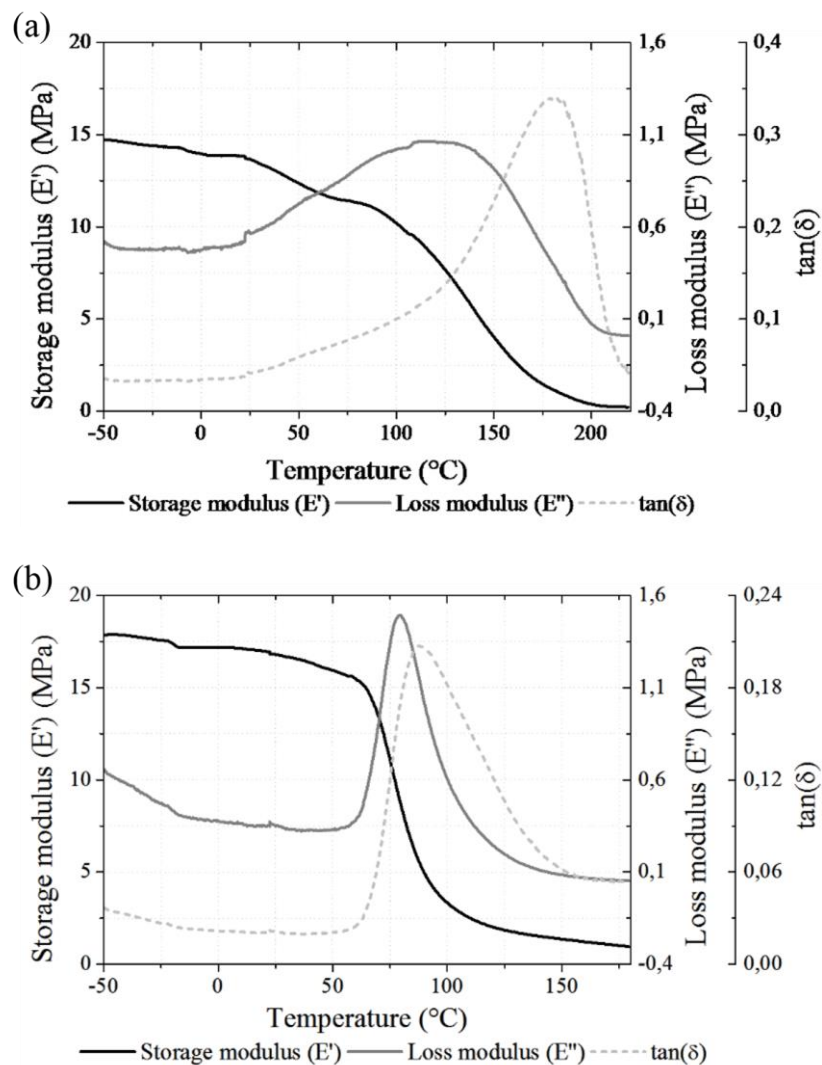


Figure 4.14. DMA results for the: (a) PUR foam, and (b) PET foam.

Table 4.3. Glass transition temperatures (in °C) of the PET and PUR foams tested at 1 °C/min (average ± standard deviation, from 3 specimens).

Foam	DMA Curve		
	E' onset	E'' peak	tan δ peak
PET	64.93 ± 0.92	79.17 ± 1.21	87.34 ± 0.73
PUR	89.54 ± 2.44	113.35 ± 3.39	181.43 ± 2.99

4.3.2.3. DSC/TGA

The two foams were subjected to differential scanning calorimetry (DSC) and thermogravimetric analyses (TGA). The experiments were performed on a *Perkin Elmer Simultaneous Thermal Analyzer (STA) 6000*, for a temperature range between 30 °C and 800 °C, at a heating rate of 5 °C/min. The analyses were performed in an air atmosphere, consistent with that used in the DMA experiments and the Iosipescu shear tests. One specimen was analysed for each type of polymeric foam.

Figure 4.15 shows the DSC/TGA results obtained for the two polymeric foams, namely the mass loss and the heat flow per unit mass, both as a function of temperature. The mass loss curve for the PUR foam exhibited two steep increases, corresponding to peaks in the derivative mass loss curves (for which the decomposition of the polymers takes place at the highest rate [12]) at temperatures of 274 °C and 532 °C. These peaks have a direct correspondence with two exothermal peaks in the heat flow curve, reflecting the decomposition process underwent by the polymeric material, involving material ignition and oxidative combustion in the air atmosphere used in these experiments. In each of those two stages of the decomposition process, the mass was reduced by approximately 45-50%.

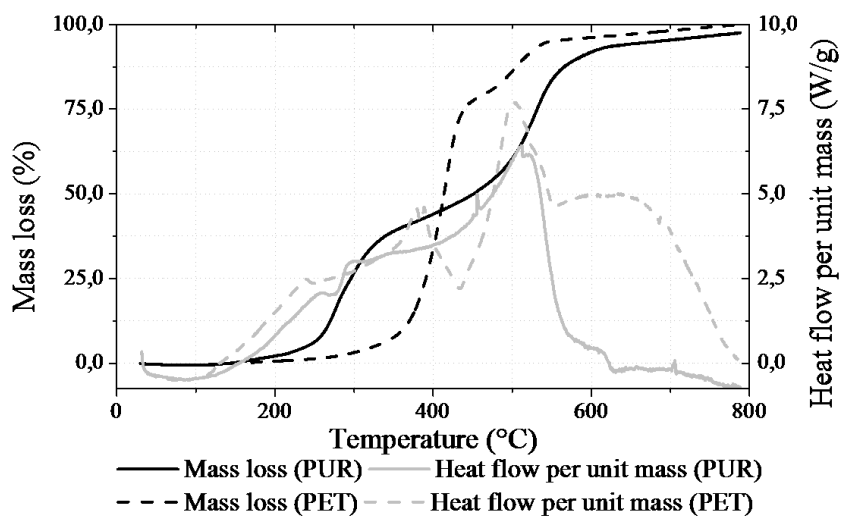


Figure 4.15. DSC/TGA results for the PUR and PET foams.

The PET foam's mass loss curve also presents two steeply increasing segments corresponding to two exothermal peaks in the heat flow curve. The mass reduction of about 80% caused by the first decomposition stage is associated with a derivative mass loss peak at 417 °C. At the end of the second decomposition stage, corresponding to a derivative mass loss peak at 503 °C, the mass was reduced by more than 95%.

The onset decomposition temperature, determined as the temperature for which 5% of the specimen mass is lost, was set as $T_{d,i} = 241$ °C for the PUR foam and $T_{d,i} = 326$ °C for the PET foam (about 35% higher than that of the PUR foam). These temperatures are far beyond the range of maximum “usable temperatures” for civil engineering applications, as well as of those used in the Iosipescu shear tests.

4.3.2.4. Iosipescu shear test

Iosipescu tests, also known as V-notched beam tests, were carried out to characterise the mechanical properties of the PET and PUR foams in shear. This experimental method is described in the ASTM D5379/D5379M standard [13] for composite (laminated) materials. However, previous studies have successfully used this method to assess the shear properties of softer materials typically used as cores of sandwich panels, such as balsa wood [8]. The fixtures used for the Iosipescu tests are shown in Figure 4.16-a. This test method was adopted due to the small fixture and specimen sizes, which combined with the fact that adhesives are not required to secure the specimens, make it a convenient method to use in a thermal chamber at elevated temperatures.

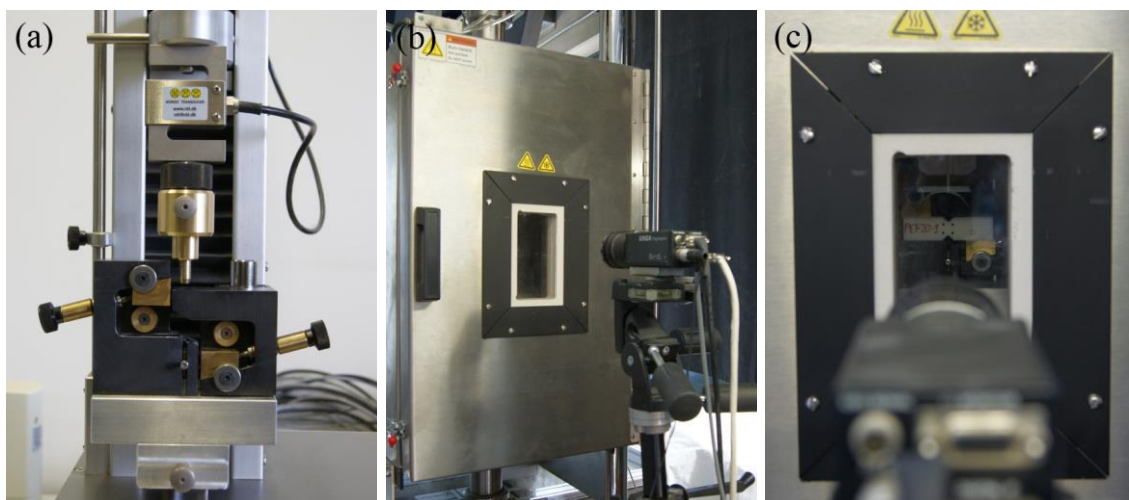


Figure 4.16. Iosipescu test setup: (a) fixtures, (b) thermal chamber and video extensometer, and (c) test execution.

Specimens with thickness of 11 mm, height of 20 mm, length of 50 mm and notched section height of 12 mm (notch depth of 4 mm on both sides) were prepared (Figure 4.17-a). The experiments were carried out using a servo-hydraulic testing machine, with a load capacity of 25 kN and an integrated load cell, coupled to a thermal chamber (Figure 4.16-b). The chamber was able to heat the specimens up to the defined test temperatures, while the lower temperatures (20 °C and below) were achieved by cooling the chamber with liquid nitrogen. The liquid nitrogen was injected into the thermal chamber in an automatically controlled process, immediately forming nitrogen gas.

The shear deformations were measured using a video extensometer (Figure 4.16-b), which continuously monitored the position of target dots marked at the notched centre of the test specimens. Four target dots were marked on each specimen, forming a square grid with a size of 6 mm (*cf.* Figure 4.17-a). The variation of their coordinates was used to calculate the shear strains (γ), considering that $\gamma = \alpha + \beta$, where $\alpha = \overline{aa'}/\overline{ac}$ and $\beta = \overline{dd'}/\overline{dc}$, according to the displacements illustrated in Figure 4.17-b.

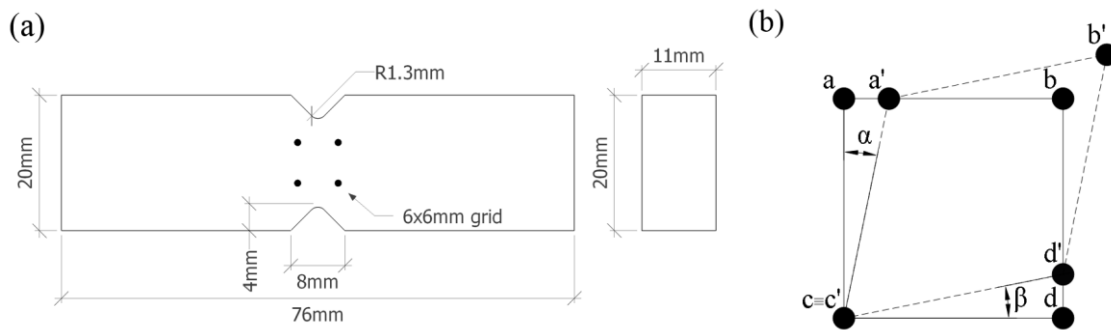


Figure 4.17. Iosipescu shear specimens: (a) dimensions and target dot locations, and (b) displacements of target dots due to shear deformation.

The PET foam was tested in the 0 to 80 °C range, while the PUR foam was tested in the -20 to 120 °C range. The thermal chamber was set at the target temperature and a heating/cooling rate of 5 °C/min was used. After temperature stabilisation inside the chamber, a minimum soaking period of 1 hour was defined to guarantee the thermal equilibrium of the test specimens. Subsequently, specimens were tested under displacement control at a rate of 1.0 mm/min. Tests were performed up to the maximum cross-head displacement allowed by the Iosipescu test fixture, yet in most cases specimen failure was not achieved. For each material and test condition, at least 2, and in most cases 3 replicates were tested. The only

exception was the PUR foam at $-20\text{ }^{\circ}\text{C}$, for which valid results could only be obtained for a single specimen.

Figure 4.18 presents representative shear stress *vs.* shear strain curves obtained for the PET and PUR foams. It is worth mentioning that the curves plotted in Figure 4.18 account only for the load applied by the test machine, *i.e.* they do not take into account the shear stresses ($\sim 0.1\text{ MPa}$) induced by the weight of the test fixture's loading block (approximately 12 N) on the specimens. This is an inherent limitation of the Iosipescu test method. In addition, due to the low stiffness of the foam specimens, the measured forces were quite low which caused some of the measurements to present a low signal-to-noise¹⁴ ratio, especially for the PUR foam. The cooling of the test chamber also caused some interference in the measurements for the lowest temperatures, owing to the bursts of nitrogen gas intermittently obscuring the target dots.

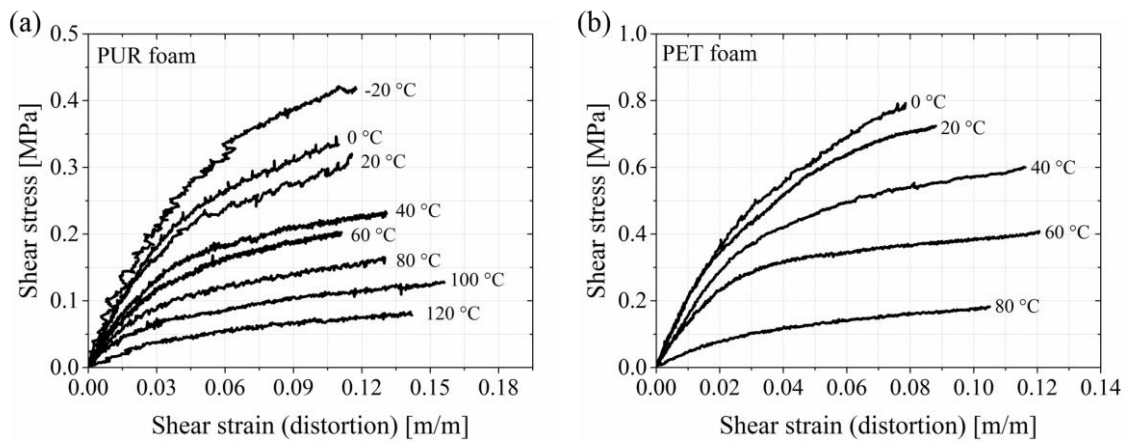


Figure 4.18. Representative shear stress *vs.* distortion curves from the Iosipescu tests: (a) PUR foam, and (b) PET foam.

The shear stress *vs.* strain curves show a high degree of nonlinearity for both materials. However, such nonlinearity stems mostly from the test method itself (in light of the results obtained in the DTS tests), which allows for: (i) slipping to occur between the test fixtures and the soft foam specimens at high strains, and (ii) crushing of the foams at the points where

¹⁴ Signal-to-noise ratio is a measure comparing the level of a desired signal to the level of background noise, and is defined as the ratio of signal power to the noise power.

load transfer occurs between the test fixtures and the specimens¹⁵. Nonetheless, it is very clear that both foams show significant variations in shear stress *vs.* strain response with temperature, particularly regarding the specimen stiffness. Considering the linear elastic segments in those curves, shear moduli values were estimated, and are presented in Table 4.4. Taking the shear moduli values at 20 °C (a typical ambient temperature) as a reference, the corresponding relative shear moduli reductions at the other test temperatures (*i.e.*, the residual values) were determined, and are given in Table 4.4 and plotted in Figure 4.19.

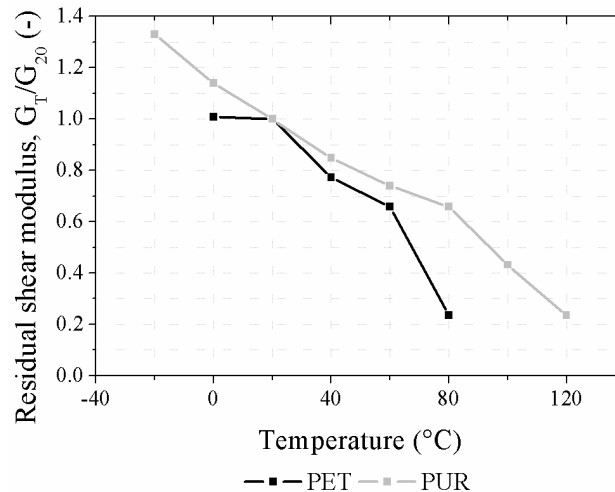


Figure 4.19. Residual shear moduli for the PUR and PET foams.

For the range of temperatures tested, the shear modulus reduction with temperature of the PET foam is much more pronounced compared to that of the PUR foam. This is in good agreement with the DMA results, in which the PET foam exhibited much lower T_g values, as well as steeper reductions of the storage modulus associated with sharper loss modulus peaks. However, for the lower temperatures tested, the PET foam seems to be more stable, with little differences being observed from 0 °C to 20 °C, while for the PUR foam the shear modulus consistently decreases from -20 °C to 20 °C.

Finally, it is interesting to note that the slopes of both curves depicted in Figure 4.19 present changes for temperature ranges that are in good agreement with the corresponding glass

¹⁵ PUR and PET foams typically present a markedly nonlinear response under compression, characterised by a yield plateau during which deformations increase with negligible stress increments, as shown in section 3.4.2 of this chapter.

transition temperatures determined from DMA tests (65 °C and 90 °C, respectively for the PET and PUR foams).

Table 4.4. Shear modulus (G) of PET and PUR foams for each temperature (average \pm standard deviation or maximum difference to average) and corresponding relative percentage reduction compared to ambient temperature (Δ_{G20}).

Temperature [°C]	PET foam		PUR foam	
	G_{PET} [MPa]	Δ_{G20} [%]	G_{PUR} [MPa]	Δ_{G20} [%]
-20	-	-	8.29*	133
0	19.09 \pm 0.04	101	7.10 \pm 0.35	114
20	18.93 \pm 1.62	100	6.23 \pm 0.09	100
40	14.63 \pm 1.54	77	5.28 \pm 0.13	85
60	12.45 \pm 0.37	66	4.61 \pm 0.29	74
80	4.46 \pm 0.63	24	4.10 \pm 0.10	66
100	-	-	2.69 \pm 0.05	43
120	-	-	1.46 \pm 0.25	23

*value obtained from a single specimen

4.4. Sandwich panel assemblies

4.4.1. Experimental procedures

4.4.1.1. Flatwise tension

Flatwise tension tests were carried out according to the recommendations of the ASTM C297/C297M standard [14]. These tests were performed to characterise the tensile response of the sandwich panels along the through thickness direction. Depending on the failure mode obtained in these tests, it is possible to determine either the tensile strength of the core material, of the core-to-face bond, or (very seldom) the through thickness strength of the faces.

In this test, a sandwich panel specimen is subjected to a uniaxial tensile force normal to the plane of the panel. Thick loading blocks bonded to the sandwich faces are used to apply this force. These are connected to self-aligning loading fixtures, as shown in Figure 4.20-a.

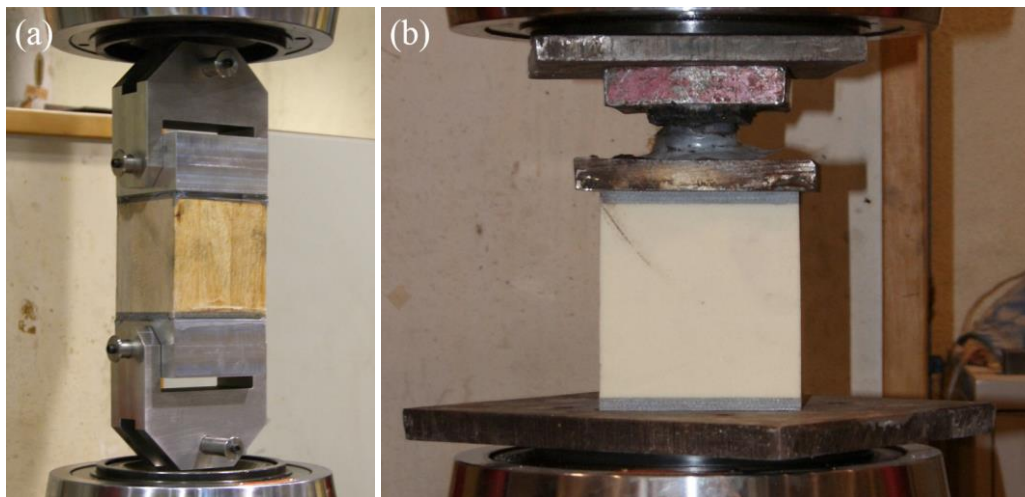


Figure 4.20. Setups for sandwich panel assemblies' tests: (a) flatwise tension, and (b) flatwise compression.

The specimens were machined from the full-scale sandwich panels using diamond tipped cutting tools to a square cross-section of 120 mm; the specimen thickness was identical to that of the panels, *i.e.*, a nominal value of 134 mm. Five specimens were tested for the balsa wood cored panels, three for the PET foam panels, and two for the PUR foam panels. Due to the limited quantity of available material, it was not possible to test more replicate specimens for the PET and PUR foam panels; however, the results obtained for both were highly consistent and showed very limited scatter, as discussed in the next section.

The specimens were adhesively bonded to the loading blocks using a two-part epoxy resin (*Sikadur 330*). For this process, all bonding surfaces were previously prepared, being thoroughly sanded down and degreased with acetone. Stainless steel spacers were used to guarantee a minimum adhesive thickness of 0.5 mm in the bonding area.

The flatwise tension tests were carried out in the same universal testing machine previously described for the tensile tests of the GFRP laminates. Load was applied under displacement control, at a constant cross-head speed of 1 mm/min. The load and crosshead displacement values were obtained from the testing machine's integrated sensors.

4.4.1.2. Flatwise compression

Flatwise compression tests were carried out according to the recommendations of the ASTM C365/365M standard [15], to characterise the compressive response of the sandwich panels along the through thickness direction. With this test, the compressive strength and apparent modulus of the sandwich core may be determined. These properties are relevant to the design

of sandwich panels, pertaining to local crushing at supports or at localized load application points. In this test method, a sandwich panel specimen is subjected to a uniaxial compressive force normal to the plane of the panel. This force is applied to the specimen using loading plates attached to the testing machine, as shown in Figure 4.20-b.

Five specimens for the balsa wood and PET foam cored panels and three for the PUR foam panels were tested with the same dimensions as in the flatwise tension tests (cross-section of 120 mm by 120 mm, nominal thickness of 134 mm). The tests were carried out in the same universal testing machine as the latter.

4.4.2. Results

Axial stress values were calculated by dividing the measured loads by the cross-sectional areas of the specimens. Axial stress vs. displacement curves representative of the behaviour observed in the flatwise tension and flatwise compression tests are shown in Figure 4.21. In the flatwise tension tests, all the panel assemblies (and consequently all core materials) exhibited linear elastic responses up to failure, which occurred in a brittle manner. In the case of the balsa wood cored specimens, the linear elastic behaviour was preceded by an initial toe region. However, since the adopted test setup does not undergo any significant adjustments with load application, this toe region seems to stem from the stretching of the balsa wood fibres during the initial part of the test. After becoming taut, these fibres provide the balsa wood specimens with its maximum stiffness along that direction, and the behaviour becomes linear elastic.

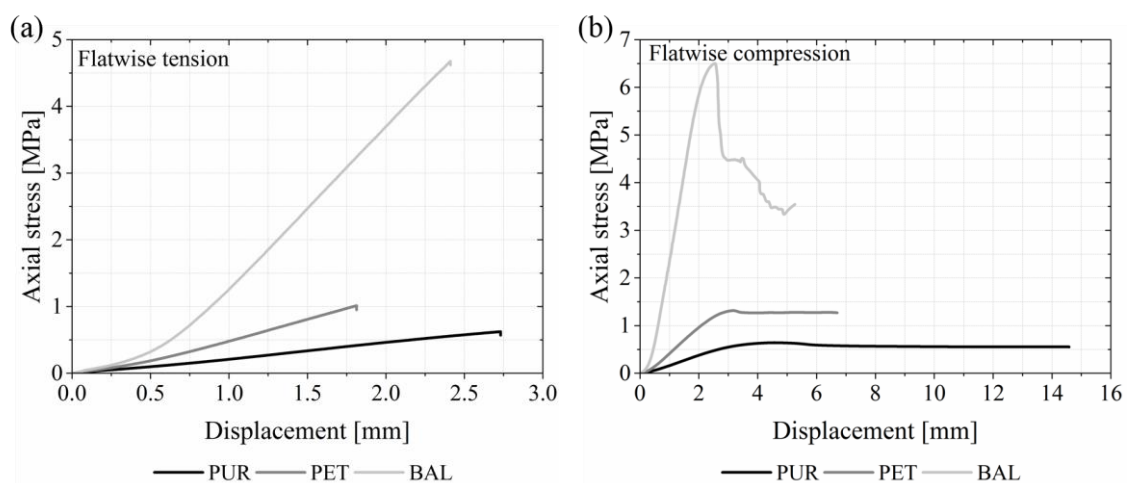


Figure 4.21. Axial stress vs. displacement curves obtained in the: (a) flatwise tension, and (b) flatwise compression tests.

The failure modes observed in the flatwise tension tests are shown in Figure 4.22-a,b,c, for the PUR, PET, and balsa wood specimens, respectively. The foam cored specimens all exhibited tensile failures within the foams, with failure surfaces perpendicular to the loading direction. This result indicates that the debonding stresses required to damage the face-core interfaces in the foam cored panels are higher than the tensile strength of the foams, *i.e.*, the quality of the face-to-core bonds is high enough to ensure that debonding will not occur before the core materials fail themselves. The balsa wood specimens typically presented both a tensile failure within the core and debonding between the core and the face sheets (Figure 4.22-c). However, it was not completely clear which one occurred first or if they occurred simultaneously.

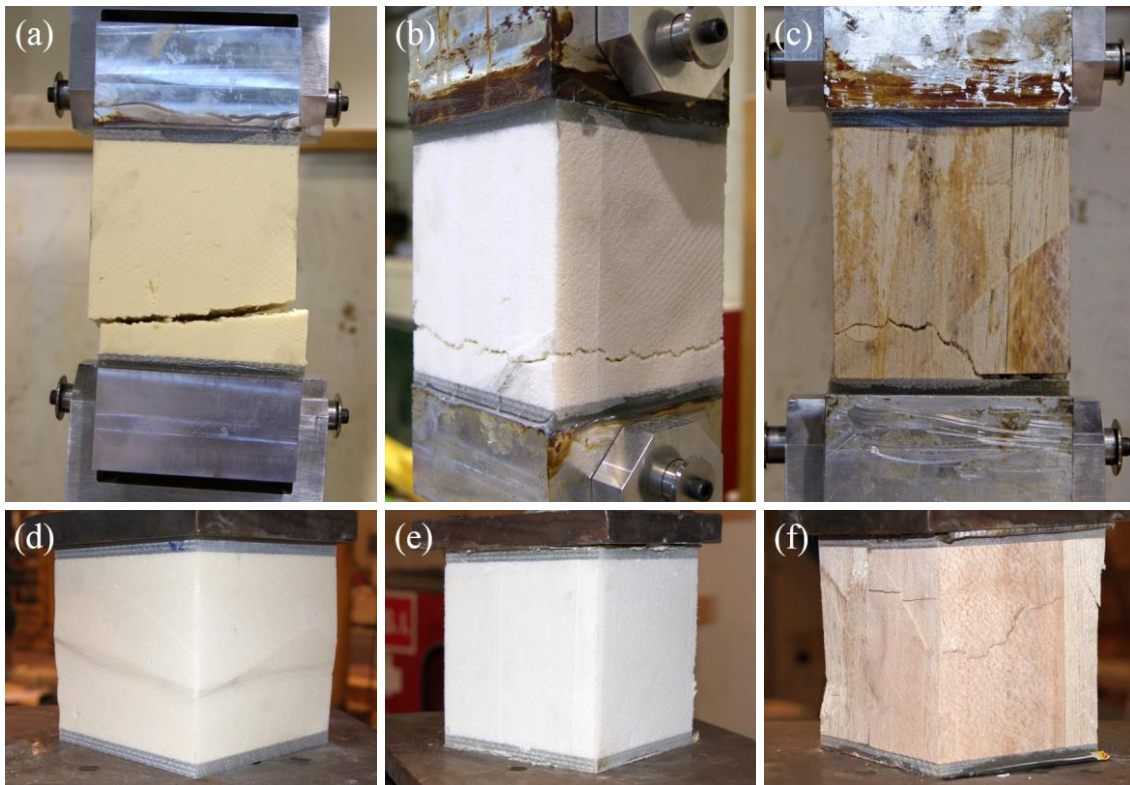


Figure 4.22. Failure modes of the sandwich panel assemblies in flatwise tension: (a) PUR, (b) PET, and (c) balsa wood; and in flatwise compression: (d) PUR, (e) PET, and (f) balsa wood.

In the flatwise compression tests, after short initial toe regions associated with adjustments between the loading plates and the specimens, linear elastic response was observed for all panel types. Preceding failure, all specimens exhibited nonlinear softening, with the foams exhibiting ductility plateaus, during which deformations increased plastically without significant load increments. The balsa wood specimens did not present such a well-defined

ductility plateau, but rather presented gradual force reduction after failure, associated with the progressive crushing and buckling of the wood fibres under the compression loading.

A summary of the main results obtained for the different sandwich panel assemblies is presented in Table 4.5 and Figure 4.23. The sandwich panels with balsa wood core presented the best performance in terms of magnitude of strength and stiffness values, while the PUR foam panels exhibited the lowest mechanical properties. However, the balsa wood cored specimens also presented the highest scatter figures (C.V. up to 19%), whereas the responses measured in the polymer foams were very consistent (C.V. lower than 5%).

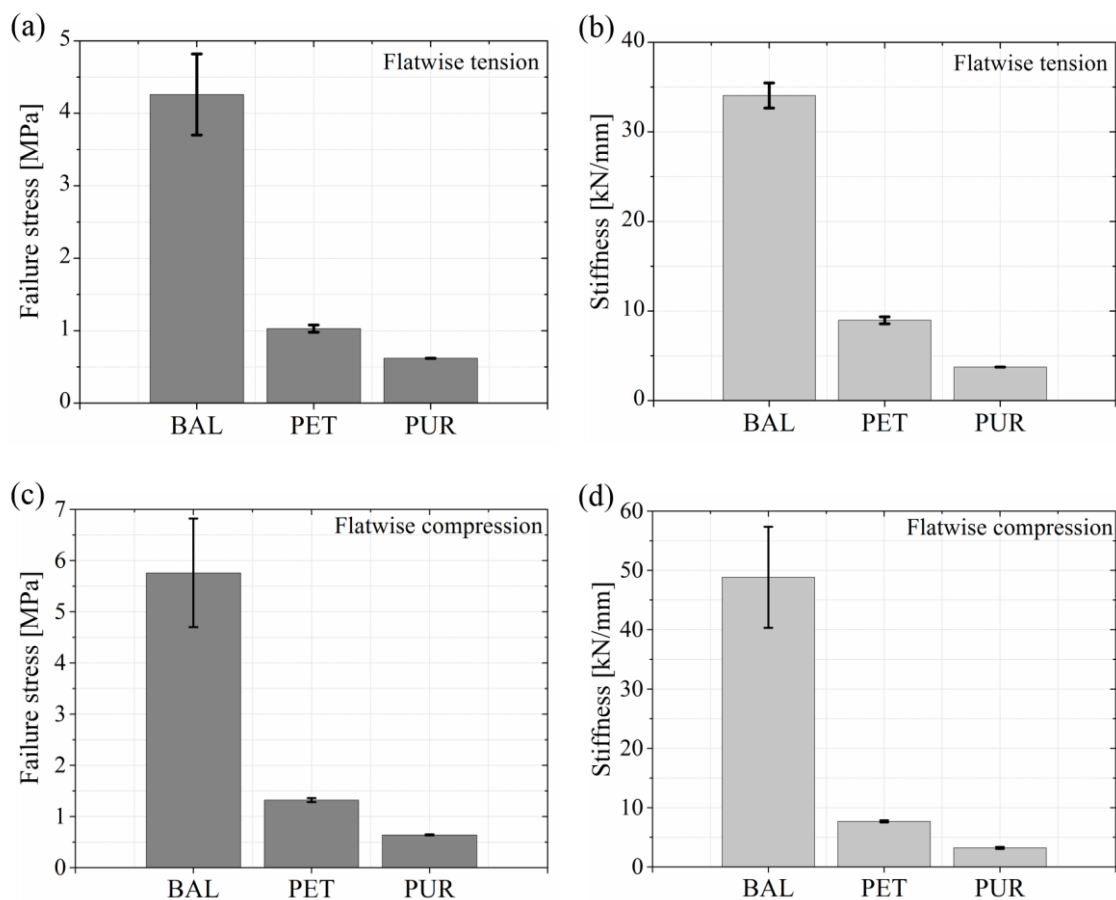


Figure 4.23. Comparison between different sandwich panel assemblies: (a) failure stresses in flatwise tension, (b) stiffness in flatwise tension, (c) failure stresses in flatwise compression, and (d) stiffness in flatwise compression.

Table 4.5. Summary of results obtained in flatwise tension and compression tests.

Core material	Flatwise tension (<i>avg. ± st. dev.</i>)		Flatwise compression (<i>avg. ± st. dev.</i>)	
	$\sigma_{FT,u}$ [MPa]	K_{FT} [kN/mm]	$\sigma_{FC,max}$ [MPa]	K_{FC} [kN/mm]
Balsa wood	4.26 ± 0.56	34.06 ± 1.40	5.76 ± 1.06	48.84 ± 8.52
PET foam	1.03 ± 0.05	8.97 ± 0.39	1.32 ± 0.04	7.68 ± 0.19
PUR foam	0.68 ± 0.001	3.76 ± 0.002	0.64 ± 0.01	3.21 ± 0.17

4.5. Concluding remarks

The current chapter summarized and discussed the main results obtained from a comprehensive material characterisation experimental programme. The following general conclusions may be drawn from the results obtained:

- The mechanical properties of the vacuum infused GFRP laminates fell within typical values for such materials, and compared well with the CLT estimates previously obtained for the adopted fibre architecture, being slightly higher than those analytical predictions.
- Shear tests were performed on the core materials using a test method specially developed for this purpose, the diagonal tension shear (DTS) method. This shear test method allowed testing relatively large specimens (with a roughly cubic shape and edges of 120 mm, corresponding to the thickness of the core in the sandwich panels), producing large enough strains to cause failure within all tested materials. Premature debonding between the test plates and the specimens, very frequent in other test setups (*e.g.*, [7]), never occurred.
- Balsa wood presented the highest shear modulus and strength, although its mechanical properties exhibited relatively high scatter. The PET foam presented the second highest mechanical properties, and very consistent results (low scatter). Concerning the PUR foams, the mechanical properties of the 40 kg/m³, 80 kg/m³ and 120 kg/m³ foams, produced by the same manufacturer, consistently increased with the density. The 100 kg/m³ foam, produced by a different manufacturer, exhibited lower mechanical properties than the 80 kg/m³ foam.

- PUR and PET foams were tested in shear at different temperatures ranging from -20 °C to 120 °C, and their shear moduli exhibited significant temperature dependence, decreasing substantially for higher temperatures. DMA tests were also carried out, indicating that the glass transition temperature of the PET foam is relatively low (65 °C), with its glass transition process occurring over a narrow temperature range; for the PUR foam, this transition occurs for higher temperatures (90 °C) and over a wider temperature range. DSC/TGA tests indicated that the onset decomposition temperatures for the foams are 241 °C for the PUR foam and 326 °C for the PET foam. These values are well beyond the normal temperature ranges possible to find in service situations.
- In the sandwich panel assembly tests, it was found that for all the considered mechanical properties, the sandwich panels with balsa wood core presented the highest values, followed by the PET foam panels, and finally by the PUR foam. The face-to-core bond strength was found to be at least as high as the tensile strength of the core materials, indicating that debonding will not occur before failure of the panels' cores. Regarding compression behaviour, all specimens failed by crushing of the core materials, which resulted in ductility plateaus for the foam cored specimens and gradual force reductions in the balsa wood.

4.6. References

- [1] Bank, L.C., 2006, *Composites for construction: Structural design with FRP materials*, John Wiley & Sons, New Jersey, 551p.
- [2] Chamis, C.C., Sinclair, J.H. (1977). "Ten-deg off-axis test for shear properties in fiber composites", *Experimental Mechanics*, Vol. 17(9), pp. 339-446.
- [3] ASTM D3039/D3039M – 08 (2008). *Standard Test Method for Tensile Properties of Polymer Matrix Composite Materials*. ASTM International, West Conshohocken, Pennsylvania, United States.
- [4] ISO 527-1:1993 (1993). *Plastics – Determination of tensile properties – Part 1: General principles*. ISO, Geneva, Switzerland.

- [5] ISO 527-4:1997 (1997). *Plastics – Determination of tensile properties – Part 4: Test conditions for isotropic and orthotropic fibre-reinforced plastic composites*. ISO, Geneva, Switzerland.
- [6] ASTM D695 – 02 (2002). *Standard Test Method for Compressive Properties of Rigid Plastics*. ASTM International, West Conshohocken, Pennsylvania, United States.
- [7] ASTM C273/C273M – 11 (2011). *Standard Test Method for Shear Properties of Sandwich Core Materials*. ASTM International, West Conshohocken, Pennsylvania, United States.
- [7] Davies JM. *Lightweight sandwich construction*. Oxford: Blackwell Science, 2001, p. 370.
- [8] Osei-Antwi, M., de Castro, J., Vassilopoulos, A.P., Keller, T. (2013). “Shear mechanical characterization of balsa wood as core material of composite sandwich panels”. *Construction and Building Materials*, Vol. 41, pp. 231-238.
- [9] Garrido, M., Correia, J.R., Keller, T. (2015). “Effects of elevated temperature on the shear response of PET and PUR foams used in composite sandwich panels”. *Construction and Building Materials*, Vol. 76, pp. 150-157.
- [10] ASTM E1640 (1999). *Standard test method for assignment of the glass transition temperature by Dynamic Mechanical Analysis*. ASTM International, West Conshohocken, PA.
- [11] Clarke, J.L. (editor) (1996). *Structural Design of Polymer Composites - EuroComp Design Code and Handbook*. E & FN Spon, London, 1996.
- [12] Tracy, C. (2005). *Fire endurance of multicellular panels in an FRP building system*. PhD thesis, École Polytechnique Fédérale de Lausanne, 2005.
- [13] ASTM D5379/D5379M – 05 (2005). *Standard Test Method for Shear Properties of Composite Materials by the V-Notched Beam Method*. ASTM International, West Conshohocken, PA, USA.
- [14] ASTM C297/C297M – 04(10) (2004). *Standard Test Method for Flatwise Tensile Strength of Sandwich Constructions*. ASTM International, West Conshohocken, Pennsylvania, United States.
- [15] ASTM C365/C365M – 11a (2011). *Standard Test Method for Flatwise Compressive Properties of Sandwich Cores*. ASTM International, West Conshohocken, Pennsylvania, United States.

Chapter 5

Flexural behaviour of full-scale panels

5.1. Introduction

In the current study, different sandwich panel architectures are proposed for the rehabilitation of building floors. The mechanical response of each panel typology is expected to be distinct from other typologies, owing to the different materials and their respective configurations. In order to assess their responses under vertical loads, the sandwich panels were submitted to flexural experiments aimed at characterising their static and dynamic behaviour. Three different types of tests were carried out: (i) static serviceability tests to assess the effective flexural properties of the panels, (ii) dynamic tests to determine their natural vibration frequencies, and (iii) static tests up to failure.

The static serviceability tests were carried out to estimate the effective flexural properties of the panels, *i.e.*, the effective Young's modulus of the faces and the effective shear modulus of the core. It is interesting to obtain such effective properties, which are related to the way the sandwich panels actually behave in bending, and compare them to the material properties obtained in the previous chapter. The agreement between the two data sets is important to assess the panel production quality and validate the design procedures, indicating if the materials are behaving as expected and/or if their properties were adequately estimated and considered.

The dynamic tests allowed assessing the natural vibration frequencies and damping ratios for the different panel types. Such dynamic properties are directly concerned with the fulfilment of serviceability requirements related to the comfort of building occupants. On the other hand, these parameters are a good basis for comparison between the material properties as manufactured, providing also relevant experimental data to assess the accuracy of analytical or numerical models of their structural behaviour.

The static flexural tests up to failure were carried out to provide information regarding the development of the load vs. deformation behaviour up to failure for all panel typologies. Such tests allowed assessing whether the panels behave in a linear elastic manner or if they exhibit nonlinear behaviour. In the latter case, it is important to assess what are the sources of such nonlinearities, so they may be adequately considered in the panel design. In addition, the flexural failure tests allowed determining the failure modes and failure loads, once again providing relevant design information that may be compared to analytical or numerical predictions of the panel failure behaviour.

5.2. Effective flexural properties tests

5.2.1. Experimental programme

The effective flexural properties tests were carried out according to the methodology outlined in the EN 13706 standard [1], with the objective of assessing the effective bending and shear stiffness values for each panel typology. The underlying principle of these tests is that the balance between the relative contribution of bending deflection and shear deflection to the total deflection exhibited by the panel changes with the span length. In fact, for longer spans, bending deflection generally represents the largest contribution to the panel's total deflection, whereas for shorter spans the shear deflection becomes more important. By testing a panel in several different span lengths, it is possible to estimate the bending and shear stiffness values, using, for example, Timoshenko beam theory.

All the panel typologies were subjected to these tests, with the exception of the VDC panels. These were excluded since this test method is not applicable to core materials with variable properties along the panel length. At least one panel per tested typology was evaluated, while two or three panels were tested independently for those typologies where higher uncertainty existed regarding the effective properties. These were the TFC and RIB typologies, for which multiple materials have significant contributions to the shear stiffness (namely, the PUR foam and the GFRP laminated elements – truss and ribs).

The sandwich panels were loaded using a three-point bending configuration, considering five different span lengths (Figure 5.1): (i) $S_1 = 0.85$ m, (ii) $S_2 = 1.50$ m, (iii) $S_3 = 2.10$ m, (iv) $S_4 = 2.70$ m and (v) $S_5 = 3.30$ m. The highest span length corresponds to the design span

(also used in the failure tests, *cf.* section 5.4), while the shortest span length corresponds to a distance of three times the panel thickness between the loading point and the supports, *i.e.*, the minimum deemed adequate in order to avoid direct load transmission to the supports. The intermediate spans were selected in order to uniformly cover the range between the maximum and minimum spans.

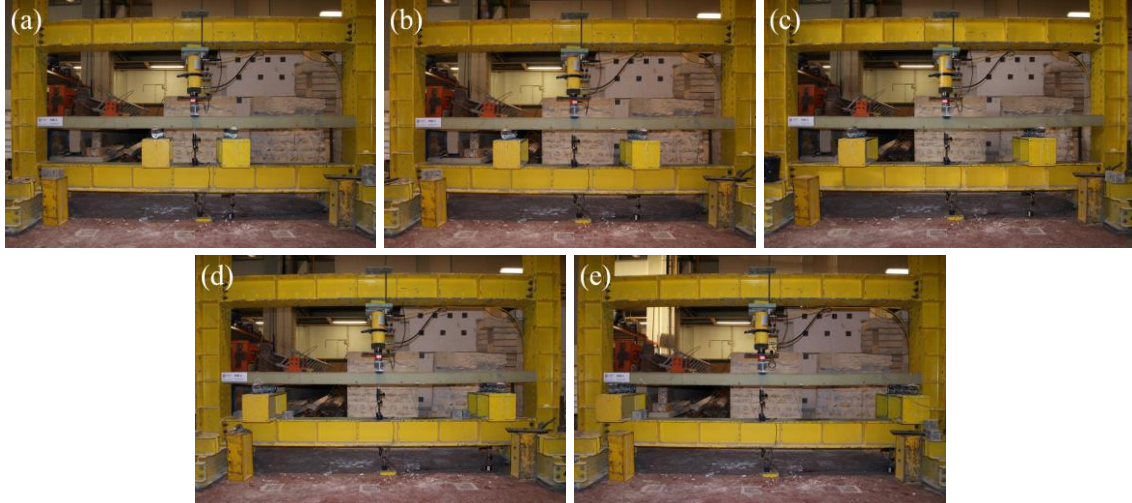


Figure 5.1. Span lengths for the effective flexural properties tests: (a) $S_1 = 0.85$ m, (b) $S_2 = 1.50$ m, (c) $S_3 = 2.10$ m, (d) $S_4 = 2.70$ m and (e) $S_5 = 3.30$ m.

A vertical load was monotonically applied at the mid-span section until a pre-determined deflection of $\text{span}/200$ was attained in that section, after which the panels were unloaded. A minimum of two loading-unloading cycles were carried out for each span and panel type.

5.2.2. Results and discussion

According to Timoshenko beam theory, the mid-span deflection ($\delta_v^{L/2}$) of a simply supported beam in three point bending may be calculated using Equation (5.1),

$$\delta_v^{S/2} = \frac{PS^3}{48D} + \frac{PS}{4U} \quad (5.1)$$

where P is the total applied force, S is the span length, D is the beam's bending stiffness, and U is its transverse shear stiffness. Rewriting this equation as follows,

$$\frac{\delta_v^{S/2}}{PL} = \frac{S^2}{48D} + \frac{1}{4U} \quad (5.2)$$

and defining $K = P/\delta_v^{S^2}$ as the stiffness measured in the linear elastic region of the load vs. displacement curve obtained for each test, the following equation is obtained:

$$\frac{1}{KS} = \frac{S^2}{48D} + \frac{1}{4U} \quad (5.3)$$

Plotting the results for each span in a S^2 vs. $1/KS$ plot, the points obtained should follow a linear development, characterised by a slope of $1/48D$ and an intercept of $1/4U$. Obtaining the slope and intercept values from a linear fitting of the results allows the calculation of estimates for the effective bending (D) and shear stiffness (U) values.

Figure 5.2 plots these results for the various sandwich panel typologies. As expected, the obtained data points follow a linear trend, with slope and intercept values as given in Table 5.1. The slope values for the panels with nominal width of 250 mm (PUR, PET, BAL and TFC) are very similar between one another. This is consistent with the fact that all panels share the same type of face sheets, and that the panels' bending stiffness is mostly attributable to its facings. Furthermore, the slope of the linear fit to data points obtained for the RIB panels is approximately half of that obtained for the remaining typologies. This is consistent with the double nominal face sheet width in these panels (500 mm).

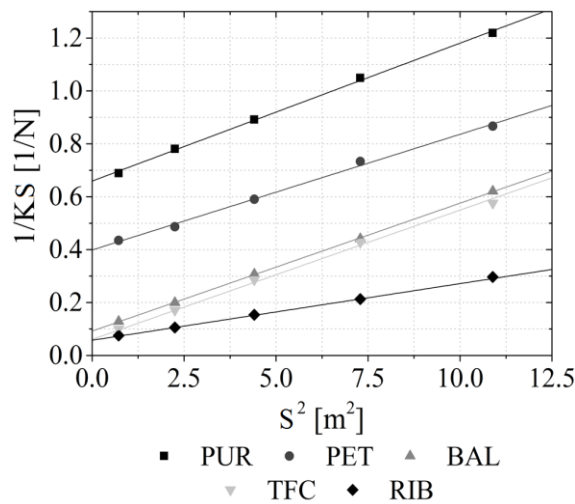


Figure 5.2. Plot of results (S^2 vs. $1/KS$) obtained from the effective flexural properties tests.

The largest differences in the effective flexural properties pertain to the shear stiffness of each panel typology, as would be expectable. The lowest shear stiffness was obtained for the PUR panels, as per the high intercept values of this typology. The PET panels present significantly higher effective shear stiffness; however, the highest shear stiffness of the

simple panel typologies was found for the BAL panels (results in good general agreement with the material characterisation presented in the previous chapter). The TFC panels showed slightly higher effective shear stiffness than the BAL panels, showing that the inclusion of a GFRP truss embedded in the foam core allows achieving significant improvements in shear stiffness. Finally, a similar result may be inferred regarding the inclusion of GFRP ribs in the sandwich panels, given that the highest effective shear stiffness values were obtained for the RIB panels.

Table 5.1. Summary of results obtained from the effective flexural properties tests.

	D [$\times 10^8$ kNmm ²]	U [kN]	E [GPa]	G [MPa]
PUR	4.0	379	28.3	12.6
PET	4.8	627	33.7	20.9
BAL	4.3	2711	30.5	90.4
TFC	4.4	3639	31.2	121.3 ⁽¹⁾
RIB	9.6 \pm 0.3	4328 \pm 129	30.8 \pm 1.5	(2.7 \pm 0.1) $\times 10^3$

⁽¹⁾ considering a homogenised core

For sandwich panels with two equal face sheets and a homogenous core, the bending and shear stiffness values may be used to estimate the Young's modulus of the face sheets (E_f) and the shear modulus of the core (G_c) according to Equations (5.4) and (5.5) [2],

$$E_f = \frac{12D}{(d^3 - c^3)b} \quad (5.4)$$

$$G_c = \frac{U(d - 2t)}{(d - t)^2 b} \quad (5.5)$$

where d is the total panel thickness, c is the core thickness, b is the panel width, and t is the face sheet thickness. Using these expressions, moduli estimates were obtained for the PUR, PET and BAL panels, as well as for the TFC panels assuming a homogenisation of the truss-foam core. For the RIB panels, the GFRP rib in-plane shear modulus (G_r) was estimated considering the contribution of both the ribs and the foam core to the shear stiffness of the panel. To this end, a total shear stiffness of $U = G_r A_{V,r} + G_c A_{V,c}$ was considered, where $A_{V,r}$ is the cross-sectional area of the GFRP ribs given by $A_{V,r} = 2t_r d$ (t_r corresponds to the rib thickness), and $A_{V,c}$ is the effective shear area of the core given by $A_{V,c} = (b - 2t_r) \times [(d - t)^2 / (d - 2t)]$. Thus, G_r was estimated using Equation (5.6), adopting

the shear modulus value estimated from the PUR panels in the current effective properties tests.

$$G_r = \frac{U - G_c A_{V,c}}{A_{V,r}} \quad (5.6)$$

The moduli estimates obtained are given in Table 5.1. The estimated Young's moduli values are in relatively good agreement with the values obtained in the material characterisation tests (29.4 ± 0.8 MPa). The highest relative differences were found for the PET panels (+15%), with the remaining estimates being within a 6% error margin of the average Young's modulus obtained in those tests.

Regarding the shear moduli estimates, results for the PET foam (20.9 MPa) showed a good agreement with the material characterisation tests (19.2 ± 1.1 MPa). For the PUR foam, the 12.6 MPa shear modulus estimated here is 45% higher than the average value obtained in the material characterisation tests (8.7 ± 1.0 MPa); however, compared to the highest shear modulus value found in those tests (10.0 MPa), this difference is reduced to 26%, and it is plausible that such differences stem from actual variability in the material properties of this foam. For the balsa wood core, the estimated shear modulus (90.4 MPa) is also significantly higher (85%) than the value obtained in the material characterisation tests (48.8 ± 6.2 MPa). Such differences may stem from this material's heterogeneity and markedly orthotropic behaviour, which can lead to size effects that affect the shear properties of the wood when comparing results from small scale specimens and full-sized sandwich panels.

For the TFC panels, an equivalent homogenous core with the same global shear stiffness as the hybrid truss-foam assembly was considered. The shear modulus value of this equivalent core was estimated to be 121.3 MPa, a value higher than that obtained for the balsa wood. As previously mentioned, this shows that the inclusion of the GFRP truss elements in the sandwich panel core significantly increases the panel's shear stiffness (albeit also increasing its self-weight).

Concerning the RIB panels, an in-plane shear modulus of 2.7 GPa was estimated for the GFRP ribs. This compares well with the value obtained in the material characterisation tests (2.3 ± 0.2 GPa). If the shear modulus of the PUR foam core was considered as being 8.7 MPa, as per the average value obtained in the material characterisation tests, the G_r value estimate would be of 2.9 GPa, a relatively small difference, slightly further overestimating the rib

shear modulus. This suggests that a G_c value higher than the average 8.7 MPa should better describe the real response of the PUR foams used in the sandwich panels.

5.3. Dynamic tests

5.3.1. Experimental programme

Flexural dynamic tests were carried out in order to determine the natural frequencies and damping ratios of the different sandwich panels. The panels were tested in a simply supported 3.30 m span (Figure 5.3). Appropriate care was taken to ensure an even contact at the interface surfaces between the supports and the panels. The dynamic excitation of the panels was achieved by applying manual strikes at their mid-span section, with at least three repetitions being performed. The strikes were applied in a position centred with the width of the panels in all specimens. For the wider RIB panels, additional strikes were applied at an eccentric position near the panel's mid-span, so as to excite the panel's torsional vibration modes. The limited width of the remaining panels did not allow for such an excitation to be applied effectively.



Figure 5.3. Experimental setup used for the dynamic tests.

The vertical accelerations originating from those strikes were measured using accelerometers (top right hand corner of Figure 5.3) reading at a 600 Hz frequency, also placed at mid span. The results were analysed using the Fast Fourier Transform (FFT) algorithm described in [3], producing power spectral density functions of frequency. The peaks of such functions indicate the frequencies for which the panels are naturally excited/resonant, *i.e.*, the natural vibration frequencies of the panels. The decay in the experimentally measured vertical accelerations was analysed using the logarithmic decrement method [4] in order to obtain an estimate of the damping ratios.

5.3.2. Results and discussion

5.3.2.1. Acceleration response

Figure 5.4 shows the typical acceleration response exhibited by the tested sandwich panels after the excitations were applied. The two accelerometers registered similar responses for each repetition, both in terms of amplitude and waveform. An instantaneous acceleration peak was consistently measured after the excitations. Oscillatory movement was then registered, with the wave amplitude of the acceleration curves decreasing quickly and steadily.

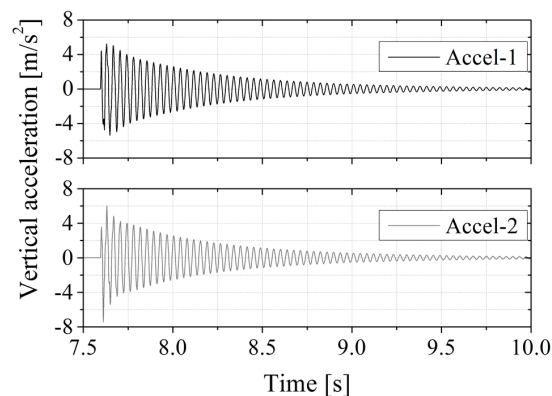


Figure 5.4. Typical acceleration response (data from RIB panels).

5.3.2.2. Natural frequencies

The flexural frequencies were determined using the semi-sum of the accelerations measured with the two accelerometers, while the torsional frequencies were obtained using the semi-difference between those measurements. The power spectral density graphs obtained for the VDC and RIB panels are shown in Figure 5.5, exemplifying the type of results obtained.

Table 5.2 presents the obtained flexural frequencies for the different panels, and also the torsional frequency for the RIB panels. Although the vibration modes were not explicitly determined, it is reasonable to assume that the determined frequencies correspond to the first flexural and first torsional vibration modes (the latter for the RIB panel), which are typically dominant and were the most excited by the strike application at the adopted positions.

The natural vibration frequencies associated with the first flexural mode of all panel typologies are above 20 Hz. While the Eurocode standards do not present general provisions concerning the minimum acceptable natural vibration frequency for building floors, the Eurocode standard that regulates the design of steel structures (EN 1993-1-1:1992 [5])

presents minimum natural frequency values (f_n) according to the use of the building floor: (i) $f_n > 3$ Hz for floors in which people walk regularly, such as the floors of dwellings or offices; and (ii) $f_n > 5$ Hz for floors which are jumped or danced on in a rhythmical manner. Consequently, the natural frequencies obtained with the different sandwich panels are well above the minimum values required for user comfort in building floors.

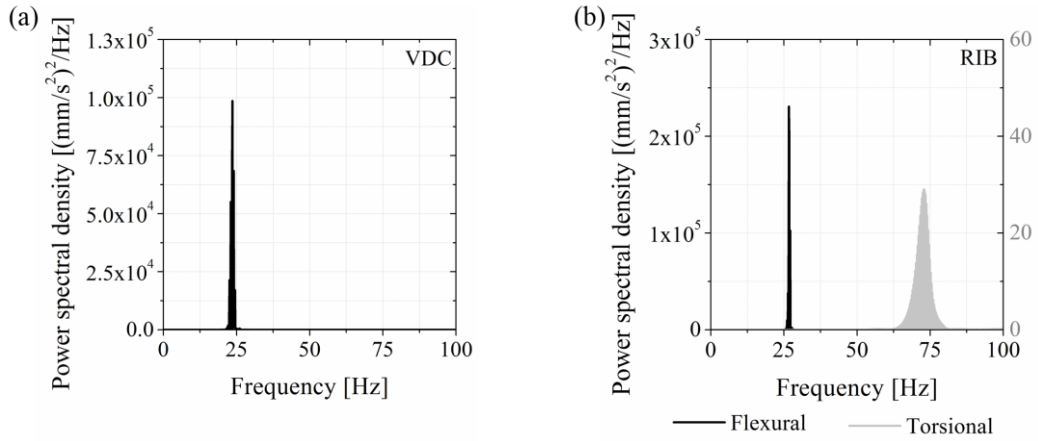


Figure 5.5. Power spectral density curves obtained with the FFT algorithm: (a) flexural curve for the VDC panels, and (b) flexural and torsional curves for the RIB panels.

Table 5.2. Natural flexural (and torsional) vibration frequencies [Hz].

Typology	Natural vibration frequency			
	Average	Standard deviation	C.V. [%]	
PUR	20.6	0.1	0.4%	
PET	23.3	0.5	2.3%	
BAL	25.5	0.2	0.6%	
VDC	23.6	0.1	0.6%	
TFC	23.9	0.1	0.3%	
RIB	Flexural	26.7	0.1	0.3%
	Torsional	73.5	0.6	0.9%

5.3.2.3. Damping ratios

The damping ratio (ζ) of an oscillatory system is defined as the quotient between the system's damping coefficient (c) and its critical damping coefficient (c_c), *i.e.*, $\zeta = c/c_c$. Using the logarithmic decrement method, the damping ratio may be estimated from the decrement in consecutive acceleration peaks in the accelerograms. Applying this method, the damping ratios were estimated for the tested sandwich panels, and the obtained values are presented in Table 5.3.

Table 5.3. Damping ratios (ζ) obtained in the dynamic tests (in percentage).

Typology	Damping ratios (ζ) [%]		
	Average	Standard deviation	C.V. [%]
PUR	0.65	6.5×10^{-3}	1.0%
PET	1.39	0.3	23.6%
BAL	1.94	0.1	7.3%
VDC	2.86	0.4	13.3%
TFC	0.56	8.8×10^{-3}	1.6%
RIB	0.83	6.5×10^{-2}	7.8%

The bar-graph presented in Figure 5.6 compares the damping ratio values obtained for the tested panels. The damping ratio values obtained ($\zeta \ll 1$) indicate that the damping coefficients in all panels are well below critical (*i.e.*, $c \ll c_c$). In general, the damping ratios were in line with typical values reported in the literature for structural elements comprising other FRP components (e.g., [6,7]). The highest damping ratio was exhibited by the variable density core panels. Among the simple sandwich panels, the panels with PUR foam core presented the lowest damping ratio, while the balsa wood core panels presented the highest value. Truss-foam core panels presented the lowest damping ratio among all the tested panel types.

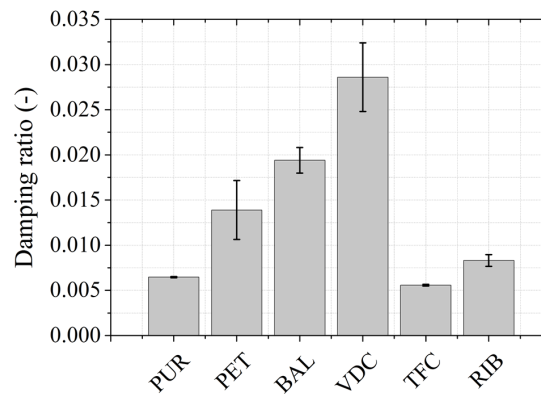


Figure 5.6. Comparison between estimated damping ratios for the different panel typologies.

The damping ratios obtained fall within a range of 0.65-2.86%, which is quite similar to the typical range of damping ratios found in concrete (0.5-3.0%) and significantly higher than those exhibited by steel members (0.05-0.40%) [4], suggesting that the sandwich panels are able to effectively dissipate energy from structural vibrations. This observation, coupled with the panels' relatively high natural frequencies, suggest that user comfort issues related to vibrations should not be encountered with the sandwich panel floors.

5.4. Failure tests

5.4.1. Experimental programme

For the flexural failure tests, the sandwich panels were set up in a simply supported configuration with a span length of 3.30 m, and were loaded in: (i) four-point bending for the PUR, PET, BAL, TFC and RIB panels (Figure 5.7-a), and (ii) six-point bending (*i.e.*, four load application points and two support points) for the VDC panels (Figure 5.7-b). The latter configuration was adopted in order to optimise the core material distribution along the length of the variable density core panels.

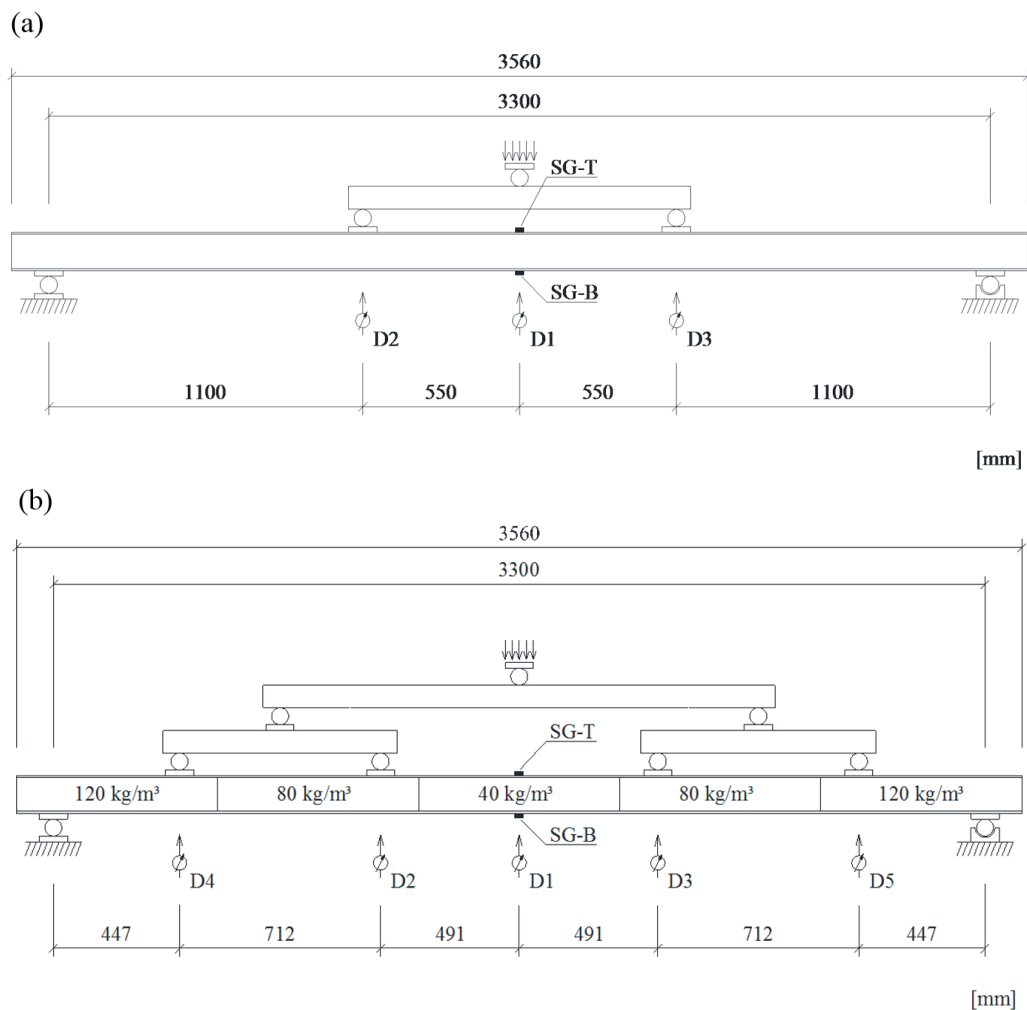


Figure 5.7. Failure test setups: (a) four-point bending configuration, and (b) six-point bending configuration.

The panels were supported on steel bearings, guaranteeing a negligible rotational restriction at the fixed support and negligible rotational and translational restrictions at the sliding

support. A layer of plaster was applied between the panels and the support surfaces, in order to ensure their full and even contact, accounting for possible defects in the sandwich panels.

The load was applied monotonically at an average speed of 0.1 kN/s (load control) up to failure using a hydraulic jack, and transferred to the panels via load transmission beams (a single beam in the four-point bending configuration, and a main beam coupled with two secondary beams in the six-point bending configuration, *cf.* Figure 5.7). Steel rollers were used to apply the loads to the panels at the loading points. Between the panel facings and the steel plates, 3 mm thick neoprene sheets were placed to avoid local damage to the panels.

The loads were measured using a load cell with a capacity of 200 kN and precision of 0.01 kN. The vertical displacements at mid-span and at the load application points were measured using displacement transducers with a precision of 0.01 mm. Strain gauges were installed in the top and bottom face sheets, at cross sections located within the constant bending moment portion of the panels, to measure axial strains in the faces. For some panel typologies, additional instrumentation was adopted in order to measure specific relevant information. In particular, for the TFC panels, strain gauges were installed on the GFRP truss webs (lateral edges) in order to assess the truss' effectiveness; for the RIB panels, strain gauge rosettes were installed on the ribs in order to measure the shear strain in those elements.

A minimum of three specimens per panel typology were tested (a higher number was used in multiple cases). However, some of the obtained results were discarded, as some of the panels (one of the PUR type and one of the BAL type) were found to present production defects that affected their mechanical response. Thus, the number of valid results obtained per panel typology were as follows: (i) two for PUR, (ii) three for PET, (iii) two for BAL, (iv) four for TFC, (v) four for VDC, and (d) three for RIB.

5.4.2. Results and discussion

5.4.2.1. PUR

The tested PUR panels presented very consistent flexural responses. Figure 5.8 presents a comparison between the load *vs.* displacement and load *vs.* strain curves obtained for the two

specimens. Table 5.4 presents a summary of the results obtained, including the average values for each property¹⁶.

The load vs. displacement responses (Figure 5.8-a) showed consistent load paths between the two panels, characterised by a linear elastic behaviour for loads up to approximately 20 kN. This segment was followed by a gradually increasing loss of stiffness, culminating in a short yielding plateau at approximately 31 kN of applied load. For the PUR-1 panel, this plateau was preceded by a slight load reduction. In both panels, the yielding plateau segment was accompanied by visible crushing (compression failure) in the foam core under the load application points. Both panels finally failed in a brittle manner due to the shear failure of the PUR foam core, which occurred in one of the shear spans along approximately 45° oriented planes (Figure 5.9).

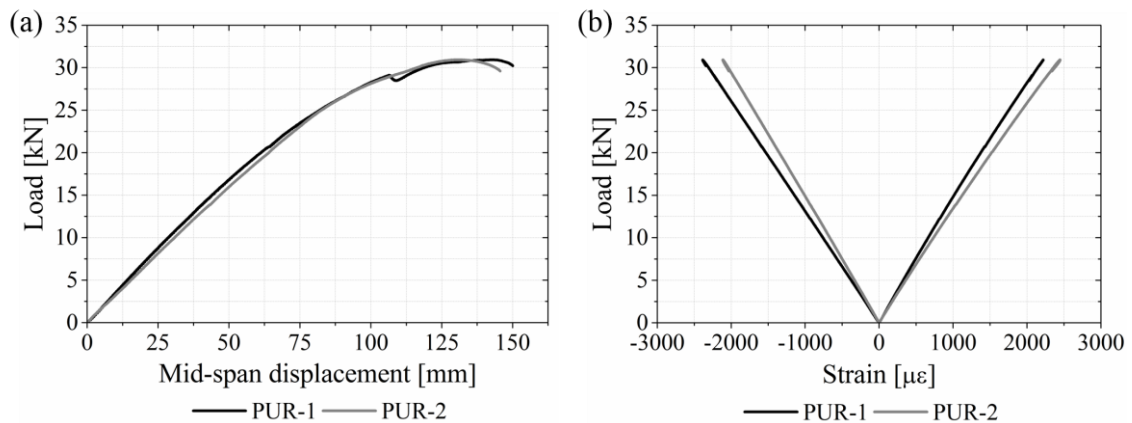


Figure 5.8. Results obtained in the failure tests of the PUR panels: (a) load vs. displacement curves, and (b) load vs. strain curves.

The nonlinearity in the load vs. displacement response of the PUR panels mostly stems from the compressive yielding of the foam under the load application points. In fact, the compressive strength of the PUR foam, as determined in the material characterisation tests (flatwise compression) is 0.64 ± 0.01 MPa. Considering the dimensions of the load application areas (60 mm by 250 mm), a conservative estimate of 19.2 kN is obtained for the force necessary to induce crushing in the foam. Such an estimate is fairly conservative, as the GFRP faces help distribute the applied loads over a large area of the core, by acting as a rigid plate on an elastic foundation. However, as mentioned, the nonlinearity in the

¹⁶ Standard deviations and coefficients of variation were not calculated due to the limited sample size.

panels' response was observed for loads above approximately 20 kN, which is in good agreement with the estimated onset of foam crushing.

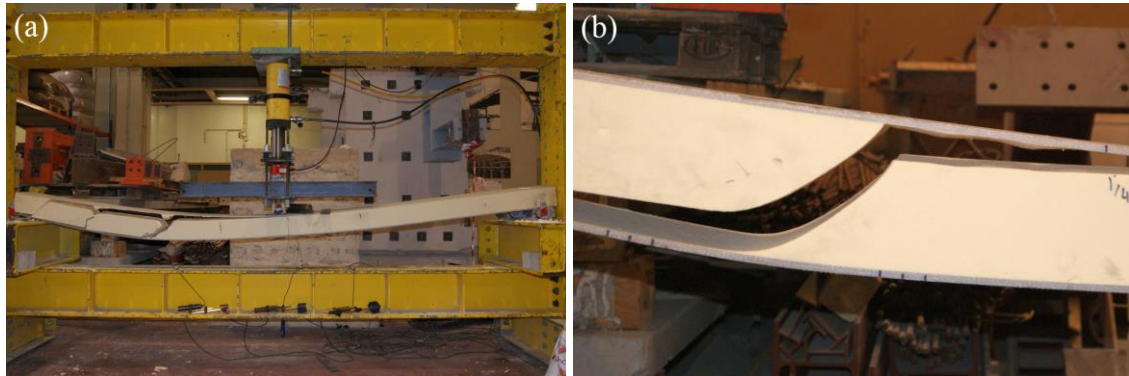


Figure 5.9. Failure of the PUR panels: (a) general view of PUR-1, and (b) shear fracture in PUR-2.

Additionally, part of this response may also be attributed to the slightly nonlinear shear response of the polyurethane foam, as presented in chapter 4. Regarding the GFRP face sheets, their load vs. strain response was linear elastic up to the panel's failure, as shown in Figure 5.8-b.

Table 5.4. Summary of results obtained in the flexural failure tests of the PUR panels.

	PUR-1	PUR-2	Average
Failure load (F_u)			
	[kN]	30.9	30.9
Stiffness (K)			
	[kN/mm]	0.35	0.33
Maximum shear force (V_{max})			
	[kN]	15.5	15.5
Maximum bending moment (M_{max})			
	[kNm]	17.0	17.0
Maximum shear stress (τ_{max})			
	[MPa]	0.52	0.52
Maximum axial stress (σ_{max})			
	[MPa]	65.1	65.0
Maximum mid-span displacement ($d_{1/2,max}$)			
	[mm]	150.1	145.6
Maximum strain in top face ($\epsilon_{top,max}$)			
	[$\mu\epsilon$]	-2387	-2113
Maximum strain in bottom face ($\epsilon_{bottom,max}$)			
	[$\mu\epsilon$]	2220	2449
			2334

The average maximum shear stress obtained was 0.52 MPa, computed by considering that core resists to the total shear force. This value is significantly higher (+63%) than the shear strength of the PUR foam (0.32 ± 0.06 MPa) obtained in the material characterisation tests presented in chapter 4. This result follows the trend observed in the effective flexural properties tests (section 5.2.2, where an effective shear modulus of 12.6 MPa was estimated for the foam) for higher mechanical performance of the PUR foam when incorporated into

the sandwich panels than in small-scale coupons (for which an average shear modulus of 8.7 MPa was obtained). It was not possible to further investigate this aspect, and consequently the reasons behind the different performances of the PUR foam are not clear and should be the subject of future research.

5.4.2.2. PET

A comparison between the load *vs.* displacement and load *vs.* strain curves obtained in the PET panel tests is presented in Figure 5.10, and Figure 5.11 shows the failure modes observed. Table 5.5 presents a summary of the results obtained for the three tested panels. The PET panels consistently presented an initial linear elastic response, which was kept during most of the test. The initial flexural stiffness exhibited by all three panels was very consistent, with an average value of 0.43 ± 0.01 kN/mm. The axial strains in the face sheets, however, presented relatively higher scatter, both in terms of “stiffness” and maximum values, particularly for the top face (compressive) strains.

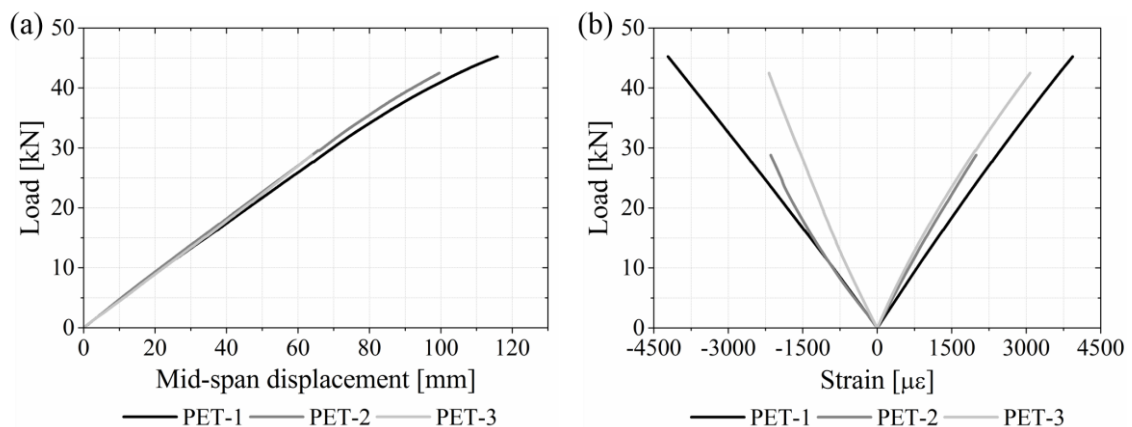


Figure 5.10. Results obtained in the failure tests of the PET panels: (a) load *vs.* displacement curves, and (b) load *vs.* strain curves.

While panels PET-1 and PET-3 presented a slight stiffness reduction preceding failure, the PET-2 panel seems to have failed prematurely, still within the linear elastic region, possibly due to material defects. This panel failed for a load (28.8 kN) that was 34% lower than the average failure load of the two other panels (43.9 kN). The global average failure load was 38.8 ± 8.8 kN.

The compression strength of the PET core, as determined in the flatwise compression tests, was 1.32 ± 0.04 MPa. Similarly to what was presented for the PUR panels, a conservative estimate of 39.6 kN may be obtained for the force necessary to induce crushing of the foam.

Chapter 5 Flexural behaviour of full-scale panels

This load agrees well with the onset on the panels' nonlinear response (at ~ 40 kN), suggesting that the slight nonlinearity found before failure of the PET-1 and 3 panels may have stemmed from crushing of the PET foam, possibly in combination with the nonlinearity found in the PET foam's shear response (*cf.* chapter 4).

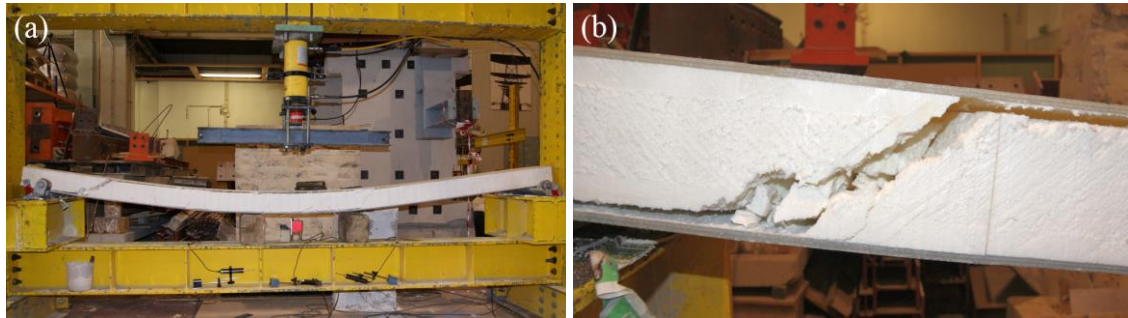


Figure 5.11. Failure of the PET panels: (a) general view of PET-1, and (b) shear fracture in PET-1.

Table 5.5. Summary of results obtained in the flexural failure tests of the PET panels.

	PET-1	PET-2	PET-3	Average	Standard deviation	Coefficient of variation	
Failure load (F_u)							
	[kN]	45.2	28.8	42.5	38.8	8.8	22.6%
Stiffness (K)							
	[kN/mm]	0.42	0.44	0.44	0.43	0.01	3.1%
Maximum shear force (V_{max})							
	[kN]	22.6	14.4	21.2	19.4	4.4	22.6%
Maximum bending moment (M_{max})							
	[kNm]	24.9	15.8	23.4	21.4	4.8	22.6%
Maximum shear stress (τ_{max})							
	[MPa]	0.79	0.50	0.75	0.68	0.16	22.8%
Maximum axial stress (σ_{max})							
	[MPa]	121.1	78.8	117.1	105.7	23.4	22.1%
Maximum mid-span displacement ($d_{1/2,max}$)							
	[mm]	115.9	63.9	99.6	93.1	26.6	28.6%
Maximum strain in top face ($\epsilon_{top,max}$)							
	[$\mu\epsilon$]	-4213	-2145	-2180	-2846	1184	41.6%
Maximum strain in bottom face ($\epsilon_{bottom,max}$)							
	[$\mu\epsilon$]	3937	1991	3078	3002	975	32.5%

All panels collapsed due to the shear failure of the PET foam core, which occurred in the shear span along approximately 45° oriented planes (Figure 5.11), for an average maximum shear stress of 0.68 ± 0.16 MPa. This value is 28% lower than the shear strength of 0.94 ± 0.04 MPa obtained in the small-scale material characterisation tests. Not considering the results of the PET-2 panel, for which a shear stress at failure of 0.50 MPa was estimated (indicating possible defects in the foam core), the average shear stress increases to 0.77 MPa; however, this value is still 18% lower than that obtained in the material characterisation tests. This suggests that the shear strength of the PET foam in the full-scale panels may possibly

have been generally affected by material defects within the foam, indicating possible size effects affecting the two sets of results.

5.4.2.3. BAL

Figure 5.12 presents the load vs. displacement and load vs. strain curves obtained in the flexural failure tests of the BAL panels. The panels exhibited very similar responses in terms of mid-span displacement and axial strain in the GFRP faces. Table 5.6 provides a summary of the average results obtained for different properties¹⁷.

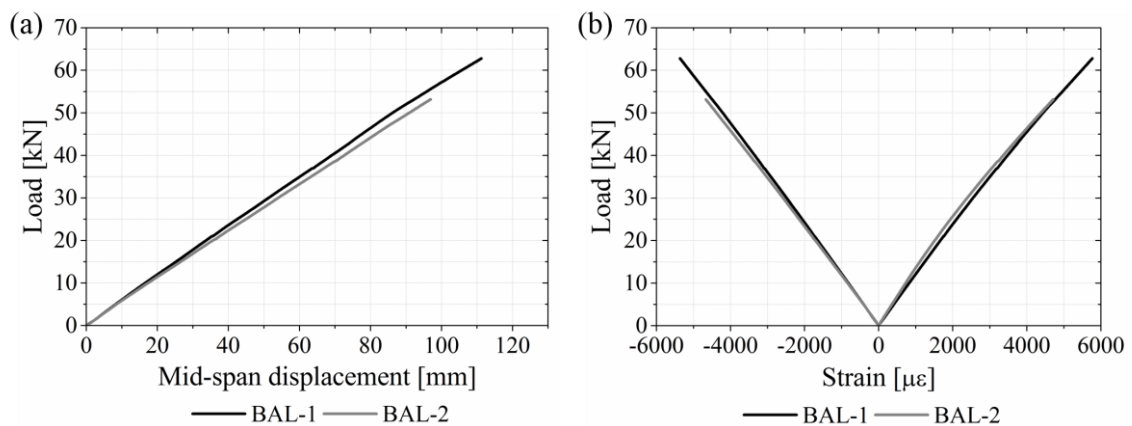


Figure 5.12. Results obtained in the failure tests of the BAL panels: (a) load vs. displacement curves, and (b) load vs. strain curves.

The BAL panels presented linear elastic response up to failure, which occurred in a brittle manner due to shear failure of the balsa wood core (Figure 5.13). Unlike the PUR and PET panels, the balsa wood cores failed along vertical planes, parallel to the wood fibre direction and the joints between adjacent balsa wood blocks. These are natural weakness planes for this material, as observed in the small-scale diagonal tension shear tests reported in chapter 4. From those tests, a shear strength of 0.93 ± 0.19 MPa was obtained, which agrees well with the average maximum shear stress (1.00 MPa) obtained in the flexural failure tests. The differences in failure loads for both panels (maximum deviation of 4.8 kN, or about 8%, from the average failure load) also fall within the normal scatter in the mechanical properties that characterises balsa wood.

¹⁷ Standard deviations and coefficients of variation are not presented in this case due to the sample size.

Table 5.6. Summary of results obtained in the flexural failure tests of the BAL panels.

		BAL-1	BAL-2	Average
Failure load (F_u)	[kN]	62.8	53.2	58.0
Stiffness (K)	[kN/mm]	0.58	0.55	0.57
Maximum shear force (V_{max})	[kN]	31.4	26.6	29.0
Maximum bending moment (M_{max})	[kNm]	34.5	29.2	31.9
Maximum shear stress (τ_{max})	[MPa]	1.07	0.92	1.00
Maximum axial stress (σ_{max})	[MPa]	167.9	144.6	156.3
Maximum midspan displacement ($d_{1/2,max}$)	[mm]	111.3	97.0	104.1
Maximum strain in top face ($\epsilon_{top,max}$)	[$\mu\epsilon$]	-5362	-4665	-5013
Maximum strain in bottom face ($\epsilon_{bottom,max}$)	[$\mu\epsilon$]	5770	4713	5241

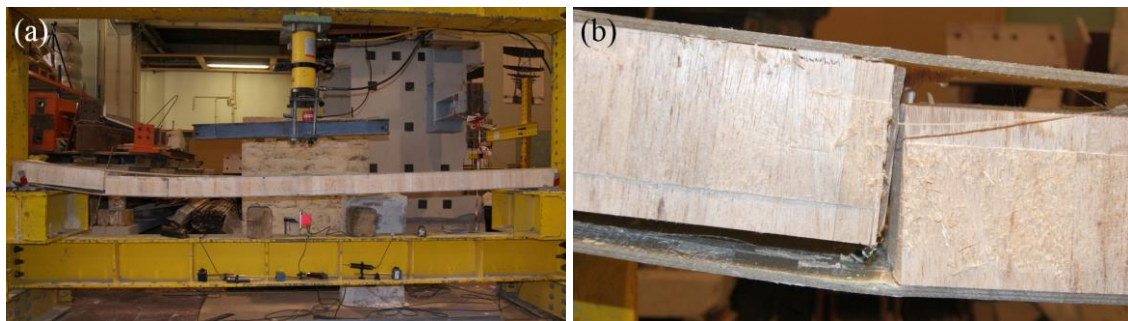


Figure 5.13. Failure of the BAL panels: (a) general view of BAL-1, and (b) shear fracture in BAL-1.

5.4.2.4. TFC

A comparison between the load *vs.* displacement and load *vs.* strain curves obtained for all TFC panels is shown in Figure 5.14, while Table 5.7 presents a summary of the results obtained in those tests, including average properties, standard deviations and coefficients of variation.

A relatively high scatter of results was obtained in these tests, with coefficients of variation of approximately 25% in terms of failure loads and 13% in terms of stiffness. This scatter may be mostly attributed to the production defects found in the TFC panels, which exhibited significant flatness deviations in the face sheets along the panel length (stemming from misalignment of the PUR foam blocks in the hybrid core during the vacuum infusion process).

The average failure load obtained in the tests was 12.24 ± 3.05 kN, a value that is significantly lower than any of the failure loads obtained for the other panel typologies. Failure of the TFC panels typically occurred by progressive damage accumulation, with debonding occurring between the GFRP elements and the PUR foam core at multiple locations, followed by debonding between the truss webs and the faces (Figure 5.15).

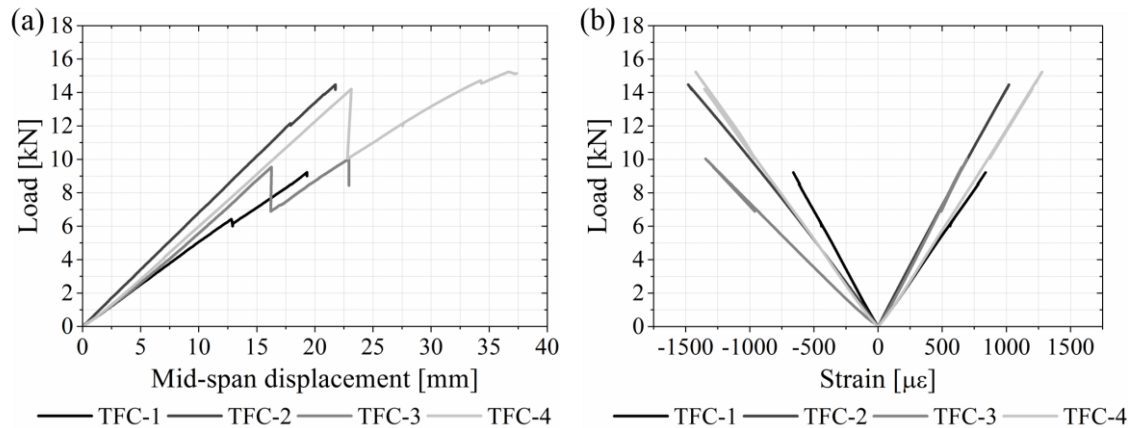


Figure 5.14. Results obtained in the failure tests of the TFC panels: (a) load vs. displacement curves, and (b) load vs. strain curves.

The average maximum (homogenised) shear stress was 0.20 ± 0.05 MPa, which is even lower than the average maximum shear stress resisted by the PUR panel, in which the same type of foam is used but without the inclusion of the GFRP truss. The absence of fibre reinforcement continuity between truss webs and face sheets, as mentioned in chapter 3, significantly limited the effectiveness of the truss nodes in transferring shear stresses between the panel faces. This aspect could be minimised by overlapping part of the reinforcement fibres in those laminates. However, this could not be achieved using the production methods and materials used in the current study. Further investigations should assess the structural effect of guaranteeing the abovementioned reinforcement continuity (even if partial) at the nodes.

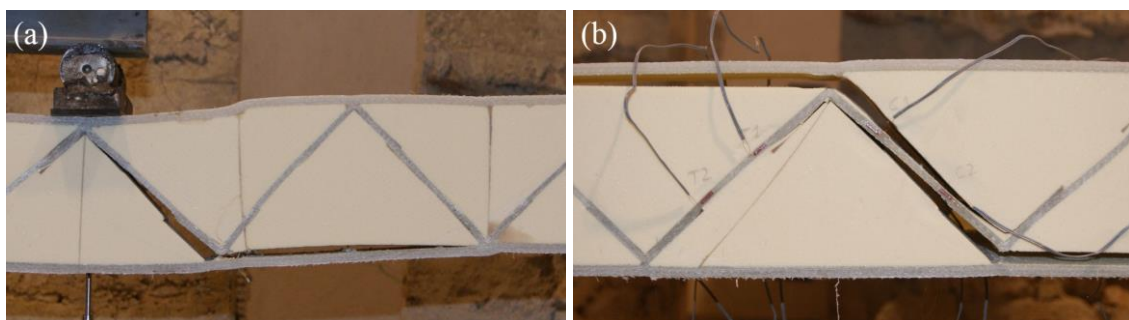


Figure 5.15. Failure of the TFC panels: (a) TFC-4, and (b) TFC-3.

Table 5.7. Summary of results obtained in the flexural failure tests of the VDC panels.

	TFC-1	TFC-2	TFC-3	TFC-4	Average	Standard deviation	Coefficient of variation
Failure load (F_u) [kN]	9.2	14.5	10.0	15.2	12.2	3.1	24.9%
Stiffness (K) [kN/mm]	0.50	0.65	0.54	0.62	0.58	0.07	12.7%
Maximum shear force (V_{max}) [kN]	4.6	7.2	5.0	7.6	6.1	1.5	24.9%
Maximum bending moment (M_{max}) [kNm]	4.6	7.2	5.0	7.6	6.1	1.5	24.9%
Maximum shear stress (τ_{max}) [MPa]	0.15	0.24	0.17	0.25	0.20	0.05	24.9%
Maximum axial stress (σ_{max}) [MPa]	22.2	34.4	22.9	34.5	28.5	6.9	24.2%
Maximum mid-span displacement ($d_{l/2,max}$) [mm]	19.9	23.2	24.7	36.7	26.1	7.3	28.0%
Maximum strain in top face ($\epsilon_{top,max}$) [$\mu\epsilon$]	-660	-1481	-1345	-1422	-1227	382	31.1%
Maximum strain in bottom face ($\epsilon_{bottom,max}$) [$\mu\epsilon$]	838	1021	693	1278	958	252	26.3%
Maximum average compressive strain at web ($\bar{\epsilon}_{wC,max}$) [$\mu\epsilon$]	-	-	-326	-	-326	-	-
Maximum average tensile strain at web ($\bar{\epsilon}_{wT,max}$) [$\mu\epsilon$]	-	-	413	-	413	-	-

Nonetheless, the strain gauges installed in the truss webs (TFC-3 panel) registered significant compressive and tensile strains in those reinforcing elements, reflecting the expected truss behaviour due to shear stress transfer. In fact, during the linear elastic phase of the panels' behaviour, the truss webs significantly contributed to the overall stiffness of the TFC panels, with their average stiffness (0.50 kN/mm) being higher than that of the PET panels (0.43 kN/mm), but lower than that of the BAL panels (0.57 kN/mm). Compared with the simple cored PUR panels, the TFC typology exhibited a 47% higher flexural stiffness.

5.4.2.5. VDC

Figure 5.16 compares the load vs. displacement and load vs. strain curves obtained for the different VDC panels, and Figure 5.17 shows the observed failure modes. Table 5.8 presents a summary of the results obtained. All panels presented very consistent behaviour, particularly in terms of load vs. displacement, albeit the VDC-1 panel stood out due to its different failure mode.

The VDC-1 panel presented linear elastic behaviour up to failure, which occurred in a brittle manner and was due to the shear failure of the core for a maximum total load of 48.4 kN. Failure occurred simultaneously at two sections of the panel: (i) at the right-side outer

loading point (within the 120 kg/m³ PUR foam), and ii) at the right-side interface between the 80 kg/m³ foam and the 120 kg/m³ foam (within the 80 kg/m³ foam). At the first failure point the shear force is maximum and its value at failure was 24.2 kN, corresponding to a shear stress of 0.81 MPa within the core. The shear strength of the 120 kg/m³ PUR foam, according to the material characterisation tests, is 0.59 ± 0.02 MPa, and consequently failure at this section for such a load level was expectable. The shear force at the second failure section was 12.1 kN, corresponding to a shear stress of 0.40 MPa, comparing to a shear strength of 0.39 ± 0.08 MPa of the 80 kg/m³ foam; again, this means that failure at this section, for such a load level, was also expectable.

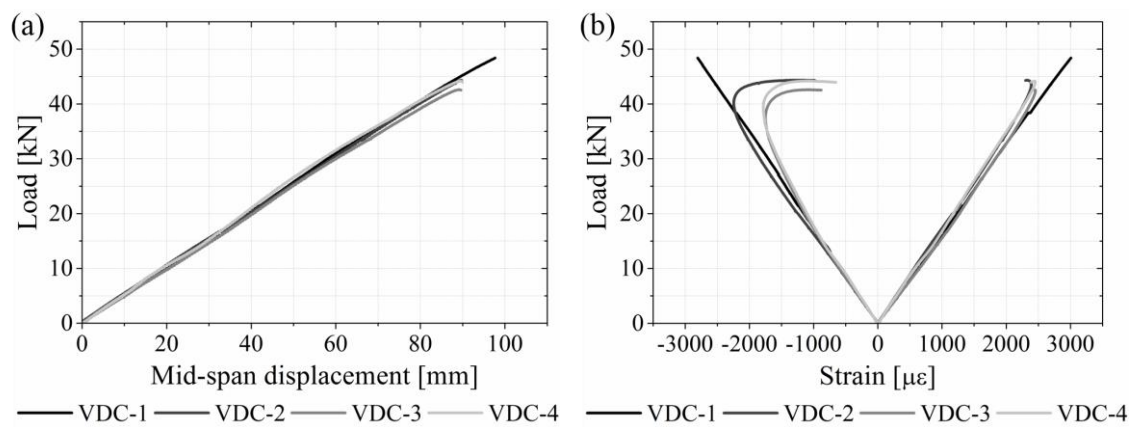


Figure 5.16. Results obtained in the failure tests of the VDC panels: (a) load vs. displacement curves, and (b) load vs. strain curves.

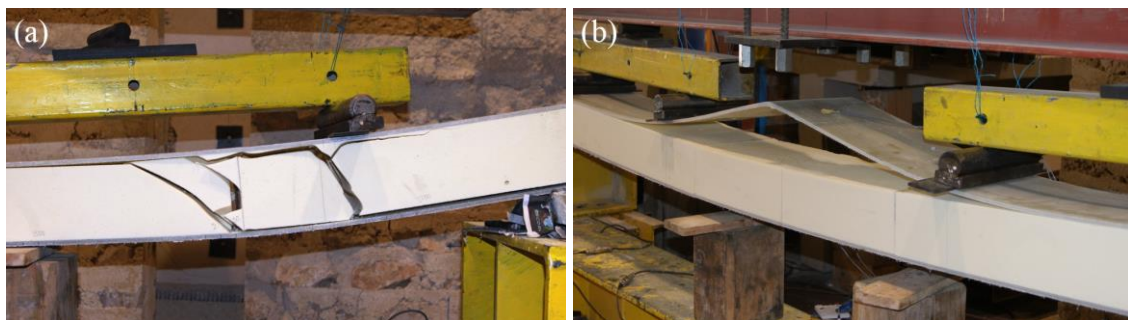


Figure 5.17. Failure of the VDC panels: (a) shear failure of the core in VDC-1, and (b) buckling failure of compressed face in VDC-2.

The remaining VDC panels presented significantly different failure modes, occurring for loads approximately 10% lower than the VDC-1 failure load. In these panels, the compressed (top) face sheets buckled and debonded from the foam cores, in some cases inducing damage within the cores. The onset of instability in these face sheets is clearly observable in the

Chapter 5 Flexural behaviour of full-scale panels

nonlinear segments of the load vs. axial strain curves of Figure 5.16-b, particularly in the top sheet.

Table 5.8. Summary of results obtained in the flexural failure tests of the VDC panels.

	VDC-1	VDC-2	VDC-3	VDC-4	Average	Standard deviation	Coefficient of variation	
Failure load (F_u)								
	[kN]	48.4	44.3	42.6	44.2	43.7	1.0	2.2%
Stiffness (K)								
	[kN/mm]	0.52	0.49	0.47	0.49	0.49	0.02	4.2%
Maximum shear force (V_{max})								
	[kN]	24.2	22.2	21.3	22.1	22.4	1.2	5.5%
Maximum bending moment (M_{max})								
	[kNm]	19.4	17.8	17.1	17.7	18.0	1.0	5.5%
Maximum shear stress (τ_{max})								
	[MPa]	0.84	0.78	0.74	0.77	0.78	0.04	5.4%
Maximum axial stress (σ_{max})								
	[MPa]	89.6	82.1	78.8	81.8	83.0	4.6	5.5%
Maximum mid-span displacement ($d_{1/2,max}$)								
	[mm]	97.7	89.8	89.6	90.0	91.8	4.0	4.3%
Maximum strain in top face ($\epsilon_{top,max}$)								
	[$\mu\epsilon$]	-2805	-2245	-1750	-1783	-2146	494	23.0%
Maximum strain in bottom face ($\epsilon_{bottom,max}$)								
	[$\mu\epsilon$]	3008	2391	2455	2452	2577	289	11.2%

This proneness to instability of the compressed faces is considered to stem from the reduced density (nominally 40 kg/m³) of the central (mid-span) PUR foam block, which presents fairly low mechanical properties. Consequently, the face sheet stabilization that the core material is supposed to provide is significantly reduced in the mid-span section.

Considering that three of the four tested panels failed due to instability of the top face sheet, this is set as the dominant failure mode. However, for the adopted loading configuration, shear failure of the core occurs for relatively similar loads, as the results obtained for the VDC-1 panel suggest, indicating a good balance between the core material properties.

5.4.2.6. RIB

A comparison between the load vs. displacement, load vs. axial strain and load vs. distortion curves obtained for all RIB panels is shown in Figure 5.18, while Table 5.9 presents a summary of the results obtained in those tests. The three panels presented a fairly consistent flexural response, with approximately linear elastic responses up to failure. The distortions measured in the two ribs for each panel were fairly similar, indicating that the shear stress distribution was relatively well balanced between them.

Table 5.9. Summary of results obtained in the flexural failure tests of the RIB panels.

		RIB-1	RIB-2	RIB-3	Average	Standard deviation	Coefficient of variation
Failure load (F_u)	[kN]	136.8	101.7	122.9	120.5	17.7	14.7%
Stiffness (K)	[kN/mm]	1.28	1.18	1.26	1.24	0.05	4.4%
Maximum shear force (V_{max})	[kN]	68.4	50.9	61.4	60.2	8.8	14.7%
Maximum bending moment (M_{max})	[kNm]	75.3	55.9	67.6	66.3	9.7	14.7%
Maximum axial stress (σ_{max})	[MPa]	165.8	141.9	177.5	161.7	18.1	11.2%
Maximum mid-span displacement ($d_{1/2,max}$)	[mm]	113.7	101.7	105.6	107.0	6.1	5.7%
Maximum strain in top face ($\epsilon_{top,max}$)	[$\mu\epsilon$]	-5406	-3795	-4808	-4669	815	-17.4%
Maximum strain in bottom face ($\epsilon_{bottom,max}$)	[$\mu\epsilon$]	5515	4208	4943	4888	656	13.4%
Maximum distortion at rosette R1 ($\gamma_{R1,max}$)	[$\mu\epsilon$]	7541	6124	6359	6674	759	11.4%
Maximum distortion at rosette R2 ($\gamma_{R2,max}$)	[$\mu\epsilon$]	6826	5091	6596	6171	943	15.3%

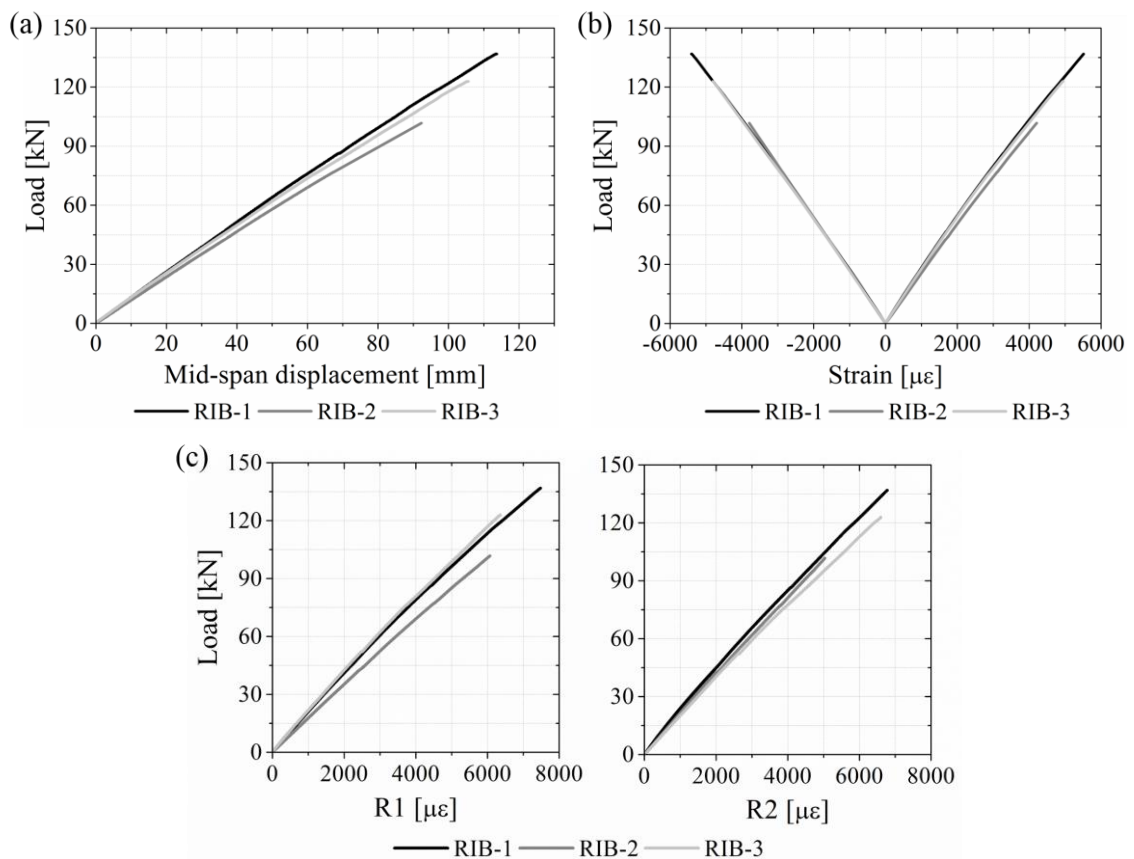


Figure 5.18. Results obtained in the failure tests of the RIB panels: (a) load vs. displacement curves, (b) load vs. strain curves, and (c) load vs. distortion curves.

Failure occurred in a brittle manner for all RIB panels, occurring due to compression of the top face sheet at the load application points for the RIB-1 and RIB-3 panels (Figure 5.19-a,b), and at a geometric imperfection located approximately 15 cm from the right-side load application point for RIB-2 panel (Figure 5.19-c,d). This geometric imperfection seems to have been caused by the misalignment of the PUR foam blocks during the vacuum infusion process. The failure loads presented a certain degree of scatter, mainly due to the results of the RIB-2 panel, which failed for a lower load due to the mentioned production defect. This defect also appears to have caused a slight reduction in the panel's initial stiffness.

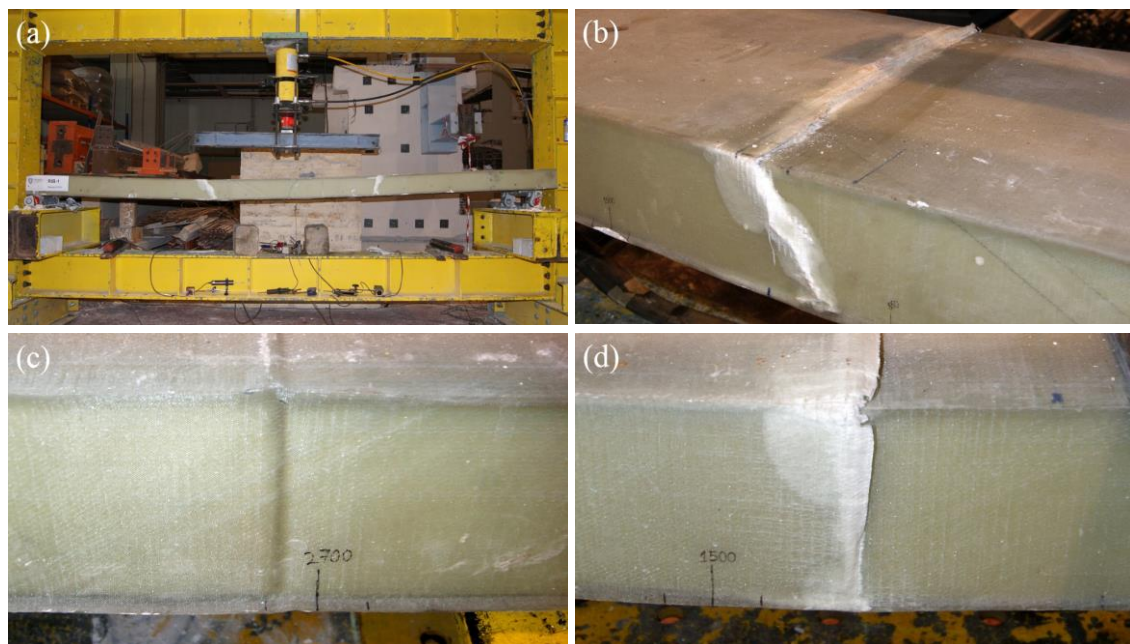


Figure 5.19. Failure of the RIB panels: (a) general view of RIB-1, (b) detail of RIB-1, (c) geometric imperfection, and (d) failure at the imperfection of RIB-2.

5.4.2.7. Performance comparison

In order to evaluate the performance of each panel typology, their respective stiffness and failure load values were compared. To perform a direct comparison between all typologies, values of stiffness and failure load per panel width were calculated. In addition, in order to identify the most weight-efficient typologies, normalized values of stiffness and failure load considering the panels' width, mass and area were also calculated. Finally, cost performance indicators based on stiffness and failure load per panel cost were calculated, to assess the cost-efficiency of each panel type. For this purpose, the production costs given in chapter 3 (section 3.5) that take into account the cost of materials incorporated in the panels were used. The VDC panel results are also presented in this comparison. However, having been

obtained using a different loading configuration, they are only presented for the sake of information completeness and should not be directly compared to the remaining values.

Figure 5.20 and Table 5.10 present a summary of the stiffness values obtained in the flexural failure tests, as well as the stiffness related performance indicators. In terms of absolute stiffness values, the RIB panels clearly outperformed the remaining typologies, as shown in Figure 5.20-a. However, analysing the results in terms of stiffness per width, as presented in Figure 5.20-b, it is possible to observe that while the RIB panels still present the highest performance, the stiffness per panel width of the TFC and BAL panels was very similar to that of the RIB panels.

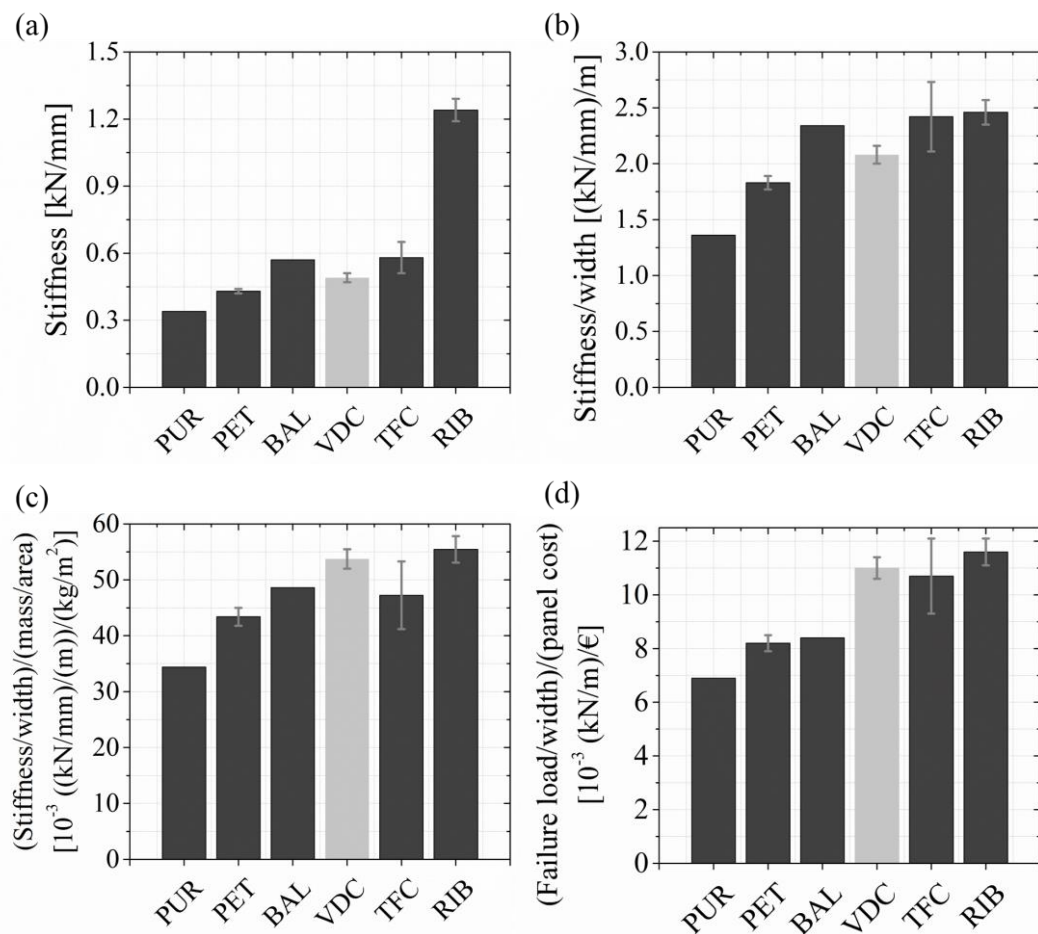


Figure 5.20. Comparison between stiffness values obtained in the failure tests: (a) stiffness, (b) stiffness per width, and (c) stiffness per width per mass per area ($\times 10^{-3}$).

Considering the mass per unit area of each panel typology, the RIB panels present the highest stiffness to weight ratio. The stiffness per width per mass per unit area of the TFC panels is significantly lower than that of the RIB panels, indicating that longitudinal GFRP ribs are a more weight effective solution to increase the flexural stiffness of sandwich panels compared

Chapter 5 Flexural behaviour of full-scale panels

to the inclusion of the GFRP truss. Similar conclusions may be drawn regarding the cost-effectiveness of the RIB typology.

Table 5.10. Summary of flexural stiffness values and stiffness related performance indicators.

Typology	Stiffness [kN/mm]		Stiffness / width [(kN/mm)/m]		(Stiffness/width) / (mass/area) [10^{-3} ((kN/mm)/m)/(kg/m ²)]		(Stiffness/width) / cost [10^{-3} ((kN/mm)/m)/€]	
	Average	Standard deviation	Average	Standard deviation	Average	Standard deviation	Average	Standard deviation
PUR	0.34	-	1.4	-	34.4	-	6.9	-
PET	0.43	0.01	1.8	0.1	43.4	1.6	8.2	0.3
BAL	0.57	-	2.3	-	48.6	-	8.4	-
TFC	0.58	0.07	2.4	0.3	47.2	6.1	10.7	1.4
RIB	1.24	0.05	2.5	0.1	55.4	2.4	11.6	0.5
VDC¹	0.49	0.02	2.1	0.1	53.7	1.7	11.0	0.4

¹values obtained for a different loading configuration;

Figure 5.21 and Table 5.11 present a summary of the failure load values obtained in the flexural failure tests, as well as failure load related performance indicators similar to those presented for stiffness. The failure loads obtained for the RIB panels were significantly higher than those obtained for any other panel typology. However, their nominal width was twice than that of the other typologies, so the comparison must be made considering the failure load per panel width.

In terms of failure load per width, the RIB panels present failure loads very similar to those of the BAL panels, which actually have a marginally better performance. However, considering the failure load per mass per area indicator, the RIB panels stand out for their weight-efficiency. The advantage of the RIB typology in relation to the remaining panel types is also clear in what concerns the solution's cost-efficiency in achieving high flexural strength.

The TFC panels present a very poor performance in terms of all failure load indicators, which as previously discussed is mainly due to the weak bond between the truss web elements and the face sheets. If these connections are improved, significant performance gains may still be potentially obtained using this panel typology. This should be pursued in further investigations.

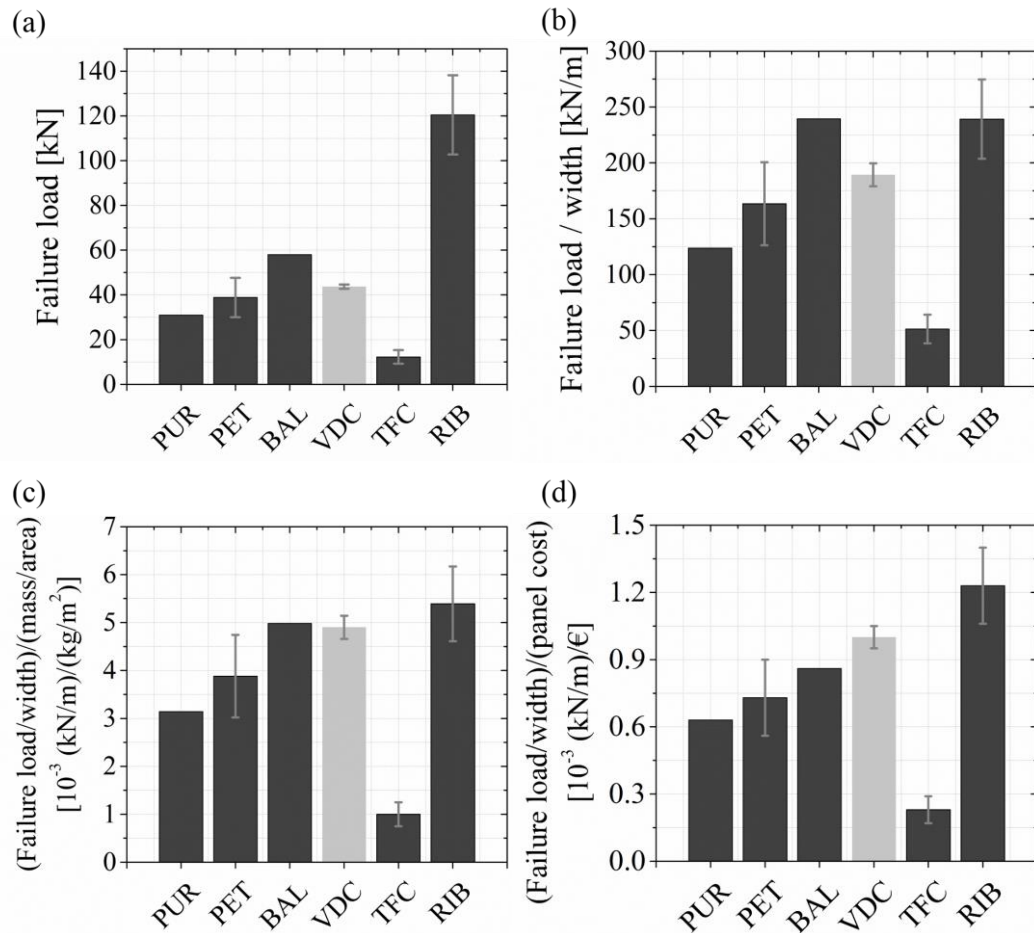


Figure 5.21. Comparison between failure load values obtained in the failure tests: (a) failure load, (b) failure load per width, and (c) failure load per mass per area.

Table 5.11. Summary of failure load values and failure load related performance indicators.

Typology	Failure load [kN]		Failure load / width [kN/m]		(Failure load/width) / (mass/area) [(kN/m)/(kg/m ²)]		(Failure load/width) / cost [(kN/m)/€]	
	Average	Standard deviation	Average	Standard deviation	Average	Standard deviation	Average	Standard deviation
PUR	30.9	-	123.8	-	3.1	-	0.63	-
PET	38.8	8.8	163.4	37.1	3.9	0.9	0.73	0.17
BAL	58.0	-	239.4	-	5.0	-	0.86	-
TFC	12.2	3.1	51.4	12.8	1.0	0.3	0.23	0.06
RIB	120.5	17.7	239.1	35.4	5.4	0.8	1.23	0.17
VDC¹	44.9	2.5	189.2	10.3	4.9	0.2	1.00	0.05

¹values obtained for a different loading configuration;

5.5. Concluding remarks

From the experimental mechanical characterisation programme carried out for the different sandwich panel typologies, several conclusions may be drawn concerning the performance of the panels for each type of test.

Regarding the effective flexural properties tests, fairly good estimates for the material properties of the GFRP faces were generally obtained. Concerning the shear properties of the core materials, the obtained results were less consistent. These tests provided a shear modulus estimate for the PET foam in very good agreement with the properties determined in the small-scale shear experiments. However, differences were found between the shear moduli values of the PUR foam and balsa wood when compared to the results obtained in the material characterisation tests (previous chapter). Such differences are most likely due to the heterogeneity of the materials and the consequent variability of their material properties. The shear modulus estimates for the GFRP ribs of the RIB panels were in good agreement with the value obtained for this property in the material characterisation tests of chapter 4.

Through dynamic testing, the natural vibration frequencies for the first flexural mode were determined for all panel types. For the RIB panels, the frequency associated with the first torsional mode was additionally obtained. The obtained natural frequency values were relatively high, and well above minimum frequency values recommended for building floors. Additionally, damping ratio values were estimated, and found to be similar to typical values for concrete and higher than those for steel structures. The obtained results indicate that the sandwich panel floors should not pose user comfort issues related to structural vibrations.

In the failure tests, different types of flexural responses and different failure modes were found for the various typologies. The simple sandwich panels with softer core materials, such as PUR foam and, to a smaller extent, the PET foam exhibited core crushing at the load application points, which conferred a non-linear response to these panels, due to the ductile nature and relatively low strength of those foams under compressive loads.

The panels with balsa wood core presented very interesting mechanical properties, exhibiting values of stiffness and failure load per width and per panel mass, among the highest obtained in the failure tests. However, due to its relatively high cost, the use of balsa wood might not be the most cost effective solution for building applications.

The sandwich panels with a variable density foam core presented good mechanical properties in terms of stiffness and failure loads, but their failure modes were typically associated with the instability of the compressed face sheet where the core material had the lowest density (and the lowest mechanical properties). As such, caution should be adopted in the use of very low-density foams, as their capability to stabilize the sandwich panel faces must be evaluated. Additionally, the variable density foam core configuration is optimised for uniform loading situations. If localised loads are applied, the failure stress of the lower density foams may be exceeded even if the stresses in the higher density foams are still below their strength.

The truss-foam core panels presented high stiffness values, and the potential to be a structurally effective core reinforcement solution. However, their execution must guarantee fibre continuity between the truss webs and the face sheets. Nonetheless, the added weight that the GFRP truss confers to the sandwich panel, in addition to the added workmanship and labour hours necessary to adequately produce this type of panel, may hinder the cost-effectiveness of this solution.

The ribbed panels presented the best mechanical performance in terms of stiffness and failure loads, even considering these properties per panel width and per panel mass. Furthermore, this panel typology was also the most cost-efficient in achieving high load capacity and stiffness figures. Their production is fairly simple and does not involve a significant amount of additional work when compared to the simple sandwich panel typology. The existence of GFRP ribs may also represent a benefit when designing panel-to-panel connection systems, given that such systems may intrinsically incorporate a longitudinal GFRP element along the edges of the panels, as will be discussed in the next chapter.

5.6. References

- [1] EN 13706-2:2002, *Reinforced plastics composites - Specifications for pultruded profiles - Methods of test and general requirements*. Annex G, European Standard, 2002.
- [2] ASTM D7250/D7250M – 06 (2012). *Standard Practice for Determining Sandwich Beam Flexural and Shear Stiffness*. ASTM International, West Conshohocken, Pennsylvania, United States.

- [3] Branco, F., Mendes, P., *Ponte Vasco da Gama - Comportamento dos Tirantes sob a Acção das Rajadas de Vento* (in portuguese). ICIST Technical Report EP 28/96, 1996.
- [4] Beards, C.F., *Structural Vibration: Analysis and Damping*. Edward Arnold Publishers Ltd., London, UK, 1996.
- [5] European Committee for Standardization (CEN) (1992). *Eurocode 3: Design of steel structures – Part 1-1: General rules and rules for buildings (DD ENV 1993-1-1:1992)*. Technical Committee CEN/TC 250, Brussels.
- [6] Sá, M.F. (2015). *Análise de painéis de laje multicelulares pultrudidos de GFRP – aplicação em pontes pedonais* (in portuguese). PhD thesis, Instituto Superior Técnico, Universidade de Lisboa, 640p.
- [7] Gonilha, J.A. (2014). *GFRP-concrete hybrid structural systems: application to the development of a footbridge prototype*. PhD thesis, Instituto Superior Técnico, Universidade de Lisboa, 342p.

Part III

Connection systems

Preamble

Composite sandwich floor panels are pre-fabricated elements that must be interconnected on site, thus producing a building floor assembly. In turn, this assembly needs to be adequately connected to its supporting elements, which are often stone rubble masonry walls in the context of building rehabilitation.

Part III of this thesis aims to present the development of appropriate systems for the connections between adjacent sandwich panels, and between the panels and the building's structural walls.

The work presented in this chapter resulted in the following publications:

Garrido, M., Correia, J.R., Keller, T., Branco, F.A. (2015). "Adhesively bonded connections between composite sandwich floor panels for building rehabilitation". *Composite Structures*, Vol. 134, pp. 255-268.

Garrido, M., Correia, J.R., Keller, T., Branco, F.A. (2016). "Connection systems between composite sandwich floor panels and load-bearing walls for building rehabilitation". *Engineering Structures*, Vol. 106, pp. 209-221.

Chapter 6

Connections between sandwich panels

6.1. Introduction

Floor systems made of composite sandwich panels may be quickly assembled on site, potentially allowing for important time savings during construction [1-3]. However, sandwich panels must be adequately interconnected upon assembly, with the purpose of constituting a monolithic floor and providing diaphragm behaviour. Consequently, appropriate connection systems between composite sandwich panels need to be considered.

Different solutions for the connections between adjacent sandwich panels have been considered in the construction industry. A significant part of the current sandwich panel connection technology has been developed for non-structural or secondary structural sandwich panels (*e.g.*, [4]). Regarding connection systems for primary structural application in sandwich panels, the existing industrial experience is limited and the influence of such joints on the global behaviour of the sandwich slabs must be assessed, namely with respect to its effects on stiffness, stress distributions, and failure mechanisms.

6.2. Current practice

Several connection systems make use of inserts and profiles that are fitted and in some cases adhesively bonded to the adjoining panels [5,6]. Connections between structural sandwich panels with steel faces using bolted or welded steel plates and profiles have also been proposed for the maritime industry [7,8]. However, using additional elements for the joints increases their cost and complexity, affecting the economic competitiveness of the floor system.

Chapter 6 Connections between sandwich panels

Adhesively bonded male-female connections have been proposed and used for joining pultruded bridge deck panels [9-12]. A noteworthy example is the *DuraSpan* pultruded deck, produced by *Martin-Marietta Composites* (Figure 6.1-a). However, this type of connection requires the adjoining panels to be horizontally slid into position with the help of hydraulic jacks, rendering this solution unpractical for building floors, especially in the rehabilitation context where spatial limitations are often encountered.

Other pultruded bridge deck panels, such as the *FBD 600 (ASSET)* manufactured by *Fiberline Composites* (Figure 6.1-b), use a Z-shaped adhesive joint for the panel-to-panel connections [13,14]. This system has the advantage of allowing the adjoining panels to be lowered into position and it also does not require the use of any jacking system, which is more practical in confined spaces. An interlocking, adhesive free, connection has also been proposed for the *ASSET* decking system (Figure 6.1-c) [15]. However, the interlock joint (produced by vacuum infusion) introduces a certain (significant) joint flexibility and in addition it is not designed to cope with horizontal tensile loads, making this connection inappropriate for building floors.

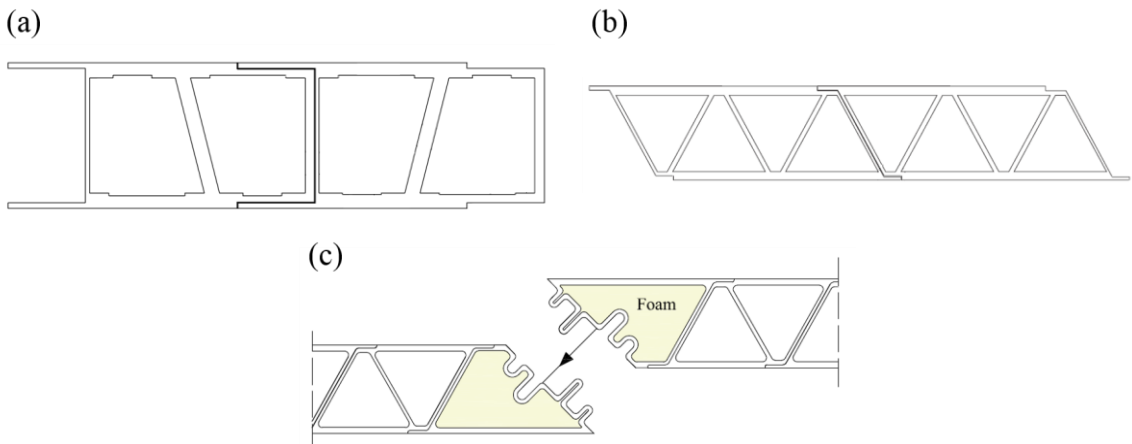


Figure 6.1. Connections in pultruded bridge decks: (a) *DuraSpan* [10], (b) *ASSET* [13], and (c) interlocking connection for *ASSET* system [15].

A Z-shaped adhesive joint has also been used in the connection of adjacent sandwich deck panels in the *Avançon Bridge*, in *Bex*, *Switzerland* [3]. The sandwich panels comprised *GFRP* faces and a *laminated veneer lumber (LVL) balsa wood* core. The Z-joint geometry at the panel's edges was built-in to the detailing of the faces and core, thus eliminating the need for further connection elements other than the structural adhesive itself (a filled two-component epoxy). The joint's performance was assessed through flexural fatigue and failure tests, which validated its viability for use in the final structure.

6.3. Investigated connection system

During the development of the sandwich panel-to-panel connection system presented in this chapter, an adhesively bonded Z-joint configuration was deemed as the most suitable for building floor applications, due to the following reasons: (i) as explained in the literature review described above, it guarantees an effective stress transfer and compatibility of deformations between the adjoining panels, (ii) it allows for an easy panel installation in confined spaces, (iii) it does not require additional connection components other than a structural adhesive, and (iv) it is easy to integrate into the sandwich panel production process.

Regarding the last point, the sandwich panels used in the current investigation were produced by vacuum infusion, with the joint geometry already included in their cross-section. The panels also include longitudinal glass-fibre reinforced polymer (GFRP) ribs/webs, integrated in the connection system, which have been shown to substantially improve the flexural performance of composite sandwich panels [16,17]. The adopted Z-joint configuration is presented in Figure 3.1-a, while Figure 3.1-b and -c schematically present the cross-section of inner and end panels, and Figure 3.1-d shows the adopted cross-sectional dimensions.

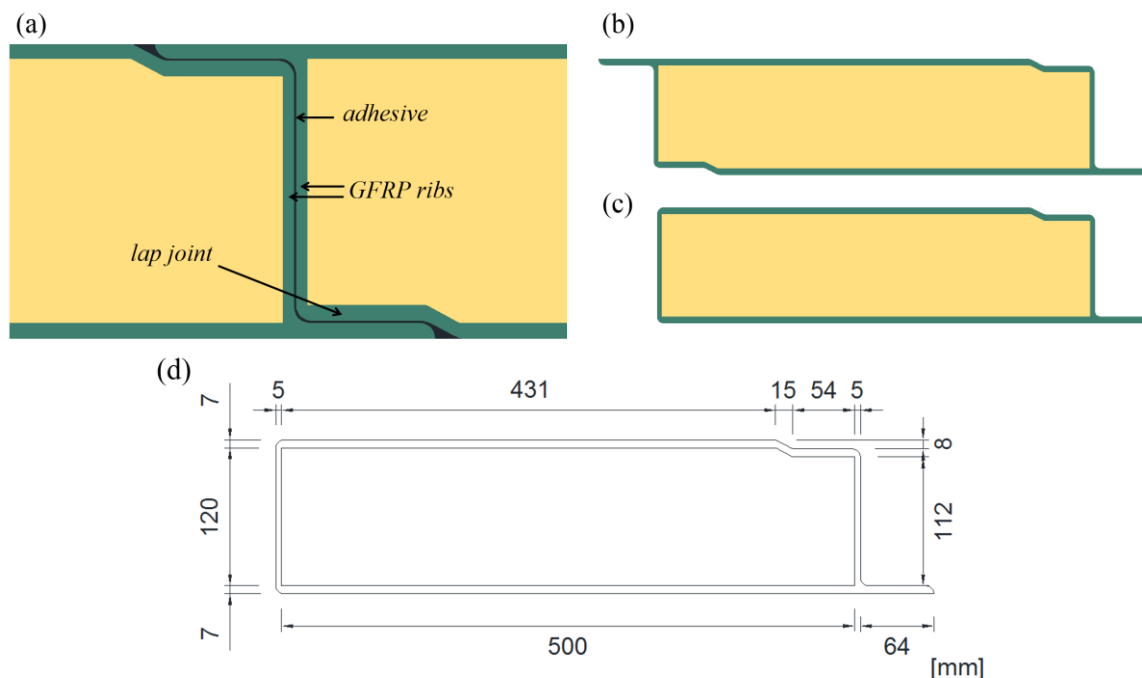


Figure 6.2. Proposed panel-to-panel connection system: (a) joint components, (b) interior panel cross-section, (c) end panel cross-section, and (d) cross-sectional dimensions.

The geometry of the connection system is anti-symmetrical so that the panels may be simply lowered into position, *i.e.*, no horizontal movement is needed. At the bottom surface, a structural adhesive may be easily applied before lowering the next panel into place, allowing for a quick installation of large floor areas. At the floor's edges, the end panels are able to lie flat against the building's walls.

6.4. Experimental investigation

6.4.1. Programme overview and materials

End-type panels (*cf.* Figure 3.1-c) were produced and adhesively bonded to each other (in pairs) to assess the behaviour of the connection and of the resulting panel assembly. The specimens comprised two longitudinal GFRP ribs at the edges and a joint in the centre. The adhesive used for the connections was a filled two-component epoxy-based adhesive, *Sikadur-31 EF* [18], applied with a thickness ranging between 2 mm and 4 mm, with such variation being due to geometric irregularities between the adherent surfaces stemming from the production process.

The behaviour of the assembly was experimentally assessed along the transverse and longitudinal directions, the latter corresponding to the floor's main span. The tests carried out along the transverse direction aimed at assessing the joint's behaviour at a local level for two different load configurations with different moment-to-shear ratios. The tests carried out along the longitudinal direction had the objective of characterising the global flexural behaviour of the full assembly and assessing the joint's performance and influence on that behaviour, namely (i) analysing its ability to effectively distribute stresses and match strains between adjacent panels under eccentric loading, (ii) evaluating its contribution to the flexural stiffness of the floors, and (iii) assessing the behaviour up to failure of the connected panels. The following sections (6.4.1.1 and 6.4.1.2) describe the experimental setups and details for the transverse and longitudinal direction tests, respectively.

6.4.1.1. Transverse direction

Tests in the transverse direction were carried out using specimens with nominal length of 1023 mm and width of 250 mm. Two types of specimens were manufactured, using two different core materials (described in chapter 3 and mechanically characterised in chapter 4,

section 4.3.1): (i) PUR foam (87.4 kg/m^3), and (ii) balsa wood (101.4 kg/m^3). As mentioned, the transverse direction behaviour was experimentally investigated for two different loading configurations, illustrated in Figure 6.3, namely: (i) four-point bending (simply supported), and (ii) cantilever. Four specimens were tested in each configuration, three of them made of PUR foam core (B-PUR and C-PUR specimens for the bending and cantilever configurations, respectively) and one made of balsa wood core (B-BAL and C-BAL specimens).

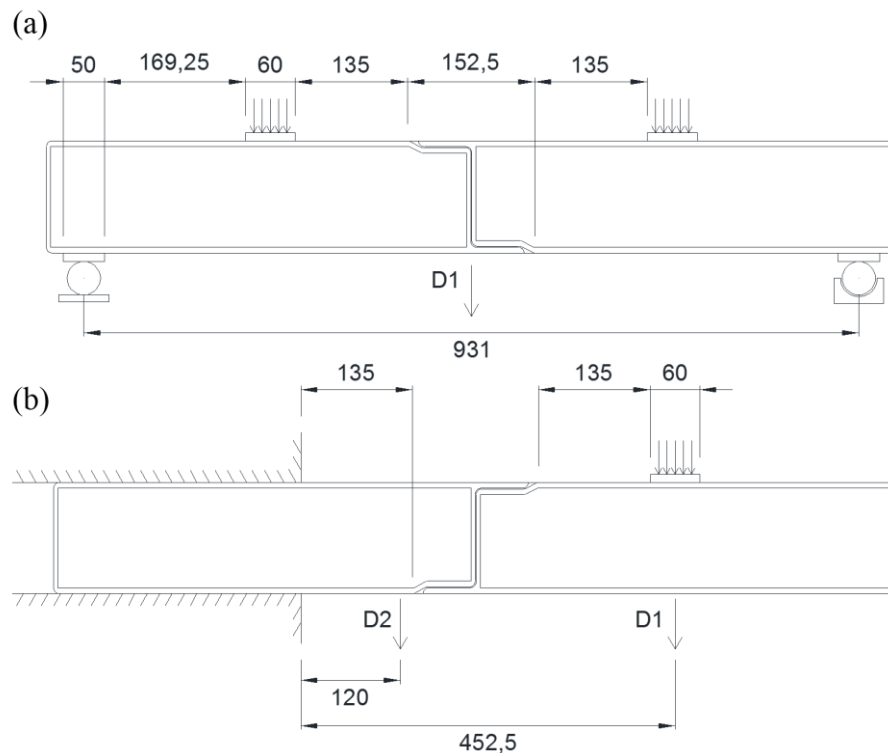


Figure 6.3. Transverse direction test setups: (a) four-point bending, and (b) cantilever.

The vertical deflections were measured at mid-span (position “D1”, Figure 6.3-a) in the four-point bending tests, and at two sections (positions “D1” and “D2”, Figure 6.3-b) in the cantilever tests. Loading was applied along the full width of the specimens and at a minimum distance from the joints of 135 mm (approximately the thickness of the sandwich panel) using a hydraulic jack.

For the cantilever tests, the specimens were anchored between two thick steel plates, by applying a compression pre-load in the through thickness direction of the panels before loading the cantilever. This pre-load was maintained during the test using two pairs of *Dywidag* steel bars and two hydraulic jacks placed at the front edge of the anchorage (Figure 6.4).



Figure 6.4. Support anchoring system for the cantilever tests.

6.4.1.2. Longitudinal direction

The longitudinal direction tests were carried out on a jointed sandwich panel with PUR foam core (87.4 kg/m^3), a nominal length of 3560 mm and width of 1023 mm, and comprised (i) alternate loading, (ii) effective flexural properties, and (iii) four-point bending failure. Simply supported conditions were adopted for all the tests along the longitudinal direction.

The alternate loading tests consisted of applying static loads at different positions along the panel’s span and width, and measuring the resulting displacements and strains. Four different loading areas were defined (L1 to L4), as illustrated in Figure 6.5. The loading was performed using concrete blocks of known weight according to the seven load cases indicated in Table 6.1.

Table 6.1. Alternate loading test programme (*cf.* Figure 6.5).

Load case	Number of loads	Applied weight [kN]
L1	1	4.68
L2		
L3		
L4		
L1+L3	2	4.68+4.68
L2+L4		
L1+L2+L3+L4	4	4.68+4.49+4.53+4.68

Figure 6.5 also illustrates the instrumentation plan used in the alternate loading tests. Displacement transducers were used to measure the vertical displacements at thirds of the span ($d-1/3$ and $d-2/3$) and at mid-span ($d-1/2$) on both sides of the joint (L and R). The

strains along the mid-span cross-section (SG1 to SG6 on the top face sheet, and SG7 to SG12 on the bottom) were measured using electrical strain gauges. Additionally, two 45° strain gauge rosettes (R1 and R2), each comprising three gauges, were installed on the GFRP ribs, at the mid-height of a cross-section distanced 300 mm from one of the panel’s supports. Figure 6.6 illustrates two examples of the alternate loading test configurations, namely the L1 and the fully loaded (L1+L2+L3+L4) cases.

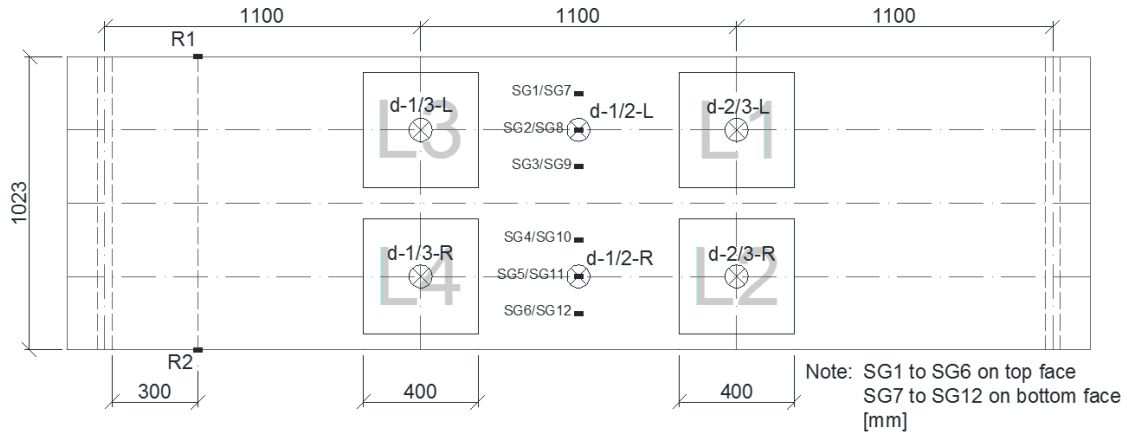


Figure 6.5. Instrumentation and load application areas for alternate loading of jointed panel.

The effective flexural properties tests were aimed at estimating the effective bending and shear stiffness of the jointed panel, and were carried out according to the graphical methodology of EN 13706-2 standard [19], also used in the flexural tests conducted in the scope of chapter 5. For this purpose, the jointed panel was loaded in three-point bending (load applied along the full width of the panel) for three different span lengths: (i) $S_1 = 0.85$ m, (ii) $S_2 = 2.10$ m, and (iii) $S_3 = 3.30$ m, until a mid-span deflection of $S_i/200$ was achieved. Load and mid-span displacement data were registered and used to estimate the effective stiffness values based on Timoshenko beam theory, according to which the following relation may be drawn between a beam’s flexural stiffness (K), span (S), bending stiffness (D) and shear stiffness (U) [19]:

$$\frac{1}{KS} = \frac{S^2}{48D} + \frac{1}{4U} \quad (6.1)$$

In addition to the jointed sandwich panel, three simple panels with longitudinal edge GFRP ribs were tested using the same setup (as described in chapter 5), along five test spans (0.85 m, 1.50 m, 2.10 m, 2.70 m and 3.30 m), to assess the joint’s contribution to the flexural

Chapter 6 Connections between sandwich panels

stiffness of the sandwich floors. The simple ribbed panels used for this purpose had a nominal width of 510 mm, corresponding to half of the jointed panel’s width, and were manufactured with the same vacuum infusion process and using identical materials.

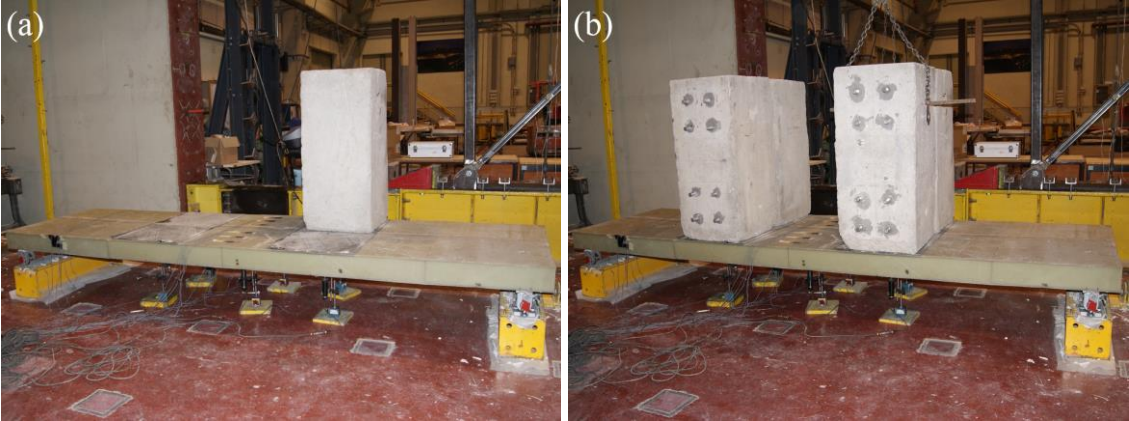


Figure 6.6. Alternate loading cases: (a) L1, and (b) L1+L2+L3+L4.

A final failure test was carried out in the jointed sandwich panel using a four-point bending configuration and a span of 3.30 m. The panel was instrumented as shown in Figure 6.7 and monotonically loaded (along the full width) up to failure at an average speed of 0.27 kN/s. Vertical deflections were measured with displacement transducers at the load application points and at three different positions across the width of the mid-span section. The strain gauge arrangement was identical to that used in the alternate loading tests.

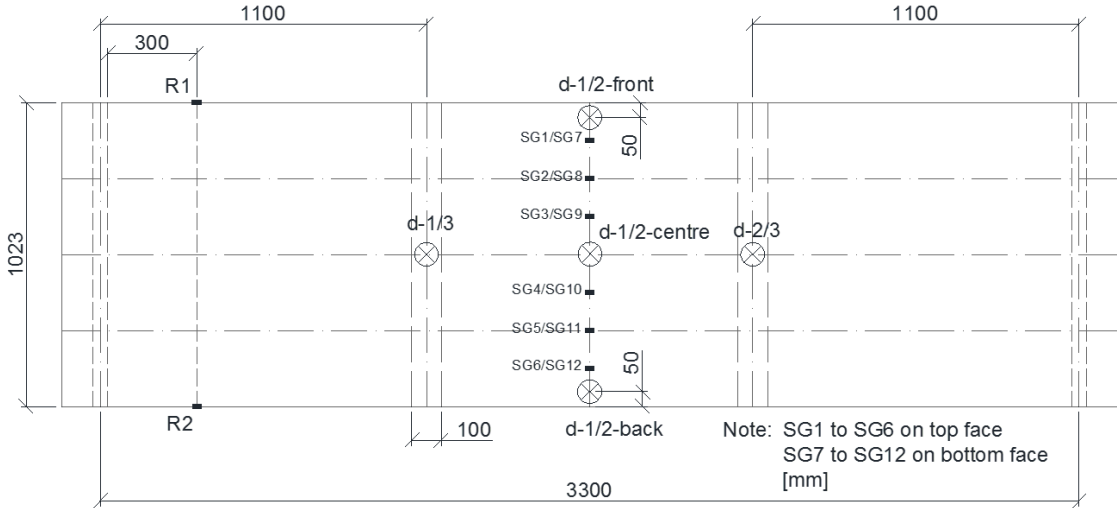


Figure 6.7. Test setup and instrumentation for the flexural failure test of the jointed panel.

Similarly to what was done for the effective flexural properties estimation, three simple sandwich panels with longitudinal edge ribs were also tested up to failure using the same test procedure and setup described for the jointed panel.

6.4.2. Transverse direction results

The load vs. displacement curves obtained in the transverse direction tests are presented in Figure 6.8, while the failure modes observed are illustrated in Figure 6.9. Regarding the four-point bending tests (Figure 6.8-a), the specimen with balsa wood core presented approximately linear-elastic behaviour up to failure (stiffness of 14.1 kN/mm), which occurred at the joint (Figure 6.9-a) in a brittle manner for a load of 49.8 kN. The PUR foamed specimens failed at the core due to excessive shear stress (Figure 6.9-b). The B-PUR-1 and B-PUR3 specimens exhibited core crushing in the zones between the supports and the load application points prior to the shear failure of the PUR foam, which occurred for loads of 43.1 kN and 40.8 kN, respectively. These two specimens exhibited markedly nonlinear load-displacement behaviour for deflections above ~10 mm. The B-PUR-2 specimen failed prematurely in a brittle manner for a load of 26.3 kN; this result was considered anomalous and may have stemmed from local defects (albeit not visible on the specimen surface) negatively affecting the strength of the PUR foam. All three B-PUR specimens presented similar initial linear-elastic behaviour characterised by an average stiffness of 2.6 ± 0.3 kN/mm.

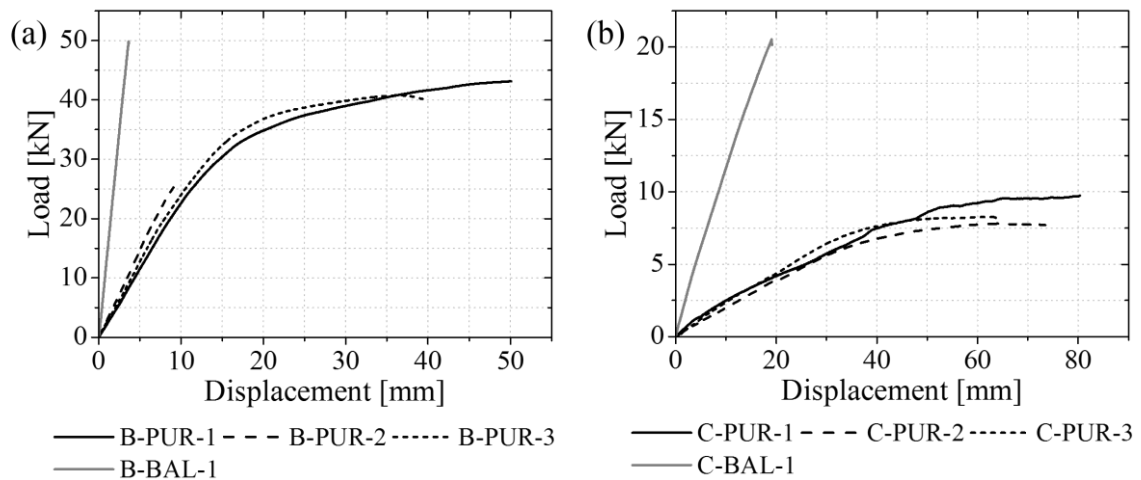


Figure 6.8. Experimental load vs. displacement curves for the transverse direction: (a) four-point bending, and (b) cantilever.

Concerning the cantilever tests (Figure 6.8-b), the behaviour observed was qualitatively similar to that obtained in the four-point bending tests. The specimen with balsa wood core presented linear-elastic behaviour (stiffness of 1.1 kN/mm) up to failure, which occurred in the joint area (Figure 6.9-c) for a load of 20.5 kN. The specimens with PUR foam core presented initial linear-elastic behaviour (stiffness of 0.20 ± 0.01 kN/mm) until a deflection of approximately 30 mm was reached, after which nonlinear behaviour was observed, associated

with the crushing of the PUR foam at the lower edge of the support (Figure 6.9-d). The tests were interrupted when a yield plateau was reached (due to the crushing of the foam) for an average maximum load of 8.6 ± 1.0 kN.

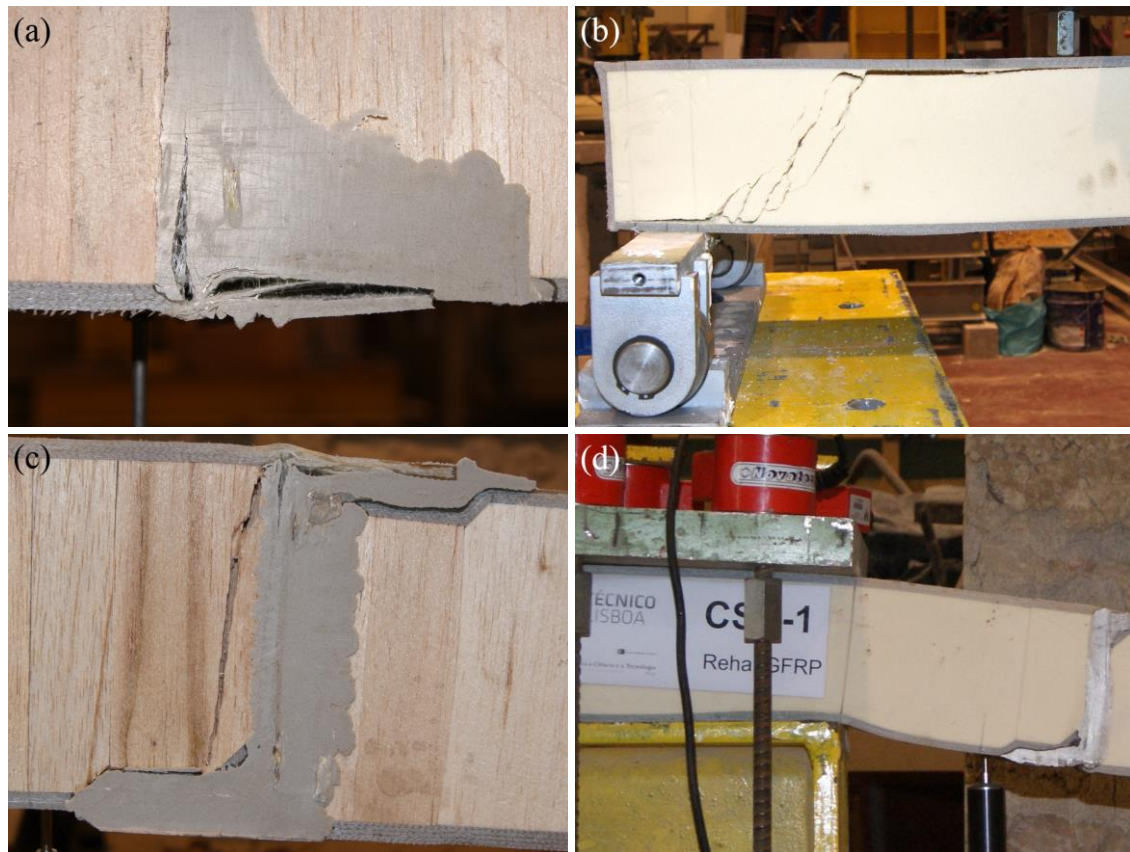


Figure 6.9. Failure modes in the transverse direction: specimens (a) B-BAL-1, (b) B-PUR-1, (c) C-BAL-1, and (d) C-PUR-1.

Regarding the failures observed in the joints for the balsa wood cored specimens, both occurred (or were initiated) in the GFRP elements at the tensile region (bottom side of the specimen in four-point bending, top side in the cantilever), namely at the angle between the inner ribs and the face sheet extensions of the lap joint (*cf.* Figure 6.9-a,c). Besides naturally being a stress concentration zone due to the variations in the geometry of the GFRP elements, at this area the laminate exhibited a kink (defect from the vacuum infusion process), which very likely increased such stress concentrations. These caused the delamination of the GFRP, which was the main failure mode found in the transverse direction tests. In the cantilever configuration, cracking in the balsa wood core was also observed (Figure 6.9-c), however this damage took place subsequently to the failure of the GFRP elements. Failure directly in the adhesive layer between the panels was never observed.

6.4.3. Longitudinal direction results

6.4.3.1. Alternate loading

Figure 6.10 shows the mid-span strain profiles in the top and bottom face sheets for the various load cases. It is possible to observe that the mid-span section's strain profile is almost identical for loads applied at one- and two-thirds of the span, both considering loading at the left side (L1 and L3) and at the right side (L2 and L4). Furthermore, as expected, strain distributions for configurations L1 and L3 are symmetrical to those obtained for configurations L2 and L4. Additionally, strain reductions are observed (also as expected) as the position in the cross-section departs from the load application area, independently of the load case considered, following a development that depends on the jointed panel's torsional stiffness.

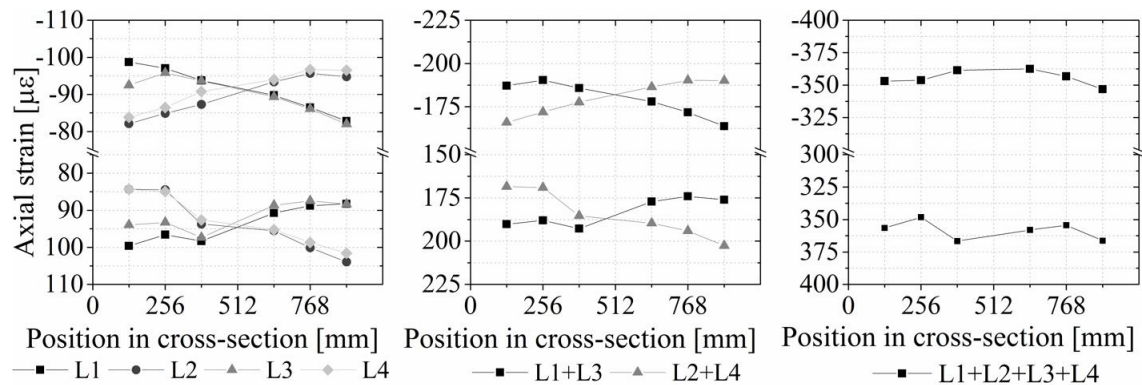


Figure 6.10. Strain profiles at the mid-span section for the various alternate load cases of the jointed panel.

Considering the L1+L3 (full loading at the left side) and L2+L4 (full loading at the right side) load cases, once more the results are consistent with an effective connection, as the variation of axial strains across the panel width is relatively smooth, not exhibiting any signs of local abrupt variations due to the panel-to-panel connection. For the L1+L2+L3+L4 load case (full loading), as expected, relatively uniform axial strain profiles were obtained and the values are roughly the sum of those corresponding to the individual load cases, thus agreeing with the superposition of effects principle.

In general, the measured responses in terms of deflections and strains were consistent and showed the effectiveness of the panel-to-panel connection in terms of transverse load transfer capacity, as well as in the mobilization of both individual panels for the torsional response of the resulting jointed panel.

6.4.3.2. Effective flexural properties

The S^2 vs. $1/KS$ plots obtained for the sandwich panel with the connection system (jointed panel) and for the simple panels with longitudinal ribs (ribbed panels) are shown in Figure 6.11. For the ribbed panels, the points plotted in the figure correspond to the average values from the three tested panels, which provided consistent results (coefficients of variation under 4% for each test span).

The bending stiffness obtained for the panel with the connection system was 1940 kNm², which compares with an average value of 956 kNm² for the ribbed panels; the two values differ by a factor of 2.03. Since the total width of the jointed panel is twice that of the ribbed panels (and, consequently, so is the width of the GFRP faces), it is possible to conclude that the joint’s influence on the panel’s bending stiffness is negligible.

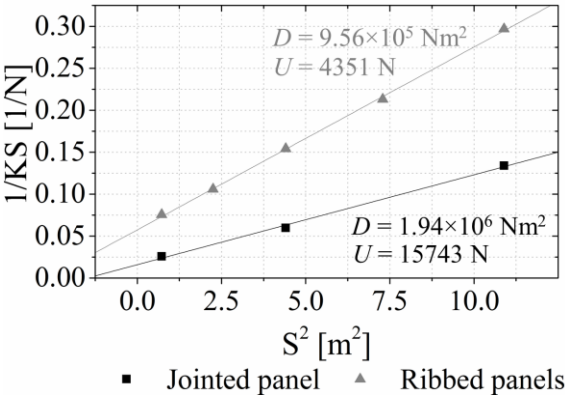


Figure 6.11. Graphical determination of effective flexural properties of jointed and ribbed panels.

Regarding shear stiffness, values of 15743 N and 4351 N were obtained for the jointed and ribbed panels, respectively; in this case, the two values differ by a factor of 3.62. In this regard, it should be noted that while the ribbed panels comprise two outer ribs at the panel’s edges (the main elements providing shear stiffness to the panel), the jointed panel has the same two outer edge ribs, two additional inner ribs, the local doubling of the face sheet thickness where the faces overlap, and the epoxy adhesive that fulfils the connection. This result therefore shows that the connection system as a whole significantly contributes to the shear stiffness of the sandwich panel, and that such contribution is higher than the one resulting from the higher (double) number of ribs in the jointed panel compared to the ribbed panels.

6.4.3.3. Failure

The load vs. mid-span displacement curves obtained in the failure tests of the jointed and ribbed panels are shown in Figure 6.12-a. The results shown correspond to the deflections measured at the centre of the panels, albeit the deflections measured at the edges followed similar developments (*i.e.*, the panels did not show any rotation about the longitudinal axis, in spite of the relatively high width of the jointed panel and its antisymmetric connection system). Furthermore, similar developments were also found for the displacements measured at the load application points, attesting that the load application was (longitudinally) symmetrical throughout the test.

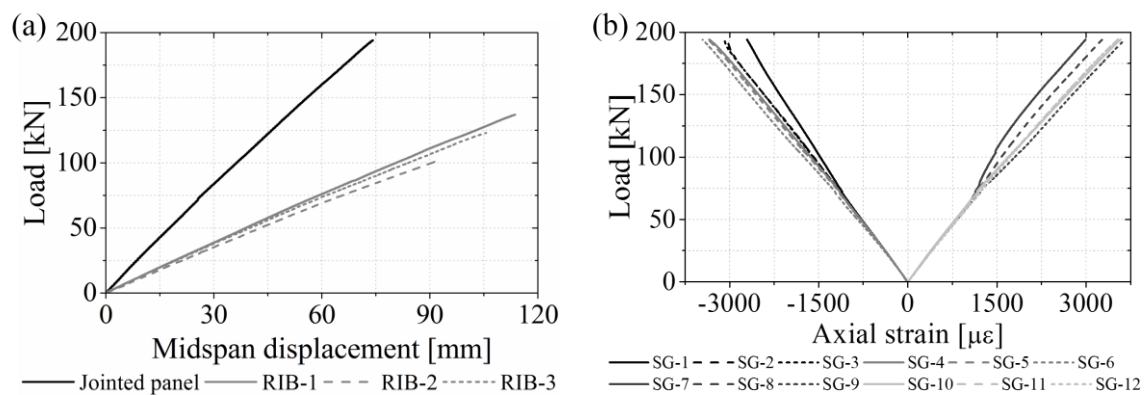


Figure 6.12. Experimental results of four-point bending failure tests: (a) load vs. mid-span displacement curves for jointed and ribbed panels, and (b) axial strains at mid-span (strain gauges *cf.* Figure 6.7) in the jointed panel.

The observed flexural load vs. deflection responses of the jointed and ribbed panels were approximately linear elastic up to failure. The stiffness of the jointed panel was 2.68 kN/mm, whereas that of the ribbed panels was 1.24 ± 0.05 kN/mm. The normalized stiffness values with respect to the width were 2.62 (kN/mm)/m for the jointed panel and 2.46 ± 0.11 (kN/mm)/m for the ribbed panels. The higher stiffness per width obtained for the panel with the longitudinal joint relative to the ribbed panels is presumably due to its higher shear stiffness, conferred by the connection system, as previously discussed.

Failure of the jointed panel occurred in a brittle manner for a load of 194.1 kN and a mid-span deflection of 74.2 mm in a section located between the loading points, and seems to have been triggered by a geometrical imperfection. This imperfection, apparently caused by the misalignment of two core material blocks during production, first showed signs of damage for a load of approximately 75 kN, as shown in Figure 6.13-a. The damage at that

location then progressed during the test, with the panel ultimately failing in compression at the top face sheet (Figure 6.13-b).

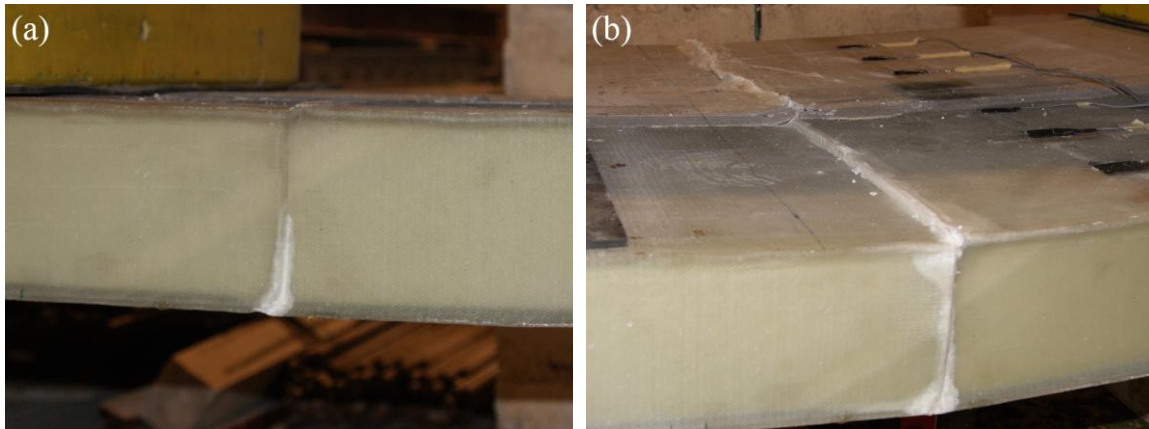


Figure 6.13. Failure of the jointed panel in four-point bending: (a) damage initiation at imperfection (load of 75 kN), and (b) final failure.

The average failure load for the ribbed panels was 120.5 ± 17.7 kN. It is interesting to note that one of the ribbed panels (RIB-2) failed for a load of 101.7 kN due to a geometrical imperfection similar to that of the jointed panel, corresponding to approximately half of the failure load obtained in that panel (*cf.* Figure 6.14-a). The remaining two ribbed panels failed for higher load values, with the brittle failure occurring by compression of the top face sheet at the load application points (*cf.* Figure 6.14-b,c).



Figure 6.14. Failure of the ribbed panels in four-point bending: (a) failure at geometrical imperfection, (b) general view of failure at the loading points, and (c) detail of top face sheet and rib after failure at loading point.

The effects of the damage initiation at the imperfection for a load of 75 kN are visible in Figure 6.12-a, namely the slight kink and slope variation in the load vs. deflection curve, as well as in the divergent axial strain measurements at mid-span obtained for higher loads, plotted in Figure 6.12-b. This effect was particularly noticeable in the strains measured at SG-7, which was located in the bottom face sheet closest to the imperfection's position.

6.5. Numerical simulation

6.5.1. Objectives

Nonlinear finite element (FE) models were developed to simulate the behaviour of the connections in the transverse and longitudinal directions using the commercial package ABAQUS/CAE (*Dassault Systèmes*).

The models for the transverse direction were developed to assess the local stress distributions within the joints when tested in the four-point bending and cantilever configurations, focusing especially on the adhesive layer and the GFRP elements that comprise the connection system. Conversely, the models for the longitudinal direction mainly aimed at investigating the stress distributions in the various panel components (core, outer and inner ribs, adhesive and faces) for different types of loading. The influence of the core material properties on the overall flexural behaviour of the panels and on the shear stress distributions among the panel components was also assessed, by considering either the balsa wood or the PUR foam as the core material in the longitudinal direction FE models (in the experiments only the PUR foam was tested).

6.5.2. Simulation of transverse direction behaviour

6.5.2.1. Models description

Two-dimensional (2D) FE models were developed for the simulation of the transverse direction behaviour. Four-node plane stress elements (*CPS4R*) were used to model all the GFRP parts of the specimen assembly, using an approximate global size of 1 mm for the elements dimensions (*i.e.*, seven elements along the face sheet thickness and five for the ribs). For the adhesive layer, three-node plane stress elements (*CPS3*) were used with an approximate global size of 1 mm (corresponding to approximately five elements along the 3 mm thick adhesive layer, due to the triangular shape of the elements). Finally, for the core, six-node plane stress elements (*CPS6M*) were used with an approximate size of 5 mm. The adopted meshes were selected based on sensitivity checks regarding the influence of the mesh refinement on the results obtained.

The contacts between all adherent surfaces (face-core interfaces, adhesive bonds) were modelled using the “cohesive behaviour” option for the interaction properties in ABAQUS/CAE. To simulate the supports and the load application in the four-point bending

configuration, auxiliary parts were modelled using typical steel material properties and equivalent geometry to that used in the experiments. Both translational degrees of freedom (DOF) were fixed for one of the supports, while for the other horizontal translations were allowed, with rotations being free in both, simulating a simply supported boundary condition. For the cantilever configuration, boundary conditions were defined by fixing all DOF for the elements of the bottom face located in the region corresponding to the contact area between the specimens and the lower support in the experimental setup. The top face was left unrestrained, as the top steel plate and the *Dywidag* bar system used to clamp the specimen did not significantly restrict the deformations on that face (mainly due to the relatively low stiffness of the core materials).

The material properties presented in chapter 4 were used in the FE models. The GFRP (faces and ribs) and balsa wood parts were modelled using linear-elastic orthotropic material properties, whereas the PUR foam was modelled as a nonlinear isotropic material, with a constitutive relation defined by the average elastic moduli provided in Table 4.2 (foam with nominal density of 100 kg/m^3) and a yield stress of 0.5 MPa and a maximum stress of 0.64 MPa for a plastic strain of 0.0155 m/m followed by a yield plateau (according to the results obtained in material characterisation tests for compression loading). The effects of geometric nonlinearity were also considered in the models.

6.5.2.2. Results and discussion

Figure 6.15 shows the deformed shapes obtained from the FE models for the two configurations considering the PUR foam cored panels (for which the highest deformations are observed).

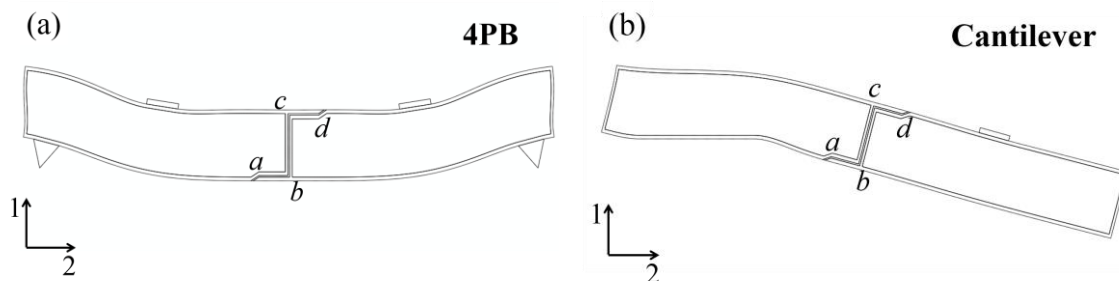


Figure 6.15. Deformed shapes for the FE models of the transverse direction behaviour: (a) four-point bending, and (b) cantilever.

The load vs. deflection (at D1) curves obtained are presented in Figure 6.16 for the four-point bending and cantilever configurations, for which a generally good agreement was observed between the numerical predictions and the experimental results. The most significant differences in initial stiffness were observed for the balsa wood cored panels. These differences are considered to stem from the very significant inherent variability of that material's mechanical properties (typical coefficients of variation range between 20% and 30% [20]).

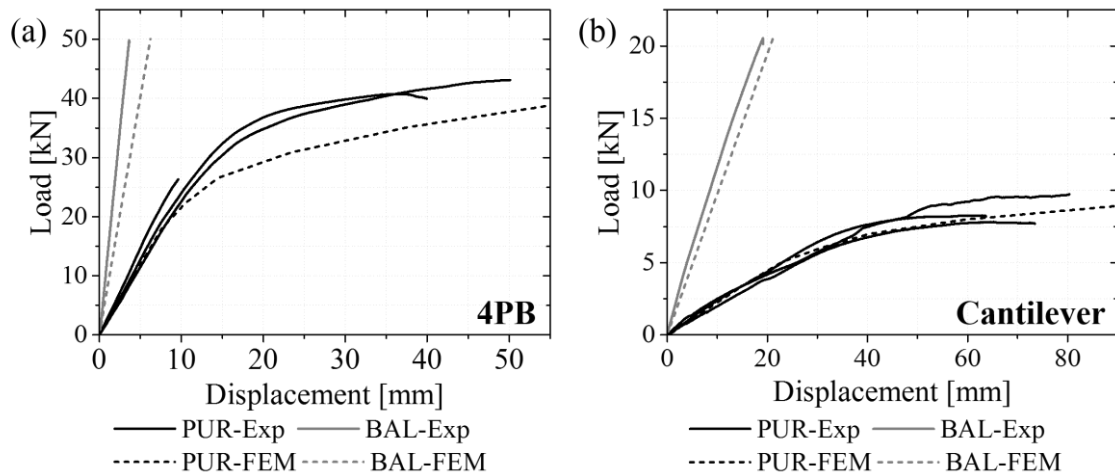


Figure 6.16. Comparison between experimental and numerical load vs. displacement curves for the transverse direction: (a) four-point bending, and (b) cantilever.

For both test configurations, the FE models of the PUR foam cored panels reasonably reproduced the nonlinearity observed in the experimental load vs. displacement curves. The maximum shear stress estimated for the PUR foam in the four-point bending configuration is 0.38 MPa, which exceeds (slightly) the foam's average shear strength (0.32 MPa), thus justifying the shear failures observed in the experiments. For the balsa wood cored panels, the maximum estimated shear stress was 0.83 MPa, being slightly lower than the 0.93 MPa strength of that core material.

The Tsai-Hill criterion [21] was used to assess the failure of the GFRP elements in both configurations for the specimens with the balsa wood core. The failure stresses determined from the laminates' material characterisation tests were considered and a through-thickness tensile failure stress of 10 MPa (in the range of typical values found in the literature [22]) was assumed.

Figure 6.17-a shows a plot of this criterion for the four-point bending configuration subjected to the experimental failure load. In this plot, it is possible to observe the existence of stress concentrations approaching the laminate’s strength in the interface between the inner rib and the bottom face sheet (as indicated in the figure). The analysis of local stresses in this region shows that the limiting factor is the excessive tensile through-thickness stress in the inner rib, which develops due to the local transfer of tensile stresses from the face sheet to the rib. This observation agrees well with the experimentally observed failure for this configuration (Figure 6.9-a), in which through-thickness delamination was observed in the inner rib, propagating into the GFRP face due to the existing fibre continuity.

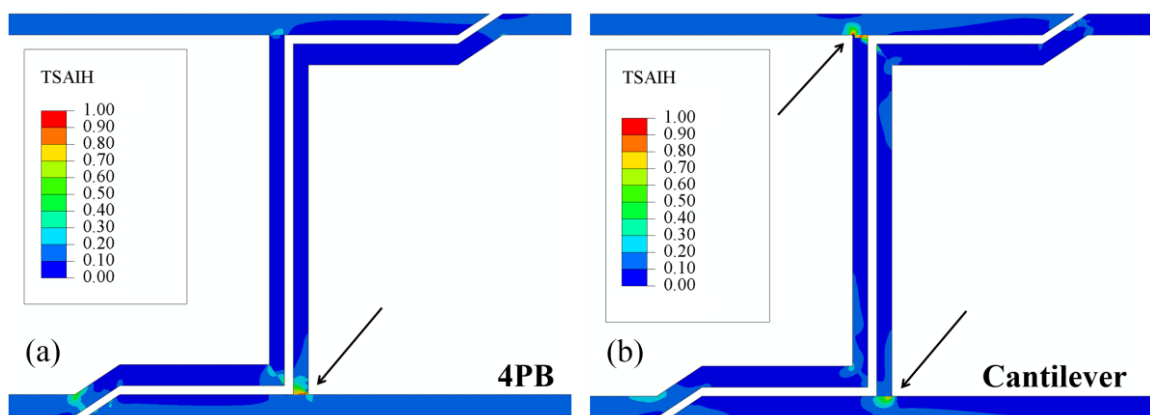


Figure 6.17. Tsai-Hill criterion (at experimental failure load) for the laminates in the balsa wood cored specimens (transverse direction): (a) four-point bending, and (b) cantilever.

For the cantilever configuration (Figure 6.17-b), failure initiation is predicted by the Tsai-Hill criterion for the two (top and bottom) interfaces between the inner ribs and the face sheet extensions. In this case, the limiting factor is the transfer of axial tensile stresses in the inner ribs into through-thickness tensile stresses in the face sheets. This also agrees well with the experimentally observed failure mode (Figure 6.9-c), which was initiated by the delamination of the GFRP laminate in the top face sheet at that location.

The axial, through-thickness and shear stress profiles developed within the adhesive layer at failure for the two types of core materials and test configurations were also analysed. Figure 6.18 presents those stress profiles for the four-point bending configuration, while the cantilever case is depicted in Figure 6.19 (stress values at the adhesive midline). The (1,2) plane coordinate system used corresponds to that shown in Figure 6.15. The “a” to “d” points also shown in that figure represent the direction changes in the adhesive layer, and their positions are indicated along the stress profiles.

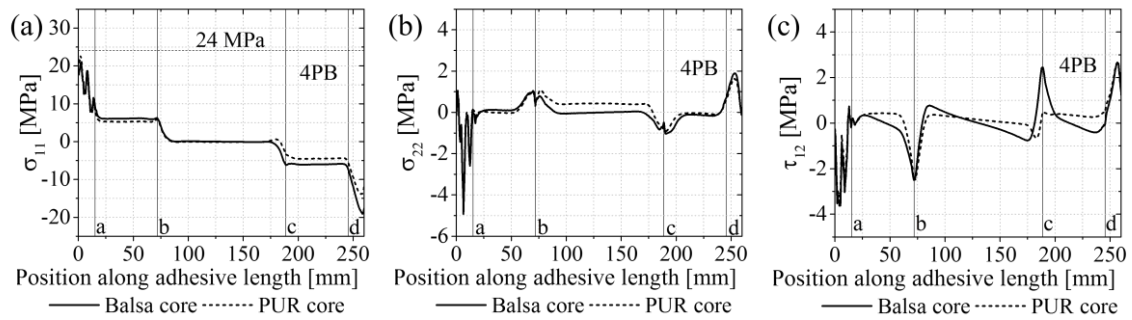


Figure 6.18. Adhesive stresses (midline) at failure for the four-point bending configuration (transverse direction): (a) σ_{11} , (b) σ_{22} , and (c) τ_{12} .

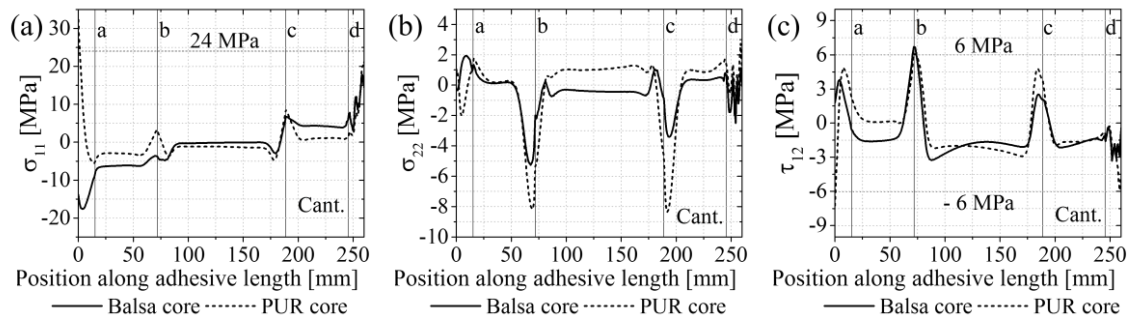


Figure 6.19. Adhesive stresses (midline) at failure for the cantilever configuration (transverse direction): (a) σ_{11} , (b) σ_{22} , and (c) τ_{12} .

In the four-point bending configuration (Figure 6.18), the most significant stresses are the σ_{11} , with average values between ~ 5 MPa to ~ 6 MPa in the horizontal segments of the adhesive (for which these stresses are axially oriented). Peaks in the slanted adhesive tips indicate that a significant part of the axial stress transfer between the face sheets occurs directly in this region. According to the manufacturer, the strength of the adhesive is 24 MPa in tension and 53 MPa in compression [18]. The estimated stresses were below these values, even at peak stress locations. Regarding the σ_{22} and τ_{12} stresses, relatively low values are observed (in good agreement with what would be expectable given this particular loading configuration, for which the joint is mainly subject to bending moment), with the highest stress values being observed at the points of direction change in the adhesive's geometry.

For the cantilever configuration (Figure 6.19), significant stresses are calculated for all three components. Once more, stress peaks are observed at the points of geometry change in the adhesive layer. With this regard, it is important to notice the important τ_{12} stresses at those locations, which approach values of ~ 6 MPa. While the adhesive manufacturer does not provide a definite shear strength value for the adhesive, it states that this value is higher than 6 MPa [23].

A significant tensile σ_{II} stress peak is predicted by the FE model for the PUR foam cored panel at the adhesive tip in the bottom face sheet. However, for this loading configuration, the bottom face of the panel would be expected to be mostly in compression. Nonetheless, such peaks occur due to the high shear deformability of the PUR foam, which causes the flexural deformation of the panel's bottom GFRP face sheet, characterised by a local curvature opposing that of the global deformation. Such an effect is also observed for the stiffer balsa wood cored panels (albeit with a lower magnitude), for which the compressive stresses at the adhesive tip are locally reduced. A parametric study was performed by changing the shear modulus of the core material and observing the magnitude of such tensile stress peaks, and the results obtained confirmed the correlation between the two.

In general, the stress profiles in the adhesive encompass values that are lower than the adhesive strength, with the exception of some localised stress peaks that approach the strength values (lower bound) indicated by the manufacturer. This result further indicates the good performance of the joint.

6.5.3. Simulation of longitudinal direction behaviour

6.5.3.1. Models description

Three-dimensional (3D) models were developed to simulate the longitudinal direction behaviour of the jointed sandwich panels. Two load cases were investigated: (i) eccentric loading, and (ii) four-point bending.

The eccentric load cases were aimed at assessing the joint's performance in distributing locally applied loads between the connected panels. A model was developed, simulating the L1+L3 loading configuration of the alternate loading tests described in section 3.3.1. The loading blocks used in the tests were simulated as relatively thick and rigid plates (20 mm thickness and typical steel material properties), having the same square area (400 mm side) as the aforementioned blocks. Pressure loads equivalent to the average block weight (4.60 kN) were applied to the plates. In this loading configuration, the actions were applied to the lower panel relative to the connection position (*i.e.*, the panel that during floor installation would already be in place as the next panel would be lowered into position).

In the four-point bending load case, one of the main goals was to analyse the shear force distribution between the core, the ribs and the joint. For this purpose, the four-point bending failure test carried out on the jointed panel with a PUR foam core was simulated. An

additional model was developed considering balsa wood as the core material to investigate the influence of the core properties on the shear force distribution.

In both models, fifteen-node wedge elements (*C3D15*) were used, and an approximate global element size of 20 mm for the GFRP parts and adhesive, and 40 mm for the core, were adopted following sensitivity checks regarding the influence of the mesh refinement on the model's results. The material properties, the contacts between adherent surfaces, and the simulation of support geometry were defined similarly to what was described for the four-point bending transverse direction FE models. Symmetry boundary conditions were defined at the panel's mid-span to reduce the model size. Nonlinear geometric effects were considered for the four-point bending simulations, for which large deformations were expected.

6.5.3.2. Eccentric loading results and discussion

Figure 6.20 shows the deformed shape obtained for the eccentric loading model simulating the L1+L3 configuration of the alternate loading tests. In Figure 6.21, the axial strain predictions, as well as the experimental strain data (*cf.* section 2.3.3.1) are shown. A reasonably good agreement between the numerical and experimental results is observed, with the magnitude and general evolution trend of the experimental strains along the panel width being captured by the model.

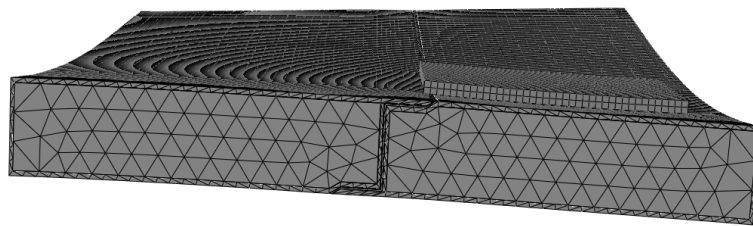


Figure 6.20. Deformed shape for the model with eccentric loading corresponding to the L1+L3 configuration used in the alternate loading tests.

The stress profiles in the adhesive joint, measured at its midline, for this load configuration are shown in Figure 6.22 (same notation as in Figure 6.18 and Figure 6.19). As expected, the general development of the σ_{11} , σ_{22} and τ_{12} stresses is similar to that previously described for the transverse direction simulation of the cantilever tests (Figure 6.19). However, the value of the σ_{33} stress component was not significant in those tests; in this case, it represents the highest stress component in the adhesive, being caused by the longitudinal bending

moment at the panel’s mid-span. Nevertheless, its maximum value of approximately 1.2 MPa (in tension) is well below the tensile strength of the adhesive (24 MPa).

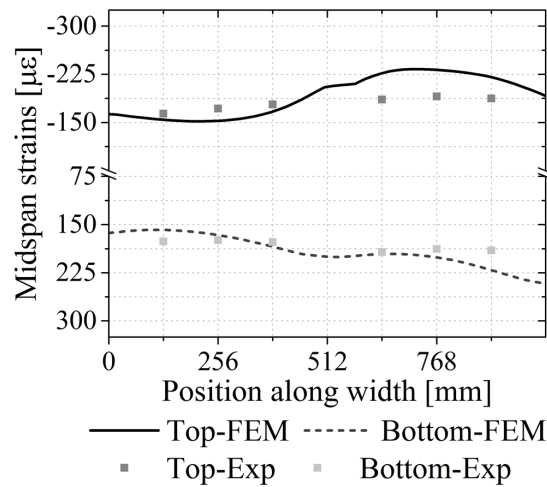


Figure 6.21. Comparison between experimental results and numerical predictions for the axial strains in the face sheets of the jointed panel at the mid-span section (alternate loading).

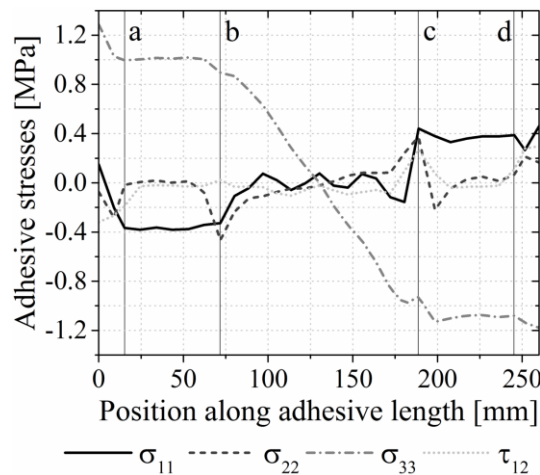


Figure 6.22. Stress profile predictions along the adhesive length (midline) at the mid-span section for the L1+L3 load configuration.

6.5.3.3. Four-point bending results and discussion

The load vs. mid-span displacement curves obtained from the FE models for the two cores are shown and compared with the experimental results from the PUR foam cored panel test in Figure 6.23.

A good agreement between the numerical and experimental results for the PUR foam cored panel under four point bending was obtained. Comparing the numerical results for the two core materials, the model for the balsa wood cored panel is slightly stiffer than that for the

panel with PUR foam. However, such differences are not very significant suggesting that, for the considered panel geometry, adopting a stiffer core (within the range of material properties considered herein) has a limited effect on the jointed panel's overall flexural performance.

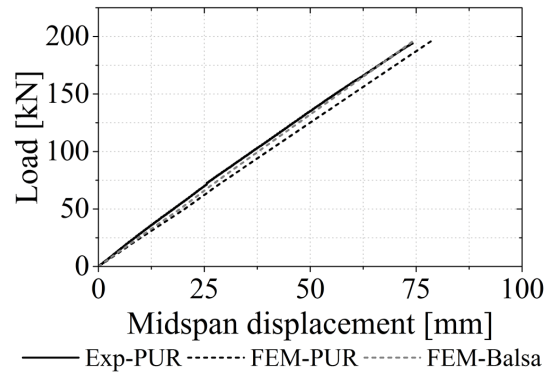


Figure 6.23. Load vs. mid-span displacement curves from FEM and comparison with experimental results (four-point bending).

Figure 6.24 shows the shear stress distributions in the FE model of the PUR foam cored panel, considering: (i) a transverse cut of the core at a section distanced 300 mm from the edge of the support area (Figure 6.24-a), (ii) a longitudinal cut along the mid-width of one of the core blocks (Figure 6.24-b), and (iii) an inner (joint) rib and an outer rib (Figure 6.24-c). The equivalent plots for the model of a balsa wood cored panel are presented in Figure 6.25.

The predicted shear stresses in the PUR foam core (Figure 6.24-a,b) are: (i) lowest near the ribs, increasing with the distance from these elements (along the transverse direction); (ii) decrease with increasing height (along the thickness direction), and (iii) are highest near the load application area and have a gradual reduction towards the support (along the longitudinal direction). A maximum shear stress of 0.16 MPa was obtained, corresponding to 50% of the foam's 0.32 MPa average shear strength. The inner ribs (Figure 6.24-c) also present the highest shear stresses at the load application area, particularly at the top of the rib. This relieves the shear stresses at the top half of the PUR foam, accounting for the through-thickness shear stress variations observed in the core. In the outer ribs, the shear stresses increase in the direction of the support from the load application area, indicating a transfer of shear load from the inner to the outer ribs.

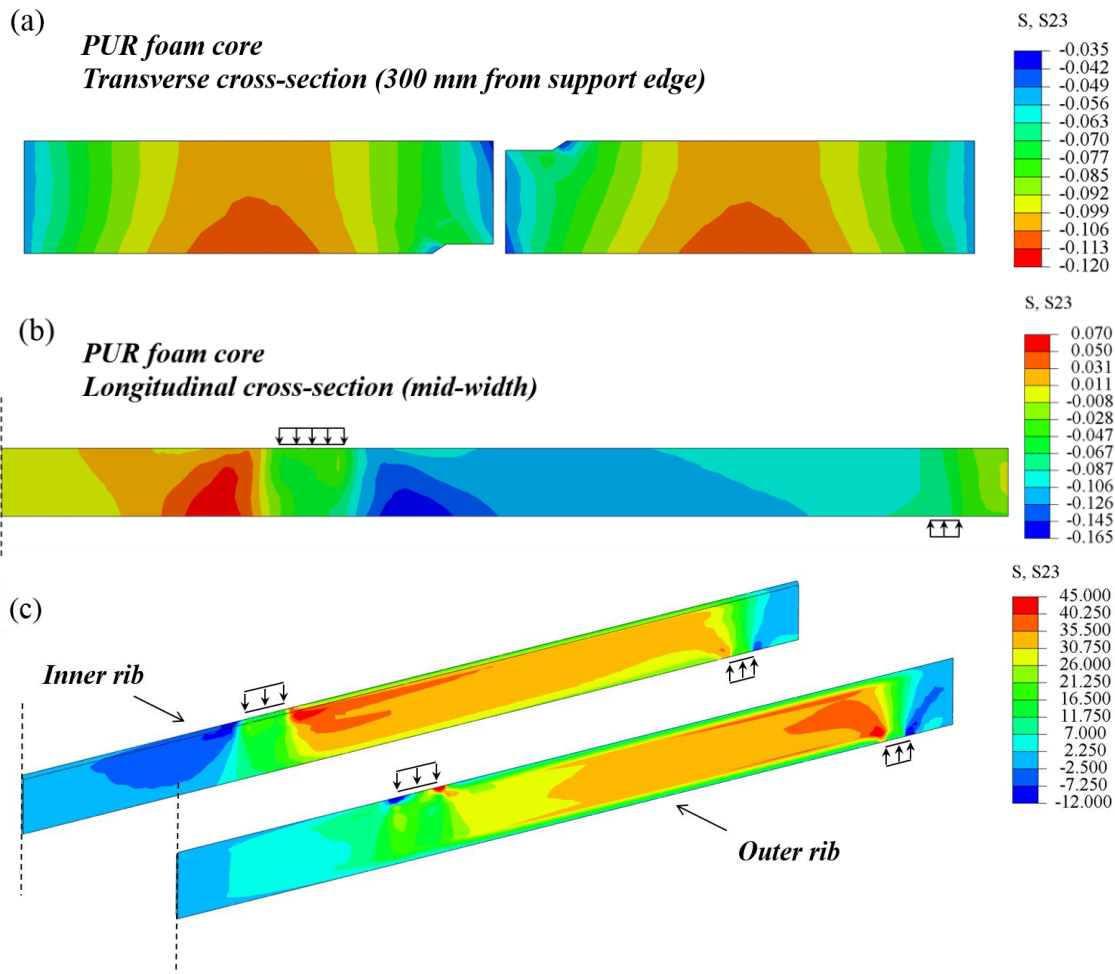


Figure 6.24. Shear stresses (in MPa) in the PUR foam core in (a) a transverse section view, (b) a longitudinal section view, and (c) the inner and outer ribs (four-point bending).

The shear stress distributions in the model for the balsa wood cored panel (Figure 6.25) follow relatively similar developments as those described above. However, due to the higher stiffness of the balsa wood compared to that of the PUR foam, the core material takes a higher portion of the loading at the load application area. This is visible in the more homogeneous through-thickness shear stress profile and in the less pronounced shear stress concentrations in the inner ribs near the load application area, by comparison with the results obtained for the softer PUR foam core. The maximum shear stress in the balsa wood core amounts to 0.55 MPa, corresponding to 59% of its average shear strength (0.93 MPa).

Table 6.2 presents the contribution of the different panel components to the shear force resistance of the panel, taken from the FE models at the cross-section distanced 300 mm from the support edge (same as shown in Figure 6.24-a and Figure 6.25-a). The presented shear force values were obtained by integration of the shear stresses in each component (extracted at the element centroids) over their respective areas.

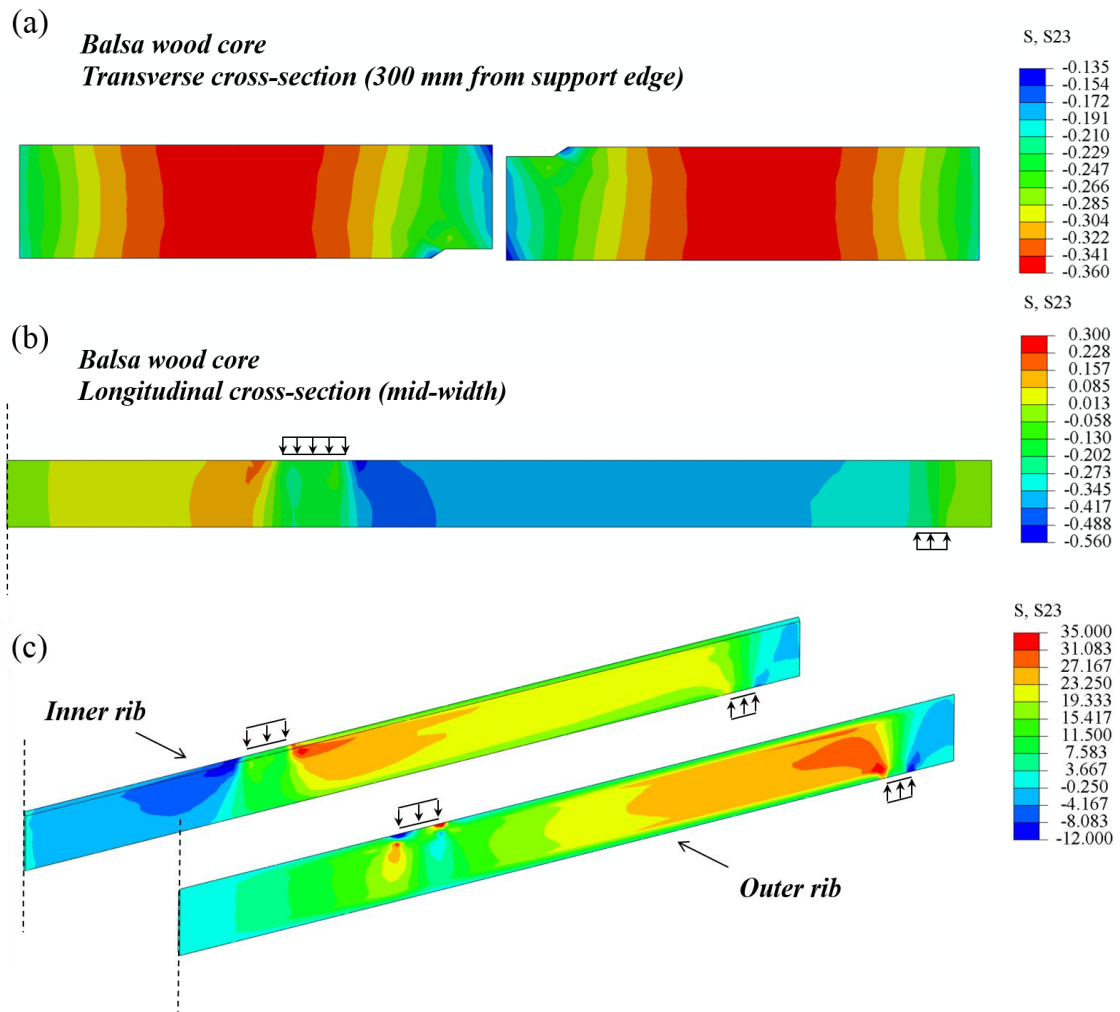


Figure 6.25. Shear stresses (in MPa) in the balsa wood core in (a) a transverse section view, (b) a longitudinal section view, and (c) the inner and outer ribs (four-point bending).

Table 6.2. Contribution of the different panel components to shear force resistance (300 mm from support edge, experimental failure load applied).

Component	PUR core		Balsa core	
	Average shear force [kN]	Relative contribution (%)	Average shear force [kN]	Relative contribution (%)
Core	10.8	10.9%	37.1	37.7%
Adhesive	5.1	5.2%	3.4	3.4%
Inner ribs	35.7	36.1%	23.1	23.5%
Outer ribs	39.4	39.9%	28.2	28.6%
Faces	7.8	7.9%	6.7	6.8%
Total	98.8	100%	98.5	100%

It is interesting to note that the shear force distribution between the panels' components is significantly affected by the core material adopted, even though the flexural stiffness of the panels did not seem to be greatly affected by that change (for the materials and geometries

considered herein; *cf.* Figure 6.23). In fact, the core's contribution for shear force resistance is only 10.9% for the PUR foam cored panel and it increases to 37.7% when considering the balsa wood core. Conversely, the outer ribs and the joint components (inner ribs and adhesive) are responsible for supporting 81.2% of the shear forces in the first case, a value that is reduced to 55.5% in the second case. Such a reduction suggests that when using stiffer core materials, the GFRP ribs may be designed with a lower stiffness (*e.g.*, by appropriate changes in their fibre architecture and total thickness), and a more even stress distribution may be achieved among the panel components.

6.6. Concluding remarks

The proposed panel-to-panel connection system consists of a Z-joint, integrated into the sandwich panels at the moment of their production and adhesively bonded on-site. Experimental and numerical investigations were carried out regarding the mechanical and structural response of these joints and of the jointed sandwich floor panels, in both their transverse and longitudinal (main span) directions.

In the transverse direction investigations, failure of the connection occurred in the GFRP elements due to excessive through-thickness tensile stresses, in one of the inner ribs for the four-point bending configuration, and in the top face sheet for the cantilever configuration. Connection failures only occurred for the balsa wood cored specimens; in the specimens with PUR foam core, failure was due to excessive shear in the core; failure in the adhesive layer was never observed. The FE models were able to simulate the behaviour of the connections, providing reasonably accurate predictions for the deformations and failure modes experimentally observed in the transverse direction, and were used to estimate stresses along the adhesives.

Regarding the longitudinal direction investigations, the alternate loading tests attested the connection's effectiveness in transferring stresses and guaranteeing deformation compatibility between adjacent panels. The joints significantly increased the panels' shear stiffness, while having a negligible influence on their bending stiffness. The FE models simulating the four-point bending load in the jointed panel indicate that shear stresses partially transfer from the core to the ribs/joint between the load application area and the supports. For the materials and geometries considered, negligible differences were found in

the predicted flexural stiffness values between jointed panels with PUR foam core and those with balsa wood core. However, the balsa wood core absorbed a significantly higher portion of the shear forces in the panel, indicating that when using stiffer core materials, the ribs and joints may be accordingly designed to be less stiff, thus optimising the structural use of each panel component.

6.7. References

- [1] Keller, T., Haas, C. and Vallée, T. (2008). “Structural concept, design and experimental verification of a GFRP sandwich roof structure”. *Journal of Composites for Construction*, 14(4), 454-468.
- [2] Durand, S., Lubineau, G., Chapelle, H. (2012). “Design analysis of GRP panels for the roof of the Haramain High Speed Railway Jeddah Station”. *Proceedings of the 10th International Conference on Sandwich Structures (ICSS-10)*, Nantes, France, August 27-29.
- [3] Keller, T., Rothe, J., de Castro, J., Osei-Antwi, M. (2014). “GFRP-balsa sandwich bridge deck: concept, design, and experimental validation”. *Journal of Composites for Construction*, Vol. 18(2), p. 04013043.
- [4] Rautaruukki Corporation (2009). *Assembly instructions – Sandwich panels: Packaging, transport, delivery, storage, assembly*, manufacturer technical data sheet.
- [5] Hexcel Composites (2001). *Sandwich panel fabrication technology*, manufacturer technical data sheet.
- [6] Banea, M.D., da Silva, L.F.M. (2009). “Adhesively bonded joints in composite materials: An overview”, *Proceedings of the Institution of Mechanical Engineers, Part L: Journal of Materials: Design and Applications*, 223(1), 1-18.
- [7] Feldhusen, J., Krishnamoorthy, S.K. (2008). “Fast joining and repairing of sandwich materials with detachable mechanical connection technology”, *13th European Conference on Composite Materials (ECCM 13)*, 2-5 June, Stockholm.
- [8] Niklas, K. (2008). “Search for optimum geometry of selected steel sandwich panel joints”, *Polish Maritime Research*, 15(2), 26-31.

- [9] Winkelman, T.J. (2002). *Fiberglass reinforced polymer composite bridge construction in Illinois*, Illinois Department of Transportation, Construction Report FHWA/IL/PRR 145, Illinois, USA.
- [10] Turner, M.K., Harries, K.A., Petrou, M.F., Rizos, D. (2004). “In situ structural evaluation of a GFRP bridge deck system”, *Composite Structures*, 65(2), 157-165.
- [11] Liu, Z., Majumdar, P.K., Cousins, T.E., Lesko, J.J. (2008). “Development and evaluation of an adhesively bonded panel-to-panel joint for a FRP bridge deck system”, *Journal of Composite for Construction*, 12(2), 224-233.
- [12] Zhou, A., Keller, T. (2004). “Joining techniques for fiber reinforced polymer composite bridge deck systems”, *Composite Structures*, 69(3), 336-345.
- [13] Zetterberg, T., Aström, B.T., Bäcklund, J., Burman, M. (2001). “On design of joints between composite profiles for bridge deck applications”, *Composite Structures*, 51(1), 83-91.
- [14] Luke, S., Canning, L., Collins, S., Knudsen, E., Brown, P., Taljsten, B., Olofsson, I. (2002). “Advanced composite bridge decking system – Project ASSET”, *Structural Engineering International*, 12(2), 76-79.
- [15] Mara, V., Al-Emrani, M., Haghani, R. (2014). “A novel connection for fibre reinforced polymer bridge decks: Conceptual design and experimental investigation”, *Composite Structures*, 117, 83-97.
- [16] Correia, J.R., Garrido, M., Gonilha, J.A., Branco, F.A., Reis, L.G. (2012), “GFRP sandwich panels with PU foam and PP honeycomb cores for civil engineering structural applications: Effects of introducing strengthening ribs”, *International Journal of Structural Integrity*, 3(2), 127-147.
- [17] Fam, A., Sharaf, T. (2010). “Flexural performance of sandwich panels comprising polyurethane core and GFRP skins and ribs of various configurations”, *Composite Structures*, 92(12), 2927-2935.
- [18] Sika AG (2014). *Sikadur[®]-31 EF*, Product Data Sheet, Edition 23/01/2014.
- [19] EN 13706-2:2002 (2002). *Reinforced plastics composites – Specifications for pultruded profiles – Methods of test and general requirements*, Annex G, European Standard.

- [20] Osei-Antwi, M., de Castro, J., Vassilopoulos, A.P., Keller, T. (2013). “Shear mechanical characterization of balsa wood as core material of composite sandwich panels”, *Construction and Building Materials*, 41, 231-238.
- [21] Tsai, S.W. (1965). *Strength Characteristics of Composite Materials*, NASA CR-224.
- [22] Vallée, T., Correia, J.R., Keller, T. (2006). “Probabilistic strength prediction for double lap joints composed of pultruded GFRP profiles – Part II: Strength prediction”, *Composites Science and Technology*, 66(13), 1915-1930.
- [23] Sika AG (2013). *Declaration of performance: Sikadur[®]-31 EF*, Edition 01/07/2013.

Chapter 7

Connections to building walls

7.1. Introduction

The connections between the floor elements and their vertical supports must be considered in the development of a sandwich panel floor solution. In old buildings, such vertical supports are frequently load-bearing rubble masonry walls. The primary function of floor-to-wall connection systems is to guarantee the transfer of vertical and horizontal (seismic and wind) loads between the floors and the load-bearing walls. In addition, it is also useful to guarantee some rotation restriction at these connections, as this reduces the floor's flexibility, *i.e.* the maximum deflections along the span. This can be a significant advantage given that maximum allowable deformability criteria are usually the limiting factor in the design of FRP composite sandwich floor panels [1].



Figure 7.1. Connection between a timber floor and timber-framed masonry walls using steel angles.

In the rehabilitation of old timber floors one of the typical connection solutions comprises embedding the new joists in the load-bearing walls and/or using steel angles to anchor them to the walls (Figure 7.1). These steel angles provide additional support length and in-plane stiffness to the floors [2,3], while also contributing to improve the out-of-plane behaviour of the exterior masonry walls [4]. The proposed connection systems, illustrated in Figure 7.2, are based on that practice, with the steel angles acting as the main supporting element.

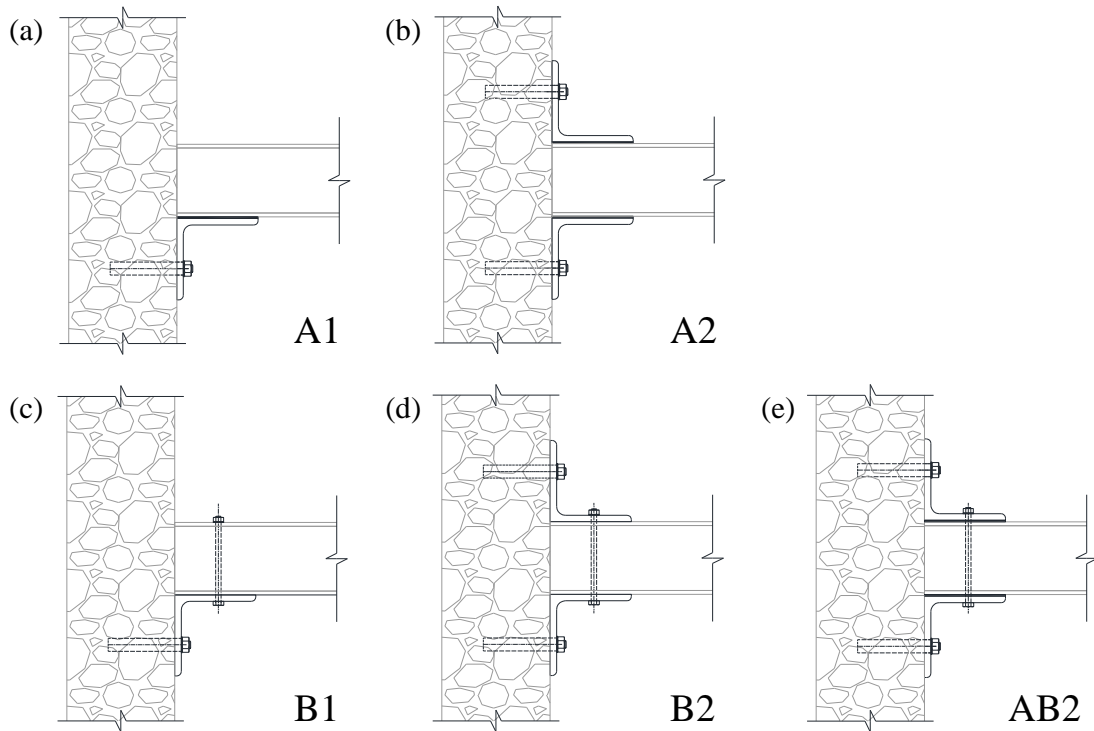


Figure 7.2. Proposed connection systems (A – adhesive, B – bolted, 1 – single bottom steel angle, 2 – top and bottom steel angles): (a) A1, (b) A2, (c) B1, (d) B2, (e) AB2.

The option of embedding the panels inside the walls was discarded, due to the continuous nature of this connection (as opposed to the discrete embedding of timber joists) – its implementation would significantly affect the walls’ structural integrity and would be very labour intensive. Therefore, to increase the rotation stiffness of the connection, a second steel angle connected to the top face of the sandwich panels is considered in addition to the bottom steel angle where the floor panels are supported. These steel angles can be embedded in the walls by anchors fixed to the masonry using compatible grouts/mortars. Furthermore, the angles can be covered by the baseboard (top angle) or the moulding/suspended ceiling (bottom angle). Three different methods were used to join the panels and the steel angles: (i) adhesive bonding (Figure 7.2-a,b), (ii) bolting (Figure 7.2-c,d), and (iii) a combination thereof (Figure 7.2-e).

7.2. Experimental investigation

7.2.1 Test setup and materials

A large sandwich panel of 3560 mm length \times 1250 mm width \times 134 mm thickness was manufactured by vacuum infusion. After curing, the sandwich panel was cut into specimens

with a length of 850 mm and width of 250 mm. The panels comprised 7 mm thick GFRP face sheets (nominal dimensions) enclosing the 120 mm thick core, made of either (i) rigid PUR foam (87.4 kg/m^3), or (ii) balsa wood.

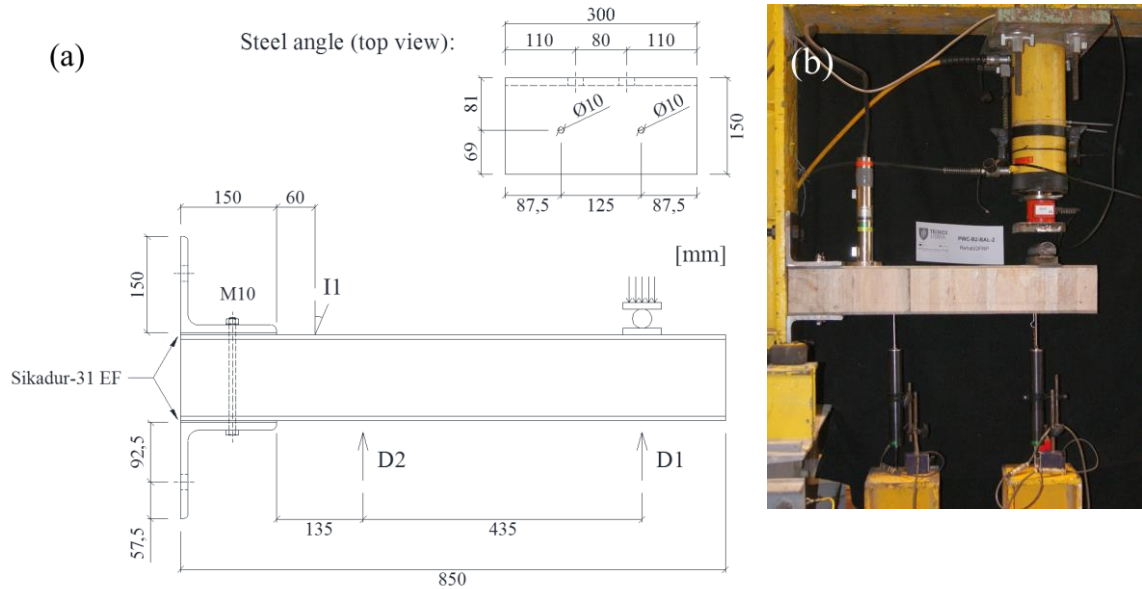


Figure 7.3. Experimental setup and instrumentation: (a) schematic, and (b) general view.

One of the extremities of the test panels was supported in a single cantilever configuration and a point load was applied at the free edge, as illustrated in Figure 7.3. The angles that supported the sandwich panels were connected to a closed steel frame comprised of HEB 300 profiles, simulating a rigid rubble masonry load-bearing wall with a thickness of 1 m and a Young's modulus of 2 GPa. The angles consisted of L-150×12 steel profiles of S275 JR grade, with a leg width of 150 mm and wall thickness of 12 mm. These were cut to a width of 300 mm, and bolt holes were drilled according to the specifications presented in Figure 7.3. M10 bolts were machined and threaded to the required length from smooth S275 JR grade steel bars and used to connect the sandwich panels to the steel angles. An epoxy adhesive supplied by *Sika AG (Sikadur 31 EF)* was used for the adhesively bonded connections, all presenting a thickness of 2 mm (guaranteed using appropriate spacers).

Regarding the test instrumentation, vertical displacements were measured at the bottom face of the panels at the load application point (D1) and at a cross-section distanced 135 mm (approximately the same as the panel thickness) from the edge of the support (D2), using displacement transducers, with stroke of 100 mm and precision of 0.01 mm. Displacement at D1 was also measured using a wire displacement transducer (500 mm of stroke, precision of 0.1 mm), in order to measure the high displacements attained in some tests. Additionally,

the panel rotation (I1) was measured on the top face sheet at a cross-section distanced 60 mm from the edge of the support using an inclinometer, with range of $\pm 10^\circ$ (precision of 0.01°). The applied load was measured using a load cell with capacity of 100 kN and precision of 0.01 kN.

Load was applied with a hydraulic jack, reacting against the rigid steel frame. A load distribution steel plate (15 mm thick, 250 mm long and 60 mm wide) and a roller were positioned between the test specimen and the hydraulic jack. Specimens were monotonically loaded up to failure, using a manually controlled hydraulic pressure unit. The different responses of the single and double steel angled configurations, namely in terms of their stiffness values, made necessary the adoption of different loading speeds for the two cases in order to maintain consistent test durations. The experiments had durations ranging between 3 to 6 minutes, thus minimizing effects stemming from the time dependence of the materials' properties. This was achieved by adopting approximate loading speeds of 0.03-0.05 kN/s for the single steel angle connections (series A1 and B1) and 0.07-0.10 kN/s for the double steel angle connections (series A2, B2 and AB2).

Table 7.1 details the number of specimens tested (16 in total) according to the type of connection and core material. The two steel angle configurations included the higher number of replicate specimens (2 or 3), since they were expected to present the best performance and hence the highest potential for practical applications. For the remaining configurations, due to material limitations, it was only possible to test either 1 or 2 specimens.

Table 7.1. Specimen distribution per connection system and core material.

Series	Connection system Description	No. of specimens	
		PUR core	Balsa core
A1	adhesively bonded, single steel angle	1	2
A2	adhesively bonded, two steel angles	2	2
B1	bolted, single steel angle	1	1
B2	bolted, two steel angles	3	3
AB2	adhesive and bolts, two steel angles	1	-

7.2.2 Results and discussion

7.2.2.1 Overview

Figure 7.4 illustrates the load vs. D1 displacement curves obtained for all connection systems. The displacements measured at D2 and the rotations measured at I1 exhibited very similar qualitative developments and were consistent with D1 displacements, hence they are not shown. Table 7.2 presents a summary of the failure (or ultimate) loads and initial stiffness at D1 and initial rotational stiffness at I1. Detailed discussion is provided in the following sections for each type of connection.

Table 7.2. Summary of experimental results (average \pm standard deviation).

Core	Specimen	Failure load [kN]	Initial stiffness (D1)	Initial rotational			
PUR foam	A1-PUR-1	1.56	0.083	1.08			
	A2-PUR-1	9.95	$11.17 \pm 1.22^*$	0.89	$0.73 \pm 0.16^*$		
	A2-PUR-2	12.39		0.57	6.10	$8.77 \pm 2.67^*$	
	B1-PUR-1	4.81		0.051	0.61		
	B2-PUR-1	11.29		0.42	4.63		
	B2-PUR-2	13.80	13.24 ± 1.74	0.46	0.45 ± 0.02	5.21	4.92 ± 0.29
	B2-PUR-3	14.63		0.46	4.93		
Balsa wood	AB2-PUR-1	18.84		0.53	6.31		
	A1-BAL-1	3.22	$3.54 \pm 0.32^*$	0.14	$0.15 \pm 0.01^*$	1.76	$1.84 \pm 0.08^*$
	A1-BAL-2	3.85		0.16		1.92	
	A2-BAL-1	21.84	$20.24 \pm 1.59^*$	2.29	$2.26 \pm 0.03^*$	29.23	$29.75 \pm$
	A2-BAL-2	18.65		2.23		30.27	0.52^*
	B1-BAL-1	7.20		0.071		0.85	
	B2-BAL-1	16.48		1.21		14.52	
	B2-BAL-2	18.01	18.38 ± 2.11	1.00	1.11 ± 0.10	11.35	13.00 ± 1.59
B2-BAL-3	20.66		1.10		13.13		

*maximum difference between individual data points and the average value.

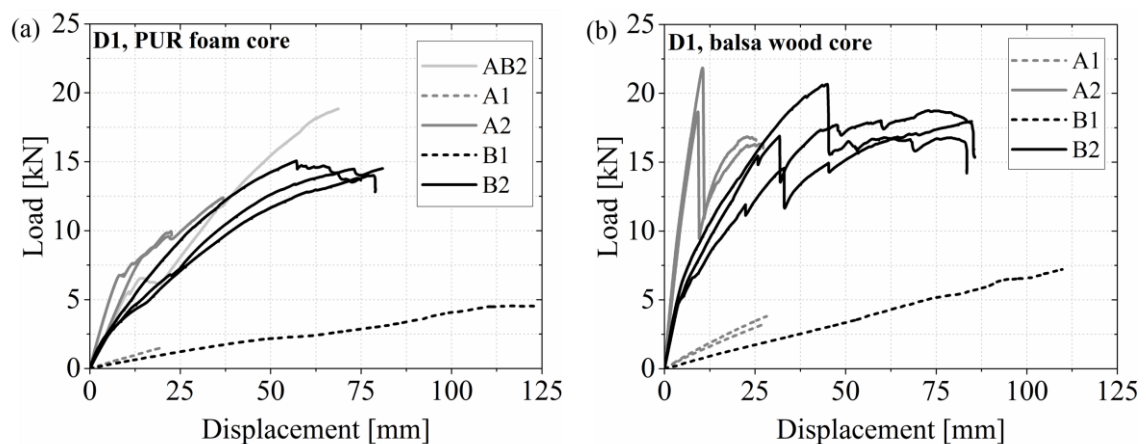


Figure 7.4. Load vs. displacement at D1 for all tested connection systems: (a) specimens with PUR foam core, and (b) specimens with balsa wood core.

7.2.2.2 Adhesively bonded connections (A1, A2)

The specimens with an adhesively bonded connection system and a single bottom angle support (A1) presented approximately linear elastic behaviour up to failure, which occurred for relatively low load values. The failure modes observed in this series are shown in Figure 7.5. Failure occurred in a brittle manner, and for both types of cores it initiated at the support length near the bottom face sheets, either at the interface between the steel angle and the adhesive (A1-BAL-1), or at the interface between the core and the bottom face sheet (specimens A1-BAL-2 and A1-PUR-1).

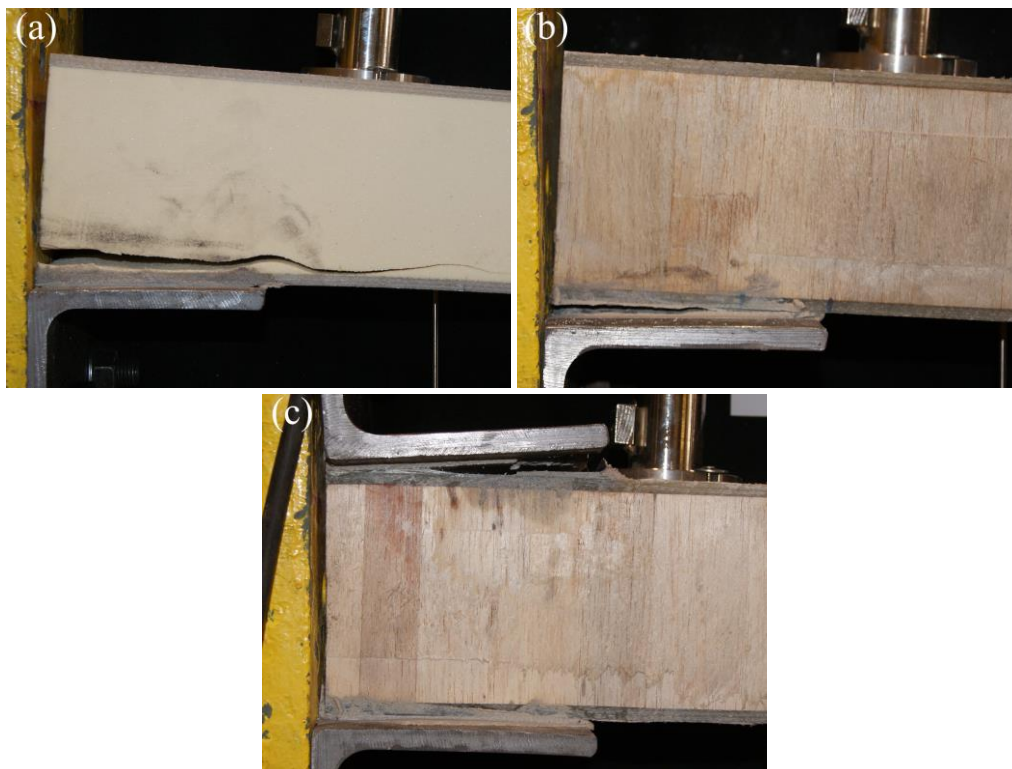


Figure 7.5. Failure modes of the A1 and A2 connection systems: (a) A1 specimen with PUR foam core, (b) A1 specimen with balsa wood core, and (c) A2 specimen with balsa wood core.

Adding a top steel angle to the adhesively bonded connection systems (A2) substantially increased the initial stiffness (about 9 and 15 times for the panels with PUR foam and balsa wood cores, respectively), as well as the ultimate load (approximately 7 and 6 times, respectively). The balsa wood specimens presented nonlinear behaviour, characterised by a gradual loss of stiffness, until the brittle failure of the foremost part of the adhesive bond (50-70% of the bond area) between the top face sheet and the top steel angle occurred, which caused a sudden load reduction. Subsequently, the connections were still able to carry some load (yet, lower than the failure load), while the cracking gradually opened in the remaining

top adhesive bond. A yielding plateau was reached when that bond was completely open, and the tests were interrupted. The PUR foam specimens also presented a non-linear response characterised by a progressive and substantial loss of stiffness (yet without load reduction), which was attributed to the progressive crack opening at the bond between the top face sheet and the top steel angle, with no visual evidence of foam crushing being observable throughout the test or at failure.

7.2.2.3 Bolted connections (B1, B2)

The B1 specimens presented an approximately linear-elastic response. For the panel with balsa wood core, plastic deformations were observed in the steel angle (Figure 7.6-a) and in the bolts for loads above 3.5 kN. Regarding the panel with PUR foam core, the steel angle did not present this type of deformation and the panel showed clear signs of foam crushing between the bolted area and the support's edge, as illustrated in Figure 7.6-b. Both tests were interrupted as a safety measure in order to protect the test instrumentation; although collapse had still not occurred, specimens exhibited very large deformations at this stage and the bolts presented plastic deformations at the interface zone between the steel angles and the bottom face sheet of the panels.

As in the adhesively bonded connection systems, adding a top steel angle to the bolted connections (B2) provided significantly higher stiffness (approximately 9 and 13 times higher for the PUR and balsa wood cored panels, respectively) and failure loads (approximately 3 times higher for both) in comparison with the single steel angle connections (B1). A gradual loss of stiffness was observed throughout the tests, caused by the progressive damage accumulation within the various connection components. The bolt holes in the GFRP faces of the sandwich panels presented bearing deformations (Figure 7.6-c); the bolts themselves presented very significant plastic shear deformations (Figure 7.6-d), more pronounced than those observed in the bolts of the B1 specimens, indicating the higher capacity of the B2 connections to further exploit the ductility of the steel bolts. The balsa wood specimens also exhibited crack opening within the core, particularly in the direction parallel to the bolts (Figure 7.6-e), causing the sudden load reductions observable in the load-displacement curves.

It is worth highlighting the ability of bolted connections to deform plastically (either in B1 or B2 configurations) and thus sustain high deformations without brittle failure. This increased ductility of bolted connections is a structural advantage over adhesively bonded

connections, being an important feature for civil engineering design and application. However, the bolted connections presented significantly lower stiffness compared to the adhesively bonded counterparts. For the specimens with a PUR foam core, the A1 connections were 63% stiffer than the B1 connections, and the A2 connections were 62% stiffer than the B2 configuration. Among the balsa wood cored specimens, the stiffness of A1 connections was 111% higher compared to B1 configuration, whereas the A2 connections were 104% stiffer than the B2 ones.

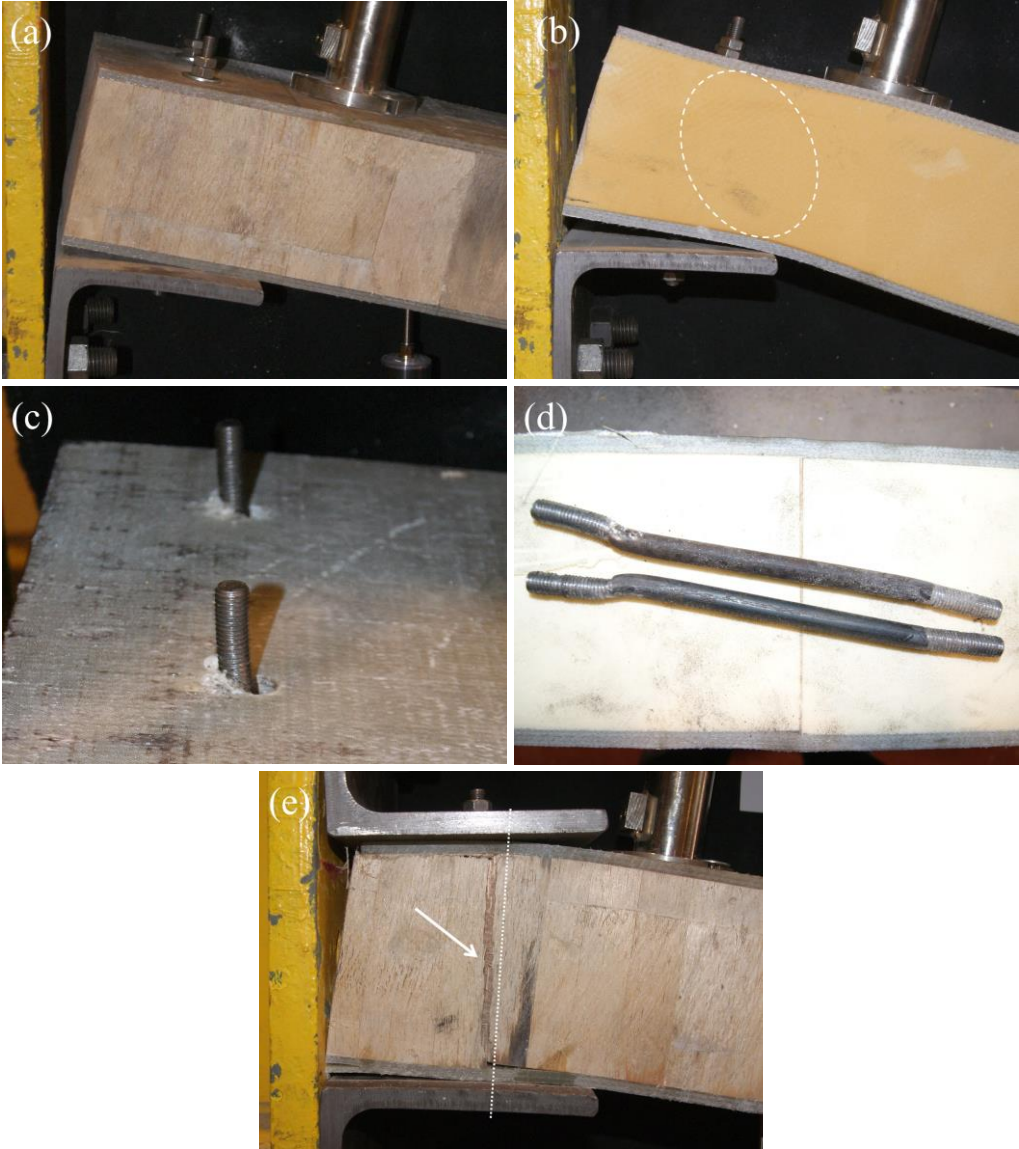


Figure 7.6. Failure modes for the B1 and B2 connection systems: (a) B1 specimen with balsa wood core, (b) B1 specimen with PUR foam core, (c) damage in GFRP for a B2 connection, (d) damage in the bolts for a B2 connection, and (e) B2 specimen with balsa wood core.

7.2.2.4 Adhesively bonded and bolted connection (AB2)

In order to evaluate the potential advantages of combining the higher connection stiffness of adhesively bonded connections with the plastic deformation capability and higher ductility of bolted connections, an additional test was performed in a connection (PUR foam specimen) combining adhesive bonding and bolting with top and bottom steel angles (AB2 configuration).

The load-displacement response obtained in the AB2 connection was linear-elastic up to a load of approximately 6 kN, with the elastic stiffness being comparable to that of the A2-PUR connections, showing that the adhesive bonding governed the initial response. Above that load, cracks were initiated at the adhesive bond between the top steel angle and the top face sheet of the panel (Figure 7.7-a), similar to what had been observed in the A2-PUR series. The crack opening progressed gradually (corresponding to a short yielding plateau in the load-deflection curve), after which the bolts were presumably activated and conferred additional stiffness to the connection. From this point onward, the load-displacement curve presented an intermediate slope (stiffness) between that of the A2-PUR and B2-PUR configurations. The bolt activation seems to have limited the further propagation of the crack in the adhesive, which in turn limited the shear stress within the bolts themselves, and consequently the extent of their plastic deformation. A maximum load of 18.8 kN was attained, when the PUR foam core failed in shear in a section located between the load application point and the support (Figure 7.7-b).

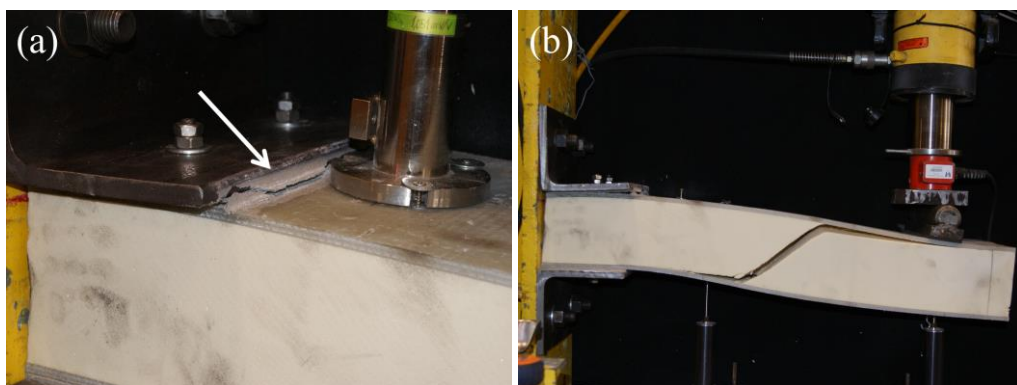


Figure 7.7. Failure in the AB2 connection system: (a) crack opening in the top adhesive layer, and (b) shear failure of the PUR foam.

The combined adhesively bonded and bolted system provided the highest failure load among all connection configurations tested using PUR foam cored panels. Additionally, it presented

high initial stiffness (comparable with the A2 systems) and some plastic deformation capability (albeit lower than in the B2 configuration). It is also worth highlighting that the high stiffness and strength together with the limited plastic deformability of the connection system shifted the failure mode from the connection to the panel (shear failure of the PUR foam core).

7.3. Numerical simulation

7.3.1 Objectives

The proposed connection systems were numerically modelled using a nonlinear FE modelling approach in order to (i) simulate the behaviour observed in the experiments, with emphasis on the linear-elastic response, *i.e.* the stiffness of the connection systems proposed, (ii) simulate the stress distributions within the connection and panel components, comparing them with the experimentally observed failure modes, and (iii) compare the deflections of the connected sandwich panels to the deflections they would exhibit if they were to be supported in a perfect cantilever (clamped) configuration (no rotation at the support), so as to obtain estimates for the characteristic moment-rotation relationships of each connection system.

7.3.2 Modelling approach

Three-dimensional (3D) FE models were developed using the commercial package ABAQUS/CAE (*Dassault Systèmes*) to simulate the A1, A2, B1 and B2 connection systems¹⁸, also considering the two different core materials used in this study.

The GFRP and balsa wood parts were modelled using linear-elastic orthotropic material properties, determined from the material characterisation tests reported in chapter 4 (Table 7.3). The PUR foam was modelled with isotropic crushable foam behaviour, using the formulation proposed by Deshpande and Fleck [5], considering a shear modulus of 8.7 MPa, a Young's modulus of 26 MPa (Poisson's ratio of 0.49), and an elastic-plastic constitutive

¹⁸ The AB2 connection system (adhesively bonded and bolted) was not explicitly modelled, since the FE analyses were mainly focused on the linear-elastic branch of the connections' response. In fact, for this range of the response, the behaviour of the AB2 connection would not differ significantly from that of the A2 configuration.

relation with a compressive yield stress of 0.64 MPa. For the adhesive layer, a linear-elastic isotropic material model was adopted, using the elasticity modulus of 6.5 GPa indicated in the manufacturer data sheet [6] (a Poisson's ratio of 0.3 was assumed). The steel elements (bolts and angles) were modelled as linear elastic-plastic, with an elasticity modulus of 210 GPa and yield stress of 275 MPa.

Table 7.3. Orthotropic material properties of GFRP and balsa wood used for FEM.

Material	E1 [MPa]	E2 [MPa]	E3 [MPa]	v12	G12 [MPa]
GFRP	29400	12780	7500	0.31	4730
Balsa wood	127	418	127	0.30	49

The contacts between all adherent surfaces (face-core interfaces, adhesive bonds) were modelled using the “cohesive behaviour” option for the interaction properties in ABAQUS/CAE, adopting the package's default contact enforcement method regarding traction-separation behaviour. This method does not allow significant slipping or separation to occur between the adherent surfaces. The non-adherent contacts (between the bolts and the bolt holes or between the panel's faces and the steel angles in the bolted connections) were modelled using “tangential behaviour” with a friction coefficient of 0.1 and the “normal behaviour” with “hard contact” for the pressure-overclosure behaviour of the interaction.

Quadratic ten-node tetrahedral solid elements (*C3D10* elements of the ABAQUS/CAE library) were used to model the different components of the panels and connections. Sensitivity checks were performed regarding the influence of the mesh density/refinement on the results obtained with the FE models, leading to the selection of the adopted meshes. Global element sizes (element average maximum edge length) of 20 mm were adopted for the faces, 30 mm for the core, 10 mm for the steel angles and adhesives, and 15 mm for the bolts.

Boundary conditions were defined by fixing all degrees of freedom for the nodes of the steel angles at the areas where these were bolted to the steel reaction frame used in the experiments. Load was defined by applying a pressure over an area of the sandwich panels' top face sheet with the same dimensions and at the same location as the loading plate used in the experimental tests. Static analyses were carried out using the above-mentioned FE models.

7.3.3 Results

The load-displacement (computed at D1) curves obtained from the FE models are presented and compared with the experimental results in Figure 7.8. Table 7.4 provides a comparison between the experimental and numerical stiffness values (for the displacement at D1 and the rotation at I1). It can be seen that a reasonably good agreement was obtained between the FE models and the experimental data. In addition to accurately predicting the initial stiffness of the systems, the models of the B2 bolted connections were able to reproduce fairly closely the nonlinearity observed in the experimental load-displacement curves, corresponding to the bolts' yielding and the PUR foam's non-linear behaviour. The deviations observed are most likely due to the occurrence of (i) slipping between the sandwich panel and the top steel plate during the tests (which occurs up to the point where the gaps between the bolt holes and the bolts are closed), and/or (ii) bearing of the top GFRP face at the bolt holes, which was not taken into account in the modelling (the FE models did not incorporate any GFRP material damage model).

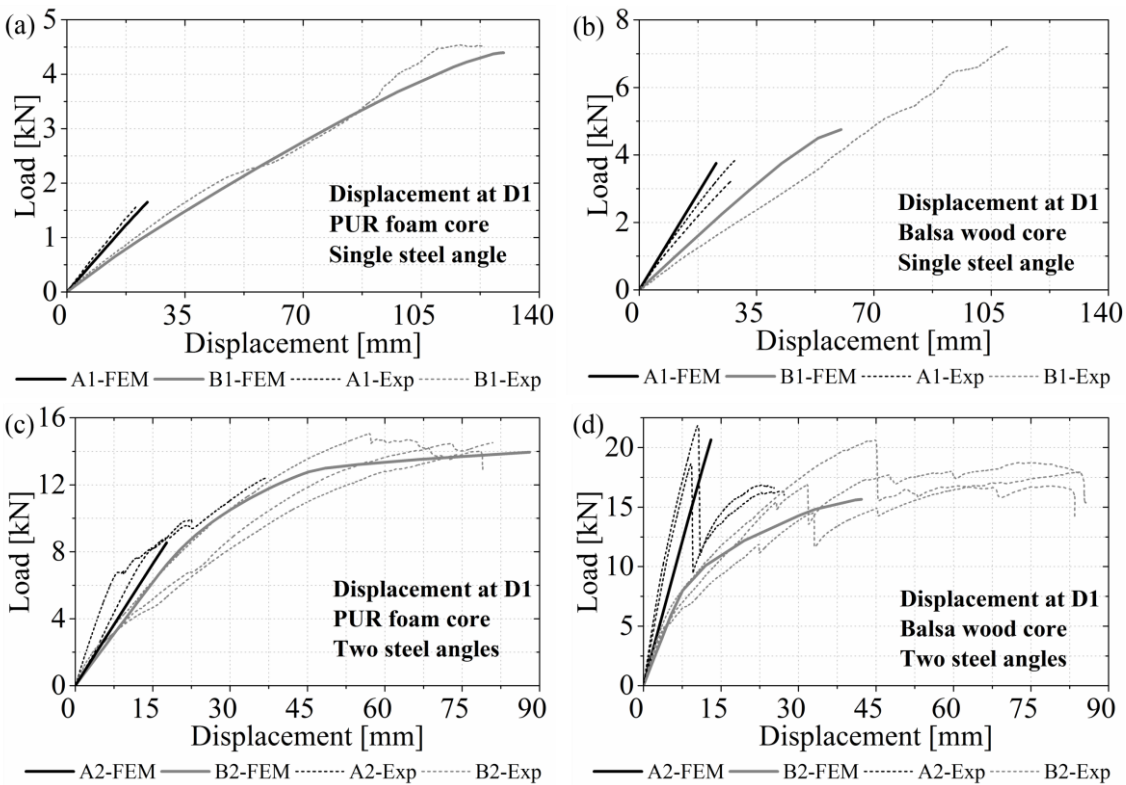


Figure 7.8. Load vs. displacement (D1) curves obtained from FEM: (a) specimens with PUR foam core and single (bottom) steel angle, (b) balsa wood core and single steel angle, (c) PUR foam core and two (top and bottom) steel angles, and (d) balsa wood core and two steel angles.

The stiffness values obtained from the FE models, either regarding the displacement at D1 or the rotation at I1, presented an overall average relative difference of ~15% to the experimental data. The highest relative differences in this regard were found for the A2 connection system, with the FE models being typically ~30% less stiff than what was experimentally observed, and also for the B1 connection system applied to balsa wood cored panels, for which the FE model was 25-30% stiffer than in the experiments. These differences are within the scatter that was obtained in the experimental data, and also within the typical scatter found for the mechanical properties of balsa wood, which has been previously reported to be as high as 28% [7].

Table 7.4. Comparison between FEM and experimental stiffness values at D1 and I1.

Core material	Connection system	Stiffness (D1 displacement) [kN/mm]			Rotational stiffness (I1 rotation) [kN/°]		
		Experimental	FEM	Difference [%]	Experimental	FEM	Difference [%]
PUR foam	A1	0.083	0.071	-14.5%	1.08	0.92	-14.9%
	A2	0.73	0.49	-33.1%	8.77	5.98	-31.8%
	B1	0.051	0.046	-11.1%	0.61	0.56	-7.0%
	B2	0.45	0.41	-7.4%	4.92	5.10	3.5%
Balsa wood	A1	0.15	0.16	7.4%	1.84	1.98	7.8%
	A2	2.26	1.65	-27.1%	29.75	19.63	-34.0%
	B1	0.071	0.093	30.0%	0.85	1.06	24.9%
	B2	1.11	1.12	1.2%	13.00	13.73	5.6%

Figure 7.9 shows the distribution of through-thickness (vertical) stresses in the adhesive (at mid-width and mid-thickness of the adhesive layer) along the length of the connection for the A1 and A2 connections obtained from the FE models. For the A1 connections, Figure 7.9-a plots the through-thickness stresses in the adhesive layer bonding the bottom face sheet of the two types of sandwich panels (balsa wood and PUR foam cores) to the supporting steel angle, for a load of 0.35 kN (for which the behaviour of both systems is well within the linear-elastic range). It can be seen that for both types of cores peeling stresses develop in the first 15 mm of the connection length. This is in good agreement with the failure initiation zone observed in the experiments for the A1-BAL-1 specimen, which failed in the adhesive bond at that same area. These localised peeling stresses occur together with through-thickness tensile stress concentrations in the bottom GFRP face and core materials, which also agree well with the failure modes experimentally observed in the A1-BAL-2 specimen (at the face-core interface) and in the A2-PUR-1 specimen (within the foam core).

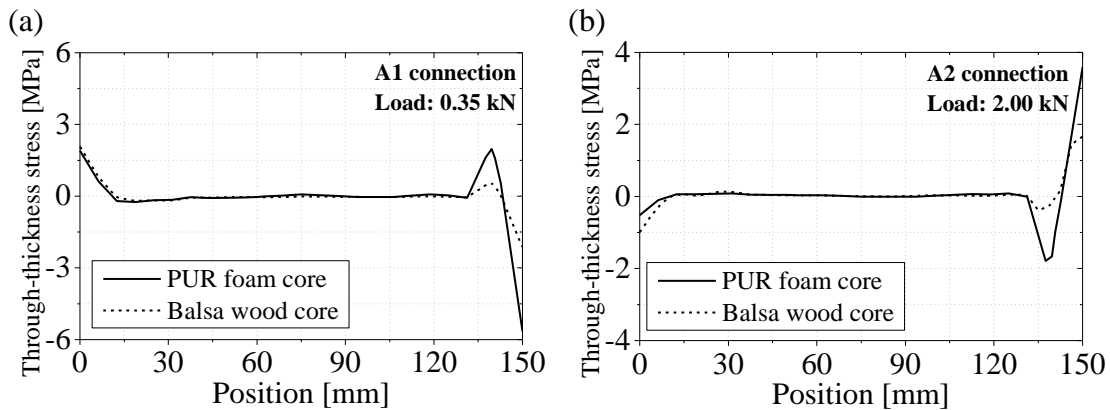


Figure 7.9. Through-thickness stresses in the epoxy adhesive: (a) A1 connections, and (b) top layer in the A2 connections.

From the FE predictions, these peeling stresses seem to be fairly independent of the type of core material, unlike the compressive stresses at the opposite end of the adhesive layer, which are significantly higher for the panel with the softer PUR foam core. This difference most likely stems from the higher curvature of the GFRP face sheets associated with the overall higher flexibility of those panels when compared to those made of balsa wood core. The curvature of the bottom GFRP face in contact with the adhesive also causes tensile stress peaks in the bond at a position circa 140 mm (Figure 7.9-a). This is due to the deformation compatibility between those two components, since the GFRP face would exhibit a certain curvature if unrestricted, whereas the adhesive layer remains approximately flat.

For the A2 connections, Figure 7.9-b shows the through-thickness stresses in the adhesive (again, at mid-width and mid-thickness of the adhesive layer) between the top face sheet of the panels and the top steel angle for a load of 2.00 kN, for which the behaviour of both connection systems was still linear-elastic. Once more, the significant peeling stresses at the front of the connection are in good agreement with the experimentally observed failure modes of the A2 connections, which initiated exactly at that location for all specimens (cf. Figure 7.5-c). In this configuration the peeling stresses show a high dependence from the core material, being significantly higher for specimens made of PUR foam core, due to the higher flexibility of these panels, as aforementioned. The compressive stress peaks in the adhesive at a position circa 140 mm are once more due to the deformation compatibility between the top GFRP face sheet and the adhesive layer.

Figure 7.10-a and Figure 7.10-b plot the deformed shape and the plastic strains in the bolts used in the B1 and B2 connections, respectively, used in PUR foam cored specimens. The

plotted values correspond to the maximum loads attained with each model: (i) 4.4 kN in the A1-PUR model, and (ii) 14.5 kN in the A2-PUR model. It can be seen that in both cases the predicted deformed shapes are in good agreement with the experimentally observed deformations (cf. Figure 7.6-a, c and e), with very significant plastic deformations in the bottom and upper parts of the bolts, respectively for the B1 and B2 connections. It can also be seen that the magnitude of such deformations is significantly higher in the latter connections, also in accordance with the experiments.

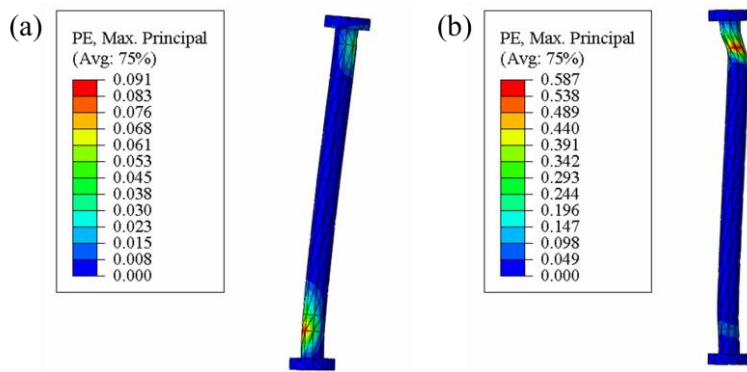


Figure 7.10. Plastic strains in the bolts: (a) B1-PUR, and (b) B2-PUR.

7.4. Moment-rotation relationships

7.4.1 Basis of calculation

As mentioned, the proposed connection systems provide some degree of rotational restriction to the sandwich panels at the supports, thus contributing to reduce the overall floor flexibility. This restriction may be considered equivalent to the effect of a rotational spring, with a characteristic stiffness k_θ , as illustrated in Figure 7.11-b for the case of the experimental setup adopted in this study (*i.e.*, a cantilever beam configuration).

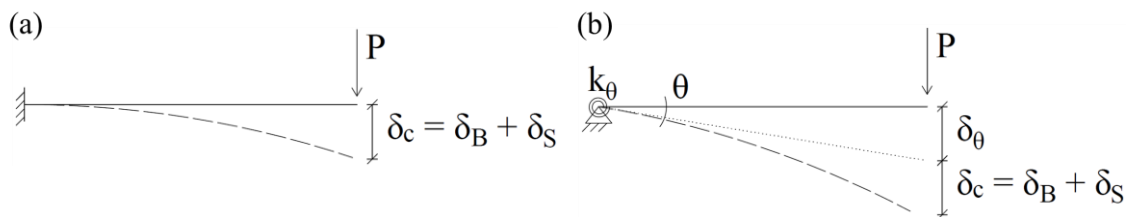


Figure 7.11. Deflections for (a) cantilever beam, and (b) elastically restrained beam (with connection system).

A perfectly clamped sandwich panel (Figure 7.11-a) would exhibit a deflection δ_c as a result of the applied point load (P). This deflection would correspond solely to the sandwich panel's deformations due to bending (δ_B) and shear (δ_S). However, as shown in Figure 7.11-b, due to the existence of bending moment at the support, the connection system's flexibility causes an additional rigid body movement of the panel (δ_θ) characterised by the rotation θ at the support. Therefore, if the panel is not fully clamped, the total deflection (δ) is the sum of the deflection due to the rigid body rotation of the panel at the support and the cantilever deflection due to the panel's bending and shear deformations, *i.e.*, $\delta = \delta_\theta + \delta_c$. Knowing both the total deflection of the system and the cantilever deflection, it is possible to determine δ_θ and, consequently, the corresponding rotation angle θ , given by $\theta = \arcsin(\delta_\theta/L)$, L being the cantilever span. Finally, considering the corresponding bending moment at the support, $M = P \times L$, a moment-rotation (M - θ) relationship and elastic rotational stiffness (k_θ) may be obtained for the connection system.

7.4.2 Cantilever models

To obtain the above-mentioned relationships, the FE models developed and validated in this study could be used to calculate the rotations at the support sections and hence to estimate the δ_θ values. However, such estimates might be influenced by the local compressibility of the sandwich panel's core; in addition, the definition of a specific node to calculate the rotation might be relatively ambiguous. To overcome such difficulties, an alternative method was adopted that consists of developing fully clamped cantilever models (Figure 7.12) for each type of sandwich panel ("PUR-Clamp" and "BAL-Clamp" models) and using those models to estimate the panels' respective δ_c values. The numerical load-deflection curves obtained in Figure 7.8 were compared with the baseline load-deflection curves given by the PUR-Clamp and BAL-Clamp models. As discussed in section 5.1, the difference between the two curves corresponds to the deflection caused by the rigid body rotation (δ_θ) resulting from the connection's flexibility.

The reference cantilever models were developed by adapting the previously described models of the connection systems tested, maintaining their basic features (identical meshes and elements, material properties, loading conditions, etc.). This adaptation basically consisted of eliminating the models' sections corresponding to the connection elements (including the panel length embedded into the connection), and fixing all degrees of freedom of the sandwich panels' nodes immediately after the connection (Figure 7.12).

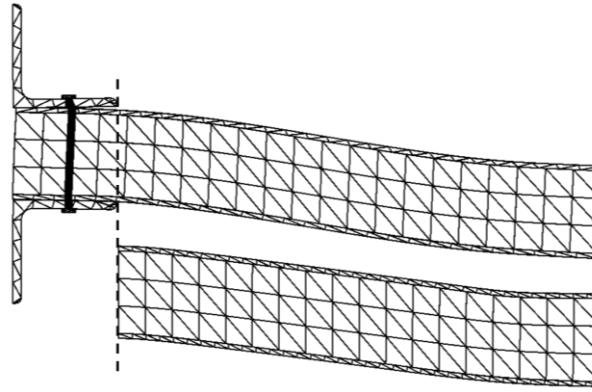


Figure 7.12. Comparison between deformed shapes for the B2-PUR model (top) and the corresponding PUR-Clamp cantilever model (bottom).

7.4.3 Characteristic curves

Figure 7.13 compares, as an example, the load-deflection curve for the B2-BAL connection model (balsa wood cored panel) to the curve obtained from the corresponding cantilever model (BAL-Clamp). As mentioned, the differences in the displacements calculated from the two models are due to the rotation at the support in the former model resulting from the connection system's deformability (*cf.*, Figure 7.11-b). Calculating that displacement difference (δ_θ) and the corresponding rotation (θ) as a function of the bending moment at the support, the $M-\theta$ curve may be obtained.

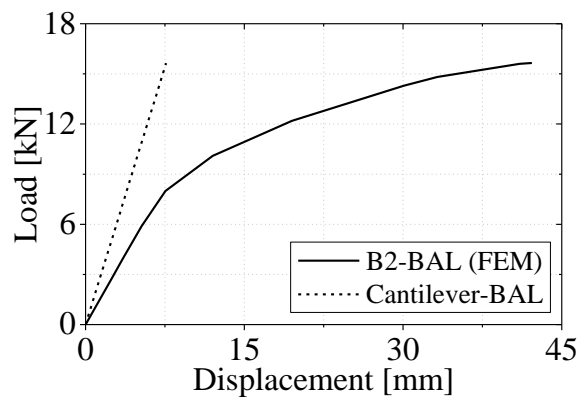


Figure 7.13. Comparison between $P-\delta$ curves of the B2-BAL and BAL-Clamp models.

Figure 7.14 presents these curves for each of the proposed connection configurations and panel types. It should be noted that for design purposes the nonlinear parts of the $M-\theta$ curves should not be considered, as progressive failure mechanisms developing within the sandwich panels and connection systems were not thoroughly modelled in this study (*e.g.*, crushing/bearing of the GFRP faces due to the bolts, cracking of the balsa wood cores and

adhesive layers). The fact that deformations at serviceability limit states should remain within the linear-elastic range of the structural response further contributes to this point. The rotational stiffness (k_θ) values (per unit width of the connection) corresponding to the linear-elastic branch of the $M-\theta$ curves are presented in Table 7.5.

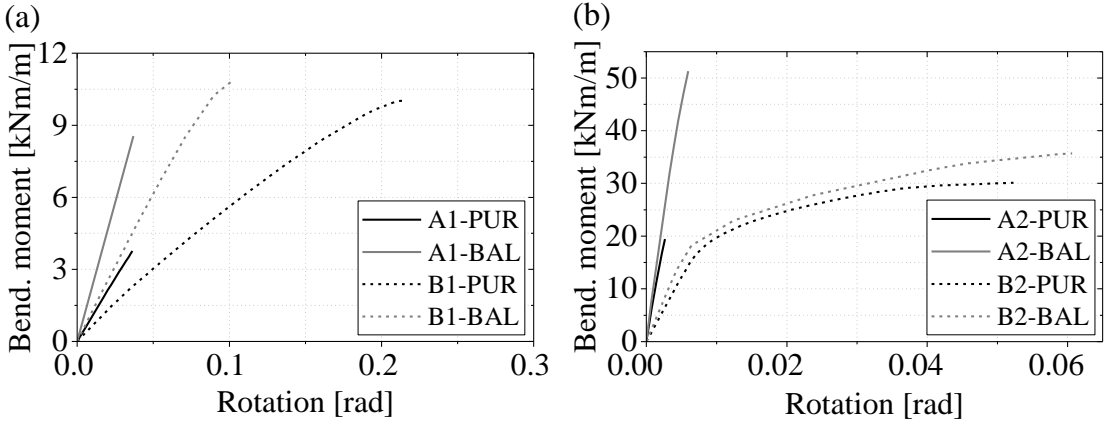


Figure 7.14. $M-\theta$ curves for connection systems (per unit width) with: (a) single steel angle (bottom only), and (b) two steel angles (top and bottom).

The low rotational stiffness of the single steel angle connections (A1 and B1) indicates that these are inefficient when bending moment mobilisation at the connection is a design requirement. In such cases, the addition of the top steel angle substantially improves the connection’s ability to mobilise negative bending moments, thus effectively reducing the maximum deflection of the sandwich panel floors (compared to a simply supported floor configuration).

Table 7.5. Rotational stiffness values of the proposed connection systems.

Core material	Connection system	Rotational stiffness (k_θ) [(kNm/rad)/m]
PUR foam	A1	105
	A2	8721
	B1	60
	B2	2447
Balsa wood	A1	231
	A2	10856
	B1	124
	B2	3199

It is also interesting to note the significant influence of the sandwich panel’s core material on the rotational stiffness of the connection. The stiffer core material (balsa wood) allowed for stiffer connections in all configurations. The rotational stiffness values of the single angle

connections, A1 and B1, for balsa wood cored panels were respectively 125% and 107% higher than those for the PUR foam cored panels, whereas for the double steel angle configurations these differences were less significant, but still important, with the A2 and B2 configurations being respectively 24% and 31% stiffer for the balsa wood panels than for the PUR foam counterparts.

7.5. Connection contribution for SLS verifications

The design of FRP sandwich panels for building floors is often limited by serviceability limit states (SLS) requirements (maximum allowable deflection), which are defined taking into account functionality aspects, users' comfort and protection of non-structural elements. The bending moment mobilisation capability offered by the connection systems proposed, particularly the A2 and B2 (and also the AB2) configurations, may provide a valuable contribution for controlling and limiting such deflections.

In a preliminary design setting, these contributions may be easily estimated by considering appropriate (and simple) structural models for the deflection calculations [8]. For instance, the mid-span deflection (δ) of a simply supported sandwich panel of span L under a uniformly distributed load (UDL)¹⁹ p may be calculated according to Timoshenko beam theory (Equation 6.1), in which the bending deflection (δ_B) is calculated using the face sheets' Young's modulus (E) and moment of inertia (I), and the shear deflection (δ_S) is estimated using the shear modulus (G) and effective shear area (A_v) of the core:

$$\delta = \delta_B + \delta_S = \frac{5}{384} \frac{pL^4}{EI} + \frac{1}{8} \frac{pL^2}{GA_v} \quad (7.1)$$

Considering the sandwich panel as being simply supported involves neglecting the rotational stiffness of the panel's supports (*i.e.*, the panel-to-wall connections). To compute the panel's mid-span deflection under a semi-rigid support situation, the following closed-form equation proposed by Turvey [9] for shear deformable beams may be used,

¹⁹ Concentrated or point loads were not explicitly considered in the current analysis (although both panel configurations used in the experiments are able to withstand the design point load defined in Eurocode 1).

$$\delta = \frac{1}{384} \frac{pL^4}{EI} \left(\frac{1 + 48\alpha + 10\beta + 96\alpha\beta}{1 + 2\beta} \right) \tag{7.2}$$

where $\alpha = EI/GA_vL^2$ is the dimensionless shear flexibility of the sandwich panel and $\beta = EI/k_\theta L$ is the dimensionless rotational flexibility of the connections.

In order to validate this formulation for the current application, an FE model of a 4 m span sandwich panel was developed, based on the previously presented models and considering PUR foam as the core material and B2 floor-to-wall connection system (Figure 7.15). Symmetry simplifications were adopted in order to reduce the model size. Maximum (mid-span) deflections were obtained from the numerical model and compared with the analytical predictions for: (i) a simply supported configuration under a 1.98 kN/m² UDL (corresponding to a panel self-weight of 0.38 kN/m², other permanent loads of 1.0 kN/m², and an imposed/live load of 2.0 kN/m² with a quasi-permanent combination factor of 0.3, according to Eurocode 1), and (ii) considering the B2 connection system and a sandwich panel with the same cross-sectional geometry used throughout this study. The results obtained for the short-term deflections are summarised in Table 7.6.

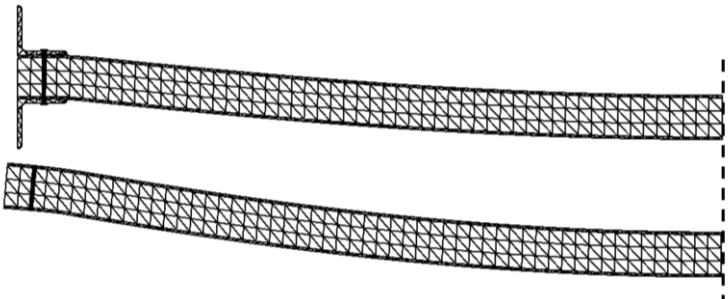


Figure 7.15. Deformed shape for the 4 m span sandwich panel, either supported using the B2 connection (top) or simply supported (bottom).

Table 7.6. Short-term deflections from analytical and FEM models for the 4 m span sandwich panel.

Model		Bending deflection (δ_B) [mm]	Shear deflection (δ_s) [mm]	Total deflection (δ) [mm]
Simply supported	Analytical	4.17	3.58	7.75
	FEM	-	-	7.64
B2 connection	Analytical	1.65	3.58	5.23
	FEM	-	-	4.87

A very good agreement was found between the analytical predictions and the numerical results for the short-term mid-span displacement of the sandwich panel connected with system B2 (relative difference of 7.5%). Additionally, the results obtained also illustrate the substantial deflection reductions that may be obtained from the sandwich floor panel-to-wall connections proposed in this chapter (compared to the deflections corresponding to simply supported panels). In the present example, a deflection reduction of approximately 35% was achieved. It is worth mentioning that this reduction is mostly achieved by limiting the bending flexibility of the panel, as illustrated by the equal analytical shear deflection estimates for the simply supported and semi-rigidly supported configurations given in Table 7.6. This is in agreement with Timoshenko beam theory.

Figure 7.16 presents those reductions for spans between 2 m and 5 m, estimated using Equations (7.1) and (7.2) for simply supported sandwich panels and for semi-rigidly supported panels, respectively. To allow for result comparability, the only parameter that was changed was the span length, *i.e.*, the cross-sectional geometry was kept constant for all spans. It should be noted that in real applications the panels' cross-sectional dimensions could be adapted and optimised for each span. However, this optimisation exercise has multiple solutions depending on many factors (*e.g.*, material properties, relative cost of materials, building physics requirements), being beyond the scope of this study.

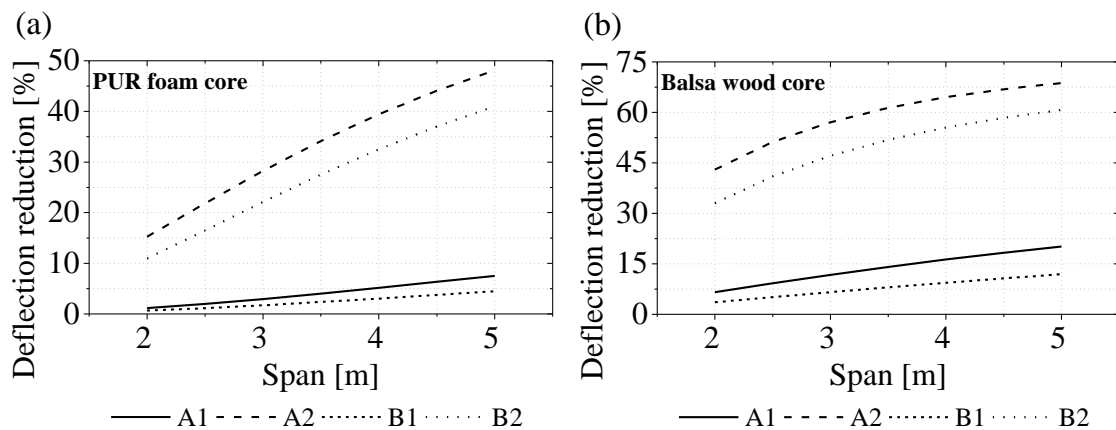


Figure 7.16. Deflection reductions for different spans using the proposed connection systems for panels with: (a) PUR foam core, and (b) balsa wood core.

For all situations presented in Figure 7.16, it can be seen that the estimated deflection reductions increase with the span length. This is due to the increasing relative importance of bending deformations to the overall panel deflection compared to shear deformations, which become less significant with increasing span for all connection configurations, as illustrated

in Figure 7.17. This also explains the higher deflection reductions obtained with the balsa wood cored panels when compared to those made of PUR foam core, since balsa wood presents a substantially higher shear modulus and thus lower shear flexibility (*cf.* chapter 4, section 4.3.1.3).

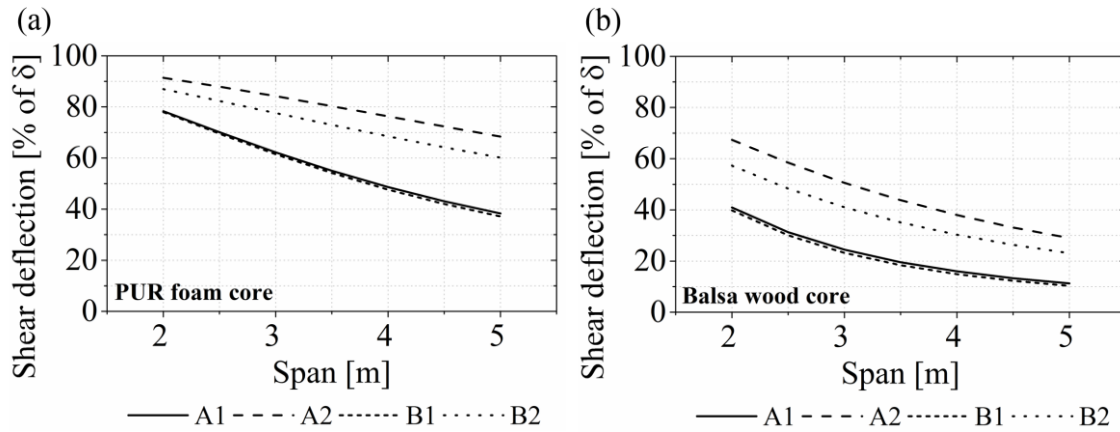


Figure 7.17. Shear contribution to total mid-span deflection (δ) for different spans using the proposed connection systems for panels with: (a) PUR foam core, and (b) balsa wood core.

Those deflection reductions can be very valuable for SLS verifications, as illustrated in Figure 7.18. This figure shows the total deflections obtained in each configuration and compares them with a typical serviceability limit states deflection limit of span/500. A curve representing half of that limit (span/1000) is also plotted.

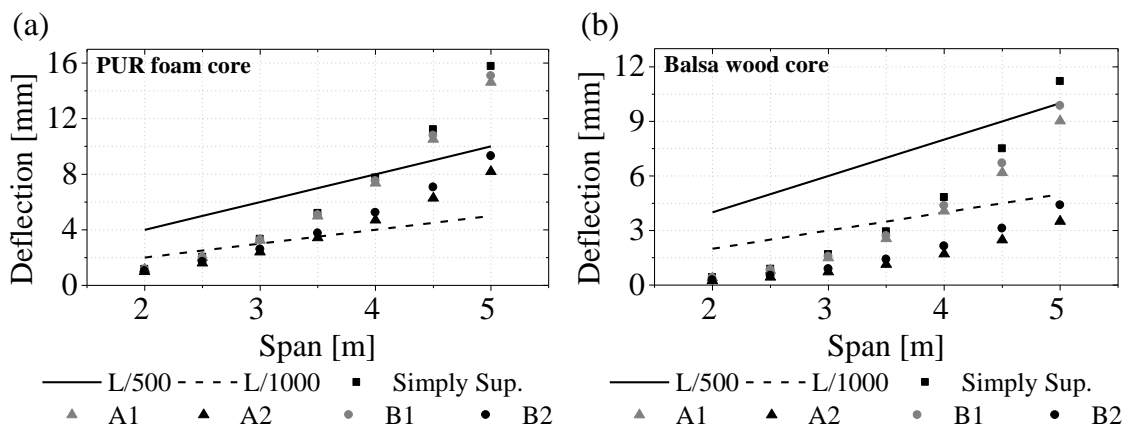


Figure 7.18. Deflections for different spans using the proposed connection systems for panels with: (a) PUR foam core, and (b) balsa wood core.

As may be observed in Figure 7.18, the adoption of either the A2 or B2 connection systems allows for in service deflections that are lower than span/500 for all considered spans (in some cases making the difference between fulfilling or not such deflection limit), and even

lower than span/1000 in most cases. It is worth mentioning the importance of guaranteeing elastic deflections at serviceability well below the SLS limit values so that when accounting for long-term deflections, namely those due to creep (a phenomenon that is addressed in Part IV of this thesis), the serviceability deflection limits may still be fulfilled.

7.6. Concluding remarks

Solutions for the connections between sandwich panel floors and load-bearing building walls for use in building rehabilitation were proposed and developed. Their performance under vertical loading was assessed experimentally, numerically and analytically, allowing the following main conclusions to be drawn:

1. The experimental and numerical investigations validated the connection systems proposed, showing their potential for application in building rehabilitation.
2. The use of a top steel angle considerably increased the rotational stiffness of floor panel-to-wall connections. This constructive detail may be useful when a certain clamping level is required at the supports.
3. Adhesively bonded connections typically presented lower deformation capacity and higher stiffness than bolted connections, exhibiting brittle failure modes. Bolted connections presented plastic deformations and damage distribution through the different connection and panel components, a potentially interesting characteristic from an energy dissipation through progressive damage standpoint (*e.g.*, under seismic actions).
4. The mechanical properties of the core material influenced the overall connection behaviour, namely the rotational stiffness of the connections, and in some circumstances their failure mode (particularly for the A2 configuration); in this regard, the best overall performance was obtained with the stiffer core material (balsa wood).
5. A method was proposed to calculate the moment-rotation relationship of the connection systems, which is based on decomposing the total deflections into those corresponding to a cantilever (perfectly clamped) and those due to the rigid body rotation about the supports; the method was duly validated by the FE models,

allowing to derive characteristic $M-\theta$ curves and rotational stiffness values (k_θ) for each connection system.

6. An analytical method proposed by Turvey [9], based on Timoshenko beam theory and that takes into account the rotation stiffness of the supports, was used to calculate the mid-span deflections of sandwich panels supported using the connection systems developed in this study. The results obtained highlighted the potential influence of the support conditions on the total floor deformability.

The last conclusion assumes special importance given the fact that the design of sandwich panels for building floors is generally governed by deformability requirements. The correct design and *in-situ* execution of the connections between the sandwich panel floors and their supports, and the consideration of their actual contribution to the structural behaviour can be a valuable resource for deflection control in SLS verifications. This could potentially allow for more cost-efficient sandwich panel designs, with thinner faces and cores, thus increasing their application potential for building rehabilitation and civil engineering projects in general.

It is worth mentioning that the current study did not consider the effects of horizontal/in-plane loading of the sandwich floors. This aspect encompasses the study of their behaviour under horizontal (seismic) loads, and the effects of the membrane stresses originating from the in-plane restriction imposed by the connections along the full perimeter of the floors. Both these aspects are potentially very relevant for the global performance of the sandwich floors and their connections, and should be addressed in future research.

7.7. References

- [1] Correia, J.R., Garrido, M., Gonilha, J.A., Branco, F.A., Reis, L.G. (2012), “GFRP sandwich panels with PU foam and PP honeycomb cores for civil engineering structural applications: Effects of introducing strengthening ribs”, *International Journal of Structural Integrity*, 3(2), 127-147.
- [2] Meireles, H., Bento, R. (2013). “Rehabilitation and strengthening of old masonry buildings”, Report DTC no. 02/2013, ICIST, IST, University of Lisbon, Lisbon.

- [3] Appleton, J. (2003). *Reabilitação de Edifícios Antigos: Patologias e Tecnologias de Intervenção*, Edições Orion, 1st ed., September 2003 [in Portuguese].
- [4] Simões, A., Bento, R., Cattari, S., Lagomarsino, S. (2014). “Seismic performance-based assessment of "Gaioleiro" buildings”, *Engineering Structures*, Vol. 80, pp. 486-500.
- [5] Deshpande, V.S., Fleck, N.A. (2000). “Isotropic constitutive models for metallic foams”, *Journal of the Mechanics and Physics of Solids*, Vol. 48, pp. 1253-1283.
- [6] Sika AG (2014). *Sikadur[®]-31 EF*, Product Data Sheet, Edition 23/01/2014.
- [7] Osei-Antwi, M., de Castro, J., Vassilopoulos, A.P., Keller, T. (2013). “Shear mechanical characterization of balsa wood as core material of composite sandwich panels”, *Construction and Building Materials*, 41, 231-238.
- [8] CEN WG4 (2014). *Fibre Reinforced Polymer Structures – Scientific and Technical Report*, submitted for approval to CEN/TC 250.
- [9] Turvey, G.J. (1997). “Analysis of pultruded glass reinforced plastic beams with semi-rigid end connections”, *Composite Structures*, Vol. 38(1-4), pp. 3-16.

Part IV

Creep behaviour

Preamble

Due to the viscoelastic nature of their constituent materials, composite sandwich panels can present significant creep deformations in the long-term. During the typical service life periods required for civil engineering works, these creep deformations may easily exceed the elastic (instantaneous) ones and, must be duly accounted for.

Part IV of this thesis presents an extensive experimental study of the creep behaviour of the various materials that comprise the composite sandwich panels, particularly focusing on the creep (and its temperature dependence) of the PUR foam and of the GFRP face laminates. The creep of response of full-scale panels of different typologies under uniformly distributed bending loads is experimentally assessed. Additionally, a simple and easily implementable analytical model is proposed for the prediction of creep deflections in sandwich panels, which may be used in their structural design.

The work presented in this chapter resulted in the following publications:

Garrido, M., Correia, J.R., Branco, F.A., Keller, T. (2014). “Creep behaviour of sandwich panels with rigid polyurethane foam core and glass-fibre reinforced polymer faces: Experimental tests and analytical modelling”. *Journal of Composite Materials*, Vol. 48(18), pp. 2237-2249.

Garrido, M., Correia, J.R., Keller, T. (2016). “Effect of service temperature on the flexural creep of vacuum infused GFRP laminates used in sandwich floor panels”. *Composites Part B: Engineering*, Vol. 90, pp. 160-171.

Garrido, M., Correia, J.R., Keller, T. (n.d.). “Effect of service temperature on the shear creep response of rigid polyurethane foam used in composite sandwich floor panels”. *Construction and Building Materials*, submitted to publication.

Garrido, M., Correia, J.R., Keller, T., Cabral-Fonseca, S. (n.d.). “Creep of sandwich panels with longitudinal reinforcement ribs for civil engineering applications: experiments and composed creep modelling”. *Journal of Composites for Construction*, submitted to publication.

Chapter 8

Effect of service temperature on the creep of PUR foam

8.1. Introduction

In the civil engineering domain, sandwich panels present high potential for application in building floors [1]. However, unlike in other industries, sandwich panels used in such structural members often support significant permanent loads, meaning that it is important to account for their creep deformability, especially when considering that the service life required for civil engineering works is usually equal to or higher than 50 years. In fact, sandwich panels frequently comprise viscoelastic materials, such as polymeric adhesives, resins, foams, honeycombs and engineered wood, which typically show significant creep under permanent loads [2-4].

Rigid polyurethane (PUR) foam is one of the most commonly used core materials in sandwich panels for civil engineering applications. Such foams have a strongly temperature dependent viscoelastic behaviour, furthermore being highly prone to creep even at room temperature [5,6]. However, experimental data regarding the influence of temperature on the creep response of rigid PUR foams is scarce. In addition, practical design methodologies need to be developed to account for the effects of temperature on the creep behaviour of such foams.

This chapter aims to address these issues, by presenting an experimental investigation on the shear creep behaviour of a rigid PUR foam exposed to different in-service temperatures (20°C to 28°C, likely to be found in building floors) and shear stress levels (11% to 44% of the foam's shear strength) for periods ranging between 1300 h and 2100 h. A modelling approach is proposed based on Findley's power law formulation [7]. This formulation was adapted to include an Arrhenius law temperature dependence for the power law parameters that define the creep rate. The generalised equation obtained was used (i) to model the foam's

time-dependent shear deformations as a function of the shear stress level and in-service temperature, and (ii) to derive expressions for the time-dependent shear moduli and shear creep coefficients, thus providing a practical tool for the design of sandwich structures comprising a rigid PUR foam core. The final part of the chapter compares the long-term creep predictions provided by the proposed model with results obtained from the application of the time-temperature superposition principle (TTSSP) [8] to the experimental data, allowing to assess the consistency and agreement between the two approaches.

8.2. Literature review

While several studies addressed the creep behaviour of polymer foams, few data exist on the influence of temperature on the creep of rigid PUR foams. Moreland *et al.* [9] and Briody *et al.* [10] have studied the influence of temperature on the compressive creep behaviour of flexible PUR foams typically used for cushioning and packaging applications. Such foams differ significantly (in chemical composition and mechanical behaviour) from the rigid type used for sandwich construction, and are typically subjected to much higher strains (a range of 10% to 60% is common), which makes the buckling of the cell walls the main deformation mechanism. However, it is interesting to note that the findings of the two works are not in agreement. On one hand, Moreland *et al.* [9] reported an overall decrease in the creep rates of such foams (the authors did not specify the density of the investigated foams) for the range of 30°C to 125°C. On the other hand, the results of Briody *et al.* [10] highlighted significant increases in creep rate as a function of temperature, with increasing temperatures causing the acceleration of the foam's creep (the authors investigated a foam with a density of 85 kg/m³).

Rigid open cell polymer foams were studied by Huang and Gibson [6], who adapted Findley's power law formulation [7] to model the creep of such foams. This adaptation was made considering the creep of the solid polymer and the ratio between the elasticity moduli of the foam and that of the solid polymer, according to the micromechanics model of Gibson and Ashby [11]. To experimentally validate the model, the authors carried out shear creep tests on PUR foams with densities ranging between 32 kg/m³ and 96 kg/m³ and shear stresses between 10% and 40% of the foam's yield stress, for durations of 1200 h. The authors found that the PUR foam was linear viscoelastic for stress levels lower than half of its yield

strength, and that creep response was higher in lower density foams. However, the influence of temperature on the foams' creep response was not considered.

Davies and Craveur [12] performed shear creep tests on closed cell poly(vinyl chloride) (PVC) foams, for shear stresses ranging from 0.24 MPa to 0.56 MPa (approximately 50% of the foam's shear strength at the highest stress level) and temperatures of 20°C and 50°C. Test durations ranged from ~2000 h to ~10000 h. Acceleration of the creep response of such foams was found to occur with increasing temperature and/or stress level. However, the authors did not provide a quantified description of the influence of these factors on the viscoelastic response.

Andrews *et al.* [13] proposed expressions for the prediction of the steady-state creep rate of cellular solids when subjected to high temperatures, following the general approach of Gibson and Ashby [11], extending it to time-dependent deformations and incorporating an Arrhenius law dependence of temperature. The authors carried out a set of compression creep experiments on an open-cell aluminium foam, for temperatures between 275-350°C (an order of magnitude higher than that typically encountered in civil engineering service conditions) and stress levels between 14-49% of the foam's yield stress (test durations ranged from 0.03 h to 80 h). They found that the proposed steady-state creep model provided good predictions of the experimental results for such a metallic foam.

As several previous studies have shown [5-7], the creep response of rigid PUR foams in the linear viscoelastic range is very well explained by a power law dependence of time. Power law (of time) creep developments contrast with steady-state approaches by not considering a constant creep rate at any point in time, but rather an exponentially decreasing one. Owing to its successful application in polymers, and polymer foams in particular, Findley's power law formulation [7] was used in the present study. This formulation was extended to include an Arrhenius law temperature dependence, as detailed in the following section.

8.3. Theoretical formulation

8.3.1. Findley's power law

Equation (8.1a) describes the basic expression for Findley's power law formulation, adapted for shear strains and stresses, where γ is the total shear strain, τ is the applied shear stress, t

is the time elapsed after load application, t_0 is the time unit considered (to normalise the time parameter, thus guaranteeing the dimensional consistency of the equation), m is the creep amplitude, and n is the time exponent. This equation separates the time-dependent shear strain in two components: (i) the elastic strain (γ_0), and (ii) the viscoelastic strain ($m(t/t_0)^n$). These two components are considered to follow a hyperbolic sine dependence of the applied shear stress, as per Equation (8.1b). In this equation, γ'_e is the reference instantaneous shear strain, τ_e is reference stress level associated with γ'_e , m' is the reference creep amplitude and τ_m is the reference stress level associated with m' .

$$\gamma(\tau, t) = \gamma_0 + m \left(\frac{t}{t_0} \right)^n \quad (8.1a)$$

$$\gamma(\tau, t) = \gamma'_e \sinh \left(\frac{\tau}{\tau_e} \right) + m' \sinh \left(\frac{\tau}{\tau_m} \right) \left(\frac{t}{t_0} \right)^n \quad (8.1b)$$

The creep amplitude (m) is typically proportional to stress, while the time exponent (n) is stress-independent and may be taken as a material constant for a given hygrothermal condition [6]. By performing creep experiments for different stress levels, it is possible to obtain multiple m values and thus estimate m' and τ_m by noting that $m = m' \sinh(\tau/\tau_m)$ and solving the resulting equation system (one equation per stress level). A similar procedure may be used to estimate γ'_e and τ_e for the elastic response. The n value may then be taken as the average value obtained from all considered stress levels.

8.3.2. Temperature dependence

The parameters γ'_e and τ_e are associated with the elastic response of the material, which may be strongly temperature-dependent for such foams [14]. However, for small temperature amplitudes well below the glass-transition temperature²⁰ (T_g) of the material (such as the 20-28°C range considered in this study), the elastic properties are not expected to be significantly affected by temperature. On the other hand, the m' and n parameters, which define the viscoelastic response of the material, are expected to be temperature-dependent if the foam's creep response is affected by temperature. Their variations reflect temperature

²⁰ For the PUR foam used in this study, $T_g = 88.5^\circ\text{C}$, as detailed in section 8.4.1.

activated physical processes affecting polymer chain mobility. Such temperature dependent processes are frequently well described by the Arrhenius equation, provided that the same process controls the response within the considered temperature range, and that it does so throughout the service life of the material. Assuming this hypothesis, the m' and n parameters may be considered as creep rate constants, related to temperature as per Equations (8.2) and (8.3), respectively,

$$m'(T) = A_{m'} e^{\left(\frac{-E_{m'}}{RT}\right)} \quad (8.2)$$

$$n(T) = A_n e^{\left(\frac{-E_n}{RT}\right)} \quad (8.3)$$

where T is the temperature (in Kelvin), R is the universal gas constant (~ 8.314 J/mol.K), $E_{m'}$ and E_n are the activation energy values associated with m' and n , respectively, and $A_{m'}$ and A_n are the respective pre-exponential factors.

As previously mentioned, the τ_e and τ_m parameters are reference stresses associated with γ_e' and m' , respectively. In the current study, it is assumed that they may be considered temperature independent, and that the temperature dependence of m' and n suffices to describe the effects of temperature on the creep behaviour of the PUR foam²¹.

8.3.3. Time and temperature dependent properties

For low values of the hyperbolic sine arguments (*i.e.*, τ/τ_e and τ/τ_m), the hyperbolic sine stress dependence in Equation (8.1b) may be replaced by a linear one [15]. In fact, such a procedure amounts to neglecting the third and higher order terms in the Taylor series expansion of the hyperbolic sine functions, and its validity depends on the relative importance of these terms. However, adopting this simplification (and also considering the temperature dependence given by Equations (8.2) and (8.3)), it is possible to rewrite Equation (8.1b) as follows:

²¹ For the material and thermomechanical conditions used in this study, this assumption is supported by the experimental results presented in section 8.5.1.

$$\gamma(\tau, t, T) = \frac{\gamma_e'}{\tau_e} \tau + \frac{m'(T)}{\tau_m} \tau t^{n(T)} \quad (8.4)$$

Furthermore, by considering $G_e = \tau_e/\gamma_e'$ and $G_t(T) = \tau_m/m'(T)$ as being, respectively, the elastic shear modulus (assumed to be nearly constant for the temperature range considered in this study) and the viscoelastic shear modulus of the material, it is possible to obtain the following expression for the time and temperature dependent shear modulus:

$$G(t, T) = \frac{G_e \cdot G_t(T)}{G_t(T) + G_e t^{n(T)}} \quad (8.5)$$

It should be noted that the temperature dependence of the elastic modulus must also be taken into account for temperature ranges in which the elastic properties of the foam present significant variations [14]. However, since this is not the case of the present study, the elastic shear modulus is assumed to be constant with temperature in the discussion that follows.

Finally, expressions for the time-temperature dependent creep coefficients and shear modulus reduction factors may be obtained. Creep coefficients (ϕ) provide a measure of how much a material's deformations will increase relative to the initial elastic deformations (γ_0), during a certain period of creep (*i.e.*, $\gamma(t, T) = \gamma_0[1 + \phi(t, T)]$). Shear modulus reduction factors (χ) are obtained from the ratio between the time-temperature dependent modulus and the initial elastic modulus of the material for a given creep time (*i.e.*, $\chi(t, T) = G(t, T)/G_e$). These values may be calculated using Equations (8.6) and (8.7), which were derived following a procedure similar to that described in [5].

$$\phi(t, T) = \frac{G_e}{G_t(T)} t^{n(T)} \quad (8.6)$$

$$\chi(t, T) = \frac{1}{1 + \phi(t, T)} \quad (8.7)$$

8.4. Experimental programme

8.4.1. Materials and test setup

The rigid PUR foam with a density of 87.4 kg/m^3 , previously characterised in terms of elastic mechanical properties in chapter 4, was used in this study. The foam's shear strength, shear modulus, and distortion at failure are, respectively, $0.32 \pm 0.06 \text{ MPa}$, $8.65 \pm 1.04 \text{ MPa}$, and $0.043 \pm 0.006 \text{ m/m}$. Figure 8.1 shows a stress vs. strain curve representative of the results obtained in the shear failure tests of the PUR foam, together with the adopted creep stress levels that are marked as an indicative reference.

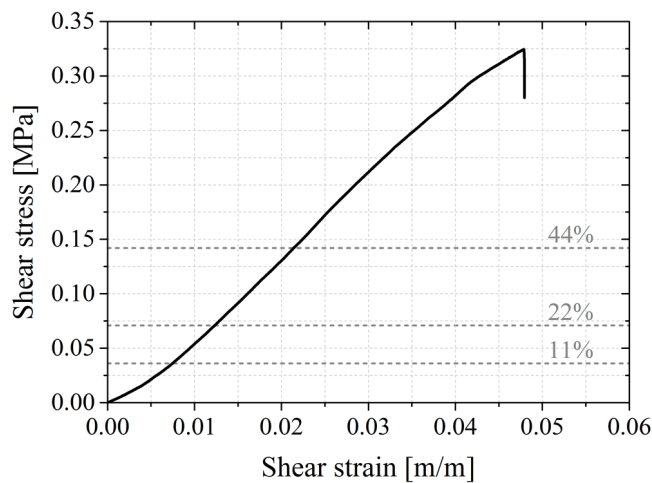


Figure 8.1. Representative stress vs. strain curve from shear failure testing of the PUR foam (horizontal lines represent stress levels used in the creep experiments).

The glass transition temperature of the material ($T_g = 88.5^\circ\text{C}$) was determined from dynamic mechanical analysis (DMA in dual cantilever setup, with heating rate of $1^\circ\text{C}/\text{min}$ and frequency of 1 Hz), considering the peak of the loss modulus curve. The DMA results were qualitatively very similar to those reported in chapter 4 for a similar, but slightly less dense (68 kg/m^3) rigid PUR foam.

Creep experiments on the rigid PUR foam were carried out at three different nominal temperatures (20°C , 24°C and 28°C) under three different nominal shear stress levels in the linear elastic range of the foam's response (11%, 22% and 44% of the foam's shear strength, *cf.* Figure 8.1). Table 8.1 lists the specimens tested (one for each condition), in which the labelling $T_i\text{-}S_j$ corresponds to a specimen tested at temperature i and stress level j . The experiments were carried out in a temperature controlled room, with relative humidity (RH) being monitored throughout the duration of the tests, which were 2107 h, 1301 h, and 1412 h

for the 20°C, 24°C, and 28°C conditions, respectively. Such test durations are higher than or within the range of the relevant creep experiments detailed in the literature review presented in section 8.2.

A custom setup was assembled (identical to that used in [11]) for the shear creep experiments, in which PUR foam specimens with nominal dimensions of 250×250×120 mm³ (height, width, thickness) were suspended from a closed steel frame and loaded in simple shear using dead weights (Figure 8.2). The specimens were adhesively bonded (using a 0.5 mm layer of polyurethane adhesive, *Sikaforce 7710 L100*) to two steel plates: (i) a posterior plate fixed to the frame's top beam, and (ii) an anterior steel plate containing a fixture designed to suspend the vertical dead load and apply it as shear loading to the specimen, while minimizing the load eccentricity due to the specimen's thickness. The dead loads consisted of a combination of steel plates, concrete blocks and water filled barrels, with the load value being fine-tuned by varying the water level inside the barrels (which were then sealed). The load values were checked before and after each creep test, with no significant weight variations being found throughout the duration of the experiments. Load application was smooth (over approximately 1-2 seconds), comprising a gradual lowering of the weights.

The vertical displacement at the unrestrained (loaded) face of the specimens was monitored using displacement transducers with precision of 0.01 mm. The transducers were mounted on the horizontal steel beam immediately next to the specimen fixation area, in order to eliminate measurement errors introduced by the beam's deformations after loading. The shear deformation (γ) was calculated dividing the measured vertical displacement (δ_v) by the specimen thickness (t), *i.e.*, $\gamma = \delta_v/t$.

The displacement measurements were made automatically during the first 72 hours. A sampling rate of 1 Hz was used during the loading operation and for the first hour. The rate was then reduced to 0.02 Hz (one reading each 50 seconds) for the subsequent duration of automatic measurement. After the first 72 hours and until the end of the creep tests, periodic measurements were made using dial gauge indicators with precision of 0.001 mm (Figure 8.2).

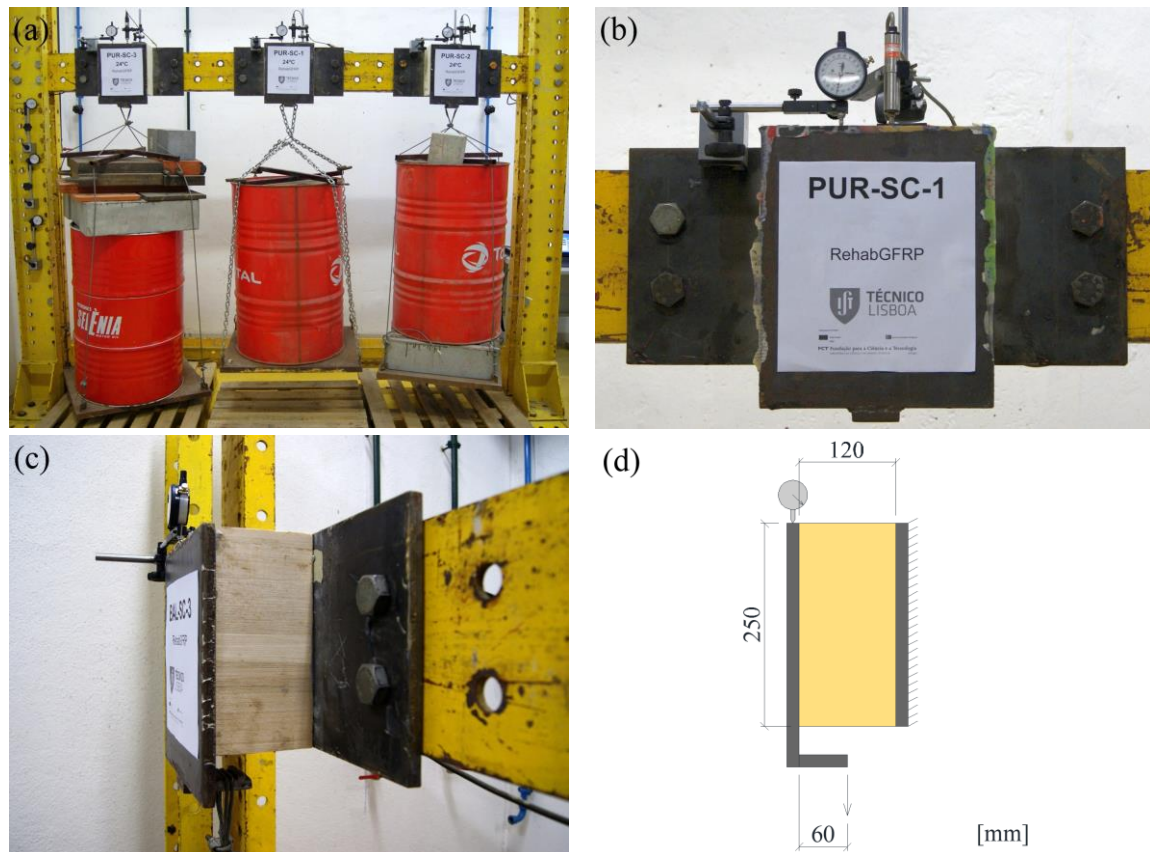


Figure 8.2. Experimental setup for the shear creep tests: (a) overall view, (b) frontal view of the assembly, (c) lateral view of the assembly²², and (d) schematic view.

8.4.2. Experimental results and simple power law fitting

Figure 8.3 shows the evolution of the shear strains with time for the different specimens and Table 8.1 provides a summary of the experimental results, discussed next.

Upon load application, a consistent elastic response was observed for all specimens characterised by a global average shear modulus of 8.03 ± 0.29 MPa, in good agreement with the foam's mechanical properties (*cf.* section 4.1). Considering the average shear moduli per test temperature (Table 8.1), a slight decrease was observed with increasing temperature, albeit such variations generally remained within the obtained standard deviations. Nonetheless, this tendency agrees well with previous findings about the reduction in the shear modulus of PUR foam with temperature [14] (*cf.* chapter 4).

²² Figure 8.2-c illustrates the exact setup that was used in the shear creep tests of the PUR foam, albeit the material depicted is balsa wood.

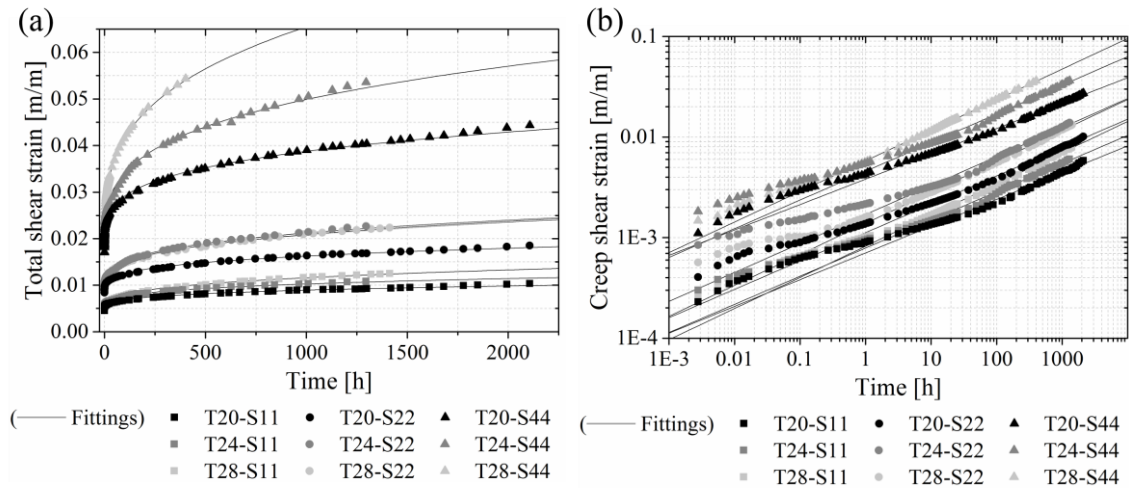


Figure 8.3. Evolution of experimental shear strains with time for the different load levels and temperatures [including power laws fittings, *cf.* Equation (8.1a)]: (a) linear plot of total strain, and (b) log₁₀ plot of creep strain.

The specimen T28-S44 (tested for the highest temperature of 28°C and shear stress level of 44% of the shear strength) failed in shear (within the bulk of the material) sometime between measurements taken after 402 h and 477 h of creep. The last shear strain measurement was 0.0543 m/m (for a creep time of 402 h), a value that exceeds the average strain at failure for this PUR foam (0.043 ± 0.006 m/m). It is worth highlighting that this failure occurred for a lower shear stress compared to half of the foam’s strength, a relatively low and easily achievable in-service temperature (28°C), and for a creep period of less than 20 days. This result supports the importance of the creep phenomenon in this type of foams, and highlights the need to duly consider it when designing composite sandwich panels with PUR foam cores.

The moments marking the end of load application (and thus the initiation of creep) were defined by the magnitude change of the derivative values of the deformation *vs.* time curves. The creep response of the PUR foam followed a typical power law development for all temperatures and load levels, characterised by linearity in logarithmic plot (*cf.* Figure 8.3-b), despite some small deviations in the first hours of creep (~10 h). As expected, total shear strains increased with both temperature and stress level. The creep amplitude (m) and time exponent (n) values of each specimen (*i.e.*, each test condition) were determined from fitting power law functions to the experimental data. As may be observed in Figure 8.3-a, a good

fit of the individual power laws to the experimental creep curves was obtained. The fitting values are listed in Table 8.1 and are plotted per temperature and stress level in Figure 8.4.

Table 8.1. Summary of experimental results.

Temperature	20°C			24°C			28°C		
	T ¹ : 19.9 ± 0.4°C, RH ² : 63.2 ± 5.4%			T: 24.0 ± 0.7°C, RH: 50.4 ± 6.3%			T: 28.0 ± 0.2°C, RH: 49.6 ± 5.5%		
Specimen	T20-S11	T20-S22	T20-S44	T24-S11	T24-S22	T24-S44	T28-S11	T28-S22	T28-S44
τ [MPa]	0.035	0.071	0.141	0.036	0.073	0.143	0.036	0.072	0.143
γ_0 [m/m]	0.0045	0.0084	0.0170	0.0048	0.0088	0.0172	0.0046	0.0092	0.0181
G_e [MPa]	7.84	8.39	8.28	7.50	8.28	8.27	7.91	7.85	7.91
(average ± standard deviation)	8.17 ± 0.29			8.02 ± 0.45			7.89 ± 0.04		
m ($\times 10^{-3}$) [-]	0.705	1.121	3.812	0.788	1.698	4.564	0.822	1.386	5.802
n [-]	0.266	0.282	0.252	0.280	0.288	0.285	0.310	0.308	0.304
(average ± standard deviation)	0.267 ± 0.015			0.284 ± 0.004			0.307 ± 0.003		

¹Average temperature ± standard deviation;

²Average relative humidity ± standard deviation;

A linear viscoelastic response typically encompasses linearly proportional creep amplitudes with regard to the stress values. However, for the specimens under the highest stress values, the creep amplitudes obtained are higher than those which would result from a linear dependence, suggesting that a shear stress of 44% of the foam's shear strength is high enough to cause a nonlinear creep response.

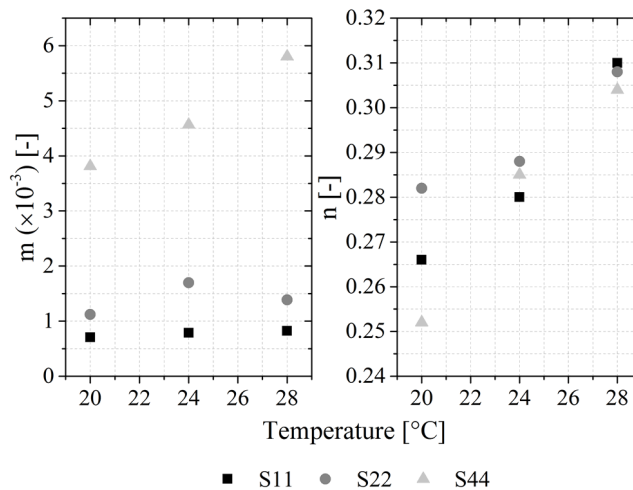


Figure 8.4. Creep amplitude (m) and time exponent (n) values per temperature and stress level.

The m values exhibited a clear dependence of temperature, typically increasing for higher temperature values. However, an exception was found for specimen T28-S22, which exhibited a lower creep amplitude (at 28°C) compared to specimen T24-S22 (same stress

level, at 24°C), reflecting the near overlap that was obtained in the creep curves of these two specimens (*cf.* Figure 8.3).

Regarding the time exponent n , as expected, no significant stress dependence was observed. However, a clear dependence of temperature was found for this parameter, which consistently presented higher average values with increasing temperature.

8.5. Modelling and predictions

8.5.1 General power law

The experimental data (Table 8.1) concerning the simple power law fitting parameters and the elastic strains and stresses were used to estimate the values of γ'_e , τ_e , m' , and τ_m for each test temperature by following the procedure briefly described in section 8.3.1 (also described in detail by Sá *et al.* [16]). The resulting general power law parameters, including the average²³ time exponents (\bar{n}), are presented in Table 8.2 for each test temperature.

In agreement with the discussion presented in section 3.2, it can be seen that the values of τ_e and τ_m remained constant for the three test temperatures, and that the considered temperature range did not induce significant changes in the values of γ'_e , for which an average value of $\gamma'_e = 0.225 \pm 0.004$ m/m was obtained. Furthermore, a clear temperature dependence was found for the \bar{n} and m' parameters – both increasing with temperature.

Table 8.2. General power law parameters per temperature.

Temperature [°C]	\bar{n} [-]	γ'_e [-]	τ_e [MPa]	m' [-]	τ_m [MPa]
20	0.267	0.221	1.809	0.038	2.002
24	0.284	0.225	1.809	0.049	2.002
28	0.307	0.229	1.809	0.054	2.002

8.5.2 Temperature dependence

The Arrhenius equation dependence of temperature for the m' and n parameters, as per Equations (8.2) and (8.3), may be rewritten in terms of the linear relationship between $\ln(k)$

²³ As mentioned in section 3.1, the time exponent is stress-independent and may be taken as the average value obtained from the various specimens at a given hygrothermal condition.

and $(1/T)$, given by $\ln(k) = (-E_k/R) \cdot (1/T) + \ln(A_k)$ with $k = (m', n)$. Consequently, estimating the Arrhenius equation parameters only requires determining the slope $(-E_k/R)$ and the intercept $(\ln A_k)$ of the linear regression between $\ln k$ and $(1/T)$. Using this procedure with the data in Table 8.2, the activation energies and pre-exponential factors associated with both parameters were estimated. The values of $A_{m'} = 8152$, $E_{m'} = 29820$ J/mol, $A_n = 53.8$ and $E_n = 12933$ J/mol were obtained (coefficients of determination of $R_{m'}^2 = 0.936$ and $R_n^2 = 0.930$), leading to the following equations describing the temperature dependence of the two parameters:

$$m'(T) = 8152e^{\left(\frac{-29820}{8.314 \cdot T}\right)} \quad (7.8)$$

$$n(T) = 53.8e^{\left(\frac{-12933}{8.314 \cdot T}\right)} \quad (7.9)$$

Figure 8.5 shows a plot of the reference creep amplitude and average time exponent values as a function of temperature, in Kelvin, and presents the Arrhenius equations fitted to the data. For the temperature range considered herein, these equations appear to follow reasonably well the general development of the two parameters with temperature. Note that their extrapolation beyond the 20°C to 28°C range would require additional experimental validation.

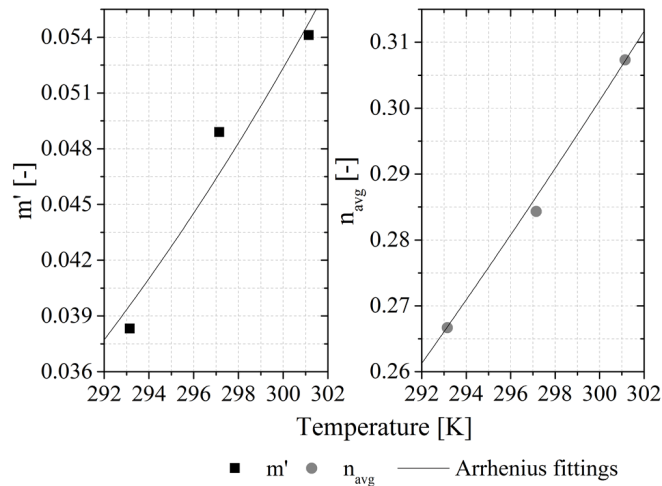


Figure 8.5. Fitting of Arrhenius equations to the reference creep amplitude (m') and average time exponent (\bar{n}).

In view of the parameters given in section 5.1 and the temperature dependencies of Equations (8.8) and (8.9), it is possible to rewrite Equation (8.1) as follows,

$$\gamma(\tau, t, T) = 0.225 \sinh\left(\frac{\tau}{1.809}\right) + \left(8152e^{\left(-\frac{29820}{8.314 \cdot T}\right)}\right) \sinh\left(\frac{\tau}{2.002}\right) t^{\left(53.8e^{\left(-\frac{12933}{8.314 \cdot T}\right)}\right)} \quad (8.10)$$

thus obtaining a general equation to model the total shear strain of the PUR foam as a function of shear stress, creep time and temperature (for the temperature range considered). The results provided by this equation are plotted in Figure 8.6 against the experimental creep curves.

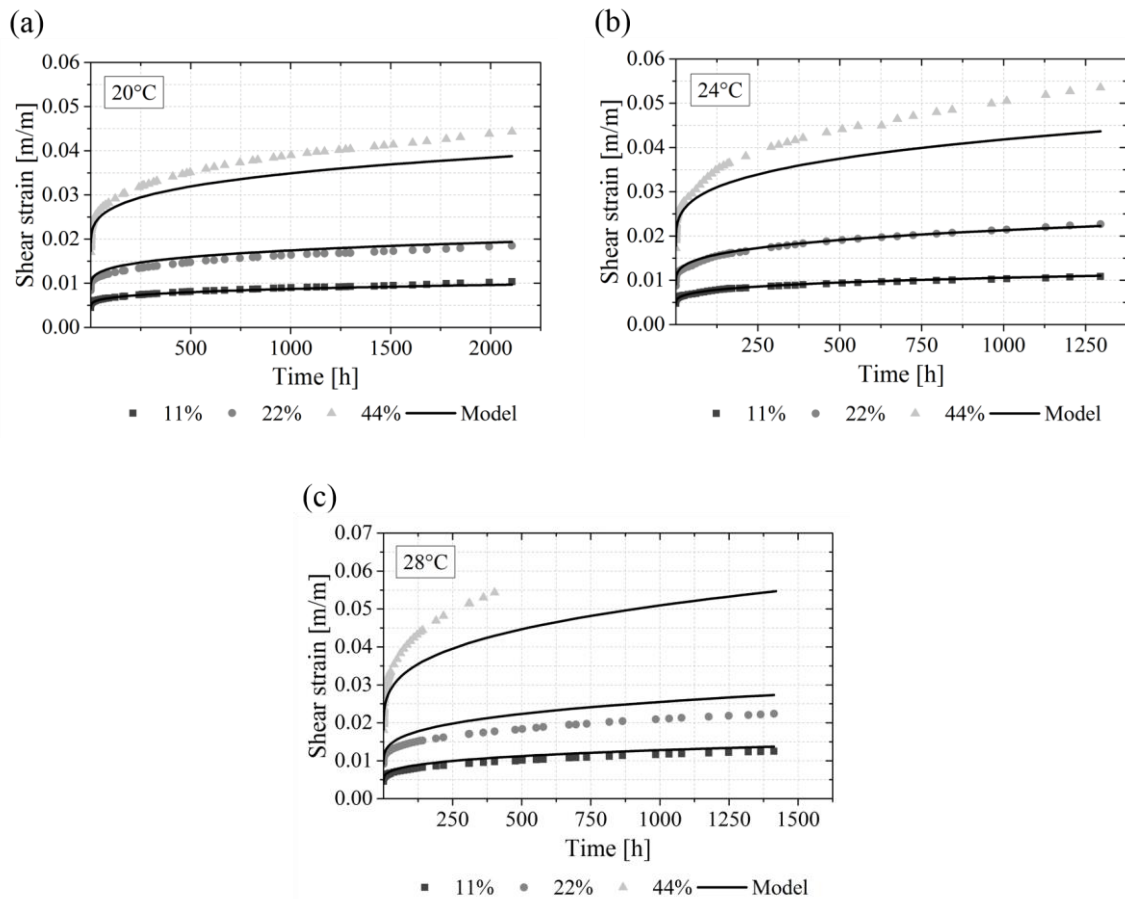


Figure 8.6. Comparison between experimental creep curves and model [Equation (8.10)] estimates of shear strain over time as a function of stress and temperature.

A good general agreement between the model and the experimental curves was obtained for the 11% and 22% shear stress levels (with the exception of the 22% shear stress level at

28°C, specimen T3-S2, which had been previously considered as an outlier regarding its creep amplitude). Due to the nonlinearity in creep response observed at the highest stress level (44%), which is not duly accounted for in the proposed general equation, the model underestimates the shear strains obtained for such a stress value. However, the creep amplitudes obtained for the highest stress level, which were considered in the modelling, did not negatively affect the model's accuracy at lower stresses. Overall, the proposed general equation is able to model the effect of temperature on the shear creep response of the PUR foam, as well as the effect of stress level for stresses within the range of linear viscoelasticity.

8.5.3 Time and temperature dependent properties

By considering the previously discussed simplification of replacing the hyperbolic sine stress dependencies for linear relationships [15], it is possible to obtain the elastic shear modulus (G_e), the temperature dependent viscoelastic shear modulus ($G_t(T)$) and the time-temperature dependent shear modulus ($G(t, T)$) of the PUR foam, as follows:

$$G_e = \tau_e / \gamma'_e = \frac{1.809}{0.225} = 8.04 \text{ GPa} \quad (8.11)$$

$$G_t(T) = \tau_m / m'(T) = \frac{2.002}{8152} e^{\left(\frac{29820}{8.314 \cdot T}\right)} = 2.46 \times 10^{-4} \cdot e^{\left(\frac{29820}{8.314 \cdot T}\right)} \quad (8.12)$$

$$G(t, T) = \frac{1.97 \times 10^{-3} \cdot e^{\left(\frac{29820}{8.314 \cdot T}\right)}}{2.46 \times 10^{-4} \cdot e^{\left(\frac{29820}{8.314 \cdot T}\right)} + 8.04 \cdot t^{53.8} e^{\left(\frac{-12933}{8.314 \cdot T}\right)}} \quad (8.13)$$

In order to assess the impact of this simplification against the results directly yielded by Equation (8.10), shear deformations were calculated for all stress levels considered (11%, 22% and 44% of the foam's shear strength), for various temperatures within the 20°C-28°C range, using both the original and the simplified power laws. The relative differences found between the two results were always lower than 0.1%, indicating that for such a magnitude of stresses the adopted simplification does not significantly affect the model's accuracy.

Considering the results of Equations (8.9), (8.11) and (8.12), it is possible to obtain an expression for the time-temperature creep coefficient, rewriting Equation (8.6) as follows:

$$\phi(t, T) = \frac{8.04}{2.46 \times 10^{-4} \cdot e^{\left(\frac{29820}{8.314 \cdot T}\right)}} t^{53.8e^{\left(\frac{-12933}{8.314 \cdot T}\right)}} \quad (8.14)$$

This equation can be used in combination with Equation (8.7) to readily calculate the time-temperature dependent shear modulus reduction factor. The time-temperature dependent shear modulus predictions are plotted in Figure 8.7-a for the test temperatures considered in this study, over a 50 year period. The creep coefficient and shear modulus reduction factor curves are plotted in Figure 8.7-b for a period of 100 years (logarithmic time scale), considering temperatures ranging between 20°C and 28°C in steps of 2°C.

The results plotted in Figure 8.7 highlight the substantial influence of temperature on the different predicted curves. In fact, the 50 year shear modulus prediction for 28°C (0.62 MPa) is 53% lower than that for 20°C (1.32 MPa). In either case, considerable creep deformations are expected to develop in the PUR foam. Most of these deformations are estimated to occur within the first year of creep, with the predicted time-temperature dependent shear modulus being reduced by 64% of its elastic value at 20°C, or 78% at 28°C. Such reductions are estimated to be 77% and 88% after 10 years of creep, and 84% and 92% after 50 years of creep, for 20°C and 28°C, respectively. In terms of creep coefficients, the 1 year coefficient for 20°C is 1.79, whereas for 28°C this value increases to 3.57. For 50 years, these coefficients are predicted to be as high as 5.07 and 11.86 for 20°C and 28°C, respectively.

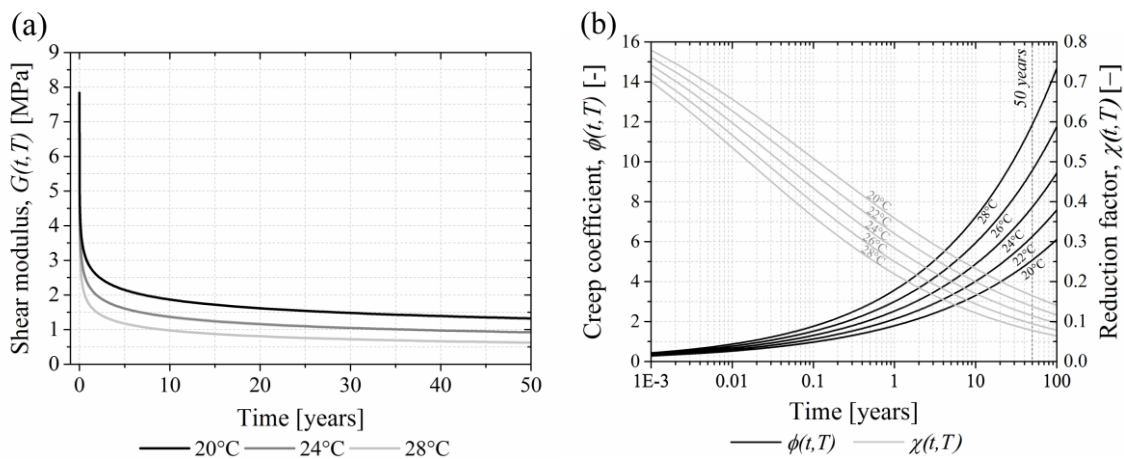


Figure 8.7. (a) Time-temperature dependent shear modulus of the PUR foam, and (b) creep coefficient and shear modulus reduction factor curves.

The presented prediction curves are stress independent, but are only valid for foams under stresses within the linear viscoelastic range, for which the general creep law of Equation

(8.10) from where they originate has been shown to provide a good agreement with the experimental results.

8.6. Comparison with TTSSP

The Time-Temperature-Stress Superposition Principle (TTSSP) is frequently used to process data from various accelerated material characterisation procedures, among which accelerated creep testing [17]. This principle is based on the assumption that molecular modes of motion of the polymer chains are dependent on their thermomechanical conditions (often viewed under the scope of free energy or free volume theories), and that the material's response (*e.g.*, creep curves) will follow developments with identical shapes for such different conditions [8,17,18]. If a material satisfies this assumption, the curves that represent its response may be “rigidly” shifted along the two axes (time and deformation), according to horizontal and vertical shift factors, to form a “master curve” with respect to a reference thermomechanical state.

The creep curves presented in the current study, obtained for different temperatures and stress levels, were used to plot a “master curve” with reference to the 20°C temperature and 11% shear stress conditions, considering that results obtained at higher temperatures and stresses provided an accelerated creep condition with regard to such reference state. In order to obtain a “master curve” from the individual power laws, shift factors may be calculated for the creep strain curves using the following expressions [18],

$$a_v = \frac{\gamma_0(\tau, T)}{\gamma_0(\tau_0, T_0)} \quad (7.15)$$

$$a_h = \left[\frac{\gamma_0(\tau_0, T_0) \cdot m(\tau, T)}{\gamma_0(\tau, T) \cdot m(\tau_0, T_0)} \right]^{-\frac{1}{n_0}} \quad (7.16)$$

where a_v and a_h are respectively the vertical and horizontal shift factors, $\gamma_0(\tau_0, T_0)$ and $m(\tau_0, T_0)$ are the elastic deformation and creep amplitude for the reference conditions, $\gamma_0(\tau, T)$ and $m(\tau, T)$ are likewise for the accelerated conditions, and n_0 is the time exponent

for the reference conditions. These shift factors are determined so as to obtain the following relationship between the accelerated and reference curves:

$$\gamma(\tau, T, t) = a_v \left[\gamma_0(\tau_0, T_0) + m(\tau_0, T_0) \left(\frac{t}{a_h} \right)^{n_0} \right] \quad (7.15)$$

By shifting the curves that concern solely the creep part of the deformation (*i.e.*, not considering the elastic deformation), the need for a vertical shift is eliminated and the expression for the horizontal shift factor is simplified into:

$$a_h = \left[\frac{m(\tau, T)}{m(\tau_0, T_0)} \right]^{-\frac{1}{n_0}} \quad (7.16)$$

Using this expression, horizontal shift factors (*cf.* Table 8.3) were calculated based on the parameters of the power law fittings presented in Table 8.1. The specimen T28-S22 (28°C, 22% stress level) was not included in this analysis due to its creep amplitude value having been previously considered as an outlier. The results obtained at the highest stress level were included, despite being in the nonlinear range of the foam's response, given that the respective creep curves were consistent in terms of shape with those in the linear viscoelastic range (power law developments with time), and the analytically determined shift factors provided reasonable continuity of the obtained master curves. The resulting shifted curves for the reference conditions of 20°C and 11% shear stress are plotted in Figure 8.8, together with the predictions of the model proposed in section 5.

Using the TTSSP, the shifted curves cover a total time period in excess of 1.45 million hours (over 165 years). A good general agreement between the two approaches (TTSSP and the proposed creep model) is found throughout that time period. However, in order to verify the proposed model's ability to provide similarly consistent results for different temperatures, a time-stress superposition (TSSP) was also developed for each test temperature, considering the 11% stress level as the reference condition. The corresponding shift factors are presented in Table 8.3.

The master curves obtained for each temperature are plotted in Figure 8.9 together with the respective model predictions. Slight discontinuities may be observed in the master curves²⁴, stemming from irregularities in the experimental data, which is assumed to perfectly follow a power law development. While the experimental data follows such a development, oscillations around that tendency are to be expected, and may cause such discontinuities when applying graphical shifting techniques such as those based on the TTSSP or TSSP.

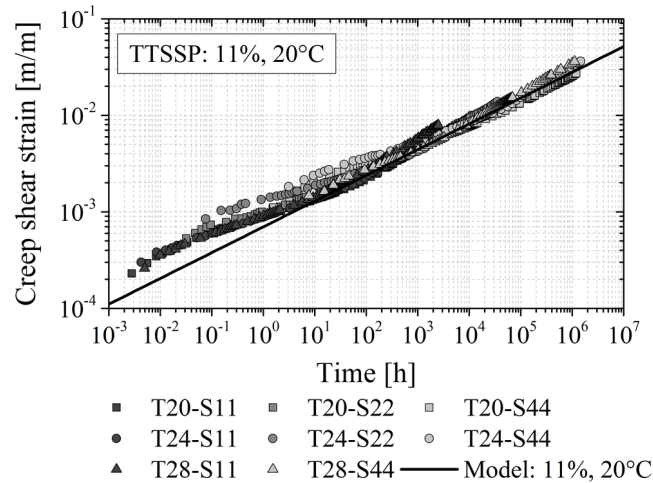


Figure 8.8. Time-temperature-stress superposition of experimental creep curves for reference conditions of 20°C and 11% shear stress and comparison with model predictions.

Table 8.3. Horizontal shift factors (a_h) used for TTSSP and TSSP.

Temperature [°C]	20°C			24°C			28°C	
Shear stress (% of strength)	11%	22%	44%	11%	22%	44%	11%	44%
Specimen	T20-S11	T20-S22	T20-S44	T24-S11	T24-S22	T24-S44	T28-S11	T28-S44
Reference: 11%, 20°C	1.0	0.1749	0.0018	0.6581	0.0367	0.0009	0.5615	0.0788
Reference: 11% at each temperature	1.0	0.1749	0.0018	1.0	0.0645	0.0019	1.0	0.0018

Notwithstanding the slight irregularities found in the “master curves” for each test temperature, the proposed model closely follows the general development of the shifted

²⁴ Such discontinuities are often eliminated through fine-tuning of the shift factors. However, in this study, for the sake of consistency, the authors preferred not to adopt such procedure and presented the curves obtained using the shift factors analytically determined.

curves for all temperatures. Such a result indicates that the creep predictions provided by the proposed model are in good agreement with the predictions obtained through the application of superposition principles for different temperatures, considering temperatures within the range for which the model has been calibrated.

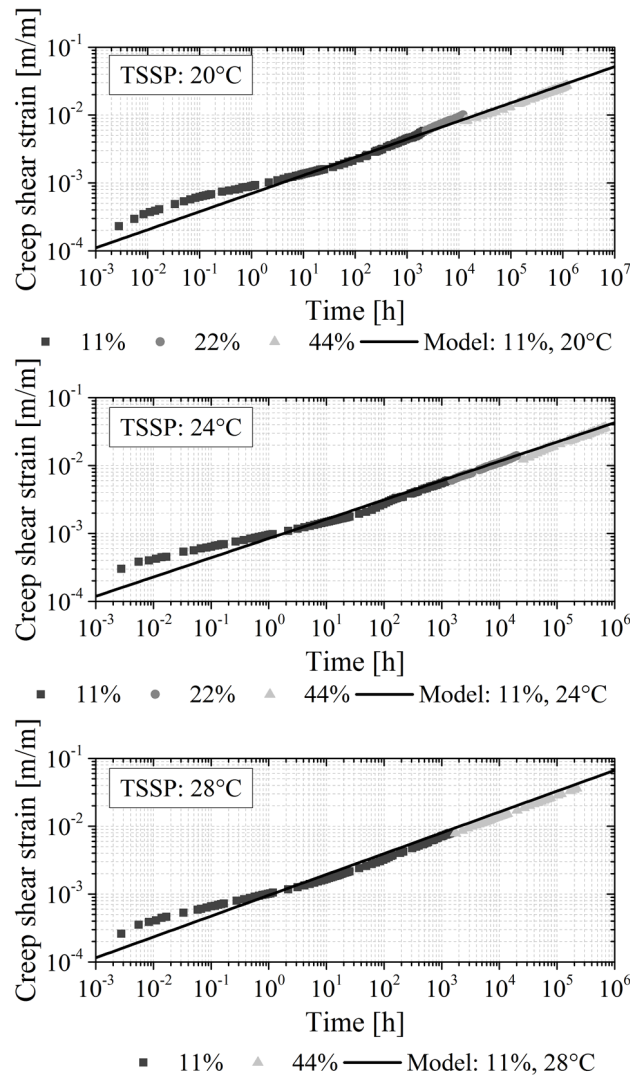


Figure 8.9. Time-stress superposition of experimental creep curves at different temperatures for the reference shear stress of 11% and comparison with model predictions.

8.7. Concluding remarks

Shear creep experiments were carried out on a rigid PUR foam, for shear stress levels of 11%, 22% and 44% of the foam's shear strength, and for temperatures of 20°C, 24°C and 28°C. The creep response of the foam was found to be strongly dependent on both stress

level and temperature, even within the 8°C amplitude considered, with higher creep rates being obtained at higher stresses and temperatures.

Findley's power law was fitted to the experimental creep curves. It was found that the parameters γ_e' and τ_e , while being temperature dependent, presented only minor variations within the temperature range considered, and hence they were assumed as constant. The parameter τ_m was also found to be constant within that temperature range. The parameters m' and n presented strong temperature dependence, both increasing with temperature. Arrhenius equations were proposed to model such dependence and used to adapt the general equation of Findley's power law, thus providing a model for the time-temperature-stress dependent shear strain in the PUR foam.

The proposed model, valid in the range of linear viscoelasticity, provided a good fit to the experimental creep curves for the 11% and 22% stress levels. However, the model underestimated the experimental shear strains for the highest stress level of 44% and this was attributed to the nonlinear creep response of the foam at that stress level.

A set of practical design equations to estimate the viscoelastic properties of the PUR foam was also derived, including the time-temperature dependent (i) shear modulus, (ii) creep coefficient, and (iii) shear modulus reduction factor. These properties were found to be substantially affected by temperature within the considered range (20°C to 28°C) likely to be found in service conditions.

The TTSSP was used to shift the experimental curves with regard to the reference level of 20°C and 11% shear stress, yielding a "master curve" covering a time period in excess of 165 years. The predictions obtained via TTSSP were compared with those from the proposed model for the reference conditions, and a good agreement between the two methodologies was found. In order to perform a similar assessment for 24°C and 28°C, the TSSP was used to shift curves obtained at higher stress levels to the reference stress level of 11%, for each test temperature. The three "master curves" obtained also compared well with the proposed model's predictions for all temperatures.

Finally, it should be noted that both the proposed model and the curve shifting procedures of the TTSSP and TSSP do not account for the possible effects of external degradation factors acting on the PUR foam, nor the material's intrinsic physical ageing, which may affect the long-term development of its creep response [19].

8.8. References

- [1] Correia, J.R., Garrido, M., Gonilha, J.A., Branco, F.A., Reis, L.G. (2012), “GFRP sandwich panels with PU foam and PP honeycomb cores for civil engineering structural applications: Effects of introducing strengthening ribs”. *International Journal of Structural Integrity*, 3(2), 127-147.
- [2] Zenkert, D. (1997). *The Handbook of Sandwich Construction*. Worcestershire, UK: Engineering Materials Advisory Services (EMAS), 442 p.
- [3] Davies, J.M. (2001). *Lightweight Sandwich Construction*. Blackwell Science, Oxford, 370 p.
- [4] Mills, N.J. (2007). *Polymer foams handbook: engineering and biomechanics applications and design guide*. Oxford: Butterworth-Heinemann, 562 p.
- [5] Garrido, M., Correia, J.R., Branco, F.A., Keller, T. (2014). “Creep behaviour of sandwich panels with rigid polyurethane foam core and glass-fibre reinforced polymer faces: Experimental tests and analytical modelling”. *Journal of Composite Materials*, 48(18), 2237-2249.
- [6] Huang, J.S., Gibson, L.J. (1991). “Creep of polymer foams”. *Journal of Materials Science*, 26(3), 637-647.
- [7] Findley, W.N. (1960). *Mechanism and Mechanics of Creep of Plastics and Stress Relaxation and Combined Stress Creep of Plastics*, Rhode Island, U.S.A.: Division of Engineering, Brown University.
- [8] Schapery, R.A. (1969). “On the characterization of nonlinear viscoelastic materials”. *Polymer Engineering and Science*, 9(4), 295-310.
- [9] Moreland, J.C., Wilkes, G.L., Turner, R.B. (1994). “Viscoelastic behaviour of flexible slabstock polyurethane foams as a function of temperature and relative humidity. II. Compressive creep behavior”. *Journal of Applied Polymer Science*, 52, 569-576.
- [10] Briody, C., Duignan, B., Jerrams, S., Ronan, S. (2012). “Prediction of compressive creep behaviour in flexible polyurethane foam over long time scales and at elevated temperatures”. *Polymer Testing*, 31(8), 1019-1025.

- [11] Gibson, L.J., Ashby, M.F. (1988). *Cellular solids: Structure & properties*, Oxford: Pergamon Press, 357 p.
- [12] Davies, P., Craveur, L. (1996). “Prediction of long term behaviour of sandwich structures”. *Proceedings of the 7th European Conference on Composite Materials (ECCM-7)*, London: Woodhead Publishing, 367-376.
- [13] Andrews, E.W., Gibson, L.J., Ashby, M.F. (1999). “The creep of cellular solids”, *Acta Materialia*, 47(10), 2853-2863.
- [14] Garrido, M., Correia, J.R., Keller, T. (2015). “Effects of elevated temperature on the shear response of PET and PUR foams used in composite sandwich panels”, *Construction and Building Materials*, 76, 150-157.
- [15] Scott, D.W., Zureick, A.-H. (1998). “Compression creep of a pultruded E-glass/vinylester composite”. *Composites Science and Technology*, 58(8), 1361-1369.
- [16] Sá, M.F., Gomes, A.M., Correia, J.R., Silvestre, N. (2011). “Creep behavior of pultruded GFRP elements – Part 2: Analytical study”. *Composite Structures*, 93(9), 2409-2418.
- [17] Papanicolaou, G.C., Zaoutsos, S.P. (2011). “Viscoelastic constitutive modeling of creep and stress relaxation in polymers and polymer matrix composites”. In *Creep and fatigue in polymer matrix composites*, Guedes, R.M. (ed.), Woodhead Publishing, 3-47.
- [18] Yen, S.-C., Williamson, F.L. (1990). “Accelerated characterisation of creep response of an off-axis composite material”. *Composites Science and Technology*, 38, 103-118.
- [19] Janas, V.F., McCullough, R.L. (1987). “The effects of physical aging on the viscoelastic behavior of a thermoset polyester”, *Composites Science and Technology*, 30(2), 99-118.

Chapter 9

Effect of service temperature on the creep of GFRP laminates

9.1. Introduction

As discussed in the previous chapter, one of the legitimate concerns about the application of composite sandwich panels in building floors subject to significant permanent loads is the creep deformability of the polymeric constituent materials, which include the glass-fibre reinforced polymer (GFRP) laminates. Indeed, throughout the service life required in civil engineering works, typically equal to or higher than 50 years, those deformations may be substantial [1]. Furthermore, the effect of temperature on the creep response of such materials, and also in the particular case of GFRP, while being qualitatively known, is yet to be adequately quantified. Consequently, there is lack of information and of suitable models for its expeditious consideration in structural design (as discussed further ahead in the literature review).

This chapter aims to address this issue, by experimentally investigating the flexural creep behaviour of GFRP laminates used in sandwich floor panels produced by vacuum infusion, exposed to different temperatures within a range typically found for building floors. Flexural creep was considered for providing a combination of compressive and tensile creep responses in the same laminate, the former being expected to be higher than the latter [2]. While face sheets in sandwich panels are typically either compressed or tensioned (and not in pure bending), flexural creep is expected to accurately capture the overall creep response of the GFRP faces. Creep experiments were carried out at 20°C, 24°C and 28°C, for stress levels corresponding to 15%, 25% and 35% of the laminate's flexural strength, with test durations ranging between 1000 h and 2200 h.

A modelling approach similar to that followed in the previous chapter was adopted. Findley's power law formulation [3] was used, and adapted to include an Arrhenius law

temperature dependence for the power law parameters that define the creep rate. A generalised power law equation was obtained, capable of modelling the GFRP laminate's time-dependent deformations as a function of axial stress and in-service temperature. Expressions were obtained for the time and temperature dependent elastic modulus, creep coefficients and elastic modulus reduction factors, thus providing practical design tools for estimating creep deformations in the GFRP laminates. In the final part of the chapter, long-term creep predictions provided by the proposed model are compared with creep master curves obtained from the application of the time-temperature-stress superposition principle (TTSSP) [4,5] to the experimental data, and the consistency and agreement between the two approaches is assessed.

9.2. Literature review

The number of studies found in the literature regarding the effects of temperature on the creep response of FRPs is quite limited. However, noteworthy examples are found in the publications by Yen and Williamson [6], Dutta and Hui [2] and Daniali [7].

Yen and Williamson [6] studied the tensile creep of a sheet moulding compound (SMC) comprised of unidirectional continuous glass fibres (50% weight fraction) embedded in a polyester matrix. The authors performed the creep experiments (200 min duration) for stress levels between ~10% and ~80% of the laminate's tensile strength, for temperatures of 23°C, 52°C, 79°C, 107°C, 135°C, and 149°C. Findley's power law formulation [3] was successfully used to fit the experimental data, and its parameters were used to analytically calculate horizontal and vertical shift factors for application of the time-temperature-stress superposition theory (TTSSP). Shifting the creep curves obtained at higher temperatures and stresses allowed deriving a master curve for a temperature of 23°C and a stress of 10.8 MPa (~10% of the of the laminate's tensile strength).

Dutta and Hui [2] performed a study on the tension and compression creep behaviour of GFRP composite material (the authors did not specify the production method) under sustained loads, with test durations of up to 30 min, for three different temperatures: 25°C, 50°C, and 80°C. The authors observed higher creep responses of the GFRP laminates associated with elevated temperatures, and suggested that Findley's power law formulation could be adapted in order to model such temperature dependence considering the power

law's time exponent as being linearly dependent on temperature. However, the authors did not present a systematic study on such dependence, nor they suggested values for the model parameters, or provided an adequate validation for the proposed model.

Daniali [7] studied the flexural creep behaviour of pultruded GFRP profiles with T-shaped cross-sections, comprising either polyester or vinylester resin matrices. Profiles were tested at room temperature, loaded to 50%, 75%, 80% and 85% of their respective failure load, and at 54°C, subjected to 50%, 60% and 80% of their load capacity at that elevated temperature, for periods up to 10,000 h. The author reported an overall higher creep deformability of the polyester based profiles for room and elevated temperatures. Both types of profiles (polyester and vinylester based) showed significantly higher creep responses at 54°C than at room temperature. For example, at 54°C the vinylester resin profiles loaded to 80% of their ultimate capacity were reported to fail after only 50 h. Their deflection prior to failure was approximately 4.2 times that measured at room temperature, for which no sign of failure was reported even after 500 h of creep.

More recently, Sá *et al.* [8,9] also presented a noteworthy study regarding the creep behaviour of GFRP laminates, however they did not consider the influence of temperature. The authors studied the flexural creep behaviour of a pultruded GFRP profile (I-section) comprised of E-glass fibres and polyester resin matrix. Creep tests were carried out at room temperature on the full-scale profile (loaded in four-point bending) and on small-scale specimens extracted from its flanges and web (loaded in three-point bending), for periods of approximately 1600 h and 1220 h, respectively. The small-scale specimens were tested under three different stress levels – 20%, 30% and 40% of their respective failure stress – with additional stress levels of 50% and 60% for the flange specimens. The I-profile was tested at 33% of its failure load. The authors reported higher creep rates in the web specimens, which were attributed to the different fibre architectures between web and flange laminates [9], and a creep behaviour of the full-scale pultruded profile that was similar to that of the small-scale specimens, particularly the flange laminates [8]. Creep ruptures were also reported for the flange specimens loaded to 50% and 60% of the laminate's failure stress, after 27 and 7 days of creep, respectively. The authors performed an assessment of analytical methods for modelling the creep response of FRPs, and found that Findley's power law model provided accurate results, being also convenient for long-term predictions, which makes it useful for civil engineering design applications [8].

Several other studies have been carried out on the creep behaviour of FRPs within the context of civil engineering. Scott *et al.* [10] and Sá *et al.* [8] have presented fairly comprehensive literature reviews of those studies. These reviews show that no investigations were performed about the creep behaviour of GFRP laminates produced by vacuum infusion. Furthermore, to the best of the author's knowledge a systematic experimental quantification and analytical modelling of the influence of in-service temperature on the creep response of FRPs have not yet been presented in the literature. Nonetheless, the literature review presented above clearly suggests that Findley's power law is well suited to describe the creep behaviour of FRPs in their linear viscoelastic range. For this reason, Findley's power law formulation was adopted in the present study, adapted to include an Arrhenius law temperature dependence, as detailed in the following section, and used to model the creep experiments described in section 9.4.3.

9.3. Theoretical formulation

9.3.1. Findley's power law

Equation (9.1a) describes the basic expression for Findley's power law, similar to that introduced in the previous chapter, but adapted for axial stresses and strains. In this equation, ε is the total strain, σ is the applied stress, t is the time elapsed after load application, t_0 is the time unit considered, ε_0 is the elastic strain, m is the creep amplitude, and n is the time exponent. As previously mentioned, this equation separates the time-dependent strain in two components: (i) the elastic strain (ε_0) and (ii) the viscoelastic strain ($m(t/t_0)^n$). Both the elastic strain and the creep amplitude are considered to follow a hyperbolic sine dependence of stress, leading to the general power law shown in Equation (9.1b), where ε'_e is the reference elastic strain, σ_e is the reference elastic stress level associated with ε'_e , m' is the reference creep amplitude and σ_m is the reference creep stress level associated with m' .

$$\varepsilon(\sigma, t) = \varepsilon_0 + m \left(\frac{t}{t_0} \right)^n \quad (9.1a)$$

$$\varepsilon(\sigma, t) = \varepsilon'_e \sinh \left(\frac{\sigma}{\sigma_e} \right) + m' \sinh \left(\frac{\sigma}{\sigma_m} \right) \left(\frac{t}{t_0} \right)^n \quad (9.1b)$$

9.3.2. Temperature dependence

Temperature affects both the elastic [11,12] and viscoelastic response of FRPs. For wide temperature amplitudes, the temperature effects on the elastic response of the laminate may have to be explicitly considered. However, for small temperature ranges well below the glass-transition temperature²⁵ (T_g) of the material, such as the 20-28°C range considered in this study, the elastic properties are not expected to be significantly influenced by temperature. Under this assumption, the variations in elastic strain, and consequently of the ε_e' parameter, are expected to be small enough for that parameter to be considered constant for the mentioned temperature range.

The m' and n parameters, defining the viscoelastic response of the material, are expected to be temperature dependent within the considered temperature range. Similarly to what was discussed for the PUR foam in the previous chapter, such temperature dependence may be described by the Arrhenius equation. Taking as an example the reference creep amplitude (m'), this parameter may be considered as a creep rate constant, related to temperature as per Equation (9.2),

$$m'(T) = A_{m'} e^{\left(-\frac{E_{m'}}{RT}\right)} \quad (8.2)$$

where T is the temperature (in Kelvin), R is the universal gas constant (~ 8.314 J/mol.K), $E_{m'}$ is the activation energy, and $A_{m'}$ is the pre-exponential factor. An equivalent temperature dependence could be assumed for the time exponent (n). However, for the GFRP laminates considered in this study, the variations in n value with regard to temperature were not found to be statistically significant and an average value was assumed independently of temperature, as discussed in section 8.4.3.2.

As previously mentioned, the σ_e and σ_m parameters are reference stresses associated with ε_e' and m' , respectively. In the current study, it is assumed that they may be considered temperature independent, an assumption that is supported by the experimental results presented in section 8.5.1.

²⁵ For the GFRP material used in this study, $T_g = 69.3^\circ\text{C}$, as detailed in section 8.4.1.

9.3.3. Time and temperature dependent properties

9.3.3.1. Simplified approach

The time and temperature dependent properties shown here for the GFRP laminates were obtained using an analogous process to that described in the previous chapter (section 8.3.3.) for the PUR foam in shear, albeit duly adapted for axial stresses and strains. This process may be considered as a simplified approach, based on the assumption that the hyperbolic sine arguments (*i.e.*, σ/σ_e and σ/σ_m) have sufficiently low values (well below 1). Such an approximation prompts the simplification of Findley's power law, by allowing the replacement of the hyperbolic sine stress dependence in Equation (9.1b) by a linear one [13]. Doing so, Equations 9.3, 9.4 and 9.5 may be obtained, where $E_e = \sigma_e/\varepsilon_e'$ and $E_t(T) = \sigma_m/m'(T)$ are, respectively, the elastic flexural modulus (assumed to be nearly constant for the temperature range considered in this study) and the viscoelastic flexural modulus of the GFRP laminate.

$$E(t, T) = \frac{E_e \cdot E_t(T)}{E_t(T) + E_e t^{n(T)}} \quad (9.3)$$

$$\phi(t, T) = \frac{E_e}{E_t(T)} \left(\frac{t}{t_0} \right)^{n(T)} \quad (9.4)$$

$$\chi(t, T) = \frac{1}{1 + \phi(t, T)} \quad (9.5)$$

However, in the current study, it was found that the mentioned simplification was not always applicable, according to the findings discussed in section 9.5. Consequently, full-form equations were developed in order to obtain the required time- and temperature-dependent properties for the GFRP laminates.

9.3.3.2. Full-form equation

For high values of the hyperbolic sine arguments (*i.e.*, σ/σ_e and σ/σ_m close to or greater than 1.0), the relative importance of the third and higher order terms in the Taylor series expansion of the hyperbolic sine functions increases, and the simplifications assumed in the previous section are no longer valid. Consequently, the full-form power law with hyperbolic

sine stress dependence (Equation (9.1b)) should be considered. In this case, the time-temperature-stress dependent elastic modulus may be obtained from Equation (9.6).

$$\begin{aligned}
 E(\sigma, t, T) &= \left(\frac{\varepsilon(\sigma, t, T)}{\sigma} \right)^{-1} \\
 &= \left(\frac{\varepsilon'_e}{\sigma} \sinh \left(\frac{\sigma}{\sigma_e} \right) + \frac{m'(T)}{\sigma} \sinh \left(\frac{\sigma}{\sigma_m} \right) \left(\frac{t}{t_0} \right)^n \right)^{-1}
 \end{aligned} \tag{9.6}$$

The expressions for the creep coefficients and elastic modulus reduction factors given in Equations (9.4) and (9.5) may still be used by considering the appropriate stress dependent elastic and viscoelastic moduli, according to Equations (9.7) and (9.8), respectively.

$$E_e(\sigma) = \frac{\sigma}{\varepsilon'_e \sinh \left(\frac{\sigma}{\sigma_e} \right)} \tag{9.7}$$

$$E_t(\sigma, T) = \frac{\sigma}{m'(T) \sinh \left(\frac{\sigma}{\sigma_m} \right)} \tag{9.8}$$

9.4. Experimental programme

9.4.1. Material properties

The GFRP laminates used in this study were identical to those incorporated in the panels' face sheets. These are described in chapter 3, and their mechanical properties are given in chapter 4. The glass transition temperature (T_g) of the material was also determined from dynamic mechanical analysis (dual cantilever setup, heating rate of 1.0°C/min and frequency of 1 Hz), considering the onset of the storage modulus curve. A value of $T_g = 69.3^\circ\text{C}$ was obtained.

9.4.2. Static failure tests

To assess the flexural properties of the GFRP laminates, static flexural failure tests were carried out according to the guidelines of the ISO 14125 standard [14]. Specimens with nominal width of 25 mm and nominal thickness of 7 mm were tested in three-point bending

over a 200 mm span. The experiments were carried out in load control at a speed of 1.5 kN/min (corresponding to approximately 10 mm/min within the linear elastic range of the material's response). Deflections were measured using a displacement transducer with a stroke of 25 mm and precision of 0.01 mm, and loads were measured using a load cell with precision of 0.01 kN. The maximum flexural stresses and strains (at the outermost layer of the laminates) were estimated according to Euler-Bernoulli beam theory (*cf.* ISO 14125) and are plotted in Figure 9.1 for the three specimens tested.

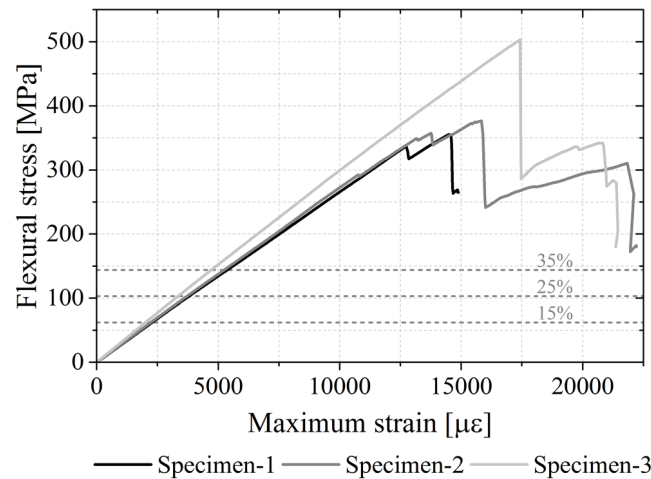


Figure 9.1. Flexural stress vs. strain curves obtained in the failure tests.

A linear elastic behaviour (average stiffness of 0.15 ± 0.01 kN/mm and elastic flexural modulus of 28.8 ± 1.8 GPa) was observed up to failure, which occurred in a brittle manner by delamination and buckling of the uppermost lamina at the mid-span section (Figure 9.2). Some load bearing capacity was still observed after the first ply failure, typically followed by the progressive failure of the innermost laminas. Slight delamination in the bottom surface of the laminate was also observed at mid-span. An average failure load of 1.93 ± 0.39 kN was obtained, corresponding to an average maximum bending moment of 96.6 ± 19.5 kN.mm and maximum axial stresses of 411.7 ± 79.9 MPa. The average strain at failure was $15,919 \pm 1,463$ $\mu\epsilon$.

In Figure 9.1, three horizontal lines are also plotted, indicating the stress levels (15%, 25% and 35%) that were adopted for the creep experiments carried out on the GFRP laminates (described in detail in the following section).



Figure 9.2. Typical flexural failure of the GFRP laminates.

9.4.3. Creep tests

9.4.3.1. Test setup and details

Creep experiments were carried out in a room with controlled temperature and monitored relative humidity (RH). Nominal test temperatures of 20°C, 24°C and 28°C were adopted, a range that is commonly found in service conditions for building floors. Three GFRP specimens were tested per temperature, each subjected to a different load level. The adopted loads corresponded to 15%, 25% and 35% of the laminate's flexural strength (*cf.* Figure 9.1). The duration of the experiments was 1320 h, 1000 h, and 2215 h for the 20°C, 24°C, and 28°C conditions, respectively. Specimens were labelled “Ti-Sj”, *i.e.*, specimen tested at temperature *i* and stress level *j*.



Figure 9.3. Flexural creep tests: (a) general view, (b) detail of specimen, and (c) dial gauge indicators.

Independent support structures were assembled for each specimen, as shown in Figure 9.3-a. These comprised steel wedges, to which steel angles, used to support the specimens, were welded. A span of 200 mm was adopted, and mid-span loads were applied to the GFRP

laminates using dead weights. Stainless steel D-shaped shackles were used to suspend the loads from the specimens (*cf.* Figure 9.3-b).

Load application was smooth (over approximately 1-2 seconds), comprising a gradual lowering of the weights to avoid impacts or changes in the specimens' position/alignment. Deflection measurements were made at a cross-section distanced 20 mm from mid-span. During load application and for the subsequent 72 hours of creep, the measurements were carried out automatically (5 Hz frequency during the initial minutes, later reduced to 0.02 Hz) using displacement transducers with stroke of 10 mm and precision of 0.01 mm (*cf.* Figure 9.3-b). After the first 72 h, periodic measurements were made using dial gauge indicators with precision of 0.001 mm, as shown in Figure 9.3-c.

The deflections at mid-span were estimated based on the measured values (at the section located 20 mm from mid-span) by considering their theoretical relationship, as given by the Euler-Bernoulli beam theory. According to this theory, the deflections at the instrumented cross-section can be computed from Equation (9.9) with $x = 80$ mm (where b is the specimen width, h is the specimen thickness, δ is the measured deflection, and L is the total span), while the mid-span deflections may be calculated using Equation (9.10). A ratio between the two values of 1.059 is readily obtained. After computing the mid-span deflections from that ratio, the maximum mid-span axial stresses (σ) and strains (ϵ) were estimated from the mid-span load and deflection data.

$$\delta(x) = \frac{P}{6EI} \left(\frac{3L^2x}{8} - \frac{x^3}{2} \right) \quad (9.9)$$

$$\delta\left(\frac{L}{2}\right) = \frac{PL^3}{48EI} \quad (9.10)$$

9.4.3.2. Experimental results and simple power law fitting

A summary of the experimental results, including the applied stresses and strains at mid-span, the elastic flexural moduli, and the simple power law fittings to the observed creep response according to Equation (9.1a) are given in Table 9.1. The elastic response was consistent with the results obtained in the flexural failure tests; the average elastic flexural modulus was 27.4 ± 0.7 GPa, comparing well with the value of 28.8 ± 1.8 GPa obtained in those experiments. As expected, temperature did not have a significant effect on the elastic

flexural modulus within the considered temperature range. While the average elastic flexural modulus values slightly decreased with temperature, such variations were limited and remained within the experimental scatter.

Table 9.1. Summary of experimental results.

Temperature	20°C			24°C			28°C		
	T ⁽¹⁾ : 20.1 ± 1.0°C, RH ⁽²⁾ : 51.1 ± 9.4%			T: 24.1 ± 0.5°C, RH: 37.3 ± 5.9%			T: 27.9 ± 0.5°C, RH: 47.5 ± 8.3%		
Specimen	T20-S15	T20-S25	T20-S35	T24-S15	T24-S25	T24-S35	T28-S15	T28-S25	T28-S35
σ [MPa]	63.3	103.8	146.3	65.1	101.2	153.0	64.3	99.2	142.3
ϵ_0 [$\mu\epsilon$]	2283	3686	5321	2465	3705	5392	2414	3693	5097
E_e [GPa] (average ± standard deviation)	27.7	28.2	27.5	26.4	27.3	28.4	26.6	26.9	27.9
	27.8 ± 0.3			27.4 ± 1.0			27.1 ± 0.7		
m [$\mu\epsilon$]	50.2	113.3	156.1	72.9	143.7	253.7	124.7	309.7	328.3
n [-] (average ± standard deviation)	0.203	0.160	0.180	0.198	0.157	0.148	0.167	0.127	0.154
	0.181 ± 0.022			0.168 ± 0.027			0.149 ± 0.020		

⁽¹⁾Average temperature ± standard deviation;

⁽²⁾Average relative humidity ± standard deviation;

Figure 9.4 shows the evolution of creep strains throughout the duration of the experiments, in linear (Figure 9.4-a) and logarithmic (Figure 9.4-b) plots. As expected, the creep deformations followed a power law development with time, as evidenced by their linear trend in the logarithmic plot. Temperature and stress level were observed to have significant influence on the creep behaviour of the GFRP laminates. It is worth remarking the significant effect of temperature, even for such relatively narrow amplitude as that considered in this study. As an example, one may consider the results of specimens T20-S25 and T28-S15: the latter presented higher creep deformations than the former, albeit having a 38% lower stress level, *i.e.*, the effect of an 8°C increase in service temperature (T20-S15 vs. T28-S15) was higher than increasing the stress level in the laminate from 15% to 25% of its flexural strength (T20-S15 vs. T20-S25).

This effect may be analysed in terms of the power law parameters given in Table 9.1, namely in terms of the creep amplitude (m) values. At 28°C and 15% of the flexural strength, a creep amplitude of 124.7 $\mu\epsilon$ was obtained, higher than the creep amplitude of 113.3 $\mu\epsilon$ obtained at 20°C and 25% of the flexural strength. In general, the creep amplitude values were found to be significantly dependent both on stress level and temperature, increasing with higher stresses and temperatures, as depicted in Figure 9.5.

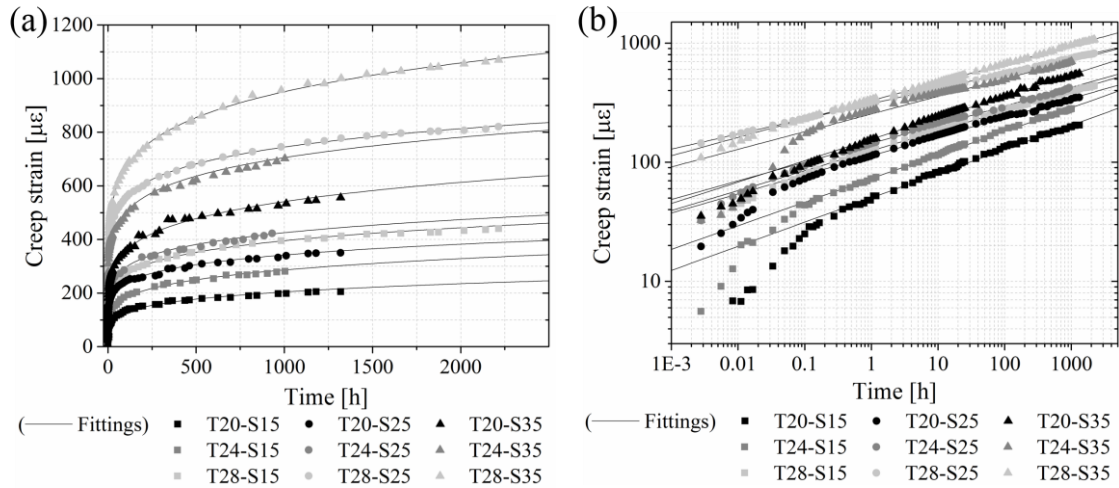


Figure 9.4. Experimental creep strains and fittings from Equation (9.1a): (a) linear plot, and (b) log₁₀ plot.

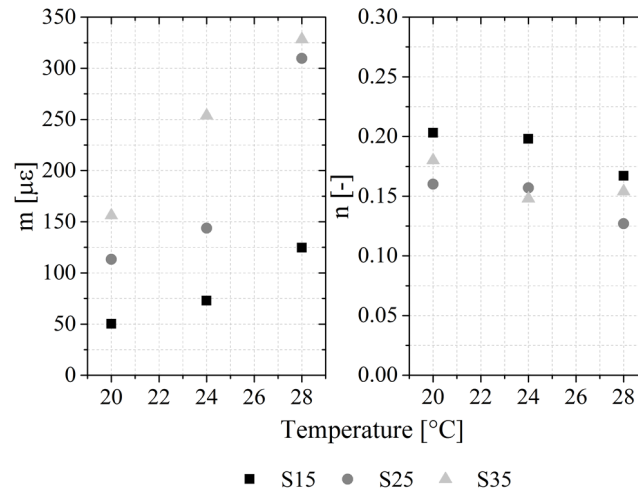


Figure 9.5. Creep amplitude (m) and time exponent (n) values per temperature and stress level.

Regarding the creep exponent (n) values, as expected, no apparent stress dependence was observed for this parameter. Concerning the temperature effect, a trend of slight reduction was observed in the values of n with increasing temperatures. Such a result was unexpected, as typically higher temperatures lead to higher creep rates, which have been found to translate to higher creep amplitudes and time exponents (*e.g.*, as observed by Dutta and Hui [2]). However, the reductions in the n values originate from a dataset with some degree of scatter. In addition, the lowest n value at 28°C, found for specimen T28-S25, was associated with an unusually high creep amplitude (m) by comparison with other specimens. If this specimen were to be considered as an outlier, the apparent reduction trend of the creep exponent values with temperature would be even significantly less evident. As such, it is

possible that the variations observed may result from the statistical variability in material properties rather than from actual effects of temperature.

9.5. Modelling and predictions

9.5.1. General power law parameters

Using the experimental data in Table 9.1, namely the simple power law fitting parameters and the elastic strains and stresses, it is possible to estimate the values of ε'_e , σ_e , m' , and σ_m (as discussed in the previous chapter, in section 8.3.1.). The resulting general power law parameters, including the average²⁶ time exponents (\bar{n}), are presented in Table 9.2 for each test temperature.

Table 9.2. General power law parameters per temperature.

Temperature [°C]	\bar{n} [-]	ε'_e [$\mu\varepsilon$]	σ_e [MPa]	m' [-]	σ_m [MPa]
20	0.181	16722	467.5	57.6	80.4
24	0.167	16958	467.5	81.2	80.4
28	0.149	17117	467.5	137.3	80.4

By determining all the fitting parameters independently for each temperature, it was found that the reference stress values, σ_e and σ_m , could be assumed as constant. In fact, for the different test temperatures, changes in the ε'_e and m' parameters were found to be enough to follow the variations of ε_0 and m . In other words, in the relationships between ε_0 and $\sinh(\sigma/\sigma_e)$ and between m and $\sinh(\sigma/\sigma_m)$, only the slope values (ε'_e and m' , respectively) are affected by temperature.

9.5.2. Temperature dependence

The ε'_e values increased slightly with temperature, reflecting the typical stiffness reduction trend of the elastic properties at elevated temperatures in GFRP laminates. However, as previously discussed, such variations are limited and may be neglected within the temperature amplitude considered in this study²⁷. Assuming this simplification, the reference

²⁶ As mentioned in section 9.3.1, the time exponent is stress-independent and may be taken as the average value obtained from the various specimens at a given hygrothermal condition.

²⁷ For broader temperature ranges, or considering temperatures closer to glass transition, the variations in reference elastic strain may not be negligible and thus must be duly accounted for. In such cases, a possible

elastic strain may be taken as the average value obtained from the three test temperatures, *i.e.*, $\varepsilon'_e = 16,932 \mu\varepsilon$.

Regarding the reference creep amplitude (m') values, these were found to increase significantly with temperature. In fact, this parameter was found to have the most important temperature dependence among all the general power law parameters, effectively defining the different creep responses obtained in the laminates as a function of temperature. The Arrhenius equation given in Equation (9.2) was fitted to the m' vs. T (in Kelvin) data, as shown in Figure 9.6. This fitting may be expeditiously carried out by rewriting Equation (9.2) in terms of the linear relationship between $\ln m'$ and $(1/T)$, given by $\ln m' = (-E_{m'}/R) \cdot (1/T) + \ln A_{m'}$. Consequently, estimating the Arrhenius equation parameters only requires determining the slope ($-E_{m'}/R$) and the intercept ($\ln A_{m'}$) of the linear regression between $\ln m'$ and $(1/T)$. Using this procedure, an activation energy of $E_{m'} = 84498 \text{ J/mol}$ and pre-exponential factor of $A_{m'} = 6.164\text{E}^{16}$ were obtained, resulting in the following Arrhenius equation:

$$m'(T) = 6.164\text{E}^{16} e^{\left(-\frac{84498}{8.314 \cdot T}\right)} \quad (9.11)$$

The average time exponent (\bar{n}) values presented a slight reduction trend with temperature, as shown in Figure 9.6. As previously discussed in section 9.4.3.2, this tendency was unexpected and it was unclear whether it resulted from the variability of material properties of the GFRP laminates or from real temperature dependence. Given the uncertainty regarding this result, as well as the reduced magnitude of the variation and its unexpected nature, the authors have considered a constant time exponent value of $n = 0.166$, resulting from the global average value obtained from the results of all temperatures and stress levels, as represented by the dashed line in Figure 9.6.

modelling approach for the ε'_e parameter could involve an adaptation of the kinetic model proposed by Bai *et al.* [23] or of the empirical models studied by Correia *et al.* [24]. However, in light of the temperature amplitude considered here, and of the resulting limited variations in the ε'_e values, such an approach was discarded for the current study.

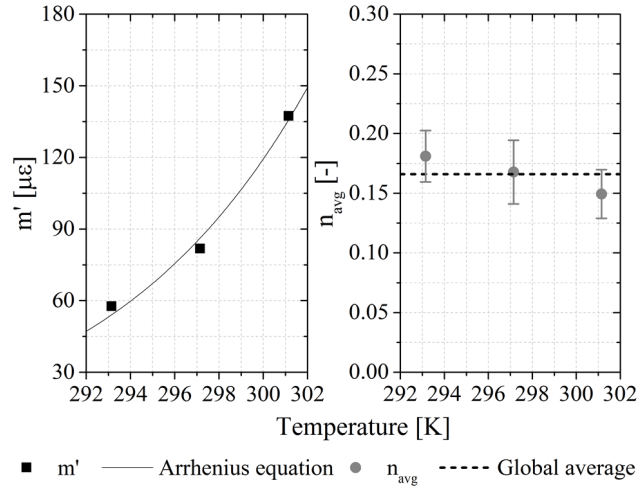


Figure 9.6. Fitting of Arrhenius equation to the reference creep amplitude (m') and average time exponent (\bar{n}).

As a result from the previous discussions, it is possible to rewrite Equation (9.1b) using the estimated parameters and temperature dependencies, thus obtaining Equation (9.12). This general equation models the total strain in the GFRP laminate as a function of flexural stress, creep time and temperature.

$$\begin{aligned} \varepsilon(\sigma, t, T) = & 16932 \sinh\left(\frac{\sigma}{467.5}\right) \\ & + \left(6.116E^{16} e^{\left(-\frac{84498}{8.314 \cdot T}\right)}\right) \sinh\left(\frac{\sigma}{80.4}\right) t^{0.166} \end{aligned} \quad (9.12)$$

The results provided by this equation are plotted in Figure 9.7 against the experimental creep curves. A good general agreement between the model and the experimental curves was obtained, both in terms of elastic strains (albeit with slight relative differences in the elastic strains for the T24-S35 and T28-S35 specimens, which exhibited higher experimental flexural moduli compared with the other specimens, *cf.* Table 9.1) and evolution of creep deformations. Overall, the proposed general equation is able to model the effect of temperature on the creep response of the GFRP laminate, considering temperatures within the 20°C to 28°C range and stresses at least up to 35%²⁸ of the laminate's flexural strength.

²⁸ Stresses in GFRP elements are typically well within this range for normal service conditions.

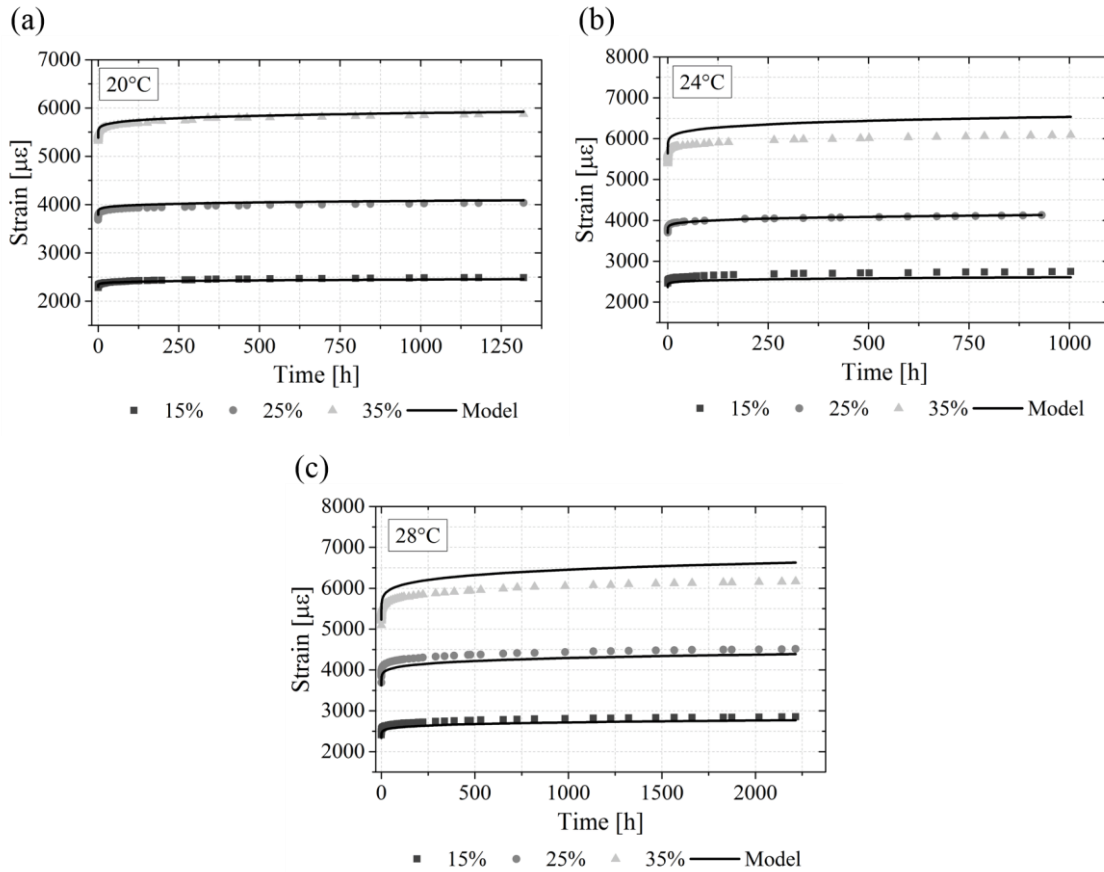


Figure 9.7. Comparison between experimental creep curves and the model [Equation (9.12)] estimates of strain over time as a function of stress and temperature.

9.5.3. Time and temperature dependent properties

Taking into account the relative magnitudes of the applied stresses (up to 35% of the flexural strength) and of the reference elastic and creep stresses ($\sigma_e = 467.5$ MPa and $\sigma_m = 80.4$ MPa, respectively), the following comments regarding Equation (9.12) are prompted: (i) the values of σ/σ_e will be low enough for the hyperbolic sine stress dependence of the elastic strain to be replaced by a linear dependence without causing significant deviations in the predicted values, and (ii) the values of σ/σ_m will be too high for such a simplification to be made. Consequently, one may consider the simplified approach described in section 9.3.3.1 to obtain the elastic flexural modulus value, *i.e.*, by assuming $E_e = \sigma_e/\epsilon'_e$. However, for the viscoelastic flexural modulus (E_t) the full-form approach detailed in section 9.3.3.2 should be considered, meaning that the modulus given by Equation (9.8) should be used. Following this procedure, the elastic and viscoelastic flexural moduli are as follows,

$$E_e = \sigma_e / \varepsilon'_e = \frac{467.5 \times 10^{-3}}{16932 \times 10^{-6}} = 27.6 \text{ GPa} \quad (9.13)$$

$$E_t(\sigma, T) = \frac{\sigma}{m'(T) \sinh\left(\frac{\sigma}{\sigma_m}\right)} = \frac{\sigma}{6.16E^{13} e^{\left(\frac{-84498}{8.314T}\right)} \sinh\left(\frac{\sigma}{80.4}\right)} \text{ [GPa]} \quad (9.14)$$

with stresses in MPa and temperature in Kelvin, resulting in flexural moduli values in GPa. The time-temperature-stress dependent flexural modulus may be obtained using Equation (9.15), where $n = 0.166$.

$$E(\sigma, t, T) = \left[\frac{1}{E_e} + \left(\frac{1}{E_t(\sigma, T)} \right) \left(\frac{t}{t_0} \right)^n \right]^{-1} \quad (9.15)$$

Flexural modulus predictions obtained using this equation are shown in Figure 9.8-a, considering a temperature of 20°C and flexural stresses of 25, 50, 75 and 100 MPa; in addition, the simplified equation is also plotted, which corresponds to considering a null stress value in Equation (9.15). Figure 9.8-b shows the influence of temperature on the flexural modulus predictions, for which the simplified flexural modulus equation was used in order to eliminate the influence of the stress value.

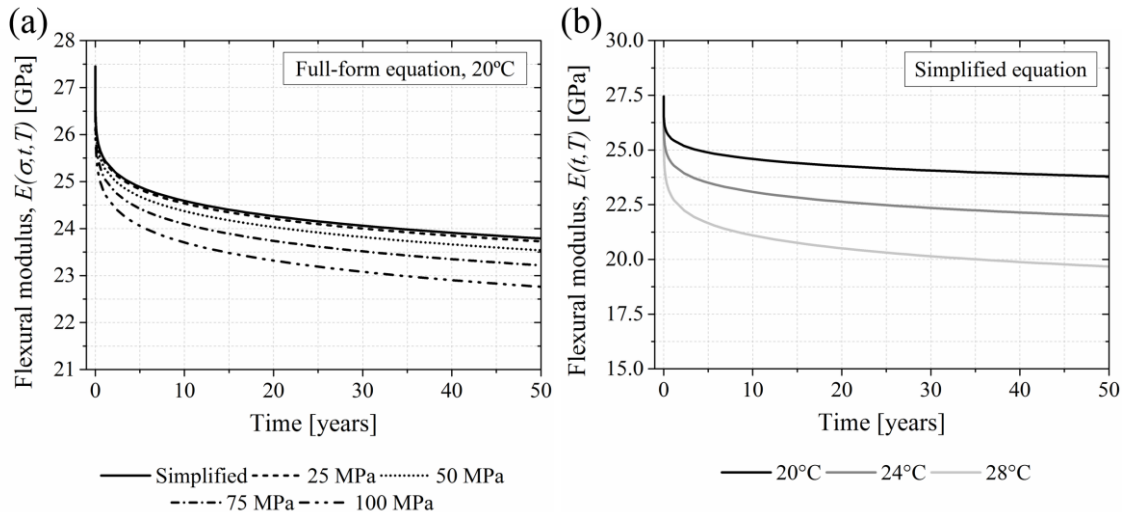


Figure 9.8. Long-term flexural modulus predictions: (a) effect of stress level, and (b) effect of temperature.

Regarding the effect of stress level, it is clear that for relatively low stresses (*e.g.*, below 25 MPa), the differences between the full-form and simplified equations are negligible.

However, with higher stresses the differences in predicted flexural moduli become increasingly important. As for the effect of temperature, the predictions in Figure 9.8-b illustrate how significant this factor is in the creep behaviour of the GFRP laminates, with the reductions in flexural modulus after 50 years of creep varying from 14% of the elastic value at 20°C to as much as 29% when considering a temperature of 28°C.

The flexural modulus reduction factor predictions for different temperatures and stress levels (analogous to the long-term flexural modulus curves of Figure 9.8) may be observed in greater detail in Figure 9.9. Also plotted in this figure are the respective creep coefficient curves, which show similar stress and temperature dependences compared to the effective flexural moduli and their reduction factors. For a 50 year creep period, and considering the simplified equation predictions plotted in Figure 9.9-b, creep coefficients are predicted to vary between 0.16 and 0.40, for temperatures in the range of 20°C to 28°C, confirming the relevance of this factor in the overall creep response of the GFRP laminates.

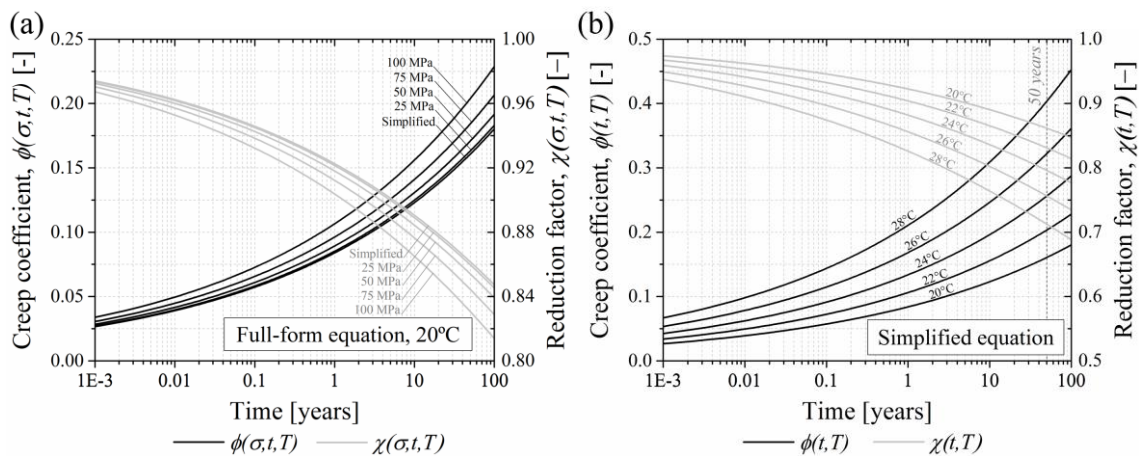


Figure 9.9. Creep coefficient and reduction factor curves: (a) effect of stress level, and (b) effect of temperature.

9.6. Comparison with TTSSP

In order to assess how the long-term creep predictions provided by the proposed model relate with commonly used methods, the viscoelastic strains obtained from Equation (9.12) were compared with a “master curve” with reference to the 20°C temperature and 15% stress

conditions, obtained through the application of the TTSSP²⁹. For this purpose, following the same procedure adopted in the previous chapter, the experimental creep curves obtained in the current study were shifted according to analytically determined shift factors, which may be calculated using the following expression [6],

$$a_h = \left[\frac{m(\sigma, T)}{m(\sigma_0, T_0)} \right]^{-\frac{1}{n_0}} \quad (9.16)$$

where a_h is the horizontal shift factor, $m(\sigma_0, T_0)$ is the creep amplitude for the reference conditions, $m(\sigma, T)$ is likewise for the accelerated conditions, and n_0 is the time exponent for the reference conditions.

Using this expression, horizontal shift factors (*cf.* Table 9.3) were calculated based on the parameters of the power law fittings presented in Table 9.1. Given the high variability in the experimental time exponent values, and the fact that the time exponent at the reference conditions (T20-S15, $n = 0.203$) was the highest value obtained, assuming this value in the shift factor calculations would provide a master curve that would overestimate the actual creep response of the GFRP laminates. To avoid this inconsistency, the average time exponent ($n = 0.166$) was considered when calculating the shift factors.

Table 9.3. Horizontal shift factors (a_h) used for TTSSP and TSSP.

Temperature [°C]	20°C			24°C			28°C		
Flexural stress (% of strength)	15%	25%	35%	15%	25%	35%	15%	25%	35%
Specimen	T20-S15	T20-S25	T20-S35	T24-S15	T24-S25	T24-S35	T28-S15	T28-S25	T28-S35
Reference: 15%, 20°C	1.0	7.33E-03	1.06E-03	1.03E-01	1.74E-03	5.63E-05	4.10E-03	1.69E-05	1.19E-05
Reference: 15% at each temperature	1.0	7.33E-03	1.06E-03	1.0	1.68E-02	5.45E-04	1.0	4.12E-03	2.90E-03

The comparison between the master curve and the model predictions is shown in Figure 9.10. It can be seen that a good general agreement between the two approaches (TTSSP and

²⁹ The assumptions and theory supporting the TTSSP are provided in the previous chapter, in section 8.6.

the proposed creep model) was found throughout the time period covered by the shifted creep curves.

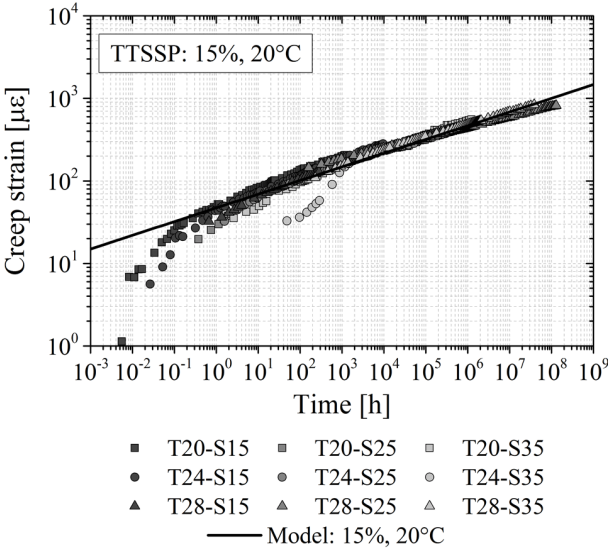


Figure 9.10. Time-temperature-stress superposition of experimental creep curves for reference conditions of 20°C and 15% stress and comparison with model predictions.

In order to verify the ability of the proposed model to provide similarly consistent results for different temperatures, a time-stress superposition (TSSP) approach was also developed for each test temperature, considering the 15% stress level as the reference condition. The corresponding shift factors are also presented in Table 9.3, while the master curves obtained are compared with the model predictions in Figure 9.11.

Once more, the proposed model closely follows the general development of the shifted curves for all temperatures. The good agreement in the comparisons shown herein indicates that the creep predictions provided by the proposed model are consistent with those resulting from the application of superposition principles, a method which has been frequently and successfully used for accelerated creep characterisation of similar materials.

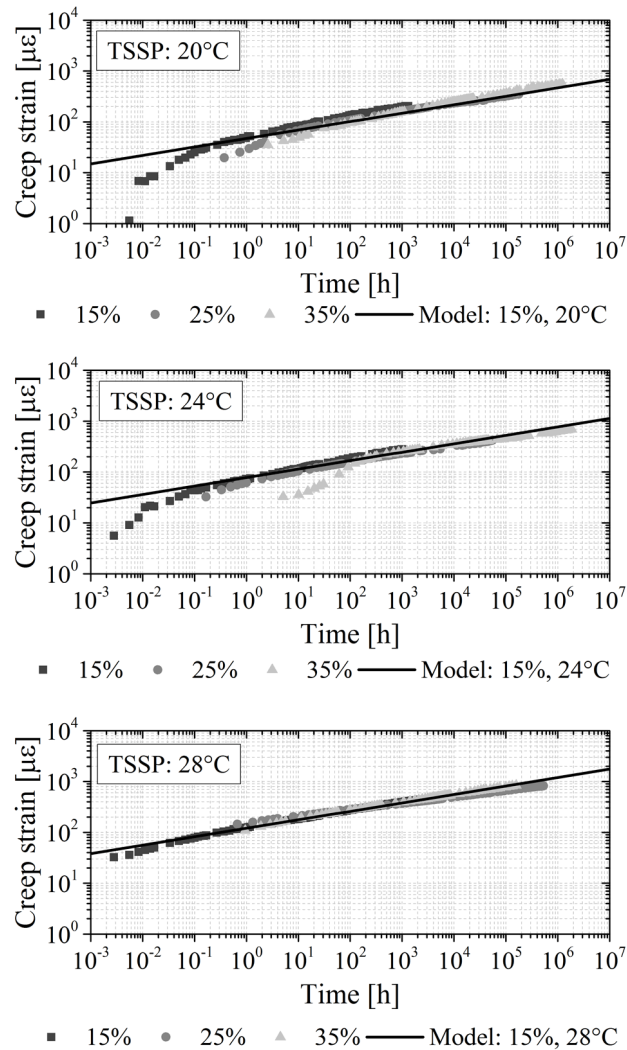


Figure 9.11. Time-stress superposition of experimental creep curves at different temperatures for the reference stress of 15% and comparison with model predictions.

9.7. Concluding remarks

Flexural creep experiments were carried out on GFRP laminates produced by vacuum infusion, a process that is frequently used for the production of composite sandwich panels. Flexural stress levels of 15%, 25% and 35% of the laminates' flexural strength and temperatures of 20°C, 24°C and 28°C were considered in this study. The GFRP's creep response was found to be strongly dependent on both the stress level and temperature, even for the 8°C amplitude considered, with higher creep rates being obtained at higher stresses and temperatures.

Findley's power law model provided good fittings to the experimental data. Regarding this model's parameters, the following conclusions were drawn for the considered temperature range (20°C to 28°C): (i) the time exponents (n) did not exhibit stress dependence; (ii) that parameter was also assumed as being temperature independent; (iii) the variation of the reference elastic strain (ε_e') values with temperature was found to be negligible; (iv) the reference creep amplitude (m') was found to increase significantly with temperature; and (v) the reference elastic stress (σ_e) and reference creep stress (σ_m) values were found to be constant with temperature.

Regarding the reference creep amplitude's temperature dependence, it was found to be well explained by the Arrhenius equation within the considered temperature range. This equation was successfully used to adapt Findley's power law model in order to include temperature dependence of the creep predictions.

The power law simplification procedure often applied to Findley's formulation was found to lead to significant differences between the creep components of the simplified and full-form equations. Consequently, the presented general power model should be used considering the hyperbolic sine stress dependence of the creep strains. Equations for design parameters, such as time-temperature-stress dependent flexural moduli, creep coefficients and flexural modulus reduction factors were provided considering the hyperbolic sine of stress level in Findley's equation.

Finally, the TTSSP and TSSP procedures were used to shift the experimental creep curves according to analytically obtained shift factors, thus providing master curves for various reference conditions. The proposed creep model was compared with the master curves, showing good agreement.

9.8. References

- [1] Sá, M.F., Gomes, A.M., Correia, J.R., Silvestre, N. (2011). "Creep behavior of pultruded GFRP elements – Part 1: Literature review and experimental study", *Composite Structures*, 93(10), 2450-2459.
- [2] Dutta, P.K., Hui, D. (2000). "Creep rupture of a GFRP composite at elevated temperatures". *Computers and Structures*, 76(1-3), 153-161.

- [3] Findley, W.N. (1960). *Mechanism and Mechanics of Creep of Plastics and Stress Relaxation and Combined Stress Creep of Plastics*, Rhode Island, U.S.A.: Division of Engineering, Brown University.
- [4] Schapery, R.A. (1969). "On the characterization of nonlinear viscoelastic materials". *Polymer Engineering and Science*, 9(4), 295-310.
- [5] Papanicolaou, G.C., Zaoutsos, S.P. (2011). "Viscoelastic constitutive modeling of creep and stress relaxation in polymers and polymer matrix composites". In *Creep and fatigue in polymer matrix composites*, Guedes, R.M. (ed.), Woodhead Publishing, 3-47.
- [6] Yen, S.-C., Williamson, F.L. (1990). "Accelerated characterisation of creep response of an off-axis composite material". *Composites Science and Technology*, 38, 103-118.
- [7] Daniali, S. (1991). "Short-term and long-term behavior of two types of reinforced plastic beams". *Proceedings of the 46th Annual Conference*, SPI Composite Institute, 13A, 1-5.
- [8] Sá, M.F., Gomes, A.M., Correia, J.R., Silvestre, N. (2011). "Creep behavior of pultruded GFRP elements – Part 1: Literature review and experimental study", *Composite Structures*, 93(10), 2450-2459.
- [9] Sá, M.F., Gomes, A.M., Correia, J.R., Silvestre, N. (2011). "Creep behavior of pultruded GFRP elements – Part 2: Analytical study". *Composite Structures*, 93(9), 2409-2418.
- [10] Scott, D.W., Lai, J.S., Zureick, A.-H. (1995). "Creep behavior of fiber-reinforced polymeric composites: A review of the technical literature", *Journal of Reinforced Plastics and Composites*, 14(6), 588-617.
- [11] Bai, Y., Keller, T., Vallée, T. (2008). "Modeling of stiffness of FRP composites under elevated and high temperature". *Composites Science and Technology*, 68(15-16), 3099-3106.
- [12] Correia, J.R., Gomes, M.M., Pires, J.M., Branco, F.A. (2013). "Mechanical behaviour of pultruded glass fibre reinforced polymer composites at elevated temperature: Experiments and model assessment". *Composite Structures*, 98, 303-313.
- [13] Scott, D.W., Zureick, A.-H. (1998). "Compression creep of a pultruded E-glass/vinylester composite". *Composites Science and Technology*, 58(8), 1361-1369.

[14] ISO 14125:1998 (1998). Fibre reinforced plastic composites – Determination of flexural properties. ISO, Geneva, Switzerland.

Chapter 10

Creep of full-scale sandwich panels

10.1. Introduction

The use of composite sandwich panels for civil engineering structural applications is increasingly being considered by practitioners, as illustrated by the successful case studies regarding their use in bridge decks [1] and roof structures [2,3]. Sandwich construction presents several advantageous characteristics to justify this interest, such as high stiffness-to-weight and strength-to-weight ratios, quick on-site assembly, or the possibility of incorporating thermal insulation into the structural elements (panels) by adopting core materials with low thermal conductivity, such as polymeric foams [4]. Their potential for use in building floors has also been highlighted by several authors [5-7], especially when the panels are reinforced with ribs/webs (hybrid core) [5].

However, polymer-based composite sandwich panels, such as those comprising fibre-reinforced polymers (FRP) and/or polymer foams, are prone to creep when subjected to significant permanent loads due to the viscoelastic nature of the polymeric materials [8,9]. This means that the effects of creep must be duly accounted for in the design of structural sandwich panels. To that end, data regarding the creep behaviour of sandwich panels and their constituent materials is necessary. Such data is still scarce and is often very much dependent on the sandwich panel architectures used in the respective experiments, meaning that its applicability in the analysis of different types of panel is limited. Furthermore, systematic comparative studies regarding the creep response of different materials used in sandwich construction are also scarce in the literature, especially regarding typical core materials, which are often the most prone to creep.

The work presented in this chapter aims to address this issue by means of an experimental assessment and analytical modelling of the creep response of four different types of sandwich panels. The proposed modelling approach separates the panels' creep behaviour

into the individual viscoelastic responses of their constituent materials. Such an approach, if successful in providing accurate estimates, allows the replacement of large scale creep testing on full sandwich systems by small scale material characterisation tests.

To this end, the creep experiments carried out on the PUR foam and GFRP laminates, presented in the two previous chapters, were complemented with shear creep tests of the PET foam and balsa wood. Additionally, full-scale panels of the PUR, PET, BAL and RIB typologies were tested in creep under flexural loads, providing experimental data for the validation of the proposed creep model. The followed modelling approach is simple and easily implementable – it involves using the creep behaviour of the individual constituent materials, given by moduli reduction factors, as input data for Timoshenko beam theory. The experimental creep curves obtained from the full-scale panels are compared with the model's predictions for different load levels to evaluate the accuracy of this approach.

10.2. Literature review

Few studies have attempted to model the creep of full-scale sandwich panels using as a basis the viscoelastic properties of their constituent materials. However, notable examples of such efforts may be found in the work of Huang and Gibson [8], Sheno *et al.* [10], Garrido *et al.* [9]³⁰, Ramezani and Hamed [11], and Hamed and Frostig [12].

Huang and Gibson [8] presented a study on the flexural creep behaviour of sandwich panels with aluminium faces and PUR foam cores with densities of 32, 48, 64, and 96 kg/m³. The aluminium faces were considered to have negligible viscoelasticity, whereas the foam core was assumed linear viscoelastic for shear stresses up to 40% of its shear strength (as per the findings of [13]). The authors performed three-point bending creep experiments at various load levels up to 40% of the panels' failure load (determined by the shear failure of the foam cores) for periods of 1200 h. Timoshenko beam theory was used in combination with the time-dependent creep compliance of the foam cores, as characterised in [13], to model the flexural creep of the sandwich panels. The authors found that the model provided reasonably

³⁰ As mentioned in chapter 1, this work corresponded to a preliminary study regarding the creep behaviour of sandwich panels, providing the basis for the investigations reported in the current part of this thesis.

good estimates, with deviations up to 10% from the experimental creep curves. For this particular case the PUR foam core was the only material in the sandwich panel that exhibited creep.

Shenoi *et al.* [10] also studied the flexural creep response of sandwich panels, equally assuming that creep of the face sheets had a negligible contribution to the panels' long-term deflections. The authors adopted this assumption while considering a polymer based facing material (hybrid glass-Kevlar fibres in an epoxy resin matrix) and a rigid polyvinyl chloride (PVC) foam core in the experimental investigations. Sandwich beams were loaded in ten-point bending (aiming at simulating a uniformly distributed load) for periods up to approximately 1000 h, and the obtained creep curves were used to estimate the creep compliance of the core material. As a consequence of their assumption regarding the face sheet viscoelasticity, the beam's creep deflections were assumed to stem solely from the core's viscoelasticity, possibly overestimating its creep response.

Garrido *et al.* [9] presented experimental and analytical investigations regarding the creep behaviour of a sandwich panel with GFRP faces and a PUR foam core with a density of 68 kg/m^3 . The authors experimentally assessed the creep response of the PUR foam in shear, as well as the flexural creep response of the sandwich panel for a period of approximately 3600 h. Using a time-dependent shear modulus reduction function for the foam, determined from the shear creep experiments, and elastic modulus reduction functions available in the literature for the GFRP, the authors obtained creep deflection estimates based on Timoshenko beam theory. These compared well with the full-scale sandwich panel's experimental creep curve, with a root mean squared deviation (RMSD) between the two curves of approximately 6% (calculated along their development).

Higher-order analytical approaches have also been used in multiple investigations regarding creep of sandwich panels, such as those of Ramezani and Hamed [11] and Hamed and Frostig [12]. These typically adopt high-order shear deformation theories (*e.g.*, Frostig *et al.* [14]) as an alternative to first-order shear deformation theories, such as Timoshenko beam theory. However, their increased complexity makes them difficult to use expeditiously, which may constitute an obstacle to their widespread adoption in the civil engineering domain. Furthermore, while Ramezani and Hamed [11] presented only a limited experimental validation of their analytical model based on creep curves with high scatter available in

literature, Hamed and Frostig [12] did not present any experimental validation of their analytical creep predictions.

To the author's best knowledge, there are no studies available in the literature regarding the creep of sandwich panels with reinforcement ribs/webs. These elements have shown high efficiency in improving the elastic behaviour of sandwich panels [5,15]. It would also be expectable that they would have a considerable influence in the creep behaviour of such panels. Additionally, in most of the mentioned studies, the only viscoelastic materials considered in the analyses were those used as core. The complexity of the problem increases when faces, core and ribs simultaneously deform viscoelastically. When considering sandwich panels comprised of polymeric materials, this problem must be duly assessed and suitable modelling approaches are necessary.

Finally, it is worth mentioning that the current normative framework for the consideration of creep in sandwich structures for civil engineering applications is fairly limited. A notable effort is being made for the development of a European pre-standard for the design of fibre reinforced polymer structures [16]. However, these guidelines still consider a rather simplistic approach to the issue of creep of sandwich structures, which may be partly attributed to the lack of experimental data and suitable/practical analytical models.

10.3. Experimental programme

10.3.1. Materials and panel architectures

In this investigation, sandwich panels of the PUR, PET, BAL, and RIB typologies were used. The cross-sectional dimensions for each panel typology are provided in Figure 10.1 for reference (the panels' characteristics are detailed in chapter 3).

The elastic mechanical properties of the materials are as determined in chapter 4, with the exception of the shear moduli of the core materials (PUR and PET foams and balsa wood), for which the effective shear moduli (values determined in the effective flexural properties tests of chapter 5) were used.

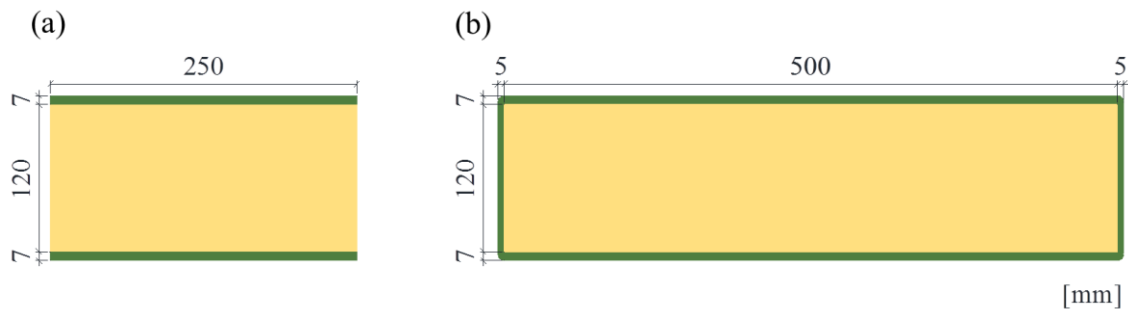


Figure 10.1. Cross-sectional dimensions of the sandwich panels: (a) PUR, PET, and BAL, and (b) RIB.

10.3.2. Experiments and test setups

10.3.2.1. Overview of experimental programme

The experimental programme included: (i) shear creep testing of the PET foam and balsa wood, and (i) flexural creep testing of the sandwich panels. The shear creep tests were carried out for the PET foam and balsa wood to gather the necessary data to complete the characterisation of the creep behaviour of the sandwich panels' constituent materials³¹. These data serve as input for the modelling of the full-scale sandwich panels' creep response. Additionally, they provide valuable experimental data regarding the creep behaviour of commonly used core materials, such as those considered here.

The full-scale flexural creep tests of the sandwich panels were aimed at providing reference creep data for the different sandwich panel typologies. Such data, which is scarce in the literature for panels of this scale, provides the means for the experimental validation of the proposed creep modelling approach. The experimental setups used for this test as well as for the other types of tests are described in the next sections.

10.3.2.2. Shear creep of PET foam and balsa wood

Following the same methodology and test setup adopted in chapter 8 for the PUR foam, shear creep tests were carried out for the PET foam and the balsa wood. Two specimens per material, with nominal dimensions of 250 mm × 250 mm × 120 mm, were tested at a nominal temperature of 20 °C. Relative humidity in the test room could not be controlled; its value

³¹ For the shear creep behaviour of the GFRP ribs, experimental results found in literature were used, as discussed in section 9.5.

Chapter 10 Creep of full-scale sandwich panels

was monitored, being relatively stable with average values of about 55-57% (*cf.* Table 10.1). The PET foam specimens were subjected to stress levels corresponding to approximately 4% and 15% of their shear strength, whereas for the balsa wood specimens stress levels of approximately 5% and 19% were used.

The vertical displacement of the loaded steel plate was measured using displacement transducers with precision of 0.01 mm during the load application phase (which had a duration of approximately 1 to 2 seconds) and during the first ~72 h of creep. After this period, the displacement transducers were replaced by analogue dial gauge indicators, with precision of 0.001 mm. A summary of the experimental conditions and results is given in Table 10.1. A labelling code was used in which the first three letters identify the material (PET or BAL), the second two letters indicate a shear creep (SC) specimen, and the final number corresponds to the specimen number.

10.3.2.3. Flexural creep of full-scale panels

Flexural creep experiments were carried out on the four different types of sandwich panel to characterise their response. The PUR, PET and BAL panels were tested in a temperature controlled environment, with a nominal temperature of 20 °C. The average RH in the test room for the duration of the experiments varied between 55-63%. The RIB panels were tested in a different room with a high thermal inertia, for which an average temperature of 21.8 °C \pm 0.7 °C and relative humidity (RH) of 63.5% \pm 6.3% was registered during the period of the creep experiment. The test durations ranged between 790 h and 1240 h, depending on the test series. The average temperatures and RH values, and the test durations per panel typology are given in Table 10.2.



Figure 10.2. Full-scale creep tests setups for: (a) PUR, PET and BAL panels, and (b) RIB panels.

A test span of 3.30 m was adopted, equal to that used in the flexural failure tests. The panels were simply supported on steel rollers, and loaded using concrete slabs (each with dimensions of 400 mm × 600 mm × 45 mm and weight of 0.26 kN) placed in six rows along the span to simulate a uniformly distributed loading, as shown in Figure 10.2. Three specimens per panel type were tested, each with a different nominal load value³²: (i) 3.75 kN/m², (ii) 7.50 kN/m², and (iii) 15.00 kN/m². The mid-span deflections were continuously measured during load application and throughout the first ~72 h of creep using displacement transducers with a precision of 0.01 mm. The displacement transducers were subsequently replaced by analogue dial gauge indicators with precision of 0.001 mm, and periodic deflection measurements were taken.

The loading was carried out manually, and the loading times were dependent on load level. For the PUR, PET and BAL panels, the loading operations took approximately 1 minute for the lowest load level and 4 minutes for the highest one. For the RIB configuration, due to the higher (double) panel width, twice as many concrete slabs were required to load the specimens. Consequently, the loading times were also approximately twice those achieved for the other typologies. During the load application process, given the magnitude of time taken by these operations, some creep deformation is expected to have occurred. It was not possible to account for these deformations in the analysis of results, given that separating the elastic deflection increments from the viscoelastic deformations would be cumbersome. However, given the relatively long time-scale of the creep experiments, it is not expected that the value of these creep deformations would be significant compared to the total magnitude of creep deflections exhibited by the panels. Furthermore, the consistency of the collected results (analysed from the moment when the loads are fully applied) also seems to support the above-mentioned hypothesis.

³² The lowest load is approximately 25% lower than the ultimate limit states (ULS) flexural design load. (according to Eurocode standards), which has a value of 5.025 kN/m², obtained by considering a permanent load $G = 1.5$ kN/m², a live load $Q = 2.0$ kN/m², and partial safety factors $\gamma_G = 1.35$ and $\gamma_Q = 1.50$. The relatively high load values adopted in the creep tests are justified by the need of inducing noticeable creep deformations in the panels that would be easily and accurately measured with the test instrumentation.

10.4. Creep of PET foam and balsa wood

The creep results for the core materials were analysed and fitted using Findley's power law, introduced in chapter 8 (section 8.3.1). The creep curves and respective individual (simplified) power law fittings are shown in Figure 10.3. The total shear strains (elastic and creep) are shown in a linear plot in Figure 10.3-a, whereas Figure 10.3-b presents a bi-logarithmic plot of the creep strains.

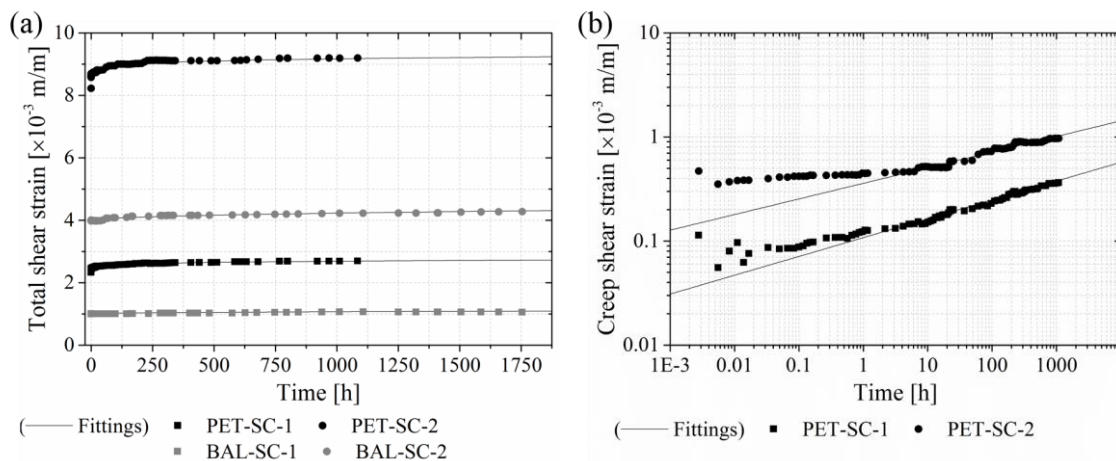


Figure 10.3. Experimental shear creep curves: (a) linear plot of total strains, and (b) bi-logarithmic plot of creep strains.

The PET foam presented a typical power law creep development throughout the duration of the test (1085 h), with creep amplitude (m) values proportional to the applied shear stresses. An average creep exponent of $n = 0.134$ was obtained for this foam. The balsa wood, on the other hand, presented very limited creep deformations during the 1755 h of the creep test. In fact, during the first hours after load application, no significant creep deformations were measured by the test instrumentation, as these were lower than the precision of the displacement transducers used (0.01 mm). After the transition from digital to analogue measurement, which occurred approximately 70 h after load application, it was possible to measure slight creep deformations, due to the analogue dial gauge's higher precision (0.001 mm). The total strains measured are shown in Figure 10.3-a; at the end of the creep test (after 1755 h), the measured strains were only 6-7% higher than the elastic deformation. Consequently, owing to these very limited creep deformations, it was not possible to obtain reliable power law fittings to characterise this material's creep response.

Regarding the creep of the PET foam, the reference parameters (γ'_e , τ_e , m' , and τ_m) of Findley's general power law were estimated considering the elastic strains (γ_0) and the creep amplitude (m) values from the individual power law fittings and their direct relation to those parameters (similar procedure to that used in chapters 8 and 9). The creep exponent was taken as the average n value obtained from the individual fittings (*cf.* Table 10.1). The resulting generalised power law for the shear creep of the PET foam is given in Equation (10.1).

$$\gamma_{PET}(\tau, t) = 0.995 \sinh\left(\frac{\tau}{16.42}\right) + 0.985 \times 10^{-3} \sinh\left(\frac{\tau}{0.37}\right) t^{0.166} \quad (10.1)$$

Using the estimated general power law parameters and the process presented in chapter 8, an expression for the time-dependent shear modulus reduction factor was derived, taking the form shown in Equation (10.2).

$$\chi_{PET}(t) = [1 + (4.4 \times 10^{-2}) \times t^{0.166}]^{-1} \quad (10.2)$$

Table 10.1. Summary of results from the shear creep tests of PET foam and balsa wood.

Material	PET foam		Balsa wood	
	$T^1: 20.0 \pm 0.7^\circ\text{C}$, $RH^2: 56.9 \pm 7.4\%$		$T: 20.4 \pm 0.9^\circ\text{C}$, $RH: 55.4 \pm 5.7\%$	
Specimen	PET-SC-1	PET-SC-2	BAL-SC-1	BAL-SC-2
τ [MPa]	0.036	0.143	0.045	0.178
γ_0 [$\times 10^{-3}$ m/m]	2.33	8.22	1.00	3.98
G_e [MPa]	15.5	17.4	44.7	44.8
(individual and average)	16.5		44.7	
m [$\times 10^{-3}$ m/m]	0.108	0.359	-	-
n [-]	0.181	0.150	-	-
(individual and average)	0.166		-	

¹average temperature \pm standard deviation;

²average relative humidity \pm standard deviation.

10.5. Creep of GFRP ribs

Regarding the creep of the GFRP ribs in shear, it was not possible to find specific data in the literature pertaining to the shear creep behaviour of GFRP laminates produced by vacuum infusion. Therefore, the experimental data reported in Bottoni *et al.* [17] and the shear moduli reduction factors proposed in EUROCOMP [18] were adopted.

Bottoni *et al.* [17] carried out shear tests on pultruded GFRP specimens (the fibre layup was not provided by the authors) at a controlled temperature of 20 °C and RH of 60%, for a period of about 760 days, having found that the shear creep deformations followed a typical power law development throughout the duration of the experiments. The time-dependent reduction factor given in Equation (10.3) was determined from the creep data provided by the authors.

$$\chi_r(t) = (1 + 0.149 \times t^{0.205})^{-1} \quad (10.3)$$

On the other hand, the EUROCOMP design code and handbook suggests a time-dependent creep reduction factor curve for the shear modulus of unidirectional GFRP composites, given by the following equation [19]:

$$\chi_r(t) = 0.897 - 4.719 \times 10^{-2} \times \ln(t) \quad (10.4)$$

10.6. Creep of full-scale panels

The creep curves obtained per panel series in the flexural creep tests are shown in Figure 10.4. Table 10.2 gives a detailed summary of the experimental results for the four different panel types. This table includes also the exact values of the applied loads for each specimen, as well as simple estimates of the shear stress percentage relative to the core's shear strength in the PUR, PET and BAL panels. By analysing those percentages, it is possible to observe that the applied loads are significantly higher (proportionally) for the PUR panels than for the PET and BAL ones. In fact, the highest load level induced shear stresses in the core of specimen PUR-3 that represent 61% of the foam core's average shear strength (0.32 MPa). This stress value should not be within the range of linear viscoelastic behaviour for this foam, as per the results of chapter 8. However, this was necessary to guarantee direct result comparability among the different core typologies by adopting equal load levels across the entire sample, while still applying high enough loads to produce a significant creep response in the PET, BAL and RIB panels.

The elastic response of each panel series was consistent with elastic compliance³³ (S_e) values showing low scatter. The average values of this parameter were highest for the PUR panels, intermediate for the PET panels, and lowest for the BAL and RIB panels (which presented nearly equivalent results), an observation that agrees well with the findings from the flexural failure experiments of chapter 5.

Table 10.2. Summary of flexural creep experimental results.

Typology/series	PUR			PET			BAL			RIB		
Environmental conditions	T ⁽¹⁾ : 19.9 ± 0.4°C RH ⁽²⁾ : 63.2 ± 5.4			T ⁽¹⁾ : 20.0 ± 0.7°C RH ⁽²⁾ : 56.9 ± 7.4			T ⁽¹⁾ : 20.4 ± 0.4°C RH ⁽²⁾ : 55.4 ± 5.7			T ⁽¹⁾ : 21.8 ± 0.7°C RH ⁽²⁾ : 63.5 ± 6.3		
Test duration	910 h			1080 h			1240 h			790 h		
Specimen	PUR-1	PUR-2	PUR-3	PET-1	PET-2	PET-3	BAL-1	BAL-2	BAL-3	RIB-1	RIB-2	RIB-3
Applied load (p) [kN/m ²] (% of failure load ⁽³⁾)	3.81 (15%)	7.64 (30%)	15.25 (61%)	4.01 (6%)	8.00 (11%)	16.12 (22%)	3.94 (6%)	7.82 (11%)	15.91 (22%)	3.80	7.57	15.07
Elastic deflection (δ_0) [mm]	6.36	14.47	28.57	5.35	10.60	21.65	4.18	8.04	16.40	4.12	8.40	16.03
Elastic compliance (S_e) [mm/(kN/m ²)] (average ± st. dev.)	1.67	1.89	1.87	1.34	1.32	1.34	1.06	1.03	1.03	1.09	1.11	1.06
	1.81 ± 0.13			1.33 ± 0.01			1.04 ± 0.02			1.09 ± 0.02		
Creep amplitude (m) [mm]	0.470	1.087	2.296	0.145	0.274	0.399	0.251	0.405	0.665	0.185	0.315	0.634
Creep exponent (n) [-] (average ± st. dev.)	0.236	0.248	0.278	0.219	0.233	0.256	0.210	0.199	0.216	0.246	0.252	0.243
	0.254 ± 0.022			0.236 ± 0.019			0.208 ± 0.009			0.247 ± 0.005		
Creep compliance (S_t) [mm/(kN/m ²)] (average ± st. dev.)	0.123	0.142	0.151	0.036	0.034	0.025	0.064	0.052	0.042	0.049	0.042	0.042
	0.139 ± 0.014			0.032 ± 0.006			0.052 ± 0.011			0.044 ± 0.004		

⁽¹⁾Average temperature ± standard deviation;

⁽²⁾Average relative humidity ± standard deviation;

⁽³⁾For the simple cored typologies, considering panel strength limited by shear failure of the core.

A typical creep response, following a power law development with time, was obtained for all panel types, as shown in Figure 10.4. Thus, individual power laws were fitted to the creep curves. The creep amplitude and creep exponent values are also given for each specimen in Table 10.2, as well as the obtained creep compliance values ($S_t = m/p$).

The creep exponents and creep compliance values do not appear to follow any clear trend with regard to load level for the PET, BAL and RIB panels, while also presenting relatively

³³ Elastic compliance is calculated from $S_e = \delta_0/p$, where δ_0 is the elastic deflection and p is the applied load, corresponding to the inverse of the flexural stiffness.

low scatter within each series. For the PUR panels, both sets of values (n and S_t) show an increasing trend, which may be due to the relatively high shear stresses within the PUR foam core, extending beyond the limit of linear viscoelasticity for that material.

The lowest average creep exponent was obtained for the balsa wood cored panels, which however presented only the third lowest creep compliance. The highest creep response was observed for the PUR foam cored panels, which presented the highest average creep exponent and creep compliance values. The PET panels exhibited the lowest creep compliance, and the RIB panels presented a creep response with the same overall magnitude of that exhibited by the PET and BAL panels. The significantly lower creep response of the RIB panels compared to the PUR panels confirms that the addition of longitudinal GFRP ribs, besides significantly increasing the elastic stiffness, is quite effective in limiting the panels' viscoelastic response. This aspect is further discussed in section 10.7.2.

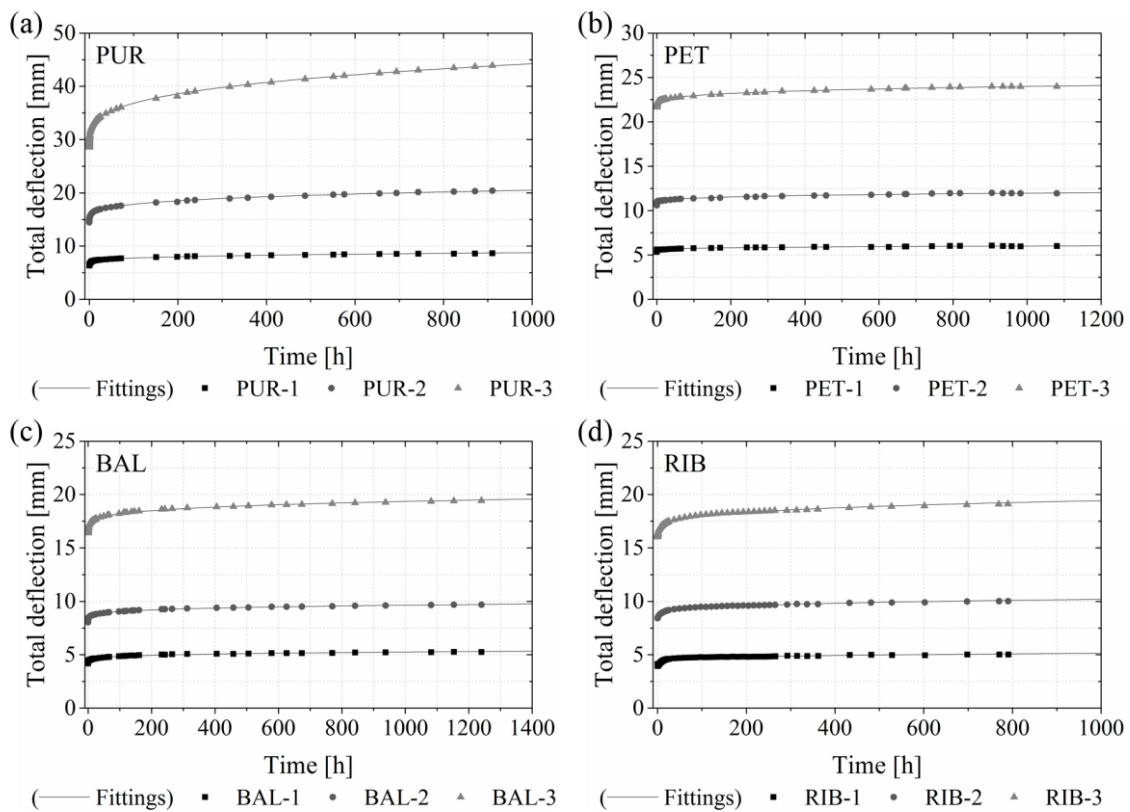


Figure 10.4. Experimental creep curves and individual power law fittings for the: (a) PUR, (b) PET, (c) BAL, and (d) RIB panel series.

Regarding the viscoelasticity of the balsa wood, the results obtained in the shear creep experiments and in full-scale flexural creep tests were inconsistent. Indeed, while the first test yielded almost negligible creep deformations in the balsa wood (impossible to measure

at times, being lower than the instrumentation precision), creep deflections of a certain significance were observed for the BAL panels. This suggests that the balsa wood core should exhibit measurable viscoelastic deformations. This apparent inconsistency may be explained by the material's orthotropic behaviour and the orientation of the wood fibres in the shear creep tests. In those tests, the wood fibres were aligned perpendicularly to the steel plates that applied shear loading, as occurs in the sandwich panels where they have a perpendicular orientation relative to the face sheets. Consequently, the measured shear deformations resulted from shear forces applied perpendicularly to the wood fibres. However, for shearing forces parallel to the wood fibres, higher creep deformability would be expectable, as the wood's properties along this direction are weaker. In the sandwich panel cores, balsa wood experiences shear forces along both directions, and thus it is reasonable to expect that its creep response will result from a contribution of both shear modes. However, under the scope of the current thesis it was not possible to conduct further creep experiments on balsa wood specimens, and consequently this hypothesis is yet to be experimentally tested.

10.7. Composed creep modelling

10.7.1. Modelling assumptions

The creep behaviour of sandwich panels was modelled using the composed creep modelling (CCM) approach, put forward in [9]. In the current study, this approach is further assessed for different panel architectures, including its application to sandwich panels with longitudinal reinforcement ribs.

The CCM approach provides predictions of a sandwich panel's creep response by considering the creep of its individual materials/components and using them as input in an appropriate model of the panel's structural behaviour. The creep behaviour of each component should be obtained for the same conditions that sandwich panels experience when subjected to permanent loading (*i.e.*, stress state, temperature, and other relevant factors). The effects of creep may be taken into account by considering the viscoelastic increase in the material's deformations, as time-dependent reductions (χ) of its stiffness or elastic moduli. Consequently, time-dependent reduction factors affecting the material's mechanical (elastic) properties may be determined and used to affect those properties in a

model of the sandwich panel's structural behaviour. This type of procedure has been suggested for FRP pultruded elements in the EUROCOMP Design Code and Handbook [18] and in the guidelines of the CNR – DT 205/2007 [20], although its experimental validation is still incomplete, as per the previously presented literature review.

In the current study, this procedure was implemented using Timoshenko beam theory. Accordingly, Equation (10.5) gives the mid-span deflection of a beam ($\delta_v^{L/2}$), considering the time (t) dependent effects of creep by affecting the Young's modulus of the faces (E_f) and the shear modulus (G_c) of the core with their respective reduction coefficients, χ_f and χ_c . In this equation, p represents the uniformly distributed load (load per unit length), L corresponds to the span length, I is the second moment of inertia of the face sheets, and $A_{V,c}$ is the effective shear area of the core. Equation (10.5) is suitable for simple sandwich panels with identical top and bottom face sheets, without longitudinal ribs, and considering a unidirectional behaviour.

$$\delta_v^{L/2}(t) = \frac{5}{384} \left(\frac{pL^4}{\chi_f(t)E_f I} \right) + \frac{1}{8} \left(\frac{pL^2}{\chi_c(t)G_c A_{V,c}} \right) \quad (10.5)$$

In sandwich panels with longitudinal reinforcement ribs, as discussed earlier (chapter 6), a very significant portion of the shear forces due to vertical loading are taken by the ribs, albeit a non-neglectable part of these are supported by the core. Consequently, in order to address the different distribution of shear forces, Equation (10.6) is proposed for the time dependent mid-span deflection of sandwich panels with longitudinal reinforcement ribs. In this equation, the sandwich panel's shear stiffness, $(GA_V)_h$, results from the contributions of the ribs and the foam core, considering a homogenised cross-section, where $(GA_V)_h(t) = \chi_c(t)G_c A_{V,c} + \chi_r(t)G_r A_{V,r}$, χ_r being the reduction factor for the rib material's shear modulus (G_r), $A_{V,r}$ the effective shear area of the ribs, the remaining symbols having the same meaning as presented above. The portions of shear force taken by the foam core and the ribs, α_c and α_r , may be estimated based on Equations (10.7a and b). It is assumed that $\alpha_c + \alpha_r = 1$, *i.e.*, the only panel components contributing to the shear stiffness of the panel are the foam core and the ribs (the contribution of the face sheets is not considered), and that these contributions change with creep time according to the time-dependent properties of the materials (as given by the respective reduction factors).

$$\delta_v^{L/2}(t) = \frac{5}{384} \left(\frac{pL^4}{\chi_f(t)E_f I} \right) + \frac{1}{8} \left(\frac{pL^2}{(GA_V)_h(t)} \right) \quad (10.6)$$

$$\alpha_c(t) = \frac{\chi_c(t)G_c A_{V,c}}{\chi_c(t)G_c A_{V,c} + \chi_r(t)G_r A_{V,r}} \quad (10.7a)$$

$$\alpha_r(t) = \frac{\chi_r(t)G_r A_{V,r}}{\chi_c(t)G_c A_{V,c} + \chi_r(t)G_r A_{V,r}} \quad (10.7b)$$

In the current study, the moduli reduction coefficients for the faces (chapter 9), ribs (section 10.5 of the current chapter), and core (chapter 8 for the PUR foam and section 10.4 of the current chapter for the remaining materials) were used. Where temperature-dependent properties were available, namely for the GFRP faces and the PUR foam core, the applicable test temperatures were considered. Thus, a temperature of 20 °C (293.15 K) was considered for the PUR typology (nominal test temperature), and a temperature of 21.8 °C (294.95 K) was considered for the RIB panels (average temperature during the experiments).

Regarding the GFRP faces, the equation adopted for the Young's modulus reduction factor was stress-dependent; however, the stresses in the panel's faces during the full-scale creep tests were lower than the threshold value of ~25 MPa above which this dependence becomes significant (*cf.* chapter 9, Figure 9.9). Consequently, it was possible to consider uniform modulus reductions throughout the length of the faces, despite their stress variation along the span.

10.7.2. Model predictions

Before analysing the predicted creep deflection curves, it is interesting to observe the time-dependent moduli reduction factors that are considered for each constituent material. These factors are plotted in Figure 10.5 for a 1000 h creep period. The highest shear modulus reductions due to creep are exhibited by the PUR foam. In fact, for this material, the reduction factor after 1000 h of creep is approximately 0.5, *i.e.*, creep deformations in the foam are predicted to be as high as the elastic deformations after only 1000 h under constant load. In contrast, the shear modulus reductions obtained for the PET foam were quite low.

The GFRP ribs are quite prone to creep, albeit having lower shear moduli reductions than the PUR foam core. This result would be expectable since the shear response of GFRP is

typically matrix dominated, and polymer matrices are well known to exhibit significant viscoelasticity. However, relatively important differences in predicted creep behaviour are found between the two shear modulus reduction functions, *i.e.*, Equations (10.3) and (10.4). Equation (10.4), suggested in the EUROCOMP design code and handbook [18], leads to higher shear modulus reductions than those obtained using the data of Bottoni *et al.* [17]. After 1000h, these differences are of about 8%, with Equation (10.3) predicting a reduction factor of 0.62 *vs.* a value of 0.57 from Equation (10.4). For longer periods, the magnitude of the differences between the two equations remains approximately the same (*e.g.*, after 50 years, reduction factors of 0.32 and 0.28 are predicted with Equations (10.3) and (10.4), respectively). Given the multitude of factors affecting the creep response of FRPs, either related to the material itself (such as the resin type and its degree of cure, the fibre architecture and volume fraction, the processing method, etc.), or to the environmental conditions during creep (temperature, relative humidity, etc.), it is normal to find a certain degree of variability in the measured viscoelastic responses among different investigations.

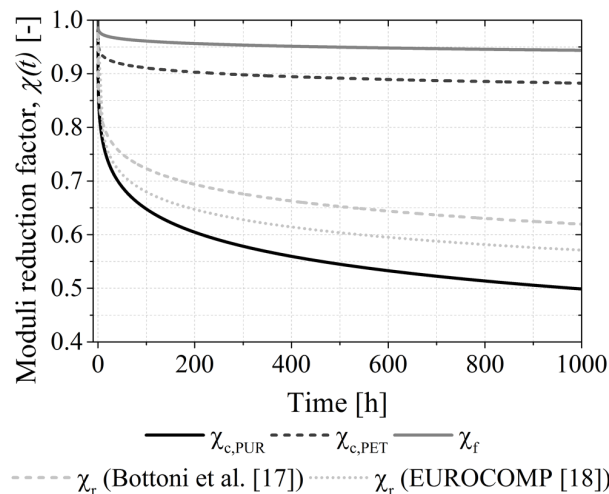


Figure 10.5. Moduli reduction factors for the shear modulus of the PUR foam, PET foam and GFRP ribs, and the Young's modulus of the GFRP faces.

For the GFRP laminates in bending, the estimated Young's moduli reductions are approximately 6% after 1000 h. This contrasts with the relatively high reduction factors for the GFRP in shear. This is a logical result due to the fibre architecture of the face sheet laminates used in this study, with much higher fibre content along the axial direction (direction of loading).

Using these modulus reductions as input in the adapted CCM formulation given by Equations (10.5) and (10.6), predicted creep deflection curves were obtained and plotted in Figure 10.6 against the respective experimentally obtained results for the PUR, PET and RIB panel typologies at each load level. For the BAL panels, the application of the CCM was not possible, since it was not possible to measure significant creep deformations in the shear creep tests of the balsa wood.

The creep predictions for the PUR panels reproduce quite well the overall development of the experimental curves. A slight overestimation of the creep deflections is obtained for the two lowest load levels. However, for the highest load, the CCM underestimates the experimental creep deflections, likely due to the nonlinearity of the PUR foam's creep behaviour at such high stresses. For this panel type, the CCM creep predictions are largely influenced by the creep response of the PUR foam, which was found to exhibit significant viscoelasticity in the small-scale shear creep tests (chapter 8). In fact, considering the CCM predictions at 900 h of creep time, the shear creep deformation accounts for 95% of the total creep deflection (for all load levels), while bending creep deformation only accounts for 5% of that deflection.

For the PET panels, the predicted creep curves follow the experimental results with reasonable accuracy for all three load levels, however showing a slight underestimation tendency. In these panels, creep deformations are distributed between the components in a more balanced way. According to the CCM predictions, at 900 h the creep of the faces accounts for 43% of the total creep deflection, and the remaining 57% is due to the core's shear creep.

Regarding the RIB panels, the CCM predictions vary significantly depending on the rib shear modulus reduction factors used. Considering the factors given by Equation (10.3), *i.e.*, the data from Bottoni *et al.* [17], the creep predictions slightly underestimate the experimental creep curves. However, using the reduction factors suggested in EUROCOMP [18], higher creep deflections are predicted, overestimating the experimental curves for the two highest load levels. These results show that small variations in the viscoelastic properties of the materials can have a significant influence on the overall creep response of the panels.

In general, the results obtained attest the adequacy of the proposed analytical approach in predicting the creep response of sandwich panels with longitudinal GFRP ribs. Using the proposed model, it is interesting to assess the variation of the shear force distribution

between the ribs and the core of the sandwich panels with creep time. Figure 10.7 plots the time-dependent α_r and α_c factors for a long-term period (50 years), considering the two different equations for the ribs' shear modulus reduction factors. Considering $\chi_r(t)$ given by Equation (10.3) (Bottoni *et al.* [17]), it is possible to observe that the overall contribution of the ribs to the shear stiffness is higher (over time) than that obtained considering $\chi_r(t)$ given by Equation (10.4) (EUROCOMP [18]). This is a direct consequence of the higher shear moduli reductions predicted by the latter reference.

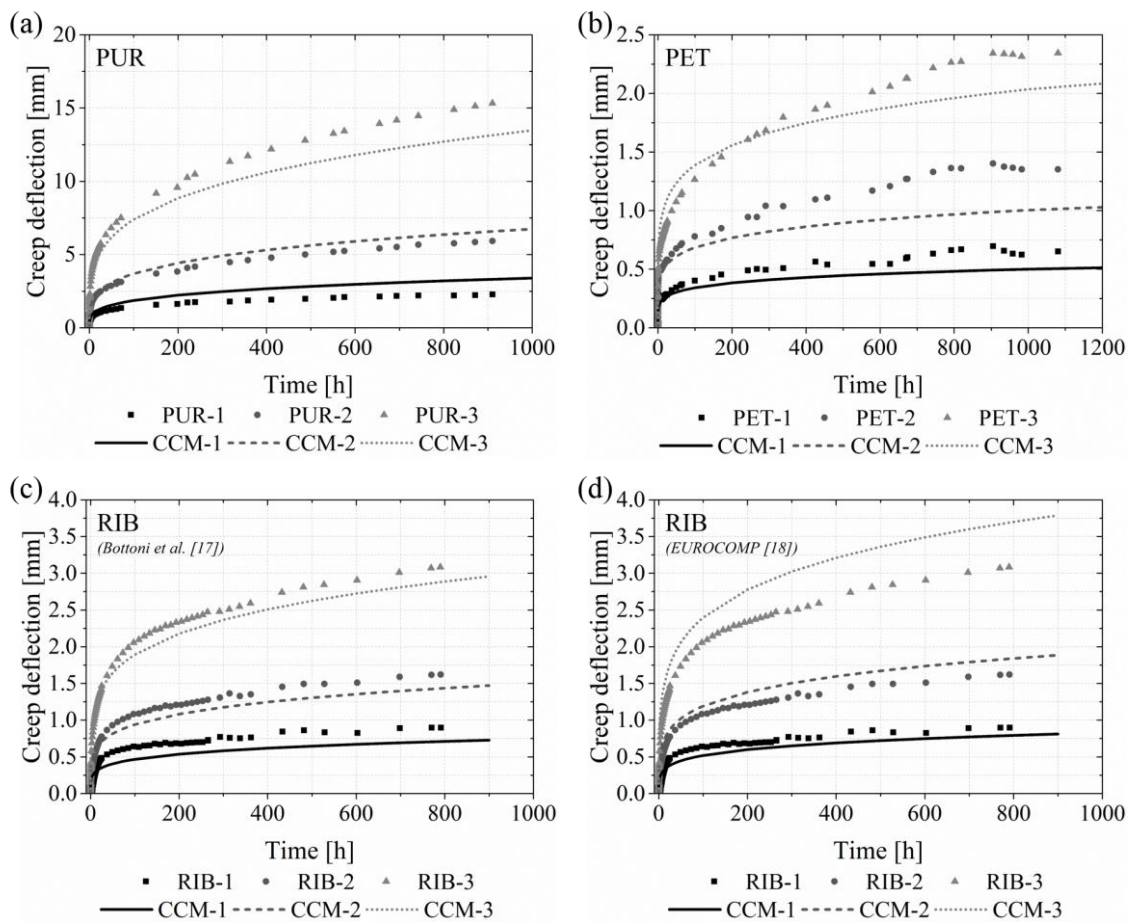


Figure 10.6. Comparison between CCM predictions and experimental creep curves for the: (a) PUR, (b) PET, and (c) RIB panel series.

Additionally, it is interesting to note that (for both formulations) the relative contribution of the ribs to the panel shear stiffness increases over time. This is due to the significantly higher shear modulus reductions in the PUR foam when compared to those experienced by the rib laminates (as previously observed). This result indicates that the shear load is partly transferred from the foam core to the ribs over time, and that consequently the relative

importance of the foam core to the shear stiffness (and load carrying capacity) of the panels is reduced due to creep.

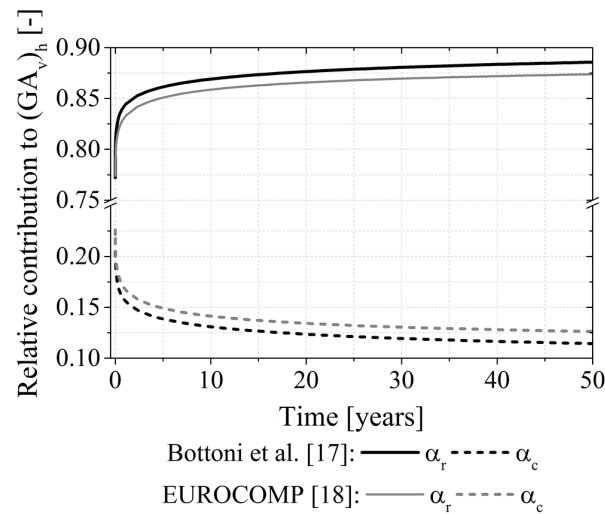


Figure 10.7. Time-dependent relative contributions of the ribs (α_r) and foam core (α_c) to the panel's shear stiffness, $(GA_V)_h$.

10.8. Concluding remarks

Sandwich panels with four different core solutions, namely (i) PUR foam, (ii) PET foam, (iii) balsa wood, and (iv) hybrid PUR foam and GFRP rib cores, were studied regarding their flexural creep behaviour under uniformly distributed loading. This study comprised an experimental investigation regarding the panels and their constituent materials, as well as the analytical modelling of the panels' creep response using a composed creep model (CCM) that predicts the panel creep by taking into account the time-dependent moduli reductions of the constituent materials determined from individual and independent small-scale tests. The following conclusions may be drawn from this study:

- The full-scale flexural creep tests showed that the simple PUR foam cored panels exhibited the highest creep deformations of the four tested configurations, greatly owing to the PUR foam's high creep deformability. The remaining three typologies (PET, BAL, RIB) presented significantly lower creep deformations, which were relatively comparable among the three in terms of overall magnitude.

- The PET foam was found to exhibit quite low creep deformations in shear, even lower than those of the GFRP ribs, making this an interesting material from a limitation of long-term deflections standpoint.
- Balsa wood exhibited almost negligible creep deformations in the shear tests, whereas the BAL panel presented relatively significant creep deflections. Such apparent inconsistency may stem from the material's orthotropic behaviour and the different directions of shearing force in the shear creep and flexural creep experiments. In the sandwich panel cores, balsa wood is subjected to shear forces along directions parallel and perpendicular to the wood fibres, whereas in the shear creep experiments, such forces were mainly applied along the wood fibres' perpendicular direction, which is expected to present a lower creep deformability.
- A simple and easily applied composed creep model (CCM), using as input the elastic moduli reduction factors determined independently from small-scale material testing, was implemented using Timoshenko beam theory and used to predict the creep deflections of the full-scale sandwich panels.
- The CCM results showed reasonable accuracy, further validating this approach for the prediction of the creep behaviour of full-scale sandwich panels. The obtained results are particularly positive, especially when taking into account the model's relative simplicity and ease of use in predicting a very complex phenomenon such as the creep of sandwich panels.
- For the RIB panels, transfer of shear forces from the foam core to the ribs is predicted to occur due to the foam's higher creep compliance, indicating that the foam core's contribution to the shear stiffness (and strength) of the panels reduces over time (for the considered materials).

10.9. References

[1] Keller, T., Rothe, J., de Castro, J., Osei-Antwi, M. (2014). "GFRP-balsa sandwich bridge deck: concept, design, and experimental validation". *Journal of Composites for Construction*, 18(2), 04013043.

- [2] Keller, T., Haas, C. and Vallée, T. (2008). “Structural concept, design and experimental verification of a GFRP sandwich roof structure”. *Journal of Composites for Construction*, 14(4), 454-468.
- [3] Durand, S., Billaudeau, E., Lubineau, G., Chapelle, H. (2012). “Design analysis of GRP panels for the roof of the Haramain High Speed Railway Jeddah Station”. *Proceedings of the 10th International Conference on Sandwich Structures (ICSS-10)*, Nantes, France, August 27-29.
- [4] Davies, J.M. (2001). *Lightweight Sandwich Construction*. Blackwell Science, Oxford, 370 p.
- [5] Correia, J.R., *et al.* (2012). “GFRP sandwich panels with PU foam and PP honeycomb cores for civil engineering structural applications: Effects of introducing strengthening ribs”. *International Journal of Structural Integrity*, Vol. 3(2), pp. 127-147.
- [6] Awad, Z.K., Aravinthan, T., Zhuge, Y. (2012). “Investigation of the free vibration behaviour of an innovative GFRP sandwich floor panel”, *Construction and Building Materials*, Vol. 37, pp. 209-219.
- [7] Mousa, M.A., Uddin, N. (2011). “Flexural behavior of full-scale composite structural insulated floor panels”. *Advanced Composite Materials*, 20(6), 547-567.
- [8] Huang, J.-S., Gibson, L.J. (1990). “Creep of sandwich beams with polymer foam cores”. *Journal of Materials in Civil Engineering*, 2(3), 171-182.
- [9] Garrido, M., Correia, J.R., Branco, F.A., Keller, T. (2014). “Creep behaviour of sandwich panels with rigid polyurethane foam core and glass-fibre reinforced polymer faces: Experimental tests and analytical modelling”. *Journal of Composite Materials*, 48(18), 2237-2249.
- [10] Sheno, R.A., Allen, H.G. and Clark, S.D. (1997). “Cyclic creep and creep-fatigue interaction in sandwich beams”. *Journal of Strain Analysis*, 32(1), 1-18.
- [11] Ramezani, M., Hamed, E. (2013). “Coupled thermo-mechanical creep behavior of sandwich beams – Modeling and analysis”. *European Journal of Mechanics A/Solids*, 42, 266-279.

- [12] Hamed, E., Frostig, Y. (2015). “Geometrically nonlinear creep behavior of debonded sandwich panels with a compliant core”. *Journal of Sandwich Structures and Materials*, doi: 10.1177/1099636215585027.
- [13] Huang, J.-S., Gibson, L.J. (1991). “Creep of polymer foams”. *Journal of Materials Science*, 26(3), 637-647.
- [14] Frostig, Y., Baruch, M., Vilanay, O., Sheinman, I. (1992). “High-order theory for sandwich beam behavior with transversely flexible core”. *Journal of Engineering Mechanics*, 118(5), 1026-1043.
- [15] Fam, A., Sharaf, T. (2010). “Flexural performance of sandwich panels comprising polyurethane core and GFRP skins and ribs of various configurations”. *Composite Structures*, Vol. 92, pp. 2927-2935.
- [16] CEN WG4 (2014). *Fibre Reinforced Polymer Structures: Scientific and Technical Report*, submitted for approval to CEN/TC 250.
- [17] Bottoni, M., Mazzotti, C., Savoia, M. (2014). “Creep tests on GFRP pultruded specimens subjected to traction or shear”. *Composite Structures*, Vol. 108, pp. 514-523.
- [18] Clarke, J.L. (editor) (1996). *Structural Design of Polymer Composites: EUROCOMP Design Code and Handbook*. The European Structural Polymeric Composites Group, E&FN Spon, London, 672 p.
- [19] Gonilha, J.A., Correia, J.R., Branco, F.A. (2013). “Creep response of GFRP–concrete hybrid structures: Application to a footbridge prototype”. *Composites: Part B*, Vol. 53, pp. 193-206.
- [20] National Research Council of Italy (CNR) (2008). *Guide for the design and construction of structures made of FRP pultruded elements*. CNR-DT 205/2007, Advisory Committee on Technical Recommendations for Construction, Rome.

Part V

Conclusions and future developments

Chapter 11

Conclusions and future developments

11.1. Conclusions

11.1.1. General conclusions

Composite sandwich panels present a remarkable combination of high mechanical performance, low self-weight, high durability, free-form design possibilities, thermal insulation abilities, as well as other multifunctional integration opportunities. These factors justify the increased use of composite sandwich panels for structural applications in the construction industry throughout the last decade. This type of solution is gradually evolving from being used in “niche” markets to more widespread applications, warranting a more generalised awareness and interest from the construction industry. In fact, composites in general are slowly gaining the confidence of the construction industry agents, being regarded as a technologically advanced option to solve structural and architectural challenges that would otherwise be unfeasible using traditional construction materials.

The development of standardised practice regarding the production, design and application of composite structures is of the utmost importance for the acceptance of such materials in the construction industry. Significant efforts have already been made to bridge the existing gaps through the drafting of several technical recommendation documents and pre-standards, attempting to regulate the production and design practice for fibre-reinforced polymers (FRPs). However, this process is dependent on the experience gathered from field application of this type of materials, and from research efforts carried out to increase the knowledge base regarding those solutions.

The main goal of the work developed in this thesis was to contribute for the advancement of such knowledge with respect to the application of sandwich panels in the rehabilitation of building floors. The study focused on three main aspects: (i) the assessment of the short-term mechanical performance of suitable panel architectures, (ii) the development of

connection systems, and (iii) the characterisation of the creep behaviour of the sandwich panels. These objectives were globally accomplished, and positive results were obtained showing the viability of using composite sandwich panels for the intended application. Specific conclusions and contributions to the state-of-the-art concerning each of the mentioned research topics are drawn in the following sections. Additionally, based on the experience gathered from the production of the panel prototypes used for this study, some considerations are drafted regarding sandwich panel production methods and their suitability for the manufacturing of floor panels.

11.1.2. Production methods

The multitude of manufacturing processes that can be used to produce FRP composites represents both a strength and a weakness for these materials. Significantly different degrees of reproducibility and consistency of the manufactured parts and their properties may be achieved depending on the production method used. Techniques like hand/wet layup are still often used due to their straightforwardness and versatility, despite the fact that even under a strict quality control the obtained material properties are inferior and less consistent compared to other production methods. On the other end of this spectrum, we find techniques like pultrusion or vacuum assisted resin transfer moulding (VARTM), which are able to produce composites with consistently higher mechanical properties and within strict geometric tolerances. These methods are inherently more suited for the production of composites for civil engineering purposes, as the reliability of mechanical properties and the inexistence of defects are essential to cope with the requirements of the construction industry and to gain the confidence of its agents.

In the development of the current thesis, the vacuum infusion method was used to produce the sandwich panels. It is fair to claim that this technique sits halfway between hand layup and techniques like VARTM or pultrusion in terms of overall quality of the produced parts. It is well suited for cases when a good quality of the parts is required, but it is not viable to produce moulds for the VARTM or pultrusion processes. Such cases may include prototyping of new designs, making “one of” pieces, producing large scale elements, and creating parts with complex shapes.

However, because a rigid exterior mould is not used in the vacuum infusion process, geometric irregularities are prone to occur when using this technique. This was the case for the sandwich panels produced for this thesis. In spite of the expertise of the panels’

manufacturer, the issues related to misalignment of core material blocks (and the consequent eccentricity in the laminates), the warping of the panels along their longitudinal direction, and low geometrical precision in the details of the panel-to-panel connections were among the most important defects encountered during this investigation.

This prompts the conclusion that for an industrialised production of sandwich floor panels a production method different from vacuum infusion should be used. This conclusion is further reinforced by the fact that the vacuum infusion process requires the use of various disposable materials (vacuum bags, sealants, injection tubes, etc.) that represent an additional direct production cost, on top of which there are the costs of workmanship related to the time-consuming layup, infusion, curing and demoulding processes. Given that the final cost of the sandwich floors is also determinant for their applicability in the construction industry, it is essential to adopt production methods that are as efficient as possible. In this context, the pultrusion technique appears to be the most suitable for an industrialised production of sandwich floor panels, as will be further discussed in section 11.2.3.5 of this chapter.

11.1.3. Sandwich panel architectures

From the different panel architectures that were developed and tested in this thesis, those with a simple polyurethane (PUR) foam core presented the lowest mechanical properties³⁴. However, these were also the panels that presented the lowest production cost, with an estimated price of 210 €/m² as produced for this thesis (accounting only for the material costs). On the other hand, the balsa wood cored panels had the best mechanical performance among the simple cored panels, but their production cost was significantly higher than that of the other panels (estimated cost of 485 €/m² as produced for this thesis). In addition, the natural variability of the wood's mechanical properties is reflected on the sandwich panels produced with this core material, which showed higher scatter in properties than the PUR or PET panels. Compared to the PUR and BAL typologies, the panels with a polyethylene terephthalate (PET) foam core presented an intermediate mechanical performance (and intermediate production cost, with an estimated value of 340 €/m²). PET foam also has the advantage of being recyclable. However, its shear modulus is more susceptible to

³⁴ With the exception of the low failure loads of truss-foam cored (TFC) panels, which were affected by the inexistence of fibre continuity between truss webs and face sheets, an aspect which may be improved in their production, presumably leading to significantly higher failure loads.

temperature variations, dropping more steeply with increasing temperature and having a lower glass-transition temperature (T_g) value when compared to the PUR foam.

Having core materials with variable density (and mechanical properties) along the panel span showed a good potential as an optimisation technique. However, the effectiveness of such an approach depends on the location of the applied loads, as having a shear stress distribution in the core different from the design assumptions may lead to excessive stresses in the weaker core segments. In building floors, such a situation may not be acceptable, as the design must take into account not only the uniformly distributed loading case, but also the actions of point loads at the most critical locations. This may limit the admissible density (and mechanical properties) reductions throughout the span.

The truss foam core improved the initial flexural stiffness of the sandwich panels, but posed production difficulties that are hard to overcome in an economically viable way. These are related to the fibre continuity between truss webs and face sheets, which could still be improved by adopting different fibre mat placement schemes. However, the additional labour required for their production and the added weight of glass-fibre reinforced polymer (GFRP) laminates in these panels offset the potential mechanical advantages of this panel typology.

By contrast, the inclusion of GFRP ribs along the panel length showed to be a very effective reinforcement solution, significantly increasing the stiffness and the failure loads of the sandwich panels. The fact that the ribs are very easily incorporated into the panel architecture and that they can also be part of the panel-to-panel connection system further increased their suitability for use in the sandwich floor panels.

11.1.4. Connection systems

In this thesis, connection systems for the sandwich panel floors were proposed and analysed. These connections included those between adjoining sandwich panels (panel-to-panel connections) and those between the floors and the load-bearing walls (panel-to-wall connections). Their performance was assessed through experimental, numerical and analytical investigations. For each connection type, a literature review was carried out to assess the state-of-the-art, based on which the most suitable connection systems were developed.

For the panel-to-panel connections, the adopted Z-joint system was based on the current adhesively bonded connection technology used for pultruded FRP decks. This type of connection was adapted for use in sandwich floor panels, and its performance was assessed accordingly. This was made considering two different core materials for the sandwich panels, a softer PUR foam and the significantly stiffer balsa wood.

Regarding the panel-to-wall connections, the current timber floor rehabilitation practice was used as the starting point for the development of novel connection systems. Steel angles embedded in the building walls are frequently used in the rehabilitation of timber floors, serving as support to the floors, increasing their in-plane stiffness, and conferring higher out-of-plane stiffness to the supporting masonry walls. This solution was adopted for the sandwich panel-to-wall connections considering multiple variants of the basic system, namely by adopting a single (bottom) steel angle or two (top and bottom) steel angles, and by assessing the performance of the panel to steel angle connections by using bolts, epoxy adhesive, or a combination thereof. The use of such steel angles afforded several advantages, providing a cost-effective connection, presenting multiple structural benefits, and constituting a technological bridge between traditional timber floor rehabilitation techniques and the novel sandwich panel floor technology. Furthermore, two different types of core material were also considered in the assessment of these connections systems, namely PUR foam and balsa wood. This was aimed at evaluating the connections' performance for sandwich panels with significantly different mechanical behaviours.

It was found that the proposed connection systems exhibited potential for structural application in a sandwich panel floor system for use in building rehabilitation, having shown an adequate mechanical behaviour. The adhesive connections were found to be stiffer by comparison with the bolted solutions, albeit generally exhibiting brittle failure. Bolted connections showed lower rotational stiffness and strength, but failed progressively through the gradual damage accumulation in different parts of the system (bolts, angles, panel faces and core). This feature may be interesting from an energy dissipation standpoint (*e.g.*, under seismic actions), and constitutes an interesting topic for future research.

In addition, the proposed connections also further improved the overall structural behaviour of the floors, especially when considered both the top and bottom steel angles. In fact, the increases in floor stiffness due to the panel-to-panel connections, or the deflection reductions

due to the rotational stiffness of the panel-to-wall connections, proved to actively improve the structural performance of the floors.

As expected, the use of stiffer core materials, such as balsa wood, generally improved the overall performance of the sandwich panel floors and their connections. Regarding the panel-to-panel connections, for example, having a balsa wood core allowed for better mechanical properties along the transverse direction of the panels and a further exploitation of the laminate's strength (failures were shifted from the core to the laminates at the connection region). Along the longitudinal direction, the balsa wood core allowed for a more balanced distribution of shear forces between core and ribs, however not increasing substantially the overall panel stiffness. Yet, the PUR foam cored panels also showed an adequate performance, also benefiting from the improved structural behaviour provided by the connection systems, prompting the conclusion that a stiffer core material does not necessarily guarantee the viability of the sandwich floors, as long as the effect of the connections is considered in the floor design (as it should).

11.1.5. Creep behaviour

A comprehensive investigation was carried out concerning the viscoelastic behaviour of the sandwich panels and their constituent materials. This study included creep tests of the core materials in shear and of the facing GFRP laminates in bending. The effects of service temperatures in the range of 20 °C to 28 °C on the viscoelastic response of the GFRP laminates and the PUR foam were also studied. Furthermore, full-scale sandwich panels with different core solutions were tested regarding their creep behaviour under uniformly distributed loads. These included the PUR, PET, BAL and RIB panel typologies, all having similar face sheets made of the same type of GFRP laminate. As such, differences in their creep behaviour may be mostly attributed to their different core materials.

For all of the tested materials and panels, the observed creep behaviour followed a power law development with time, whether in terms of axial strains, shear strains, or vertical displacements. Findley's power law was used to fit and model the experimental results, generally showing a very good agreement with the test data obtained.

The PUR panels exhibited the highest creep deformations among all tested panel types, owing to the very significant viscoelasticity of the PUR foam, also observed in the shear creep tests of individual foam specimens. On the other hand, the PET, BAL and RIB panels

exhibited much lower deformation increases due to creep, which were comparable among these three panel types.

The PET foam exhibited a surprisingly low viscoelasticity in the shear creep tests, which was confirmed in the full-scale panel tests. Indeed, being a polymeric foam, *a priori* one expected it to present higher viscoelasticity. However, its viscoelasticity was less pronounced than that measured in GFRP laminates subjected to shear, where a solid polymer is further reinforced with glass-fibres that have negligible creep response. However, it was not possible to deepen the study of this material's viscoelastic response under the scope of the current thesis.

Concerning the viscoelasticity of the balsa wood, the results from the shear creep experiments and the full-scale flexural creep tests were found to be inconsistent with one another. In the first test, the balsa wood presented almost negligible creep deformations (impossible to measure at times, being lower than the instrumentation precision). Conversely, significant creep deflections were observed for the BAL panels, suggesting that the balsa wood core should exhibit measurable viscoelastic deformations. This apparent inconsistency may be explained by the material's orthotropic behaviour and the different directions of shearing force in the shear creep and flexural creep tests. Higher creep deformability is expected to be found under shear forces parallel to the wood fibres, as the wood's properties along this direction are weaker, compared to when shear forces are perpendicular to those fibres. In the sandwich panel cores, balsa wood experiences shear forces along both directions, whereas in the shear creep experiments, such forces were mainly applied along the wood fibres' perpendicular direction. However, this hypothesis is yet to be experimentally tested, due to the fact that under the scope of the current thesis it was not possible to conduct further creep experiments on balsa wood specimens.

The longitudinal ribs proved to substantially improve the creep behaviour of the sandwich panels when compared to the PUR typology (with the same core material and no rib reinforcement). This is due to the fact that the ribs govern the overall creep response of the panels in shear, having higher stiffness and lower viscoelasticity than the PUR foam. This result enables the use of PUR foam as core material in sandwich floor panels (as an alternative to more expensive materials), as without ribs the shear creep deformability of panels made of this foam would be potentially too high for such an application. This result, combined with the integration of longitudinal ribs in the panel-to-panel connections, further

supports this reinforcement solution as one of the most promising ones for application in building floors.

Regarding the effects of service temperature on the creep response of the PUR foam and the GFRP laminates, it was found that for relatively small temperature amplitudes, significant differences in viscoelastic response exist in the two materials. In fact, small increases in temperature prompted significant increases in the observed creep deformations. In order to model this effect, the generalised Findley's power laws for each material were adapted to include creep parameters given by temperature dependent Arrhenius equations. In the case of the PUR foam, a clear temperature dependence was observed in the creep amplitude and time exponent values of the power laws. For the GFRP laminates, this dependence was only evident for the creep amplitude values, while the creep exponents were not significantly affected by temperature variations within the adopted range (20 °C to 28 °C).

Finally, a composed creep model (CCM) was proposed to predict the creep behaviour of the full-scale sandwich panels based on the results from the small-scale experiments on the core materials and facing laminates. This model, based on Timoshenko's beam theory, uses time- and temperature-dependent moduli reduction factors determined from small-scale testing to affect the shear moduli of the core materials and ribs, as well as the Young's modulus of the facings, thus simulating the effects of creep through equivalent material stiffness reductions. The model's predictions compared well with the experimental creep curves obtained from the full-scale tests on different types of panels (materials and architecture), indicating the viability of this approach to model the long-term creep deformations in sandwich panels.

11.2. Future developments

11.2.1. Connection systems

The work carried out for this thesis provided an assessment of the most suitable connection technologies for use in sandwich panel floors. For the panel-to-panel connections, an adhesively bonded joint was deemed as the best solution from a structural stand point. However, from an economical perspective, the costs associated with the additional epoxy adhesives, their application, and the time that is required for them to cure before the floors may be used reduce the floor solutions competitiveness. Thus, it would be useful to develop

panel-to-panel connection systems that do not require adhesives to provide a solid joint between panels (*e.g.*, “snap-fit” or bolted connections). This would further reduce the global cost of the floors and the time necessary for their installation.

Concerning the panel-to-wall connections, the experiments and modelling efforts carried out took into account a rigid support for the steel angles. In the experiments, this rigid support (a HEB 300 steel profile) had the same bending stiffness as a typical 1.0 m thick stone rubble masonry wall. However, stone rubble masonry is very heterogeneous, and this can locally affect the actual connections between the walls and the steel angles. Furthermore, it is necessary to assess the best techniques for embedding the steel angles in the building walls. Consequently, it would be useful to further test the panel-to-wall connections using representative stone rubble masonry substrates, so as to evaluate the above mentioned aspects.

11.2.2. Creep behaviour

The extensive creep study carried out for this thesis provided very important results for the characterisation of this phenomenon in sandwich panels. However, some of the obtained results raised additional questions regarding the viscoelastic response of the sandwich panels and their different constituent materials. It is important to fully understand why balsa wood presented inconsistent results between the small-scale shear creep tests and the full-scale panel tests. To this end, additional shear creep tests could be carried out, this time considering shear forces applied parallel to the wood fibres, to assess the differences in creep behaviour according to material orientation.

As previously mentioned, the PET foam’s viscoelasticity was quite limited, a result that was unexpected given the polymeric nature of the material, as well as its foamed physical structure. It would be interesting to further study this material’s viscoelasticity, understanding its creep deformation mechanisms and how these may justify such low creep deformations.

Regarding the sandwich panel facings, their creep response was characterised under flexural loads, under the hypothesis that the laminate’s flexural creep response presents an overall development comparable to that of the ensemble of the top and bottom face sheets in the sandwich panel under bending. However, such simplifying hypothesis still requires experimental validation, which could be achieved through an independent assessment of the

creep behaviour of the laminates in compression and in tension, and how these compare with the laminate's flexural creep behaviour.

The PUR foam and GFRP laminates were characterised regarding their creep behaviour under different service temperatures. This effort showed that temperature importantly affects the viscoelasticity of these two materials. It would be useful to extend this study for temperatures beyond the 20 °C to 28 °C range considered in this thesis. Although the range considered in this thesis already covers the temperatures most likely to be found in normal service conditions (indoors), repeating the study for a wider temperature range (*e.g.*, 15 ° to 35°C) would provide results for other conditions (namely, outdoors) and further validation of the analytical creep models that were proposed. Furthermore, it would be useful to extend this effort to other materials typically used in sandwich construction, and also to full-scale sandwich panels.

Relative humidity (RH) is an additional factor known to influence the creep behaviour of polymeric materials. In this thesis, the creep experiments were conducted under relatively controlled RH values, typically ranging between 40-60%. However, the influence of this factor on the viscoelastic response of the sandwich panels and their constituent materials was not systematically studied. Due to this factor's natural variability (RH variations can have a reasonably wide amplitude under normal service conditions), this parameter's effect on the creep of sandwich panels should be the subject of future research. Based on the results obtained, the CCM model could be extended to include the influence of RH.

Another aspect related to the creep behaviour of sandwich panels that may be studied is their creep response for complex loading histories, including incremental load applications, and recovery after partial and/or total removal. Such a characterisation is important to take into account the progressive load application and partial load removals that occur during the different phases of building construction.

Finally, it would be useful to further validate the CCM for different panel cross-sections, to confirm the model's ability to predict the creep response of sandwich panels with different face sheet, core and rib dimensions.

11.2.3. Further research topics

11.2.3.1. Seismic actions

In this thesis, the behaviour of the sandwich panels under vertical loads was assessed. However, in building floors, the action of horizontal loads is also particularly relevant, especially for stone rubble masonry buildings located in seismic regions. Consequently, the characterisation of the in-plane behaviour of the panels and of the fully assembled floors is very important, in particular regarding the influence of the panels on the overall response of the structure. This represents an area of major interest in the context of building rehabilitation, given that the floors are expected to exhibit diaphragm behaviour, effectively redistributing loads between the building's walls during seismic activity. This general research need also applies to the particular case of the panel-to-panel and panel-to-wall connections, which need to be able to withstand the subsequent in-plane loads. Additionally, it is important to evaluate the influence of those connections on the global response of the floors, and on the interactions between the floors and the building envelope.

11.2.3.2. Membrane stresses

In-plane stresses may also develop within the panels, stemming from membrane stresses that develop in the floors due to the restrictions imposed by the connections to the walls along the floor perimeter. The importance of such stresses needs to be assessed, as well as their effect on the global behaviour of the floors. On one hand, this effect may help limit the floor's total vertical deflections. On the other hand, if it is found to be detrimental to the performance, safety, or durability of the sandwich panel floors, methods of mitigating its consequences should be developed.

11.2.3.3. Punching and localised loads

The sandwich panel floors may be subjected to localised loads and this must be accounted for in their design. It is essential to determine how such loads distribute throughout the panel area and along its thickness in order to achieve optimised panel designs. In fact, the load degradation throughout the panel thickness, and its redistribution over areas greater than that where loading is directly applied to (due to the relatively rigid nature of the face sheets, supported on a relatively flexible foundation – the core material) will affect the values of the maximum allowable point loads acting on the floors. The factors affecting such stress

distributions must be determined, their effects quantified, and appropriate closed-form design equations to account for this type of loading need to be developed.

11.2.3.4. Fire behaviour and protection systems

During the development of this thesis, the effects of temperature on the physical properties and mechanical behaviour of the sandwich panels and their different constituent materials was often addressed. Throughout the different investigations, it was clear that temperature significantly affects the elastic and viscoelastic properties of such materials, with higher temperatures leading to important reductions of the elastic properties and increased viscoelasticity, in agreement with what is typically observed for such polymeric materials.

This prompts a legitimate concern regarding how such sandwich panel floors will behave under fire exposure, a critical issue to constructions made or incorporating FRP materials [1,2]. It is expectable that without adequate fire protection systems, the fire endurance periods achieved might not be enough to comply with building code requirements. Consequently, it is of utmost importance to characterise the response of the sandwich panels under fire exposure, and to assess the performance of different fire protection systems to use with the floor system, possibly integrating them into the sandwich panel architecture or in plenum spaces provided by drop-down ceilings.

11.2.3.5. Acoustic behaviour

Low weight building floors, such as the sandwich panel floors proposed in this thesis, present several advantages over heavier traditional solutions (as previously discussed). However, regarding acoustic behaviour, the low mass of such systems can be a disadvantage. In fact, to guarantee compliance with building acoustics regulations, it is very likely that additional measures are necessary to improve the performance for both airborne and impact sound insulation. These may include the installation of floating floors and/or drop-down ceilings to damp sound transmission. The purpose of such measures can be two-fold, serving also as a means to incorporate passive and/or active fire protection systems, in connection to what is mentioned in the previous section (11.2.3.3). However, the effectiveness of such measures in improving the acoustic performance of the sandwich panel floors needs to be assessed, constituting a critical point for their applicability in sound sensitive applications in the construction industry.

11.2.3.6. Optimisation of production methods

The feasibility and success of a composite sandwich floor system depends, among other factors, on the quality and consistency of the produced panels. Their mechanical properties must be reliable and they must not have significant geometric imperfections. Additionally, the manufacturing process needs to be optimised in terms of the required labour and time per production volume, so as to lower production costs.

The production methods that best respond to these requirements need to be assessed. Production using the pultrusion process appears to be a promising solution, allowing for high quality materials with consistent properties and geometries. However, this process also has its limitations in terms of the maximum cross-sectional dimensions achievable or regarding the integration of the core material into the pultruded GFRP box. For expanded foam cores, such as those using PUR foam, one possibility is to inject and expand the foam into the finished GFRP box. However, this may pose adhesion problems at the face-core interface, leading to low debonding stresses between the two components. Alternatively, pultrusion processes in which the core block is fed through the mould and the GFRP box is moulded against the core, already used before, may constitute a better way of producing sandwich panels by pultrusion. Such production related aspects could be further assessed in the scope of future research.

11.2.3.7. Full-scale installation

Finally, it would be useful to develop a full-scale pilot installation of a sandwich panel floor, in which the developed floor system could be applied in a building rehabilitation project, or alternatively in a large scale laboratorial installation. This would provide an excellent opportunity to assess the practical constructability and ease of installation of the proposed floors, and accordingly to address possible improvement needs. It would also allow for an evaluation of the structural performance of the floors when fully assembled, allowing them to function as two-way slabs. The results from such an installation would provide valuable experimental data, helping in the development of adequate design procedures and improvement of the technological aspects associated with the floors and their application in real buildings.

11.3. References

- [1] Correia, J.R., Bai, Y., Keller, T. (2015). “A review of the fire behaviour of pultruded GFRP structural profiles for civil engineering applications”, *Composite Structures*, Vol. 127, pp. 267-287.
- [2] Firmo, J.P., Correia, J.R., Bisby, L. (2015). “Fire behaviour of FRP-strengthened reinforced concrete structural elements: a state-of-the-art review”, *Composites Part B: Engineering*, Vol. 80, pp. 198-216.